Magnetisation Dynamics of Nanoscale Magnetic Materials and Spintronics

Submitted by **Prim Gangmei**, to the University of Exeter as a thesis
for the degree of Doctor of Philosophy in Physics, February 2012.

I certify that all material in this thesis which is not my own work has been identified and that no material has previously been submitted and approved for the award of a degree by this or any other University.

Prim gangmei
.....

Abstract

The magnetisation dynamics of a single square nanomagnet, the interaction between a pair of nanodiscs, a partially built writer structure and a range of magnetic tunnel junction sensor heads were studied using Time Resolved Scanning Kerr Microscopy (TRSKM) and four probe contact DC electrical transport measurements. Large amplitude magnetisation dynamics of a single square nanomagnet have been studied by TRSKM. Experimental spectra revealed that only a single mode was excited for all bias field values. Micromagnetic simulations demonstrate that at larger pulsed field amplitudes the center mode dominates the dynamic response while the edge mode is almost completely suppressed. The magnetisation dynamics occurring in a system comprised of two laterally separated magnetic nano-discs were also investigated. The polar Magneto-Optical Kerr Effect was used to measure the dynamic response of each disc independently so as to demonstrate that dynamic dipolar interactions between non-uniform spin wave modes in the different discs may be identified from the difference in their phase of oscillation. Results show a stronger dynamic dipolar interaction than expected from micromagnetic simulations highlighting both the need for characterisation and control of magnetic properties at the deep nanoscale and the potential use of dynamic interactions for the realization of useful magnetic nanotechnologies.

TRSKM measurements were made simultaneously of the three Cartesian components of the magnetisation vector, by means of a quadrant photodiode polarisation bridge detector, on partially built hard disk writer structures. The rise time, relaxation time, and amplitude of each component has been related to the magnetic ground state, the initial torque, and flux propagation through the yoke and pole piece. Dynamic images reveal “flux-beaming” in which the magnetisation component parallel to the symmetry axis of the yoke is largest along that axis. A comparison of the magnetisation dynamics excited with different pulsed excitation amplitudes was also made. The results shows that more effective flux beaming is observed for higher pulse amplitudes.

Lastly the microwave emission of Tunnel Magnetoresistance (TMR) nanopillars has been measured using a four probe contact DC electrical transport measurement technique as a magnetic field is applied in the plane of the film at different angles (ϕ_H) with respect to the easy axis. Experimental spectra revealed that a more complicated spectrum containing several modes is observed as ϕ_H is increased. The modes were identified as edge and higher order modes from the statistical distribution of modes from different devices and micromagnetic simulations. The in-plane and out-of-plane components of the Spin Transfer Torque (STT) were estimated by analytical fitting of experimental data for the lowest frequency edge mode for the value of ϕ_H where the amplitude of the said mode was a maximum and its frequency a minimum. The estimated values are larger than expected perhaps due to the macrospin approximation made in deriving the analytical model.

The results presented in this thesis can contribute to the understanding of magnetisation dynamics in industrially relevant data storage devices as well as the realization of a dipolar field coupling mechanism for arrays of nanooscillators.

Acknowledgements

I would like to thank my supervisor Prof Robert J. Hicken for accommodating me on this research project and providing the support and guidance throughout my PhD that has allowed me to make progress on many interesting projects. I will always be thankful to Rob for his encouragement, dedication, suggestions and advice. Finally I would like to thank Rob for his time to read and comment on this thesis and the short time in which he was able to do it. Thank you very much Rob.

I would like to acknowledge Dr Paul S. Keatley without whose help I may not be able to develop the experimental skills and understanding needed make Time Resolved Scanning Kerr Microscopy (TRSKM) measurements, which has been the main experimental tool during my PhD. He is the person whom I learned everything from scratch about the TRSKM. I would like to thank Paul for his patience that allowed me to understand the experimental concepts as well as his encouragement, valuable comments and suggestions throughout. Thank you Paul.

I would like to thank our past group member Dr Andreas Neudert for introducing me to electrical transport measurement techniques and allowing me to understand the underlying physics and supporting simulations. Without him that part of my research work may not of been fulfilled. Thank you Andreas.

I would like to thank Prof Peter Vukusic for agreeing to be my PhD mentor and for his encouragement and suggestion. Thank you Peter.

Thanks to Mr Russell Edge for the excellent workshop support that is required to build a complete experimental setup. I would also like to thank all other members of the mechanical workshop in Exeter for there help during my PhD. Thank you all.

Dr J. Grollier (Unité Mixte de Physique CNRS/Thales and Université Paris Sud 11, 1 av. A. Fresnel, 91767 Palaiseau, France) and C. Ulysse (Laboratoire de Photonique et de Nanostructures (LPN), CNRS PHYNANO team, Route de Nozay, 91460 Marcoussis, France) to whom I would like to express my appreciation for providing a high quality of sample for TRSKM characterization.

Further I would like to extend my thanks to Dr M. A. Gubbins (Research & Development, Seagate Technology, 1 Disc Drive, Springtown Industrial Estate, Derry, Northern Ireland BT48 0BF), Dr P. J. Czoschke and Dr R. Lopusnik (Recording Heads Operation, Seagate Technology, 7801 Computer Avenue South, Bloomington, Minnesota 55435, USA) for supplying their excellent quality write head structures and magnetic tunnel junction samples for both TRSKM and electrical transport characterization.

A special thanks goes to my colleagues and friends Max Marcham and Tom Duckworth for their time spent making corrections to, and suggestions on, the writing style of this thesis without their effort this work may not been completed in time. Thank you Max and Tom.

Thanks to all my colleagues in the Electromagnetic Materials Group and to those who I have the pleasure of working with outside the group for their valuable contributions to the work presented in this thesis. It would be impossible to have carried out such work on my own. Thank you all.

I would like to thank my parents for their inspiration. Without their love and support I may not be here today.

For financial assistance, I graciously thank the Physics Dept., University of Exeter, and Rob, and acknowledge the scholarship assistance of the Exeter University in the Exeter Research Scholarship (ERS) award.

List of Contents

List of Publications

1. P.S. Keatley, P. Gangmei, M. Dvornik, R.J. Hicken, J. Grollier, C. Ulysse, J.R. Childress and J.A. Katine, *Bottom Up Magnonics: Magnetization Dynamics of Individual Nanomagnets*, Submitted as a chapter in ‘‘Topics in Applied Physics’’.

2. P. S. Keatley, P. Gangmei, M. Dvornik, and R. J. Hicken, J. Grollier, and C. Ulysse, *Isolating the dynamic dipolar interaction between a pair of nanoscale ferromagnetic disks*, Submitted to Physical Review Letters.

3. P. Gangmei, P. S. Keatley, W. Yu, R. J. Hicken, M. A. Gubbins, P. J. Czoschke, R. Lopusnik, *Time- and vector- resolved Kerr microscopy of hard disk writers*, Applied Physics Letters 99, 232503 (2011).

4. Keatley PS, Gangmei P, Dvornik M, Hicken RJ, Childress JR, Katine JA. *Large amplitude magnetization dynamics and the suppression of edge modes in a single nanomagnet*, Applied Physics Letters 98, 082506 (2011).

5. Keatley PS, Kruglyak VV, Gangmei P, Hicken RJ. *Ultrafast magnetization dynamics of spintronic nanostructures*, Philos Transact A Math Phys Eng Sci, volume 369, no. 1948, pages 3115-3135(2011).

List of Figures

List of Tables

Declaration

The work presented in this thesis was undertaken in collaboration with colleagues from the Electromagnetic Materials group in Exeter and from further afield. Their contributions will be acknowledged at the point at which they enter into this thesis.

Chapter 1 Introduction

The introductory chapter describes the content of the thesis and is entirely my own work.

Chapter 2 Background concept of Magnetism

The ideas and concepts required to understand the latter chapters of this thesis were compiled by myself following a literature survey. My sources are referenced throughout.

Chapter 3 Experimental techniques

The discussion of the background magneto-optical effects presented in this chapter is my own work. Where inspiration was taken from the literature it has been referenced thoroughly. The time-resolved experimental apparatus used in Exeter was set up by my supervisor Prof Rob Hicken, as well as Dr Jing Wu, Dr Ralph Wilks, Dr Anjan Barman, and Dr Volodymyr Kruglyak . The current version of the Time Resolved Scanning Kerr Microscope (TRSKM), which was used throughout the TRSKM studies in this thesis, was set up by Dr Paul Keatley before I started my PhD project. In chapters 4 and 5 the experimental set up was the work of Dr Keatley. For the TRSKM studies in chapter 6, I added the electrical excitation to the existing TRSKM setup with guidance from Dr Paul Keatley and Prof Hicken. Data acquisition software was written by Prof Hicken, Dr Barman, Dr Wilks, and Dr Keatley. Dr Andreas Neudert set up the electrical transport measurement apparatus used in chapter 7 under the supervision of Prof Hicken before I started my PhD project.

Chapter 4 Large amplitude magnetisation dynamics and the suppression of edge modes in a single nanomagnet

The micro and nanoscale magnetic discs were fabricated by Dr Jeffrey Childress and Dr Jordan Katine at Hitachi Global Storage Technologies San Jose Research Center, California. The scanning Kerr microscope was set up by Dr Paul Keatley. The experimental data was acquired by Dr Paul Keatley and myself. The analysis was completely performed by Dr Paul Keatley. The micromagnetic simulation was performed by Dr Paul Keatley and Dr Mykola Dvornik.

Chapter 5 Isolating the dynamic dipolar interaction between a pair of nanoscale ferromagnetic discs

The pairs of nanoscale ferromagnetic discs were fabricated by Dr J. Grollier (Unité Mixte de Physique CNRS/Thales and Université Paris Sud 11, 1 av. A. Fresnel, 91767 Palaiseau, France) and C. Ulysse (Laboratoire de Photonique et de Nanostructures (LPN), CNRS PHYNANO team, Route de Nozay, 91460 Marcoussis, France). Dr Paul Keatley and myself performed the experiments. Dr Keatley carried out the data analysis, Dr Keatley and Dr Dvornik performed the micromagnetic simulations and analysis. Prof Hicken generated the macrospin model and associated Matlab code. Dr Keatley performed the macrospin calculations and analysis.

Chapter 6 Time resolved scanning Kerr microscopy of the vector magnetisation within hard disk writer structures

The partially built writer structures were provided by Dr M. A. Gubbins (Research & Development, Seagate Technology, 1 Disc Drive, Springtown Industrial Estate, Derry, Northern Ireland BT48 0BF), Dr P. J. Czoschke and Dr R. Lopusnik (Recording Heads Operation, Seagate Technology, 7801 Computer Avenue South, Bloomington, Minnesota 55435, USA). I set up the additional electrical excitation and modulation technique and integrated it with the current TRSKM which was setup by Dr Paul Keatley. The measurement and analysis in this chapter was done by myself.

Chapter 7 Thermal and spin transfer torque excitation of precessional modes in the noise spectra of magnetic tunnel junction recording head sensors

The magnetic tunnel junction device was provided by Dr Xin Cao (Research & Development, Seagate Technology, 1 Disc Drive, Springtown Industrial Estate, Derry, Northern Ireland BT48 0BF). The electrical transport measurement technique was setup by Dr Neudert. He also wrote the Labview data acquisition programme. The measurements were performed largely by myself with some assistance from Max Marcham, while the analysis was performed by myself. I carried out the micromagnetic simulations myself. The analytical model for the susceptibility in the linear regime was developed by Prof Hicken and applied to the interpretation of the experimental data by myself.

Chapter 1

Introduction

This thesis is divided into 7 full chapters in addition to this introductory chapter. Chapter 2 describes the background concepts and theory upon which the analysis in latter chapters is based, Chapter 3 provides an in-depth discussion of the experimental setups used to make the Time Resolved Scanning Kerr Microscopy (TRSKM) and electrical transport measurements described later in the thesis. Chapters 4 - 7 contain the various experimental data sets obtained over the course of my PhD project. Chapter 8 summarises the main results of the thesis and discusses potential future work.

Chapter 2 introduces the aspects of the theory of magnetism that are required for the analysis in latter chapters to be understood. It also serves to provide the motivation for the study of magnetisation dynamics in macroscopic and microscopic magnetic systems.

In chapter 3 the experimental setup for the TRSKM and electrical transport measurements are discussed in detail. The origins of the Magneto-Optical Kerr Effect (MOKE), upon which the TRSKM experimental setup is based, is discussed, as is the method for detecting all three components of the magnetisation vector simultaneously using a quadrant vector bridge detector. The four probe technique used to make electrical transport measurements, and the interfacing of different equipment in the experimental set up is presented and discussed.

Chapter 4 describes the Time Resolved (TR) Kerr signals taken from a single square nanomagnet. It is well known that the magnetisation dynamics of an in-plane magnetized square nanomagnet can be complicated by the excitation of centre- and edge-type modes when a bias magnetic field is applied along the element edge. The two modes can also coexist for a range of bias fields while the amplitude of the response shifts from the centre to the edge mode as the bias field is decreased. In this chapter results obtained using TR Kerr measurements and micromagnetic simulations demonstrate that large angle magnetisation dynamics in a single nanomagnet can lead to a dynamic response that is dominated by the quasi-uniform centre mode, while the non-uniform edge mode is almost completely suppressed.

Chapter 5 describes an investigation of the dynamic dipolar interaction between two laterally separated magnetic nano-discs. The dynamic dipolar interactions between non-uniform spin wave modes in the different discs may be identified from the difference in their phase of oscillation. TRSKM is used to measure separately the phase resolved response of each nanomagnet within the pair with a high degree of spatial resolution, mechanical stability and sensitivity. Supporting micromagnetic simulations are also presented and the potential use of dynamic interactions for the realization of useful magnetic nanotechnologies is discussed.

In Chapter 6 it is demonstrated that TRSKM is a suitable tool for making wafer level measurements of magnetisation dynamics within the yoke and pole piece of partially built hard disk writer structures. The magnetisation dynamics of the hard disc writer structure are characterised by acquiring three Cartesian components of the magnetisation vector simultaneously using the quadrant vector bridge detector described in Chapter 3. The rise time, relaxation time and amplitude of each component has been related to the magnetic ground state, the initial torque, and flux propagation through the yoke and pole piece. Dynamic images reveal "flux-beaming" in which the magnetisation component parallel to the symmetry axis of the yoke is largest along that axis.

Chapter 7 discusses the electrical transport measurements made on magnetic tunnel junction recording head sensors. Tunnel Magnetoresistance (TMR) nanopillars have been measured as a magnetic field is applied in the plane of the film at different angles (ϕ_H) with respect to the easy axis. The device spectrum shows a more complicated spectrum that contains several modes as ϕ_H is increased. The modes are identified as edge and center modes from comparison with micromagnetic simulations and through consideration of the statistical distribution of mode frequencies from many devices. The device shape irregularity is invoked as the cause of the randomness of the edge frequencies and the absence of any such distribution for the centre mode frequencies. The in-plane and out-of-plane components of the spin transfer torque (STT) for the 1st mode (edge mode) for three MTJs were extracted by model, fitting to an analytical model.

Chapter 8 summarizes the work presented in this thesis. Phase locking of an array of STOs using dipolar fields, so as to achieve microwave output power at the levels needed for industrial applications, is discussed as possible future work stemming from this thesis.

Chapter 2

Background concept of Magnetism

2.1 Atomic Origins of magnetism

A common atomic picture of magnetic matter involves electrons orbiting around the atomic nucleus. This allows the analogy with charged particles circulating in a loop of wire to be drawn. The dipole moment created by such a circulating current is given by $m=IA$ where I is the current in the wire, A is the area of the loop and the dipole moment is perpendicular to the plane of the loop as shown in Figure 2.1.1. Assuming that the current is generated by electrons orbiting the nucleus at radius (r) with velocity (v)then the magnitude of the current is given by

$$I = \frac{ev}{2\pi r} = -\frac{|e|v}{2\pi r}. \tag{2.1.1}$$

The resulting dipole moment and angular momentum (L) are then given by $m_{orbital} = -\frac{|e|}{2m^*}L$ and m^*vr respectively where e and m^* are the charge and effective mass of the electron. However, quantum mechanics states that the component of the orbital angular momentum projected along the magnetic field direction can only take a set of discrete values given by

$$m^*vr = m_l\hbar \tag{2.1.2}$$

where $\hbar$ is the reduced Planck's constant and m_l is a quantum number whose values are determined by the following relationship with the orbital quantum number l: m_l = -l, -l+1, …, 0,…, l-1, l.

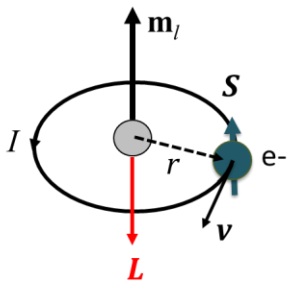

Figure 2.1.1 Schematic of an electron spin circulating around a circular conducting loop.

By re-arranging equation (2.1.2) for velocity and substituting from equation (2.1.1) the magnetic dipole moment along the field axis is given by

$$\mathbf{m}_{orbital} = -\frac{|e|\hbar}{2m^*}\mathbf{m}_l = -\mu_B \mathbf{m}_l \, . \tag{2.1.3}$$

The quantity $\mu_B = \frac{|e|\hbar}{2m^*}$ is known as the Bohr magneton. It is the elementary unit of the orbital magnetic moment of an atom and is equal to 9.274×10^{-24}J/T. A magnetic field can be applied with any orientation relative to the electronic orbit and therefore the orbital angular momentum, **L**, can have any relative orbit to the applied field **H**. A torque, $\mathbf{m}_{orbital} \times \mathbf{H}$ [1], is exerted upon the dipole by the applied field giving the equation of motion

$$\frac{d\mathbf{m}_{orbital}}{dt} = -\frac{e}{2m^*}\mathbf{m}_{orbital} \times \mathbf{H} \tag{2.1.4}$$

The magnetic moment precesses about **H** with an angular frequency $\omega_L = -\frac{e}{2m^*}H$ where ω_L is known as the Larmor frequency[2].

Zeeman effect

The energy of the magnetic moment within an applied magnetic field is given by

$$E = -\mu_0 \mathbf{m}_{orbital} \cdot \mathbf{H} = \mu_0 \frac{e\hbar}{2m^*} m_l H_z \tag{2.1.5}$$

The energy level separation being given by

$$\Delta E = \mu_0 \frac{e\hbar}{2m^*} m_l H = \mu_0 \mu_B H \Delta m_l. \tag{2.1.6}$$

The lifting of the energy degeneracy in the presence of a magnetic field results in splitting of the spectral lines and is known as Zeeman effect[3].

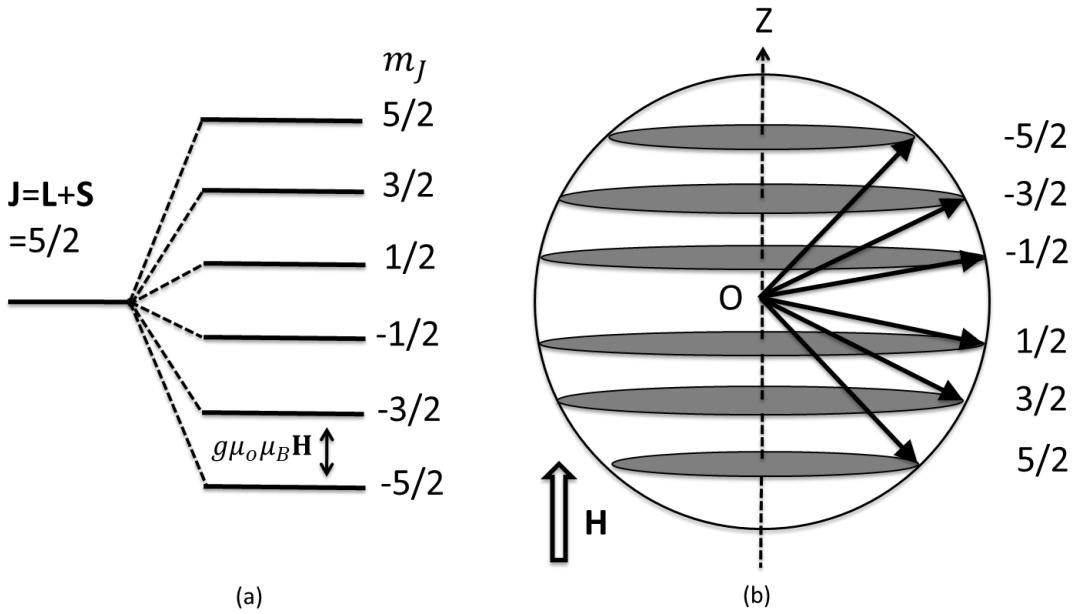

Figure 2.1.2 (a) Anomalous Zeeman splitting for *J*=5/2, and (b) projection of momentum along the applied field direction.

In addition to the above one should also note that electrons have a second form of angular momentum, namely spin angular momentum (**S**). The spin moment can also interact with a magnetic field. Zeeman's original experimental work pre-dates the discovery of this second form of angular momentum. The effect he described is known as the normal Zeeman effect. When one considers both the spin and orbital components of the angular momentum we speak of the anomalous Zeeman effect. The energy splitting under an external magnetic field due to the anomalous Zeeman effect is shown in Figure 2.1.2 for the case $J=L+S = 5/2$ where J is the total angular momentum quantum number.

Vector model of magnetic atoms

As mentioned in the previous section there are two types of magnetic moment. One is associated with the orbital angular momentum **L** while the other is associated with spin angular momentum ***S***. The corresponding magnetic moments are given by

$$\mathbf{m}_{orbital} = -\frac{e\hbar}{2m^*}\mathbf{L}, \tag{2.1.7a}$$

$$\mathbf{m}_{spin} = -g_s\frac{e\hbar}{2m^*}\mathbf{S}, \tag{2.1.7b}$$

where g_s is approximately equal to 2. The energy level splitting resulting from the anomalous Zeeman effect which considers both the spin and orbital angular momenta is given by

$$\Delta E = \mu_0 \frac{e}{2m^*}(\mathbf{L} + 2\mathbf{S}) \cdot \mathbf{H} = g\mu_{\boldsymbol{B}} m_J \mu_0 H. \tag{2.1.8}$$

Adding equation 2.1.7a and 2.1.7b the resultant magnetic moment ($\mathbf{M}_R$) is given by

$$\mathbf{M}_R = -\frac{e\hbar}{2m^*}(\mathbf{L} + 2\mathbf{S}). \tag{2.1.9}$$

In fact this relationship is true only in light atoms where **L** and **S** are good quantum numbers. Since **L** and **S** are precess about **J**, **L**+*2***S** should also precess about the **J** as shown in Figure 2.1.3. The total magnetic moment parallel to **J** and its magnitude may be written as

$$M = -g_J \frac{e\hbar}{2m^*} J \tag{2.1.10}$$

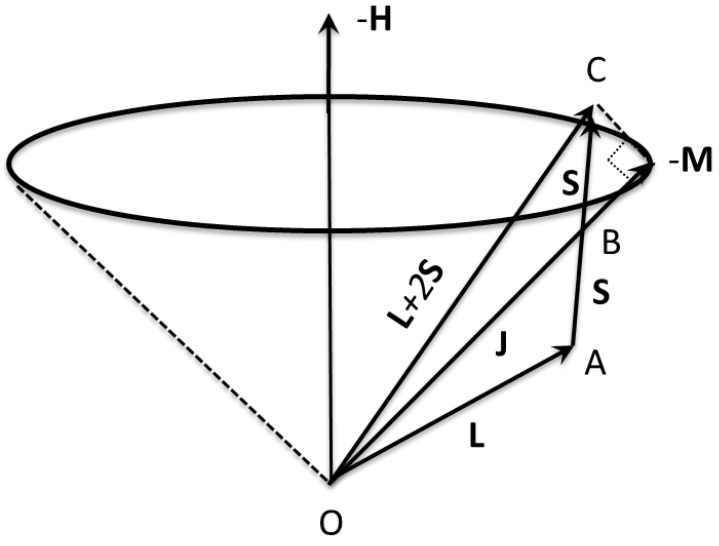

Figure 2.1.3 Vector representation of the spin (**S**), orbital (**L**) and total angular momentum (**J**) in an external field (**H**) parallel to the z-axis[14].

Comparing equation (2.1.9) and (2.1.10), we have

$$g_J J = |L + 2S| cos\angle BOC = J + S cos\angle ABO. \tag{2.1.11}$$

In ΔABO,

$$L^2 = J^2 + S^2 - 2JScos\angle ABO. \quad (2.1.12)$$

Using equation (2.1.12) in equation (2.1.11), we obtain

$$g_J = 1 + \frac{J^2+S^2-L^2}{2J^2} \quad (2.1.13)$$

In a quantum mechanical treatment, the quantities S^2, L^2 and J^2 can be replaced by $\hbar^2 S(S+1)$, $\hbar^2 L(L+1)$ and $\hbar^2 J(J+1)$. Then equation (2.1.13) reduces to

$$g_J = 1 + \frac{J(J+1)+S(S+1)-L(L+1)}{2J(J+1)} \quad (2.1.14)$$

This is the g factor describing multiplet splitting within atomic spectra developed by Landé [1].

2.2 Spin-orbit coupling

To gain a more complete understanding of the total magnetic moment one must consider the interaction that occurs between the spin and orbital components, the spin-orbit coupling. The spin-orbit coupling is strongly dependent on the proton number for a given atom (proportional to Z^4). In addition one must also consider spin-spin and orbit-orbit coupling[4].

Russell-Saunders coupling:

Russell-Saunders coupling[5] applies to low atomic number where the spin-orbit interaction is weak[6]. In this regime the coupling between individual orbital angular momenta and individual spin angular momenta is stronger than the spin-orbit coupling. Consider the case of a two electron atom whose electrons have the orbital quantum numbers l_1 and l_2. The allowed values of L are given by the series: $L=l_1+l_2$,l_1+l_2-1,.....$|l_1-l_2|$. The allowed values for the atomic orbital moment, M_L, are then given by: $-L$, $-L+1$,...,$+L$ Similarly for the spin the allowed values of S are given by: $S=s_{1+}s_2$,.....s_1-s_2 The allowed values for the atomic spin moment are then: $M_s = -S,-S+1,.....,+S$. Numerically S can only take the values *1* or *0*. For the case where $S = 1$, M_s can take the values; $-1, 0, +1$ and for the case where $S = 0$, $M_s = 0$. These are the so called triplet and singlet states respectively.

The total atomic angular momentum J is determined by the vector addition of the atomic spin angular spin momentum and atomic orbital angular momentum; $J=L+S$, $L+S-1$,.....,$|L-S|$. The magnitude of total angular momentum $|J|$ is equal to $\sqrt{J(J+1)}\hbar$ and the projection onto the magnetic field direction is given by $M_J\,\hbar$.

Hund's rule

German physicist Friedrich Hund's[7] established a set of rules to determine the lowest energy state for a partially filled atomic orbital within an isolated ion

1st rule: Electrons will fill an atomic orbital so as to maximise the multiplicity, defined by $2S + 1$. The wavefunctions for two electrons having the same spin have a greater spatial separation than the wavefunctions of a pair of electrons having the opposite spin due to the Pauli exclusion principle. This means that electrons having the same spin exert less Coulomb repulsion upon one another than electrons with opposite spin.

2nd rule: The state with the largest multiplicity will also have the largest total orbital angular momentum L.

3rd rule: For a shell that is less than half full the lowest energy state is that having the lowest value of J ($J=|L-S|$). When a shell is more than half full then the lowest energy state is the one with the highest value of J ($J=|L+S|$).

jj coupling:

Russell-Saunders coupling does not apply to heavy atoms such as the actinides where the spin and orbital angular momenta of each individual electron couple strongly with one another. This gives a total angular momenta per electron; $j_i=l_i+s_i$. The atomic total angular momentum can then be given by summing over the all electrons, i, in an atom $\mathbf{J} = \sum_i \mathbf{j}_i$.

2.3 Classification of magnetic materials

There are several different classes of magnetic material each of which exhibits its own distinct properties.

2.3.1 Diamagnetism

Diamagnetism cannot be explained by a purely classical theory as the Bohr-van LeeuWen theorem states that the net magnetisation of non-relativistic classical electrons in thermal equilibrium sums to zero. For a full description of such materials one is required to consider quantum mechanics. Assume that an electron is moving in a fixed orbit with angular velocity ω_L. The orbital radius is not modified by the presence of a magnetic field instead it induces electron precession about the direction of the magnetic field. The change in the magnetic moment is given by

$$\Delta m = \frac{-|e|\omega_L}{2\pi} A \tag{2.3.1}$$

The quantity A is the area in the xy-plane defined by the electron trajectory ($A = \pi(x^2 + y^2) = \pi r^2$). By assuming a spherically symmetric charge distribution and averaging over the electron orbit we have $< x^2 >=< y^2 >=< z^2 >$ and $< r^2 >=< x^2 > +< y^2 >$. The radius of the sphere R, $< R^2 >=< x^2 > +< y^2 > +< z^2 >$, so that $< r^2 >= \frac{2}{3} < R^2 >$. The magnetic moment per atom is $\mathbf{m} = -\frac{e^2\mu_0}{6m^*}\mathbf{H}\sum_{i=1}^{Z} < R_i^2 >$. The magnetic susceptibility is given by

$$\chi = \frac{M}{H} = -\frac{N}{V}\frac{e^2\mu_0}{6m^*}\sum_{i=1}^{Z} < R_i^2 >. \tag{2.3.2}$$

where N is the number of atoms in a volume V. The susceptibility is always negative for diamagnetic materials. In the presence of a magnetic field an additional current is induced that produces a magnetic moment orientated in the opposite direction to the magnetic field. Therefore diamagnetic materials always act to minimise their net magnetic moment, even in the presence of an applied magnetic field. One should also note that the susceptibility is independent of temperature for diamagnetic materials.

2.3.2 Paramagnetism

The Langevin theory [8] explains the temperature dependence of the susceptibility of paramagnetic materials. Langevin assumed that the atomic magnetic moments **m**, do not interact with one another and are randomly oriented in the absence of an external field **H**. However, in the presence of an applied magnetic field the magnetic moments align along the direction of the applied field. The energy required to fully align a magnetic moment along the field direction is given by the Zeeman energy mentioned in eq. (2.1.6),

$$E = -\mathbf{m}.\mu_0\mathbf{H} = -m\mu_0 H cos(\theta). \qquad (2.3.2.1)$$

where θ is the angle between the spin moment and the direction of the applied field.

Electrons can be described by the Boltzman distribution function such that the probability of a given magnetic moment aligning along the field direction is proportional to $exp\left(\frac{m\mu_0 H cos(\theta)}{k_B T}\right)$. The magnetisation can be can be written as

$$\mathbf{M} = N\mathbf{m}L(\alpha)\ . \qquad (2.3.2.2)$$

where N is the number of magnetic moments, $\alpha = \frac{m\mu_0 H}{k_B T}$ and $L(\alpha)$ is the Langevin function given by $L(\alpha) = \coth(\alpha) - \frac{1}{\alpha}$. For the case of high field and low temperature ($\alpha \gg 1$), therefore all magnetic moments are aligned along the field direction so that the total magnetic moment can be written as $\mathbf{M} = N\mathbf{m}$. For the case of low field and high temperature ($\alpha \ll 1$) one can expand equation (2.3.2.2) as a Taylor series with respect to α and keep only terms that are 1st order term in α giving

$$M = \frac{Nm\alpha}{3} = \frac{N\mu_0 m^2 H}{3k_B T}\ . \qquad (2.3.2.3a)$$

One can then define the magnetic susceptibility as

$$\chi = \frac{M}{H} = \frac{N\mu_0 m^2}{3k_B T} = \frac{C}{T}\ . \qquad (2.3.2.3b)$$

This relation is known as the Curie law where C is the Curie constant which is defined as $\frac{N\mu_0 m^2}{3k_B}$. Quantum mechanically a dipole moment has discrete possible orientations due to spatial quantization.

$$M = NJg\mu_B \left[\frac{2J+1}{2J} coth\left(\frac{2J+1}{2J}\alpha\right) - \frac{1}{2J} coth\left(\frac{\alpha}{2J}\right)\right], \quad (2.3.2.4a)$$

$$= NgJ\mu_B B_J(\alpha) = Nm_0 B_J(\alpha) = M_s B_J(\alpha) \quad (2.3.2.4b)$$

where $\alpha = JgH\mu_B/k_BT$ and $B_J(\alpha)$ is the Brillouin function, which is equal to the Langevin function in the limit J tends to infinity. For small values of α the Brillouin function is given by $(J+1)\alpha/3J$, neglecting higher order terms in α.

The susceptibitlity can be reduce from expression (2.3.2.4b) as

$$\chi = \frac{Ng^2J(J+1)\mu_B^2\mu_0}{3k_BT} = \frac{C}{T} \ . \quad (2.3.2.5)$$

Therefore in quantum mechanics the paramagnetic susceptibility is inversely proportional to the temperature as in the classical picture but the constant of proportionality takes a different form: $\frac{Ng^2J(J+1)\mu_B^2\mu_0}{3k_B} = \frac{Nm_{eff}^2}{3k_B}$, where $m_{eff}^2 = g^2J(J+1)\mu_B^2\mu_0$.

But many paramagnetic elements which do not follow Curie's law have been explained further by the Curie-Weiss law[9]. This law assumes that there is an internal field, which causes the magnetic moment to align parallel to the others. The internal field (molecular field) mainly comes from the exchange integral that tries to align the neighbouring spin. At the Curie temperature, the susceptibility diverges. This corresponds to a phase transition due to spontaneous ordering of the magnetic moment, a phenomena which will be discussed in more detail in section 2.3.3 Above the Curie temperature the thermal energy dominates and leads to a loss of alignment. One important aspect of the Brilluoin function description is that it considers the total angular momentum quantum number, *J*. This leads to a good agreement with measured values for the susceptibility in paramagnetic materials. It should be noted that in certain materials there is a considerable quenching of the orbital moment and so the total angular momentum is no longer a suitable quantum number. An example of such a class of materials are the transition metal ferromagnets that will be outlined in the next section. The electric field generated by ions in the solid causes the orbital moment to be coupled strongly to the crystal lattice making re-orientation difficult under an external field. However the spin angular momentum couples very weakly to

the lattice so the moment comes from the spin angular momentum but not from the orbital angular momentum.

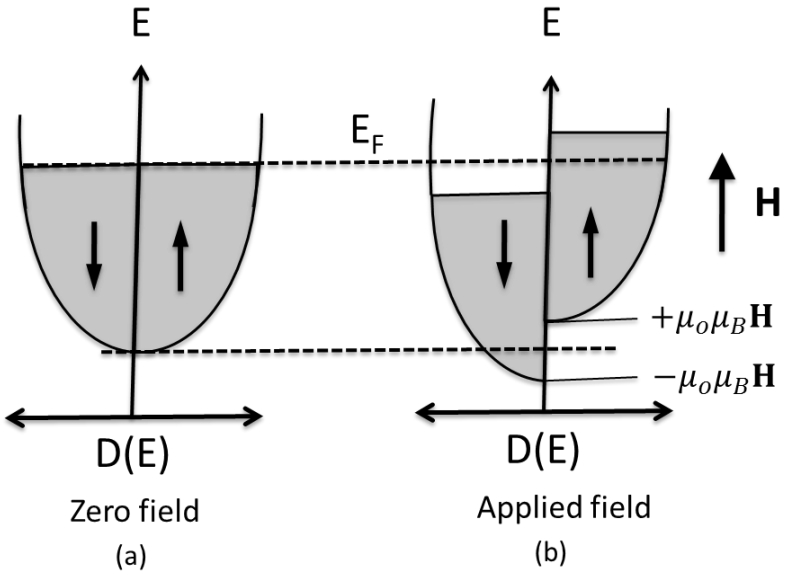

Figure 2.3.2.1 Density of state at (a) zero field, and (b) applied field.

Langevin theory[28] also assumed that the partially occupied valence shell electrons are fully localized at the respective atom. In a metal, the electrons are mobile and are responsible for the electrical conductivity of the material. The concept of electron localization does not explain the susceptibility, which is largely independent of temperature. This phenomenon can be explained by Pauli paramagnetism. Consider a free electron system where each electron has magnetic moment, $\mathbf{m} = -g\mu_B\mathbf{m}_S$. Under an external field (**H**) it changes direction and hence the projection parallel (anti-parallel) to **H** has lower (higher) energy by $\mu_0\mu_B H$ as shown in Figure 2.3.2.1. The excess electrons with spin up will transfer to spin down until a new Fermi level is formed.

2.3.3 Ferromagnetism

Ferromagnetic materials are distinct from diamagnetic and paramagnetic materials in that they possess a relatively large magnetic moment in the absence of an external magnetic field. Ferromagnetic materials also exhibit a magnetic field dependent hysteresis where the magnetisation possessed by the ferromagnet at zero applied field is known as the remanence. The first attempt to describe the origin of ferromagnetism was made by Pierre Weiss in 1906[10] who proposed a molecular field

theory to describe the presence of a large net magnetisation in the absence of an applied field.

The molecular field theory of Weiss is based on the idea that an internal field which is proportional to the magnetisation of the ferromagnet is present in the material and responsible for the high level of magnetic ordering observed. The total internal field is given by

$$\mathbf{H_i} = n_w\mathbf{M} + \mathbf{H}\ . \qquad (2.3.3.1)$$

where n_w is the Curie-Weiss constant. For the high temperature limit ($\alpha \ll 1$) the Brillouin function ($B_J(\alpha)$) is reduced to *(J+1) α/ 3J*. Now the external field *H* is replaced by H_i in expression (2.3.2.4b) so that $\alpha = Jg(n_wM + H)\mu_B/k_BT$.

$$\frac{M}{M_0} = \frac{1}{3}\frac{(J+1)}{J}\frac{Jg\mu_B}{k_BT}(n_wM + H) \qquad (2.3.3.2a)$$

where M_0 is the saturation magnetisation at zero temperature. The Curie temperature θ_C can be written as $\frac{(J+1)}{3}\frac{g\mu_B}{k_B}(n_wM)$ and is the temperature at which the ferromagnetic ordering is destroyed by the thermal energy and the material therefore becomes paramagnetic. Below the Curie temperature the spontaneous magnetisation is given by

$$\frac{M}{M_0} = \frac{1}{3}\frac{(J+1)}{J}\frac{Jg\mu_B}{k_BT}(n_wM). \qquad (2.3.3.2b)$$

Now $\alpha_0 = \mu_0 n_w m_0 M/k_BT$ and combined with M_0we may write

$$\frac{M}{M_0} = \left(\frac{NK_BT}{\mu_0 n_w M_0^2}\right)\alpha_0\ . \qquad (2.3.3.2c)$$

This expression can then be rewritten in terms of the Curie constant *C* which is related to the Curie temperature by $\theta_C = n_wC$ giving the equation

$$\frac{M}{M_0} = \left(\frac{(J+1)T}{3JCn_w}\right)\alpha_0\ . \qquad (2.3.3.2d)$$

Substituting n_wM in terms of the Curie temperature in expression (2.3.3.2a) we have

$$\frac{M}{M_0} = \frac{1}{3}\frac{(J+1)}{J}\frac{Jg\mu_B}{k_BT}\left(\frac{3k_B\theta_CM}{(J+1)g\mu_BM_0} + H\right), \qquad (2.3.3.2e)$$

$$\frac{M}{M_0}\left(1-\frac{T}{\theta_C}\right)=\frac{1}{3}\frac{(J+1)}{J}\frac{Jg\mu_B}{k_BT}H. \qquad (2.3.3.2f)$$

The susceptibility can then be written in terms of the temperature T, Curie temperature θ_C, and the Curie constant C

$$\chi=\frac{C}{T-\theta_C}\ . \qquad (2.3.3.3)$$

This is known as the Curie-Weiss law. The simultaneous solution of equations (2.3.2.4b) and (2.3.3.2d) can be found graphically and is shown in Figure 2.3.3.1 (a). Equation (2.3.2.4b) gives a curve and equation (2.3.3.2d) gives a straight line with different values of temperature (T). The slope of every line is proportional to the value of T. For the case $T<\theta_C$ the two functions intersect meaning that there exist non-zero values of $\frac{M}{M_0}$ in the absence of an external field. However for the cases $T=\theta_C$ and $T>\theta_C$ the two functions only intersect at $\frac{M}{M_0}$ = 0. This means that there is no net spontaneous magnetisation in this temperature range. The temperature dependence of $\frac{M}{M_0}$ is plotted in Figure 2.3.3.1 (b) for several values of J.

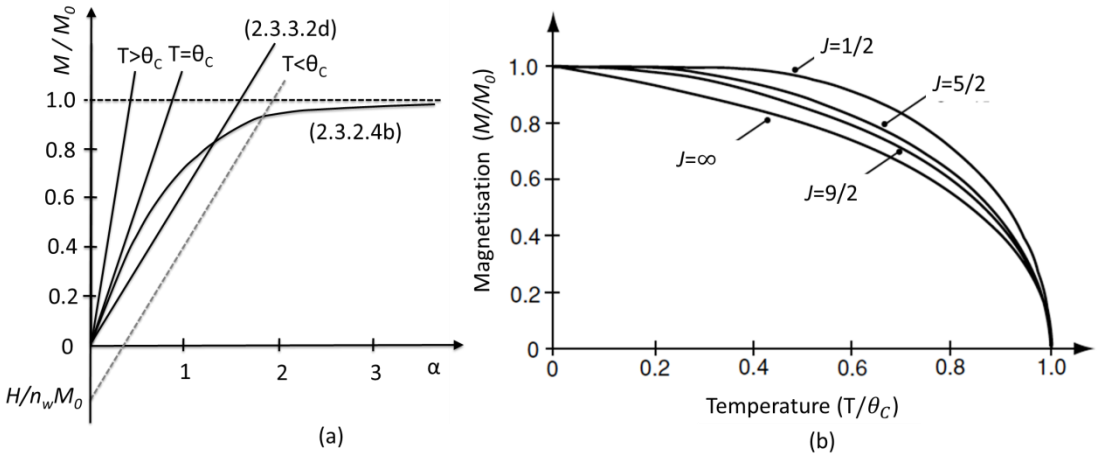

Figure 2.3.3.1 (a) Graphical solution of equation 2.3.2.4b and 2.3.3.2d for J=1/2 to find the spontaneous magnetisation at different values of temperature. (b) Spontaneous magnetisation as a function of temperature[28].

2.4 Exchange Interaction

The exchange interaction is responsible for the high level of magnetic ordering in ferromagnetic materials. Heisenberg[11] developed a theory based on the hydrogen molecule, which showed that the exchange interaction is the consequence of the electrostatic interaction between electrons and the requirement that electrons satisfy the Pauli Exclusion Principle[12].

Consider two hydrogen atoms (the proton 'a' has electron '1' and proton 'b' has electron '2') very far apart from one another such that there is no interaction between them. The Hamiltonian of the whole system can then be written as

$$H = \frac{-\hbar^2}{2m}\{(\nabla_1^2 + \nabla_2^2)\} + V(1,a) + V(2,b). \quad (2.4.1)$$

$V(r,a) = \frac{-e^2}{r}$ is the potential, where r is the distance between the electron and the proton a. The Pauli Exclusion Principle states that no two electrons can occupy the same quantum state and so the total electron wavefunction is anti-symmetric with respect to exchange of the electron coordinates i.e. $\psi(1,2) = -\psi(2,1)$. The possible wave functions for a single electron are; $\psi_a(1), \psi_a(2), \psi_b(1)\ or\ \psi_b(2)$. The total wave function for the whole system is then given by

$$\psi(1,2) = \frac{1}{\sqrt{2}}[\psi_a(1)\psi_b(2) - \psi_a(2)\psi_b(1)]. \quad (2.4.2)$$

The total electron wave function is a combination of a spatial function ϕ and a spin function χ. This gives $\psi(1,2) = \phi(1,2) \cdot \chi(1,2)$. The anti-symmetry condition for the total electron wave function can be satisfied in two different ways:

1. Spatially symmetric wave function and anti-symmetric spin wave function.

2. Anti-symmetric spatial wave function and symmetric spin wave function.

$$\psi_s(1,2) = \frac{1}{\sqrt{2}}[\phi_a(1)\phi_b(2) + \phi_a(2)\phi_b(1)].\frac{1}{\sqrt{2}}(|\uparrow\downarrow\rangle - |\downarrow\uparrow\rangle), \quad (2.4.3a)$$

$$\psi_t^1(1,2) = \frac{1}{\sqrt{2}}[\phi_a(1)\phi_b(2) - \phi_a(2)\phi_b(1)].\frac{1}{\sqrt{2}}|\uparrow\uparrow\rangle, \quad (2.4.3b)$$

$$\psi_t^2(1,2) = \frac{1}{\sqrt{2}}[\phi_a(1)\phi_b(2) - \phi_a(2)\phi_b(1)].\frac{1}{\sqrt{2}}(|\uparrow\downarrow\rangle + |\downarrow\uparrow\rangle, \quad (2.4.3c)$$

$$\psi_t^3(1,2) = \frac{1}{\sqrt{2}}[\phi_a(1)\phi_b(2) - \phi_a(2)\phi_b(1)].\frac{1}{\sqrt{2}}|\downarrow\downarrow\rangle. \quad (2.4.3d)$$

The subscripts *s* and *t* indicate the singlet (*S*=0) and triplet state (*S*=1) respectively. For large electron separations the singlet and triplet states are degenerate. This degeneracy is lifted when they are close enough to one another to interact. Such interaction gives rise to an additional interaction which is given by

$$H_{12} = V(a,b) + V(1,b) + V(2,a) + V(1,2) \quad (2.4.4)$$

where the terms on the right hand side, read left to right, are the potential energy terms describing the interaction between the protons of the two atoms, the two inter atom electron-proton interactions and the interaction between the two electrons respectively. The interaction energy $E_{s,t} = \int \psi_{s,t} H_{12} \psi_{s,t}^* dV = K_{12} \pm J_{12}$, where K_{12} and J_{12} are the Coulomb integral and exchange integral[13] respectively,

$$K_{12} = \int \phi_a^*(1)\phi_b^*(2) H_{12} \phi_a(1)\phi_b(2) dV_1 dV_2 \,, \quad (2.4.5a)$$

$$J_{12} = \int \phi_a^*(1)\phi_b^*(2) H_{12} \phi_a(2)\phi_b(1) dV_1 dV_2 \,. \quad (2.4.5b)$$

Here the operator H_{12}acts only on the spatial part of wave function.

$$H_{12}\psi = H_{12}(\phi.\chi) = \chi H_{12}\phi = \chi E_{s,t}\phi = E_{s,t}\psi. \quad (2.4.6)$$

Next one must construct a Hamiltonian, H_{spin}, of the form $H_{spin} = K_{12} - \frac{1}{2}J_{12}\mathbf{S}_1.\mathbf{S}_2$. This is known as the exchange Hamiltonian and is a consequence of the electrostatic interaction between two electrons and the Pauli exclusion principle.

For a system containing *N* number of non interacting spins the ground state will have $(2S+1)^N$ fold degeneracy. As the atoms are brought close enough together for them to interact with one another the degeneracy is lifted and the splitting energy is smaller than any other interaction energy. The energy of the whole system is given by Heisenberg Hamiltonian,

$$H_{Heis} = -J \sum_{i \neq j} S_i S_j. \quad (2.4.7)$$

The curve in Figure 2.4.1 known as Bethe-Slater curve[14] shows the variation of the exchange integral (*J*) with ratio r_a/r_{3d}, where r_a is the interatomic separation and r_{3d} is the radius of 3d shell of electrons. When two atoms of the same kind are

brought closer and closer together, but without any change in the radius of the 3d shell, the ratio will decrease. When ratio (r_a/r_{3d}) is large, J is small and positive. As the ratio decreases and the 3d electrons approach one another more closely, the positive exchange interaction, favouring parallel spin alignment ($E_s > E_t$ ferromagnet), becomes stronger and then decreases to zero. A further decrease in interatomic distance brings the electrons close together so that their spin must become antiparallel and J becomes negative ($E_s < E_t$-anti-ferromagnetic).

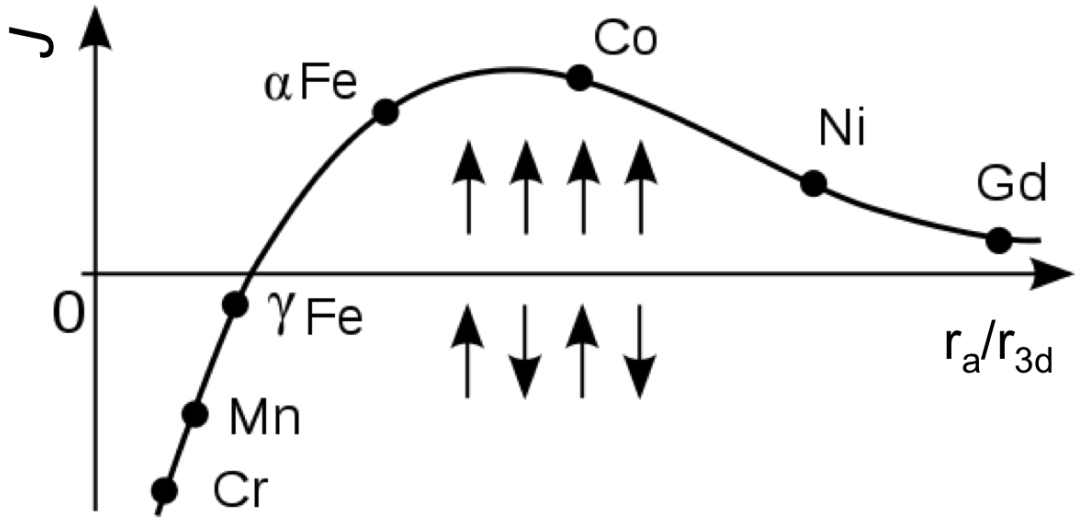

Figure 2.4.1 Bethe-Slater curve is a graphical representation of the exchange integral for transition metals as a function of the ratio of the inter-atomic distance r_a to the radius r_{3d} of the electron shell[19]. As the Fe cools to 1,394 °C its crystal structure is face centered cubic (fcc) and is known as γFe. Under further cooling to below 912 °C the crystal structure undergoes a phase change to body centered cubic (bcc) and is known as αFe is formed.

2.5 Exchange interactions in metals

2.5.1 Direct exchange

The direct exchange interaction arises from the Coulomb interaction between electrons from two neighbouring ions[15] as described in section 2.4.

2.5.2 Indirect exchange

The formalism for the indirect exchange interaction was originally developed by Ruderman, Kittel[16],Kasuya[17] and Yosida[18] and is often called the RKKY interaction.

The RKKY interaction can cause either ferromagnetic or anti-ferromagnetic ordering depending on the separation between neighbouring ions. A single magnetic impurity can create a non-uniform and oscillatory spin polarisation in the conduction band which falls off as r^{-3} (r is the distance between core electron spins). This then leads to a long range oscillatory coupling between core electron spins. This is due to different potentials being experienced by spin up and spin down conduction electrons at the site of the local moment. The spin polarisation is related to the Friedel charge density oscillation around the impurity, which has the form[19].

$$F(x) = (\sin(x) - x\,cos(x))/x^4 \tag{2.5.1}$$

where $x = 2k_F r$ and k_F is the Fermi wave vector. The spin polarisation is proportional to the Friedel function and for large x it can be expressed by

$$\rho\uparrow - \rho\downarrow \approx \frac{n^2}{E_F} J < S^2 > \frac{\cos(2k_F r)}{(k_F r)^3}. \tag{2.5.2}$$

The exchange Hamiltonian (H_{RKKY}) describing the coupling of the spin polarisation of one magnetic ion(S_i) with that of a second magnetic ion S_j is given by

$$H_{RKKY}(x) = S_i . S_j \frac{4J^2 m^* k_F^r}{(2\pi)^3} F(2k_F r) \tag{2.5.3}$$

where m^* and J are the effective mass of an electron and the spin-dependent exchange interaction between conduction electrons.

2.5.3 Superexchange

Superexchange commonly occurs in transition metal oxides where the 3d magnetic ions are separated by non-magnetic oxygen ions[20]. There is no direct overlap between d-orbitals of the magnetic ion. The d-orbital hybridizes with the p-orbital of the oxygen ion, the d electrons are partially delocalized on the oxygen and the delocalization energy is different if the two magnetic moments are parallel or antiparallel. It is an indirect and short range interaction because it involves hybridization between neighbouring ions.

2.6 Energy terms in magnetic systems

The total energy (E_{Tot}) of a given magnetic system consists of a number of different energy terms that compete with one another to determine the minimum energy state. There are contributions due to the exchange interaction (E_{ex}), the Zeeman interaction with the external applied field (E_z), magnetic-dipole interactions(E_{dip}), magneto-crystalline anisotropy(E_{ani}) and magnetoelsatic energy (E_{me}). One can then write the total energy as

$$E_{Tot} = E_{ex}+E_z + E_{dip} + E_{ani} + E_{me} . \quad (2.6.1)$$

2.6.1 Exchange energy (E_{ex})

Heisenberg formulated an expression for the exchange interaction energy between two neigbouring spins as

$$E_{ex} = -\sum_{i\neq j} J_{ij} S_i . S_j \quad (2.6.2)$$

where J_{ij} is the exchange constant ((+)ve for ferromagnetic and (–)ve for anti-ferromagnetic alignment) and $S_{i,j}$ are the spin moments for nearest neighbour spins i and j.

2.6.2 Zeeman energy (E_z)

The Zeeman energy arises from the interaction of the magnetisation (**M**) with the external magnetic field (**H**). The Zeeman energy per unit volume is given by

$$E_Z = \mathbf{M} \cdot \mathbf{H}. \quad (2.6.3)$$

The external field can include a static bias field as well as a time varying pulsed field or high frequency harmonic field.

2.6.3 Magnetostatic energy (E_{dip})

The magnetostatic field inside the ferromagnetic materials is opposite to the magnetisation such that it tends to demagnetize the ferromagnetism. The magnetostatic energy is a long range interaction in which each atomic moment

interacts with every other atomic moment within the ferromagnetic material. The magnetostatic energy per unit volume is given by

$$E_{dip} = -\frac{1}{2}\mathbf{H}_d \cdot \mathbf{M} \tag{2.6.4}$$

where the demagnetizing field $\mathbf{H}_d = -\nabla U$, where U is the magnetostatic potential. By the supersposition principle the magnetostatic potential at **r** produced by a distribution of volume charge and surface charge at position at $\mathbf{r}'$ is given by[21]

$$U(r) = -\int \frac{\nabla' \cdot \mathbf{M}(\mathbf{r}')}{|\mathbf{r}-\mathbf{r}'|} d\mathbf{r}' + \int \frac{\mathbf{n}' \cdot \mathbf{M}(\mathbf{r}')}{|\mathbf{r}-\mathbf{r}'|} ds' \tag{2.6.5}$$

where ∇' is a derivative with respect to r'. The first term on the RHS of the equation is the potential energy contribution from the volume charge $-\boldsymbol{\nabla} \cdot \mathbf{M}$, The second term arises from the surface charge density $\mathbf{n}' \cdot \mathbf{M}$, where $\mathbf{n}'$ is the unit vector normal to the surface.

2.6.4 Anisotropy energy (E_{ani})

Magneto-crystalline anisotropy

Due to the interaction between the magnetic moments and the crystal lattice via the spin-orbit interaction the orientation of the magnetic moments has preferred directions that relate to the symmetry of the lattice. The deviation of the magnetic moments from these directions increases the magneto-crystalline anisotropy energy. For cubic crystals the general form of the magneto-crystalline anisotropy energy [22]can be written in terms of direction cosines of the magnetsation: $(\alpha_1, \alpha_2, \alpha_3)$ as

$$\frac{E_{ani}}{V} = K_1(\alpha_1^2\alpha_2^2 + \alpha_2^2\alpha_3^2 + \alpha_3^2\alpha_1^2) + K_2(\alpha_1\alpha_2\alpha_3)^2 + .. \tag{2.6.6}$$

Equation (2.6.6) is an even function and is invariant under the interchange of any two direction cosines of magnetisation. Permanent magnets mainly contain rare-earth metals. Within these heavy atoms the spin-orbit coupling is very strong so the magneto-crystalline energy is very high. The elemental rare earths commonly have hcp structure and a uniaxial anisotropy energy that depends on the angle (θ) between the magnetisation and the c-axis. This is the case for rare-earth metals. Their anisotropy energy per unit volume is given as

$$\frac{E_{ani}}{V} = K_1 sin^2\theta + K_2 sin^4(\theta)\ . \tag{2.6.7}$$

Depending on the anisotropy constants K_1 and K_2 the sample has an easy axis for large $|K_1|$ $(K_1 > 0)$, or an easy plane for large $|K_1|$ $(K_1 < 0)$, or a conical easy surface for intermediate values of the constant.

Shape anisotropy

The magnetostatic energy described above depends upon the shape of a body of finite size. In the special case of a body of ellipsoidal shape, uniform magnetisation results in a surface pole distribution that produces a uniform demagnetisation field ($\mathbf{H}_d$), whose strength depends upon the orientation of the magnetisation relative to the principal axes of the ellipsoid[10].

Bodies of non-ellipsoidal shape generally have non-uniform magnetisation and demagnetisation fields which greatly complicates the analysis of the system.

2.6.5 Magnetoelastic interaction and magnetostriction (E_{me})

The magnetoelastic energy is the anisotropy energy term that arises when a magnetic sample is placed under stress. The magnetoelastic energy arises from the interaction between the magnetisation and the resulting strain (ε_{ij}) and for a cubic crystal can be written as

$$\frac{E_{me}}{V} = B_1\left(\alpha_1^2\varepsilon_{xx} + \alpha_2^2\varepsilon_{yy} + \alpha_3^2\varepsilon_{zz}\right) + B_2\left(\alpha_1\alpha_2\varepsilon_{xy} + \alpha_2\alpha_3\varepsilon_{yz} + \alpha_3\alpha_1\varepsilon_{zx}\right), \qquad (2.6.8)$$

where the B-coefficients are the magnetoelastic coupling constants and α_i are the direction cosines of the magnetisation. The magnetic material changes dimension when the magnetisation is reoriented. The saturation magnetostriction (λ_s) is the linear strain when the sample is magnetized to saturation. The relation between the saturation magnetostriction (λ_s) and the magnetoelastic energy (E_{me}) in the case of cubic crystal under stress (σ) is given by

$$\frac{E_{me}}{V} = \frac{3}{2}\lambda_s\sigma sin^2\theta, \qquad (2.6.9)$$

where θ is the angle between the direction of the magnetisation and the direction along which the magnetostriction is measured.

2.7 Collective band theory of ferromagnetism

The electrons in an isolated atom occupy different energy levels due to the Pauli Exclusion Principle which states that two or more fermions cannot exist in the same quantum state. When atoms are brought close enough to one other such that they can interact, their energy levels are modified[23, 24]. Consider the 1s level it contains two electrons that differ only in that they have opposite spin polarisation. When two atoms are moved close enough together that their wavefunctions of their respective 1s orbitals begin to overlap the two 1s levels will split into two levels of different energy. Similarly for *N* atoms there will be *N* number of sub-levels and when *N* is sufficiently large these sub-levels can be assumed to form a continuum band. The spins align along one direction so as to minimise the exchange energy.

Opposing the alignment of spin in metals is the increased band energy involved in transferring electrons from the lowest band states to band states of higher energy. This band energy prevents the metal from becoming ferromagnetic.

For the transition metals the outermost bands originate from the 3d shell, which predominately overlap with the electron cloud of a neighbouring atom. For a high density of states, the spins are close enough to be dominated by the exchange interaction. The exchange interaction causes the spin splitting between states of opposite spin creating an imbalance in the number of spin up and down electrons. This net spin produces the magnetic moment of the ferromagnet.

For transition metals such as; Ni, Fe and Co the Fermi level lies in the overlap region between the 3d and 4s bands[25]. These bands have partially filled electron states. The 4s band is wide and has a lower density of states at the Fermi level than the 3d band. Consequently, the energy required to transfer a 4s electron to a vacant state so that it can reverse its spin is more than that which would be gained by the resulting decrease in the exchange energy.

The 3d band has narrow width and a high density of states at the Fermi level. The large number of electrons near to the Fermi level reduces the energy required to reverse the spin of a given electron and so the exchange energy becomes the dominant energy term. Ferromagnetism requires a partially filled band so that electrons with unpaired spins can be accommodated. In addition, neighbouring atoms must be

closely packed so that the exchange interaction can align the atomic spins. The magnetic moment can take non-integral multiple values of the Bohr magneton[26].

2.8 Stoner Criterion

The Pauli susceptibility in paramagnetic materials is both small (positive) and independent of temperature. The delocalised electrons at the Fermi level follow the Fermi-Dirac distribution[27]. The small fraction of electrons whose energy is close to the Fermi level are those which are responsible for the material's behaviour as a function of both temperature and externally applied magnetic field. In a 3-dimensional free electron model the density of states is proportional to square root of energy. The spin up and the spin down states are shifted by $\pm\mu_o\mu_B H$ under an external field, **H**. The resulting susceptibility is given by

$$\chi_P = \mu_0\mu_B^2 D(E_F) \tag{2.8.1}$$

where $D(E_F)$ is the density of states at the Fermi level for both spin up and spin down electrons. The higher the density of states the higher the susceptibility. When the density of states is high enough the exchange interaction splits the band and the metal possesses a spontaneous magnetisation state and so is ferromagnetic. The susceptibility in response to the internal field is $\chi_P = M/(n_S M + H)$ where n_S is a coefficient introduced by Stoner to ensure a linear variation of the magnetisation with the internal field. Hence the susceptibility response to the field **H** is $\chi = \frac{M}{H} = \frac{\chi_P}{(1-n_S\chi_P)}$. The susceptibility increases at $n_S\chi_P < 1$ and diverges at $n_S\chi_P = 1$. This condition can be expressed in terms of the local density at the Fermi level ($D(E_F)$). The exchange energy $\frac{1}{2}\mu_0 H_i M = -\frac{1}{2}\mu_0 n_S M^2$ can be written as $-\frac{I}{4}\left(n^{\uparrow} - n^{\downarrow}\right)^2/n$ where $M = \left(n^{\uparrow} - n^{\downarrow}\right)\mu_B$, I is the Stoner exchange parameter and n is the no. of atoms per unit volume. From equation (2.8.1)

$$n_S\chi_P = ID(E_F)/2n. \tag{2.8.2}$$

The metal develops a spontaneous magnetisation when the susceptibility diverges spontaneously. This happens when

$$IN_{\uparrow,\downarrow}(E_F) > 1 \tag{2.8.3}$$

where $N_{\uparrow,\downarrow}(E_F) = D(E_F)/2n$ is the density of states for each spin state. This is the Stoner criterion for the existence of a spontaneous magnetisation[28]. The exchange parameter has to be comparable to the band width to observe spontaneous band splitting.

2.9 Ferromagnetic domains

Consider a block of ferromagnetic material which is in a single domain state. At the ends of the block there will be a net surface magnetic charge. This net surface charge is the origin of the demagnetising field. To reduce the magnetostatic energy to zero the block becomes divided into domains as shown in Figure 2.9. The domains are arranged in such a way that there is no magnetic charge at the block's surface so as to confine the flux inside the block. This is known as a flux closure domain state[29,30].

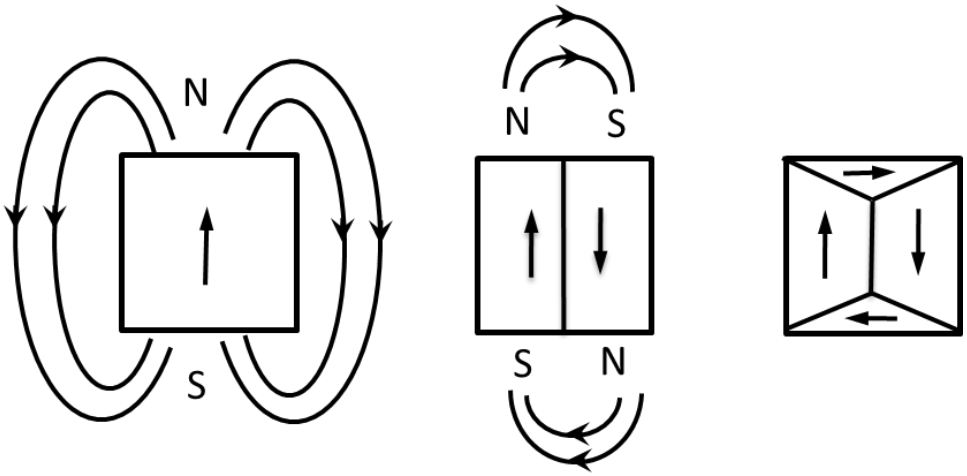

Figure 2.9 Magnetostatic energy is minimised when a domain structure is formed.

2.9.1 Domain Walls

A domain wall is the boundary between adjacent domains in a ferromagnetic material. Domain walls can have many different forms but the two basic types are known as the Bloch wall and the N*é*el wall[9]. They are distinguished from one another in the way the magnetic moments in the wall rotate: within the plane of the wall, in the case of Bloch domain walls, or perpendicular to this plane for N*é*el walls. These two arrangements are shown in Figure 2.9.1 in the case of a 180^o magnetic domain wall. The width of the domain wall is determined by the competition between the

exchange interaction, which acts to keeps the magnetic moments aligned parallel to one another, and the magnetocrystalline anisotropy which favours narrower domain walls. N*é*el walls mainly occur in thin films with weak crystalline anisotropy.

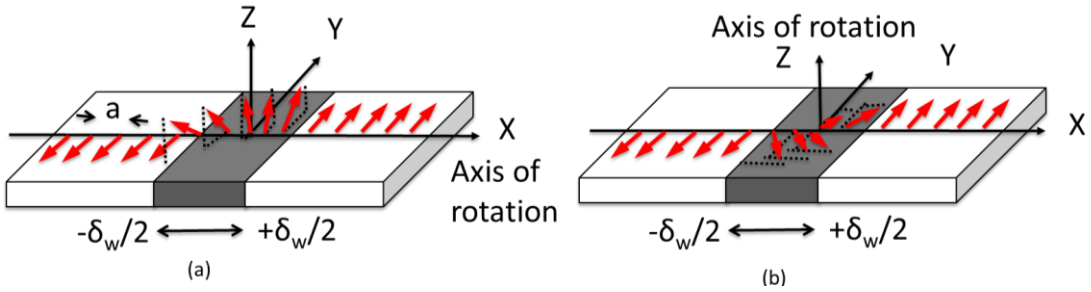

Figure 2.9.1 Two types of domain wall: (a) a Bloch wall, and (b) a N*é*el wall[28].

The spins rotate around the axis normal to length of the domain wall and the sample surface. This wall is energetically favourable in thin films as it avoids the development of a net magnetic charge on the sample surface which would give rise to a large demagnetising field and therefore increase the magnetostatic energy.

2.9.2 Domain wall dynamics

Let's assume for the 180^o Bloch wall of a simple cubic material shown in Figure 2.9.2, the magnetisation is in the *yz* plane. There is no magnetic charge created at the domain, which is the source of demagnetizing field[31].

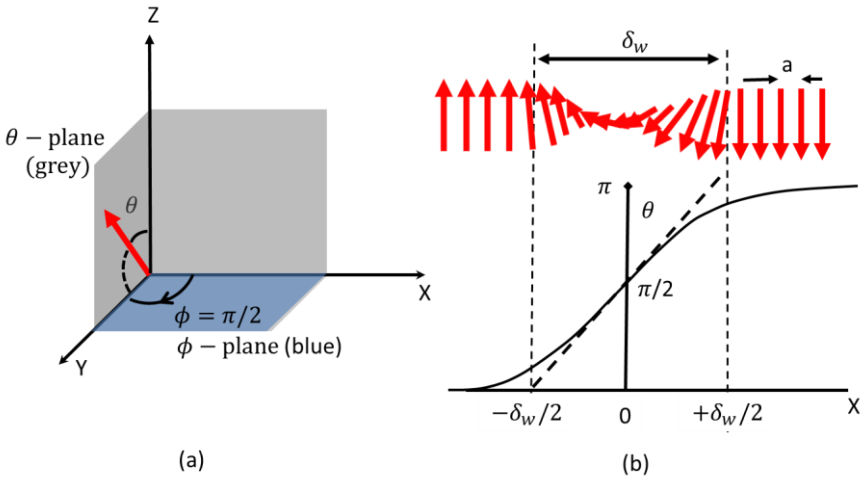

Figure 2.9.2 (a) Configuration of magnetisation in plane of rotation inside the domain wall which is confined in the plane $\phi = \pi/2$, and (b) variation of the angle θ around the center of a Bloch domain wall, showing the linear extrapolation that leads to the value of domain wall width.

The total energy is minimised through a competition between the exchange energy (E_{ex})and the anisotropy energy(E_{ani}).

$$E_{tot} = E_{ex} + E_{ani} = \int \left[A \left(\frac{\partial \theta}{\partial x} \right)^2 + K sin^2(\theta) \right] dx \qquad (2.9.2.1)$$

where *A* and *K* is the exchange stiffness constant and anisotropy constant. Minimizing the above integral, which is of the form of $\int F\big(x, \theta(x), \theta'(x)\big)dx$, is similar to solving the Euler equation $\frac{\partial F}{\partial \theta} - \left(\frac{d}{dx}\right)\frac{\partial F}{\partial \theta'} = 0$, where $\theta' = \frac{\partial \theta}{\partial x}$;

$$\frac{\partial (K sin^2\theta)}{\partial \theta} - \frac{2A\partial^2\theta}{\partial x^2} = 0 \ , \qquad (2.9.2.2a)$$

Integrating equation (2.9.2.2a) with respect to θ gives

$$K sin^2\theta = A(\partial\theta/\partial x)^2, \ \frac{\partial \theta}{\partial x} = \sqrt{(K/A)} sin\theta. \qquad (2.9.2.2a)$$

Integration yields

$$x = \sqrt{\frac{A}{K}} \ln tan\left(\frac{\theta}{2}\right). \qquad (2.9.2.3)$$

Since $\theta = \pi/2$, at the wall center at the origin, the equation can be rearranged as

$$\theta(x) = tan^{-1}[sink(\pi x/\delta_w)] + \pi/2 \ . \qquad (2.9.2.4)$$

where, the width of the domain wall (δ_w) is defined by extrapolating the tangent to the curve at the origin to equation as shown in Figure 2.9.2(b), so that

$$\delta_w = \pi \sqrt{\frac{A}{K}} \ . \qquad (2.9.2.5)$$

When an external field, **H**, is applied along the positive z-axis (anisotropy axis) a torque will be exerted on the spins in the domain wall. The magnetisation rotates in the *yz*-plane, making angle θ with Oz. The spins precess around the z-axis at angular velocity $\omega_z = \mu_0 \gamma H$. Due to the pressure from the torque, the spins are aligned at angle ϕ with the z-plane. The magnetisation acquires an additional x-component $M_x \approx M_0 \phi sin\theta$. This component gives rise to a demagnetisation field $H_x = -M_x$. This field then exerts a torque on the domain wall.

The magnetisation in the domain wall precesses around the x axis with an angular velocity, $\omega_x = \frac{d\theta}{dt} = \mu_o \gamma H_x = -\mu_o \gamma M_0 \phi sin\theta$. The effect is to move the entire domain wall at velocity(v_w). For a moving wall θ is a function of $x - v_w t$. Hence the domain wall velocity[28] is given by

$$v_w = \frac{2\mu^2 \gamma^2 H M_0 \delta_w}{\omega_0 \alpha}. \quad (2.9.2.6)$$

The ratio of impulse per unit area to velocity is an effective domain wall mass per unit area, which is known as the Doring mass:

$$m_w = \frac{2\pi}{\mu_0 \gamma^2 \delta_\omega}. \quad (2.9.2.7)$$

In the weak driving field limit the driving field amplitude is proportional to domain wall velocity, as long as the driving field is sufficiently large to overcome the depining field [32]. It is however also necessary to consider the frequency of the driving field as well as its amplitude when considering domain wall dynamics. The velocity of the domain wall ceases to be a useful quantity as the frequency of the driving field approaches the ferromagnetic resonance frequency $((\gamma \mathbf{B}_o)/2\pi)$ of the material in which the domain wall is formed. The spins comprising the domain wall precess at a frequency given by v_w/δ_w due to the driving field and when this frequency is equal to the ferromagnetic resonance frequency the material exhibits a global FMR response – a phenomenon known as Walker breakdown.

2.9.3 Single domain state

Single domain states lie in between the macrospin state and the macroscopic state. In a macrospin state the magnetisation is exactly the same at every point. In a single domain state there are no domain walls or vortices in equilibrium but such structures can form during the magnetisation reversal process. The transition from a multidomain state to a single domain state depends on the size of the magnetostatic energy in relation to the domain wall energy of the ferromagnetic particle. A phase diagram has been computed to show the conditions which favour the formation of either a single domain state or a multi-domain state. It can be shown that a single domain state is favoured when a particle has small dimensions and a large anisotropy.

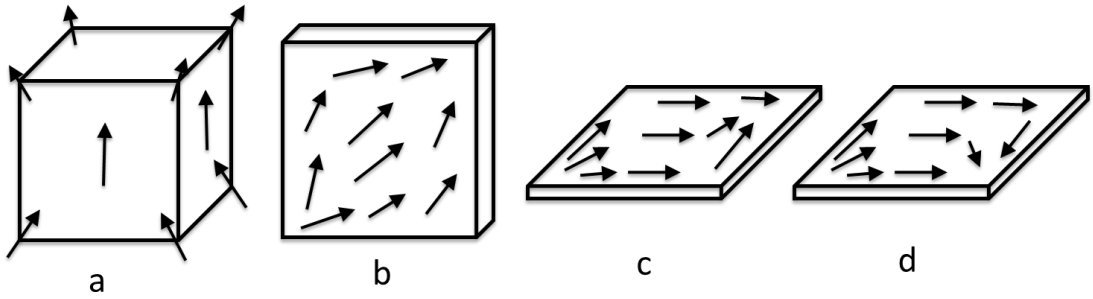

Figure 2.9.3 Magnetisation configuration in single domain states: flower-state (a), leaf-state (b), S-state (c), and C-state (d)[33].

Due to the inhomogeneity of the magnetostatic internal field and the dynamic dipolar field the particle cannot lie in a state of uniform magnetisation. Possible magnetisation configurations of a single domain are the flower, leaf, S and C states[33,34] as shown above in Figure 2.9.3. The shape induces a configurational anisotropy that effects the magnetisation reversal. Edge roughness can cause a decrease in the shape anisotropy.

2.9.4 Superparamagnetism

Consider a single domain system that has two stable states that in the absence of an external magnetic field have the same energy. Such a system has uniaxial anisotropy. At room temperature, as the size of the single domain is reduced the anisotropy, which scales with the sample volume, will decrease whilst the short range exchange interaction remains unchanged. This difference in how the two interactions scale with the sample volume results in an effect known as superparamagnetism. Superparamagnetism is realised in the limit when the energy barrier that separates the two stable magnetisation states becomes of the same order as the thermal energy; $k_B T$. The barrier energy is given by

$$E = KV, \tag{2.9.4.1}$$

where K and V are the anisotropy constant and volume of a single domain grain respectively. The relaxation time τ describes the time taken to switch the magnetisation from one stable state to another and is given by

$$\tau = \tau_0 e^{\frac{E}{k_B T}}. \tag{2.9.4.2}$$

Where τ_0 is the characteristic relaxation time indicating the time between attempts to flip the magnetisation. When the thermal energy is sufficiently large for relaxation to occur on the timescale of the measurement being made then we speak of reaching the superparamagnetic limit of the nanomagnet. Below the superparamagnetic limit the magnetisation will fluctuate on very short time scales and the time averaged magnetisation goes to zero. Such a high level of instability in the magnetic state is not desirable from an applications perspective.

2.10 Exchange bias

The exchange interaction between the interface of a ferromagnetic (FM) layer and an anti-ferromagnetic (AFM) layer plays an important role in spintronic devices. The existence of exchange bias causes the hysteresis loop taken from the FM layer to shift from the origin such that it is no longer centred on zero field. The interaction at the interface between the AFM and FM layers creates a new type of uni-directional anisotropy, of energy density $K_{unid}\cos(\theta)$, where θ describe the orientation of the magnetisation that has the same angular dependence as that due to an external field. As a result the magnetisation has only one stable state.

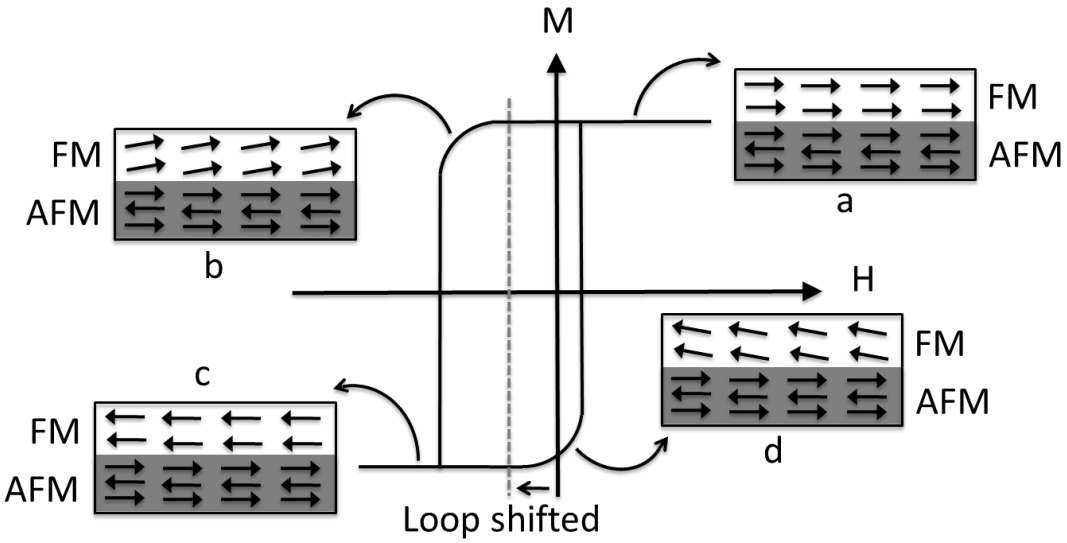

Figure 2.10 Exchange bias phenomenon at the interface between a ferromagnetic and an anti-ferromagnetic layer: (a) at saturation along **H**, (b) **H** against the magnetisation before reversal, (c) FM has reversed, and (d) with **H** increasing before the FM returns to the original direction.

The coupling between the AFM and FM layers at the interface exerts a torque on the FM spins. A shift in the FM layer's hysteresis loop from zero applied field occurs when the AFM layer has a large anisotropy. However, enhancement of the coercivity occurs for small anisotropy. Both effects may occur simultaneously due to structural defects or an irregular grain size distribution, both of which result in a spatial variation of the AFM anisotropy or coupling. For a temperature (T) that is between the Curie temperature (θ_C) and the N*é*el temperature (T_N), at high applied field the FM will be fully saturated but the spins in the AFM may still be aligned randomly. If the temperature is reduced through T_N the magnetisation near the interface with the FM will align along the FM but consecutive layers align randomly. After field cooling, the spin aligns parallel to each other. When the external field is reversed the spins in the FM rotate so that they lie along the field direction however coupling between the AFM and FM will exert a torque on the FM spins whose strength is dependent on the anisotropy of the AFM[35, 36]. This pins the FM spins so that the field required to completely saturate the FM is higher than when interfacial coupling is absent. As a result the coercive field will increase in the negative field direction. Conversely, when the applied magnetic field is switched back to the positive direction the torque will not oppose the rotation but will support it and so a smaller magnitude of magnetic field is required for parallel alignment than without exchange bias. The phenomena discussed above lead to a shift in the hysteresis loop as shown above in Figure 2.10 where the spins in FM have two stable configurations. For small values of the AFM anisotropy the applied magnetic field is high enough that it can fully saturate the FM and AFM layers. When the direction of the applied field is reversed such that it is in the negative direction the spins in the AFM rotate with those in the FM due to the low anisotropy of the AFM. This results in an enhanced coercive field rather than shifting of the loop.

2.11 Spin wave

The Brillouin function describes the quantum state of the spin system in the mean field approximation. This formalism arrives at the saturation magnetisation by fully aligning the constituent spins. Due to the random nature of the thermal fluctuations the spin fluctuations are uncorrelated which leads to an increase in the exchange energy due to the high degree of local spin misalignment. Exchange

coupling between neighbouring spins can lead to a reduction in the saturation magnetisation via the formation of collective modes of demagnetisation. The collective mode of demagnetisation is known as a spin wave. The interaction between two neighbouring spins is governed by the exchange interaction. The ground state energy is $E_0=-NJS^2$ and that of the first localised excited state is $E_1=-(N-2)JS^2+2JS^2=-(N-4)JS^2$. The normalised energy difference is inversely proportional to N.

There are other possible ways that the energy state can be lowered by a collective excitation. Let θ be the angle between a spin and the z-axis (axis about which the spin precesses) and ϕ is the angle between two neighbouring spins projected onto the *xy*-plane as shown in Figure 2.11. The angle ϕ is not determined by the number of spins but by the spin wave wavelength. The maximum possible spin wave wavelength for N spins subject to periodic boundary conditions is $N\phi = 2\pi$. The energy of the spin wave is $E_1 = NJS^2\cos(\varepsilon)$, where ε is the angle between two neighbouring spins. For a large spin ensemble ϕ, θ and ε are very small and one can obtain the following relation $\frac{(E_1-E_0)}{E_0} = 1-\cos(\varepsilon) \approx 1-\cos(\theta\phi) \approx (\theta\phi)^2/2 \propto 1/N^4$. This shows that a collective excitation in the form of a spin wave is much more favourable than a localised excitation for a system containing a large number of spins[37].

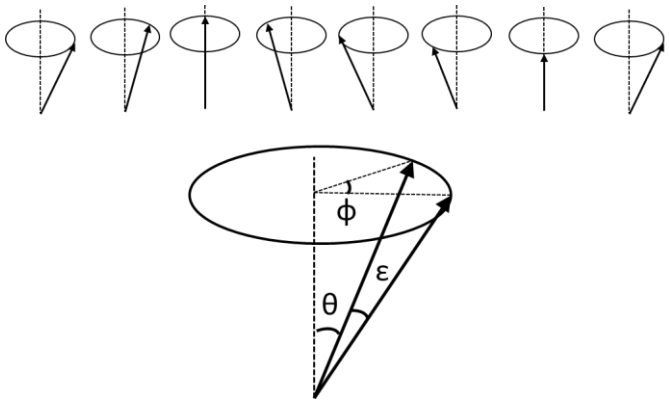

Figure 2.11 A chain of spins in which each successive spin is at an angle ε relative to its neigbours.

2.11.1 Spin wave dispersion relation

The dispersion relation for spin waves supported by a line of spins can be derived by means of a semi-classical method. The exchange energy between one spin at the position *pa* (*a* is the lattice parameter) and its neighbours at the positions *(p-1)a* and *(p+1)a* is $E = -J\mathbf{S}_p \cdot (\boldsymbol{S}_{p-1} + \mathbf{S}_{p+1})$ and it's magnetic moment is $\mathbf{m}_p = -g\mu_B\mathbf{S}_p$. The energy may be written as

$$E = -\mathbf{m}_p \cdot \frac{-J}{g\mu_B}\left(\mathbf{S}_{p-1} + \mathbf{S}_{p+1}\right) = -\mu_0\mathbf{m}_p \cdot \mathbf{H}_p \qquad (2.11.1.1)$$

where $\mathbf{H}_p$ is the exchange field. From classical mechanics the torque can be written as the rate of change of angular momentum:

$$\frac{d\hbar\boldsymbol{S}_p}{dt} = \mu_0\mathbf{m}_p \times \mathbf{H}_p, \qquad (2.11.1.2a)$$

$$\frac{d\boldsymbol{S}_p}{dt} = \frac{-g\mu_B\mu_0}{\hbar}\mathbf{S}_p \times \mathbf{H}_p = \frac{J}{\hbar}(\mathbf{S}_p \times \mathbf{S}_{p-1} + \mathbf{S}_p \times \mathbf{S}_{p+1}). \qquad (2.11.1.2b)$$

Linearisation is performed by assuming that $S_z = S$ and the amplitudes of S_x and S_y are small so that their cross products can be neglected.

$$\frac{dS_p^x}{dt} = \frac{JS}{\hbar}(2S_p^y - S_{p-1}^y - S_{p+1}^y), \qquad (2.11.1.3a)$$

$$\frac{dS_p^y}{dt} = \frac{-JS}{\hbar}(2S_p^x - S_{p-1}^x - S_{p+1}^x), \qquad (2.11.1.3b)$$

$$\frac{dS_p^z}{dt} = 0. \qquad (2.11.1.3c)$$

We then look for a lattice vibration solution of the form: $S_p^x = Ae^{i(pka-\omega t)}$ and $S_p^y = Be^{i(pka-\omega t)}$ where A and B are complex numbers. Substitution gives

$$-i\omega A = \frac{2JS}{\hbar}[1 - \cos(ka)]B \text{ , and, } -i\omega B = \frac{2JS}{\hbar}[1 - \cos(ka)]A. \qquad (2.11.1.4)$$

Setting the secular determinant of coefficients equal to zero yields

$$\hbar\omega = 2JS[1 - \cos(ka)] \qquad (2.11.1.5)$$

In the limit of small wave vectors (ka<<1), the dispersion relation becomes

$$\hbar\omega = JSk^2a^2 \qquad (2.11.1.6)$$

2.11.2 Thermal excitation of spin waves

In analogy with quantised phonon modes of a lattice, the magnon is also quantised. Magnons are boson like quasi-particles corresponding to reversal of a single spin, or change $\Delta M_S = 1$, for the whole system. n_k is the number of magnons having a wave vector *k*. The average number of quantised spin waves in a given mode *k* at thermal equilibrium is given by the Bose distribution:

$$< n_k >= 1/[\exp(\hbar\omega_k/k_B T) - 1]. \qquad (2.11.2.1)$$

It can be shown that the reduction in the magnetisation at low temperature due to magnon excitation is

$$\Delta M(T) = M(T = 0) - M(T) = \sum_{k\epsilon 1.BZ} n_k \propto T^{3/2}. \qquad (2.11.2.2)$$

This is known as Bloch's law.

2.12 Spin wave modes in an infinite slab

A major difference between spin waves and the uniform mode is that for spin waves the spins precess at the same frequency at a constant relative non zero phase to one another. Depending on the spin wave wavelength the spin wave mode will be either an exchange spin wave mode or a dipolar spin wave mode. The exchange interaction is short range and is dominant on short length scales. However, for long wavelengths the dipolar interaction will be dominant and the associated spin wave modes are known as magnetostatic spin waves[38,39,40]. The amplitude distribution and propagation properties of a given spin wave are determined by relative orientation of the propagation direction and the static magnetisation relative to the plane of the thin film. Depending on the sample geometry the group velocity and phase velocity are found to be of the same or opposite sign. There are three types of long wavelength modes magnetostatic suface waves (MSSW), magnetostatic backward volume waves (MSBVW) and magnetostatic forward volume waves (MSFVW)[41]. The dispersion relation for a given orientation of the in-plane propagation vector with the magnetisation is shown in Figure 2.12.1.

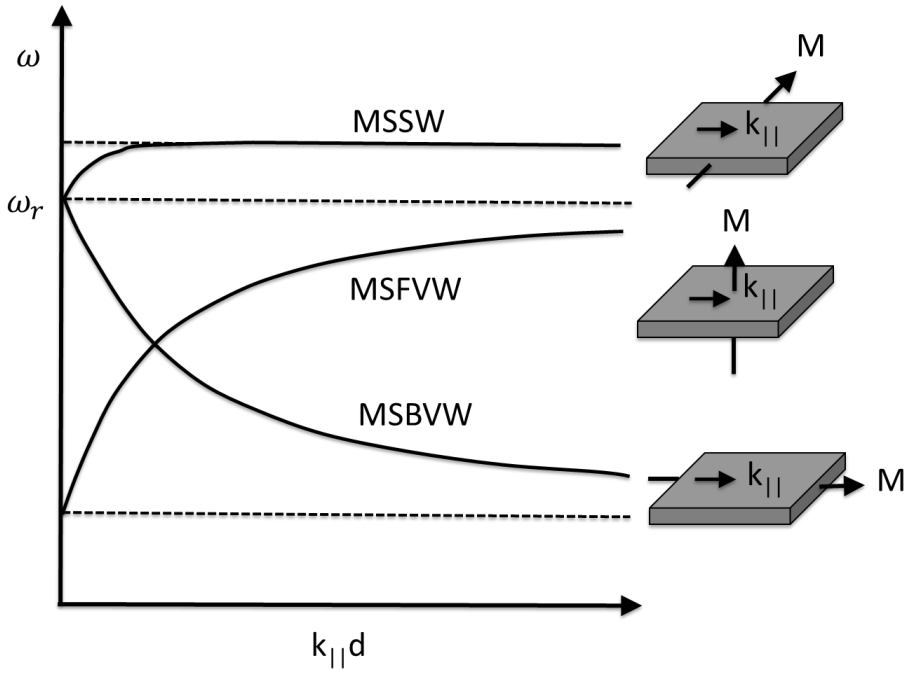

Figure 2.12.1 Dispersion relation for different magnetostatic spin waves. The frequency (ω) is plotted as a function of the product of the in-plane vector ($k_{||}$) and film thickness (d)[41].

Magnetostatic surface wave (MSSW):

The static magnetisation (**M**) is in the thin film plane but perpendicular to the in-plane propagation vector ($\mathbf{k}_{||}$). The corresponding dispersion relation[42] is given by

$$\omega_{MSSW} = \omega_H(\omega_H + \omega_M) + \frac{\omega_M^2}{4}\left(1 - e^{-2k_{||}d}\right). \quad (2.12.1)$$

For $k_{||} = 0$ the frequency reduces to that of the uniform mode (ω_r). The amplitude is highest near to the top and bottom surfaces of the sample and decays exponentially towards the centre of the sample. However spin waves at the two sample surfaces propagate in opposite directions. The dispersion relation was first calculated by Damon and Eshbach so such modes are also known as Damon-Eshbach modes[43].

Magnetostatic backward volume wave (MSBVW):

If the static magnetisation is in the film plane and parallel to the in-plane propagation vector then the solutions are referred to as backward volume magnetostatic waves, and they possess negative group velocity. The dispersion relation[44] is given by

$$\omega_{MSBVW} = \omega_H\left(\omega_H + \omega_M \frac{\left(1-e^{-2k_{||}d}\right)}{k_{||}d}\right). \quad (2.12.2)$$

Such modes have a negative dispersion relation and the amplitude is distributed throughout the film thickness. At $k_{||} = 0$ the dispersion relation reduces to a uniform resonant mode (ω_r) which is degenerate with the MSSW. It has a negative dispersion relation between ω_{MSBVW} and $k_{||}$.

Magnetostatic forward volume wave (MSFVW):

When the static magnetisation is out of the thin film plane the solutions are known as magnetostatic forward volume waves (MSFW). The solutions lie within a manifold for which all components of the in-plane wave vector are real, and the group velocity is positive. The frequency is lower than that of the MSSW.

2.13 Stoner-Wohlfarth model

When an external field is applied to a magnetic body, a M-H hysteresis loop is generated by plotting the magnetisation projected along the applied field against the applied field **H**. The main parameters of the loop are the saturation magnetisation (M_s), the remnant magnetisation (M_r), and the coercive field (H_c). The ratio $|M_r|/|M_s|$ is called the 'squareness' of the loop and has a value close to 1 when the magnetic field is applied along an easy axis. The loop has a tendency to close when the external field is applied along a hard axis.

The Stoner-Wohlfarth model [45] assumes that the ferromagnet is fully magnetised along one particular direction and acts as a single magnetic moment. For a particle with uniaxial ansiotropy, the orientation of the magnetisation **M** is determined by the competition between the uniaxial anisotropy, characterised by the anisotropy constant *K*, and the external field **H** as shown in Figure 2.13.1. The total energy may be written as

$$E = E_{ani} + E_z = Ksin^2(\theta) - \mu_0 HMcos(\theta - \phi) \qquad (2.13.1)$$

where θ is the angle between **M** and **K**. ϕ is the angle between **H** and **K**.

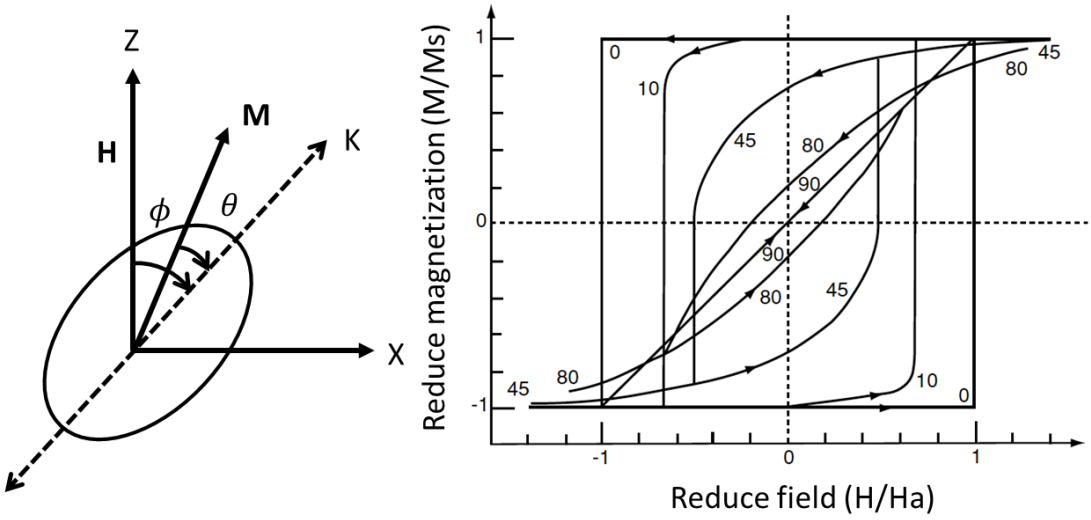

Figure. 2.13.1 Single domain grain with magnetisation **M** and an external applied magnetic field **H**. The anisotropy competes with the magnetic field in determining the orientation of the magnetic moment which is assumed to lie in the 2D *xz*- plane. Hysteresis loops are obtained when the magnetic field is applied at an arbitrary angle, ϕ, to the anisotropy axis. The straight line is the hysteresis loop when the field is along the hard axis (ϕ=90^o degrees) and square for easy axis (ϕ=0^o degrees)[28].

The moment will align along the direction for which the total energy is a minimum. Changes of orientation might occur smoothly by rotation or suddenly by switching in which case the magnetisation becomes discontinuous at some value of the magnetic field (**H**). More generally, for an ellipsoidal particle, one can define an effective anisotropy constant $K_{eff} = [K + 2\pi M_0^2(N_\perp - N_\parallel)]sin^2\theta$ due to the competition between the magnetocrystalline and shape anisotropies such that

$$E = K_{eff}sin^2\theta - \mu_0 MHcos(\theta - \phi) \qquad (2.13.2)$$

where $N_\perp$ and $N_\parallel$ denote the demagnetisation coefficients for the magnetisation oriented parallel and perpendicular to principal axis of the ellipsoid. The minimum energy condition with respect to θ is given by

$$\left(\frac{\partial E}{\partial \theta}\right)_\theta = 0 \text{ and } \left(\frac{\partial^2 E}{\partial \theta^2}\right)_\theta > 0. \qquad (2.13.3)$$

Solutions of these equations yield the Stoner asteroid equation for the point at which the local energy minimum becomes unstable.

$$\left(\frac{H_\perp}{H_K}\right)^{\frac{2}{3}} + \left(\frac{H_\parallel}{H_K}\right)^{\frac{2}{3}} = 1 \qquad (2.13.4)$$

where $H_K = \frac{2K}{M}$. It can then be written in a normalised format as

$$(h_\perp)^{\frac{2}{3}} + (h_\parallel)^{\frac{2}{3}} = 1 \qquad (2.13.5)$$

where $h_\perp$ and $h_\parallel$ are the normalised components of the field along the hard and easy axes respectively.

2.14 Magnetisation process

When the external field is swept so as to obtain a hysteresis loop the magnetisation typically undergoes several different motion i.e. domain wall motion and coherent rotation as is shown in Figure 2.14.1. The initial change of magnetisation from point 1 to 2 involves domain walls that are pinned and only displaced by a very small amount such that they can return to their original position when the external field is removed. This section therefore contains reversible magnetisation processes. For section 2 to 3, the domain walls moves so as to form a favourable domain of increased size with magnetisation along the field direction at the expense of the unfavourable domains. Irreversible Barkhausen jumps are observed in this section. Section 3 to 4 involves a reversible process in which the entire favourable domain rotates coherently toward the applied field to reach a saturated state. For section 4 to 5, the magnetisation remains quasi-aligned due to the exchange interaction until the field returns to zero. The existence of a significant magnetic moment at remanence is unique to ferromagnetic materials and so is one of their key distinguishing characteristics. In section 5 to 6, where the field is reversed, domains in which the magnetisation is reversed are nucleated and the associated domain walls propagate until finally a multi-domain state with zero net magnetic moment is formed when the external field is equal to the coercive field (Hc).

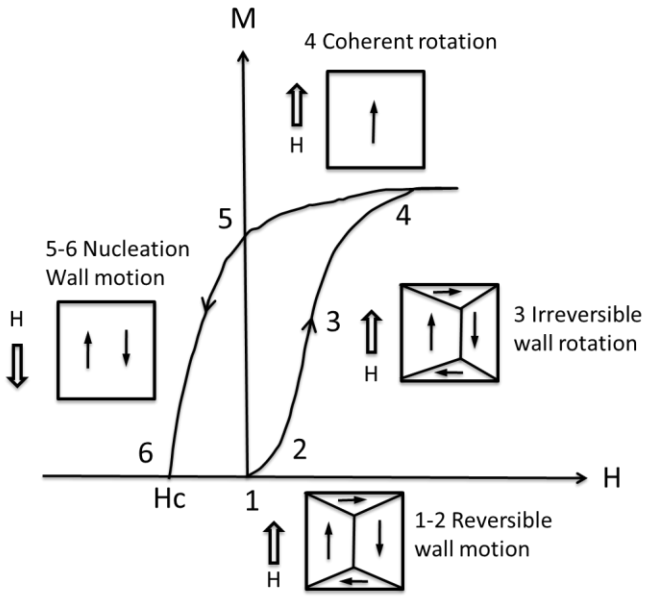

Figure 2.14.1 Initial magnetisation curve and demagnetisation curve in the first and second quadrants of a cubic ferromagnet showing the different magnetisation processes involved.

2.15 Landau-Liftshitz and Landau-Liftshitz Gilbert equation

The precession of the magnetisation under the influence of an magnetic field is described by the Landau-Liftshitz equation

$$\frac{\partial \boldsymbol{M}}{\partial t} = -\gamma\mu_0\left(\mathbf{M}\times\mathbf{H}_{eff}\right) - \frac{\lambda}{M_0^2}\mathbf{M}\times\mathbf{M}\times\mathbf{H}_{eff} \qquad (2.15.1)$$

where γ is the gyromagnetic ratio, M_0 is the saturation magnetisation and λ is the damping parameter. In the first term $\mathbf{H}_{eff}$ is the total effective field acting upon the magnetisation about which the magnetisation precesses. The second term describes the damping that causes the precessing magnetisation to spiral down towards the effective field. This equation is valid in the limit of small damping. The above equation was modified by Gilbert to describe the large damping factor case and gives rise to the Landau-Liftshitz Gilbert (LLG) [46] equation:

$$\frac{\partial \mathbf{M}}{\partial t} = -\gamma^*\mu_0\left(\mathbf{M}\times\mathbf{H}_{eff}\right) + \frac{\alpha}{M_0}\left(\mathbf{M}\times\frac{\partial \mathbf{M}}{\partial t}\right). \qquad (2.15.2)$$

The LLG equation (2.15.2) is equivalent to the Landau-Lifshitz equation (2.15.1) if $\alpha = \frac{\lambda}{\gamma M_0}$ and $\gamma^* = \gamma(1+\alpha^2)$. A schematic representation of torque appearing in the LLG equation is shown in Figure 2.15.1.

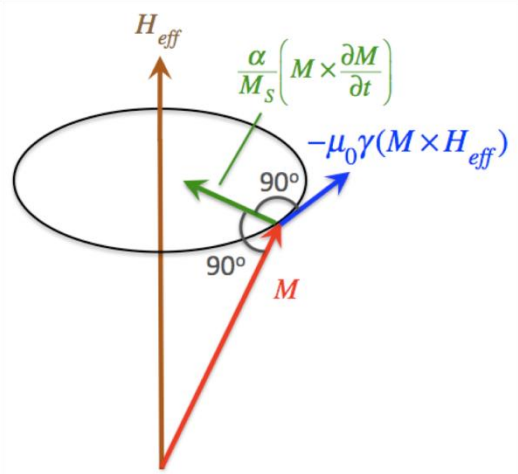

Figure 2.15.1 Schematic representation of the torques appearing in the LLG equation: the magnetisation precesses about the effective field.

2.16 Ferromagnetic Resonance

A magnetic system that is placed in a uniform magnetic field will absorb radio frequency radiation whose frequency matches that of the Larmor precession frequency. To observe the resonance condition most easily, the uniform magnetic field and radio frequency (RF) magnetic field (h) must be oriented perpendicular to each other. The equation of motion of the magnetisation in the absence of damping can be written in vector form as:

$$\frac{d\mathbf{M}}{dt} = -\mu_0\gamma\left(\mathbf{M}\times\mathbf{H}_{eff}\right). \tag{2.16.1}$$

Larmor precession occurs about the z-axis at a frequency $f = \omega_0/2\pi$. $\mathbf{H}_{eff}$ is the effective field consisting of the external field $\mathbf{H}$, anisotropy field and demagnetizing field such that $\mathbf{H}_{eff} = \mathbf{H}_{ext} + \mathbf{H}_{ani} + \mathbf{H}_d$. The effective field can be deduced from the total energy (E_{tot}) by the relation $\mathbf{H}_{eff} = -\frac{1}{M}\frac{\partial E_{tot}}{\partial \mathbf{M}}$. The demagnetising field can be written as

$$\mathbf{H}_d = -\mathcal{N}\mathbf{M} \tag{2.16.2a}$$

where, the demagnetizing tensor [47] $\mathcal{N}$ can be diagonalized if the coordinate axes are chosen to coincide with the principle axes of the ellipsoid $\mathcal{N} = \begin{bmatrix} \mathcal{N}_x & 0 & 0 \\ 0 & \mathcal{N}_y & 0 \\ 0 & 0 & \mathcal{N}_z \end{bmatrix}$.

so that

$$\boldsymbol{H}_d = -\mu_0\left[\mathcal{N}_x M_0 \mathbf{e}_x + \mathcal{N}_y m_y \mathbf{e}_y + \mathcal{N}_z m_z \mathbf{e}_z\right], \tag{2.16.2b}$$

$$\mathbf{H}_{eff} = (H + H_{ani} - \mathcal{N}_x M_0)\mathbf{e}_x + \left(h - \mathcal{N}_y m_y\right)\mathbf{e}_y - \mathcal{N}_z m_z \mathbf{e}_z\,. \tag{2.16.3}$$

The external field points in *x*-direction and the crystal anisotropy of the sample has easy axis along the *x*-direction. Since the radio frequency (RF) magnetic field (**h**) lies along the *y*-direction, the oscillating components of the magnetisation will be constrained to be in the *yz*-plane as shown in Figure 2.16.1.

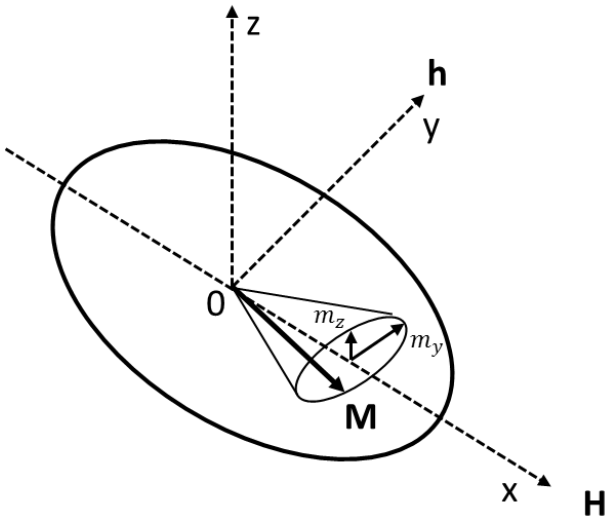

Figure 2.16.1 A schematic showing the *y* and *z*- component of the magnetisation under the excitation of an RF field (**h**) orthogonal to the external magnetic field (**H**).

The dynamic magnetisation components can be obtained from the LLG equation (2.15.2) which after linearization may be written in the form

$$0 = -\gamma\mu_0\left(-m_y\mathcal{N}_z m_z - m_z\left(h - \mathcal{N}_y m_y\right)\right) + \frac{\alpha}{M_0}\left(m_y\frac{dm_z}{dt} - m_z\frac{dm_y}{dt}\right), \tag{2.16.4a}$$

$$\frac{dm_y}{dt} = -\mu_0\gamma(m_z(H + H_{ani} - \mathcal{N}_x M_0) - \mathcal{N}_z M_0 m_z) - \alpha\frac{dm_z}{dt}\,, \tag{2.16.4b}$$

$$\frac{dm_z}{dt} = -\mu_0\gamma\left(M_0\left(h - \mathcal{N}_y m_y\right) - m_y(H + H_{ani} - \mathcal{N}_x M_0)\right) + \alpha\frac{dm_y}{dt}. \tag{2.16.4c}$$

Since $h \ll H$**,** the magnetisation has been written as $\mathbf{M} \approx M_0\mathbf{e}_{\boldsymbol{x}} + \mathbf{m}(t)$. Discussing $\boldsymbol{m}(t) \propto e^{-i\omega t}$ leads to the following expressions:

$$0 = -i\omega m_y + (\omega_H + (\mathcal{N}_z - \mathcal{N}_x)\omega_M - i\alpha\omega)m_z, \tag{2.16.5a}$$

$$\omega_H h = i\omega m_z + \left(\omega_H + \left(\mathcal{N}_y - \mathcal{N}_x\right)\omega_M - i\alpha\omega\right)m_y \tag{2.16.5b}$$

where $\omega_M = \mu_0\gamma M_0$ and $\omega_H = \mu_0\gamma(H + H_{ani})$.

We can write the above in matrix form as

$$\begin{pmatrix}0\\h\end{pmatrix} = \frac{1}{\omega_M}\begin{pmatrix}-i\omega & \left(\omega_H + \left(\mathcal{N}_z - \mathcal{N}_x\right)\omega_M - i\alpha\omega\right)\\ \left(\omega_H + \left(\mathcal{N}_y - \mathcal{N}_x\right)\omega_M - i\alpha\omega\right) & i\omega\end{pmatrix}\begin{pmatrix}m_y\\m_z\end{pmatrix}. \tag{2.16.6}$$

This gives the relationship between the magnetic moment and the RF field (**h**) which can then be used to deduce the necessary components of the magnetic susceptibility tensor given by $\mathbf{m} = \chi\mathbf{h}$. The real and imaginary components of the susceptibility as a function of RF frequency (ω) are then given by

$$\chi'_{yy} = \frac{\omega_M(\omega_H + (\mathcal{N}_z - \mathcal{N}_x)\omega_M)(\omega_r^2 - \omega^2)}{(\omega_r^2 - \omega^2)^2 + \alpha^2\omega^2\left[2\omega_H + \left(\mathcal{N}_z + \mathcal{N}_y - 2\mathcal{N}_x\right)\omega_M\right]^2} \tag{2.16.7a}$$

$$\chi''_{yy} = \frac{\alpha\omega\omega_M\left[(\omega_r^2 - \omega^2) + (\omega_H + (\mathcal{N}_z - \mathcal{N}_x)\omega_M)\left(2\omega_H + \left(\mathcal{N}_z + \mathcal{N}_y - 2\mathcal{N}_x\right)\omega_M\right)\right]}{(\omega_r^2 - \omega^2)^2 + \alpha^2\omega^2\left[2\omega_M + \left(\mathcal{N}_z + \mathcal{N}_y - 2\mathcal{N}_x\right)\omega_M\right]^2}. \tag{2.16.7b}$$

For small damping the resonance condition of the ferromagnetic sample is given by

$$\omega_r = \sqrt{\left(\omega_H + \left(\mathcal{N}_y - \mathcal{N}_x\right)\omega_M\right)(\omega_H + (\mathcal{N}_z - \mathcal{N}_x)\omega_M)}. \tag{2.16.8}$$

This expression is known as the Kittel equation[48, 49, 50]. The real part of the susceptibility expression is antisymmetric about the resonance frequency and is said to be of dispersive character whereas the imaginary part is of absorptive character and takes a Lorentzian line shape.

2.17 Magneto-transport

The conduction electrons in transition metals such as Ni, Pd and Pt and the alloys they form with Cu, Ag, and Au are all s-state electrons. The mean free path is reduced by lattice vibrations as the electrons are scattered to unoccupied d-states. Since the d-state electrons are responsible for ferromagnetism in transition metals there is a direct connection between the magnetic properties and the electrical properties of the transition metal ferromagnets.

Figure 2.17 shows the comparison of density of states (D(E)) for alkali metals (s^1), noble metals ($d^{10}s^1$), non-magnetic transition metals (d^ns^1) and magnetic transition metals ($d^{n\uparrow}d^{n\downarrow}s^1$). Alkali and noble metals have low resistivity. For noble metals a filled d band lies below the Fermi level. Non-magnetic transition metals have higher resistivity and both d and s bands lie at the Fermi level. However, for transition metals the Fermi level lies within the d-and s-state bands and the density of states for spin up and spin down d-band electrons are not necessarily the same.

Consider a simple model proposed by Drude to describe the free electron conduction, which can be written as

$$\frac{1}{\rho} = \sigma = \frac{ne^2\tau}{m^*}. \qquad (2.17.1a)$$

where m^*, n ,τ, and e are the effective mass, number of charge carriers per unit volume, relaxation time and the electron charge respectively. For magnetic transition metals the presence of d-band electrons at the Fermi level modifies the conductivity and there is overlap with the s-band at Fermi level.

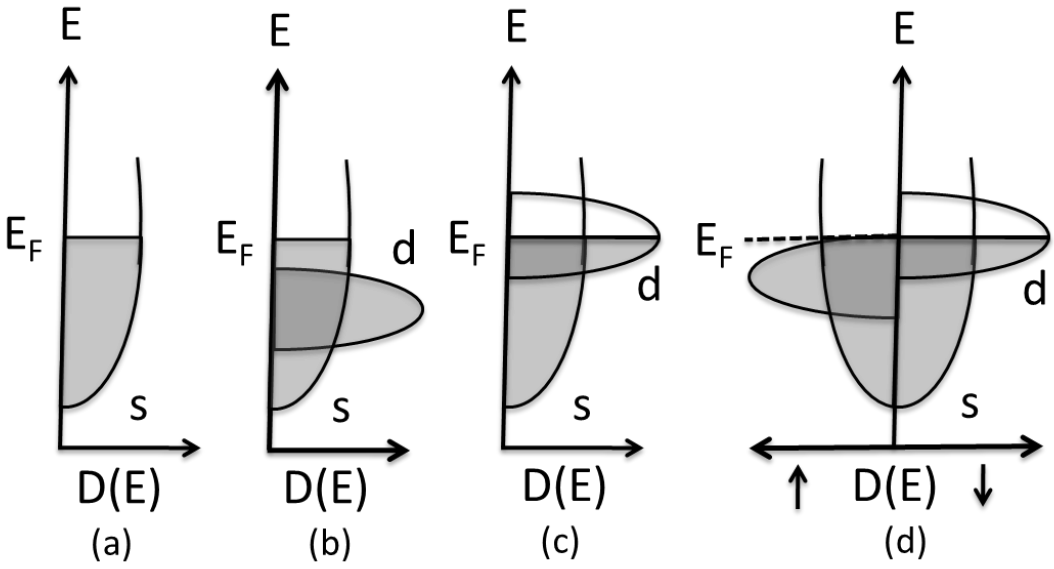

Figure 2.17 Schematic of the idealized density of states for (a) Alkali metals, (b) Noble metals, (c) Non-ferromagnetic, and (d) Ferromagnetic transition metals[19].

The d-band is spin split with a different density of states at the Fermi level for spin up and spin down electrons. The s-band is not spin split but s-state electrons at the Fermi level acquire predominantly spin up or spin down characteristics due to

hybridization with d-state electrons. s-d hybridization acts to partially localise the s electrons (decrease n) and partially delocalise the d-electrons (increase n). This results in a small net free electron concentration. Due to s-d hybridisation the parabolic s-state acquires characteristics of the flatter d-state and the effective mass of the conduction electron is increased which reduces the mobility. Overlap of the s and d bands allows conduction electrons to be scattered into more localised states of the same energy. The large density of states for d –state electrons enhances the scattering which reduces the relaxation time. The s-d scattering and other effects can be expressed in term of a scattering potential (V_{scatt})[28,60] and relaxation time.

$$\tau^{-1} = |V_{scatt}|^2 n(E_F). \qquad (2.17.1b)$$

where $n(E_F)$ is the density of states at Fermi level. Intersection of the d band with the Fermi level causes a reduction of $\frac{\tau}{m^*}$ that result in a resistance increase. Spin flip processes are very rare compared to normal momentum scattering processes at low temperature. This led Mott to propose the two current model[51, 52, 53, 54] in 1936 which is described in the following section.

2.17.1 Two current model for transition metals

Below the Curie temperature (θ_C) the spin polarisation carried by a charge current can be considered to be conserved during a scattering process. Spin waves that are responsible for mixing of spin up and spin down electrons have less effect at low temperature. Thus the charge carriers having spin up and spin down spins can be considered as two parallel channels of conduction that are independent of one another[55]. The resistivity of the spin up channel and the spin down channel can be represented by $\rho_\uparrow$ (spin up) and $\rho_\downarrow$ (spin down) respectively. The net resistivity resulting from a combination of the two channels is then given by

$$\frac{1}{\rho_{lowT}} = \frac{\rho\uparrow+\rho\downarrow}{\rho\uparrow\rho\downarrow}. \qquad (2.17.1.1)$$

The temperature also plays a very significant role in the functional form of the resistivity, especially near to the Curie temperature (θ_C). The most important contributions to the conductivity are:

1. The spin is scattered by spin disorder at high temperature. The magnetic order is related to the exchange interaction between the conduction s-electron spin and the local paramagnetic moment whose magnetic moment is proportional to $\sqrt{J(J+1)}$ [19]. The contribution of spin disorder to be resistivity above θ_C is given by $\rho_{para} = \frac{k_F(m\mathcal{J})}{4\pi e^2 Z h^2} J(J+1)$ where k_F is the Fermi wave vector, Z is the atomic number, e/m is the ratio of charge and mass of an electron, h is the Plank's constant and $\mathcal{J}$ is the exchange interaction coefficient.

2. Creation and annihilation of magnons flips the spin direction with increasing temperature. The existence of spin waves causes mixing i.e. spin up electrons are scattered to spin down states by the creation of magnons. Spin mixing equalizes the conduction electron spin so net resistivity increases as the shunting effect of the lower resistivity channel is increased. The resistivity due to spin mixing[56] is written as $\rho_{high\,T} = \frac{\rho\uparrow\rho\downarrow+\rho\uparrow\downarrow(\rho\uparrow+\rho\downarrow)}{\rho\downarrow+\rho\uparrow+4\rho\uparrow\downarrow}$, where $\rho\uparrow\downarrow$ is the spin mixing resistivity.

2.17.2 Anisotropic magnetoresistance (AMR)

The electric field that generates the current causes a distortion of the d-electron wavefunction. In addition the wavefunction is also distorted by the spin orbit interaction resulting ina an anisotropy that is dependent upon the orientation of the magnetisation[55,57]. The spin-orbit interaction energy is proportional to $\mathbf{L} \cdot \mathbf{S}$ which modifies the spherically symmetric electrostatic potential that is produced from a point charge where the spin-orbit interaction is neglected. This results in a the d-state electrons being subject to an energy term which is dependent on the orientation of the magnetisation, the result of which is that the magnetisation preferentially lies along a specific direction relative to the crystallographic axes. Due to the spin-orbit interaction, spin up and spin down electrons lie in different energy levels, resulting in the formation of spin split sub bands. The d-state wavefunction must then be recalculated due to the modification of the S_z eigenfucntion due to the spin-orbit interaction. This phenomenon causes the difference in resistance between the cases that the current is parallel or perpendicular to the magnetisation.

2.17.3 Giant magnetoresistance (GMR)

Giant magnetoresistance was first discovered in 1988 in Fe/Cr magnetic multilayers by Baibich et al. [58] at 4.2 K. It was observed that the strength of anti-ferromagnetic coupling between successive Fe layers varied with Cr thickness and that the resistance has largest when the Fe layers were anti-ferromagnetically aligned. Giant Magnetoresistance (GMR) is dependent on the relative orientation of the magnetisation within different layers rather than the angle between the current and the magnetisation. This distinguishes GMR from AMR. Conventionally the GMR ratio is defined as $\frac{\Delta R}{R} = \frac{R_{AF} - R_F}{R_F}$. In addition, Parkin[59] observed that the magnetoresistance ratio in Fe/Cr multilayers oscillates as a function of the exchange coupling and the Cr layer thickness.

2.17.3.1 Microscopic origin of GMR

Conduction electrons experience a varying electronic potential across a multilayer and a distinction can be drawn between intrinsic and extrinsic phenomena. Intrinsic phenomena are initiated by the band mismatch between the magnetic and non-magnetic interfaces. The existence of an exchange split d-band means that ↑d and ↓d provide different potentials for the different conduction electron spins[60]. Extrinsic phenomena are associated with impurities and interfacial roughness. Since the scattering is spin dependent the scattering potential will differ for majority and minority spin electrons. By adding impurities the magnetoresistance can be tuned, the spin asymmetry $\left(\alpha = \frac{\rho\downarrow}{\rho\uparrow}\right)$ can be reversed and therefore one can reverse the GMR effect. Spin asymmetry is the ratio of conductivity for spin up and spin down electrons.

The GMR vanishes if the thickness of the non-magnetic layer is greater than the mean free path of the conductions electrons. Electrons undergo spin dependent scattering at interfaces. Therefore strong spin dependent scattering is likely to occur for the case of anti-ferromagnetic coupling and weak spin –dependent scattering is likely to occur for the case of ferromagnetic coupling. Consequently, higher resistance values are observed for anti-ferromagnetic coupling than for ferromagnetic coupling between successive ferromagnetic layers.

2.17.3.2 Geometry of the current flow direction

The GMR effect has been observed for two current geometries; current in-plane (CIP) and current perpendicular to plane (CPP)[61]. CPP GMR is larger than CIP GMR and occurs in thicker films. The main difference between the two geometries is the relevant conduction electron path length. The mean free path (λ) is the relevant path length in the CIP case, while the spin diffusion length (l_{sf}) becomes important in CPP due to the spin accumulation effect[62]. Consider a current of electrons going from a ferromagnetic layer to a nonmagnetic layer in the CPP geometry. Electrons in the current whose spin is aligned along the majority electron spin direction in the ferromagnet will have a larger conductivity than those electrons with other spin oreintations. This is in contrast to the nonmagnetic material in which there is no spin-split band structure and therefore no spin dependent conductivity. When an electron current with a net spin polarisation, due to the polarising effect of the ferromagnet, passes into a nonmagnetic metal the Fermi level becomes spin split and a net spin accumulation occurs. The governing path length for CPP is much larger than for the CIP case.

The simplest Giant Magnetoresistance (GMR) device consists of two ferromagnetic layers separated by a non-magnetic conducting spacer layer. Parallel and antiparallel alignment of the magnetisation of the two ferromagnetic layers then lead to different electrical resistance, the resistance associated with antiparallel alignment usually being larger than that associated with parallel alignment of the ferromagnetic layers. The CPP GMR configuration is shown in Figure 2.17.3.2.1. The electrical resistance of a ferromagnetic layer, including the scattering at the interface with the spacer layer, for spin up (down) electrons will be denoted by R↑ (R↓).

For parallel orientation of the two ferromagnetic layers the resistance for the spin up channel is 2 R↑ and for the spin down channel is 2 R↓ as shown in Figure 2.17.3.2.2 (b). This gives a total resistance of

$$R_{parallel} = 2R\uparrow R\downarrow/(R\uparrow + R\downarrow). \qquad (2.17.3.2.1a)$$

For antiparallel orientation of the two layers the electrons are predominately spin up in one layer and spin down in the other as shown in Figure 2.17.3.2.2 (a). The total resistance will then be given by

$$R_{antiparallel} = (1/2)(R\uparrow + R\downarrow). \qquad (2.17.3.2.1b)$$

The difference in resistance between the two cases can then be written as

$$\Delta R / R_{parallel} = (R_{antiparallel} - R_{parallel}) / R_{parallel} = (R\uparrow - R\downarrow)^2 / 4R\uparrow R\downarrow . \qquad (2.17.3.2.1c)$$

Therefore the larger the difference between R↑ and R↓, the larger the magnetoresistance. This expression clearly shows that the magnetoresistance arises from the different resistances of the spin up and down electrons within a ferromagnetic material.

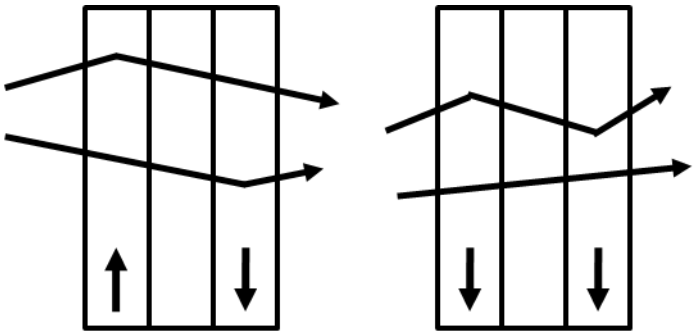

Figure 2.17.3.2.1 Schematic of electron transport in a multilayer with (a) antiparallel and (b) parallel magnetisation. Arrows show the magnetisation direction.

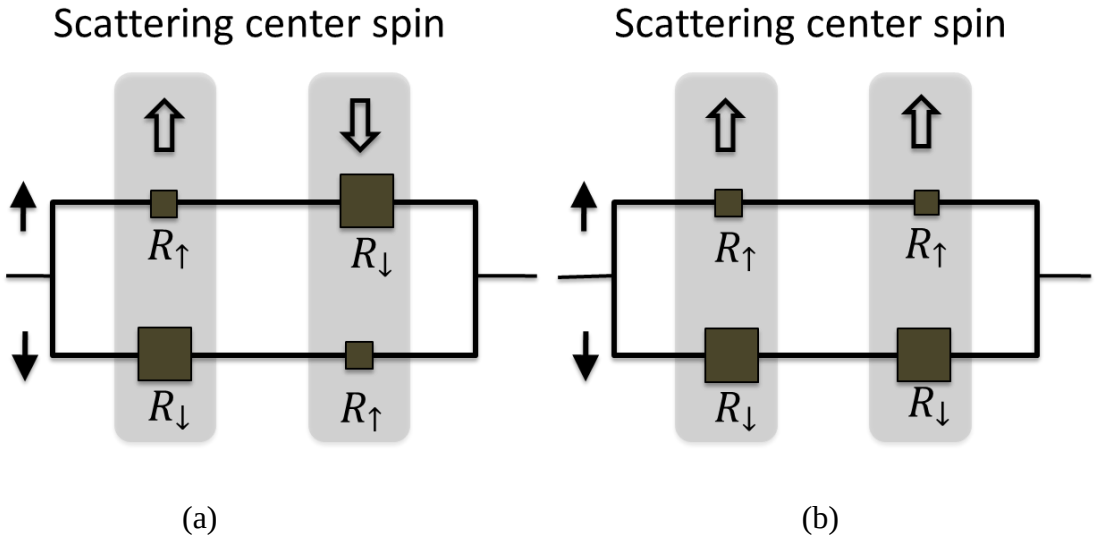

Figure 2.17.3.2.2 The magnetic layers are now represented by resistances $R_\uparrow$ and $R_\downarrow$, (a) antiparallel magnetisation and (b) parallel magnetisation. Unfilled arrows indicate the direction of magnetisation for the two ferromagnetic layers.

Increased GMR is of great utility from a device point of view. A spin-valve is a GMR device consisting of two magnetic layers separated by a non-magnetic conducting spacer layer. One of the two layers is magnetically soft and very sensitive to a small field and is known as free layer. However the other layer is magnetically hard layer and its magnetisation is intended to be fixed in a particular direction which is known as fixed layer. The fixed layer magnetisation direction is fixed by either its high coercivity or exchange bias by a antiferromagnetic material (FeMn or IrMn). The GMR occurs during reorientation of the free layer between anti- parallel (parallel) alignment relative to the fixed layer yielding high (low) resistance. Another important concept is to utilise the oscillatory exchange coupling of the 3d-transition metal layers through non-magnetic or noble metal spacer layers. The non-magnetic layer provides the medium through which the long range interlayer exchange coupling oscillates between anti-ferromagnetic and ferromagnetic character. By choosing an appropriate thickness for the non-magnetic layer one can achieve anti-ferromagnetic coupling which reduces the dipolar field from the ferromagnetic layers, forming what is known as a synthetic antiferromagnet[63].

2.17.4 Tunneling magneto-resistance (TMR)

If the spacer layer of the GMR device is replaced by an insulator in the CPP configuration then the resulting device is known as a Magnetic Tunnel Junction (MTJ)[64,65,66]. Again the resistance of the MTJ depends upon the relative alignment of the magnetisation of the two layers and is determined by a spin dependent tunneling effect. The current passed through the MTJ is forced to tunnel quantum mechanically through the insulator[67]. The Julliere Model is used to explain the phenomenon of TMR. A first assumption is that the electron spin is conserved during tunneling. Thus the conduction is the sum of spin up electron tunneling and spin down electron tunneling. With this assumption, the majority spin electrons will tunnel to majority spin states and the minority spin electrons will tunnel to minority spin states for the parallel magnetisation configuration. For the antiparallel magnetisation state an electron from a majority spin state will tunnel to a minority spin state and vice-versa. A second assumption is that the conductance for a particular magnetisation orientation is proportional to the product of the effective densities of state of the two ferromagnetic layers. Therefore the tunneling current for parallel and antiparallel states is different, as is shown in Figure 2.17.4.1. The spin polarisation state can be

expressed in terms of the spin up $n_{\uparrow}(E_F)$ and spin down $n_{\downarrow}(E_F)$ density of states at the Fermi level as

$$P = \frac{n_{\uparrow}(E_F) - n_{\downarrow}(E_F)}{n_{\uparrow}(E_F) + n_{\downarrow}(E_F)} . \qquad (2.17.4.1)$$

In 1975 Julliere observed 14% TMR [67, 68] in an iron/germanium/cobalt MTJ. According to his model the TMR is given by

$$\text{Tunneling magneto-resistance} = \frac{\Delta R}{R_{AP}} = \frac{R_{AP} - R_P}{R_{AP}} = \frac{2P_1P_2}{1+P_1P_2} . \qquad (2.17.4.2)$$

where P_1 and P_2 are the spin polarisations for the two layers.

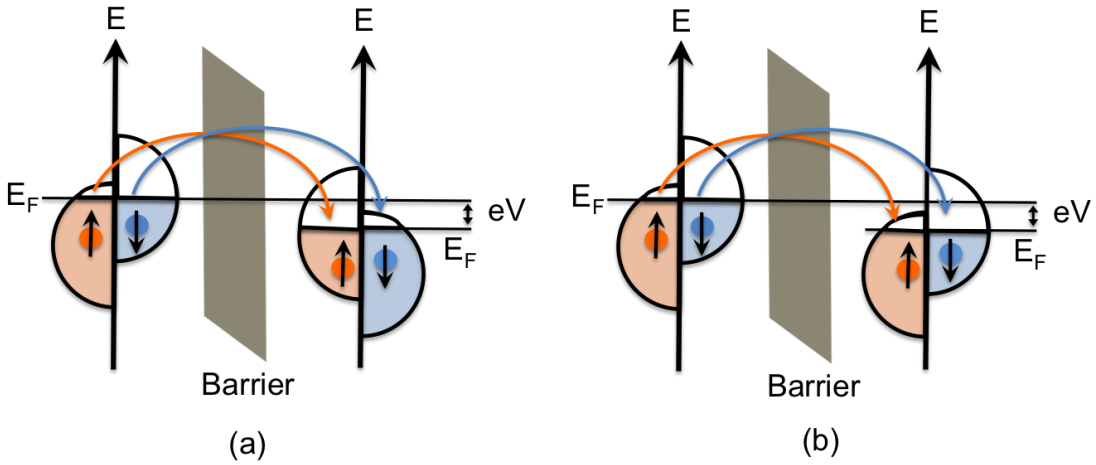

Figure 2.17.4.1 Schematic representation of tunnel magnetoresistance. The magnetisation of the two layers are orientated antiparallel (left) and parallel (right).

2.17.5 Spin transfer torque

The flow of charge (current) has an associated current density is given by $j = nev_d$. This current density has an associated spin polarisation P_e where ($0<P_e<1$). The current therefore carries an angular momentum (j_S) which is given by

$$j_S = n\frac{\hbar}{2}P_e v_d = n\frac{\hbar}{2}P_e\frac{j}{ne} = \frac{\hbar P_e j}{2e} \qquad (2.17.5.1)$$

where n and v_d are the number of charge carriers and the associated drift velocity respectively. Since angular momentum is conserved, any loss in the angular momentum of the current must be accounted for by a transfer of angular momentum

to the material through which the current passes. One possible channel of angular momentum transfer is the exertion of spin transfer torque by the current upon the local magnetisation. An unpolarised charge current can also exert a torque on the local magnetisation if it is first polarised by a ferromagnetic lattice via spin dependent scattering. Spin transfer torque can excite magnons, microwave excitations, domain wall motion and cause the reversal of the magnetisation. The first theory of spin transfer torque was proposed by Luc Berger[69] and John Slonczewski[70]. Their theory suggested that Spin Transfer Torque (STT) can be used to manipulate the orientation of the local magnetisation. The rate of flow of angular momentum is independent of the sample dimensions and so STT devices are generally of nanoscale dimension where one can generate high current densities with only a small input current, thus minimizing the Oersted field from the current as well as Joule heating.

Consider a spin polarised electron entering a ferromagnetic thin film which is uniformly magnetised. Initially, the electron travels along the *x*-axis and it's associated spin is polarised in a direction making an angle θ with *z*-axis. The electron can then scatter from the interface and this scattering is angle dependent. For example, for a Cu-Co interface[71] the majority spin polarisation will have a higher transmission probability than the minority spin polarisation. If the Co layer is then subject to an exchange bias field along the *z*-axis then the Co electrons will precess at the Larmor frequency about the effective internal field, the dominant term of which is the exchange field, completing many cycles as they scatter from site to site. When the electrons leave the ferromagnetic layers the *xy*-components of the magnetic moment are dephased[72] but the *z*-component is unchanged provided that the thickness of the thick layer (Co layer) is less than the diffusion length. The angular momentum transfer from the spin polarised current to the thin ferromagnetic layer occurs at a rate of $\frac{\hbar P_e j}{2e}\sin(\theta)$[28]. The STT modifies the magnetisation of the thin layer by rotating the magnetisation toward the direction of the spin-polarisation of the incoming current as shown in Figure 2.17.5.1 (top). Now consider electrons flowing in the opposite direction. Electrons become spin polarised upon passing through the thin layer and then travel on to the thick layer. There is not sufficient torque to cause rotation of the magnetisation of the thick layer. Some of the spin states that are minority spins in the thick layer will be reflected back into the thin layer. The transverse component of the spin angular momentum is transferred to the thin layer and as a result the stable state

is the case where the magnetisation of the thick and thin layers are aligned anti-parallel to one another as shown in Figure 2.17.5.1 (bottom).

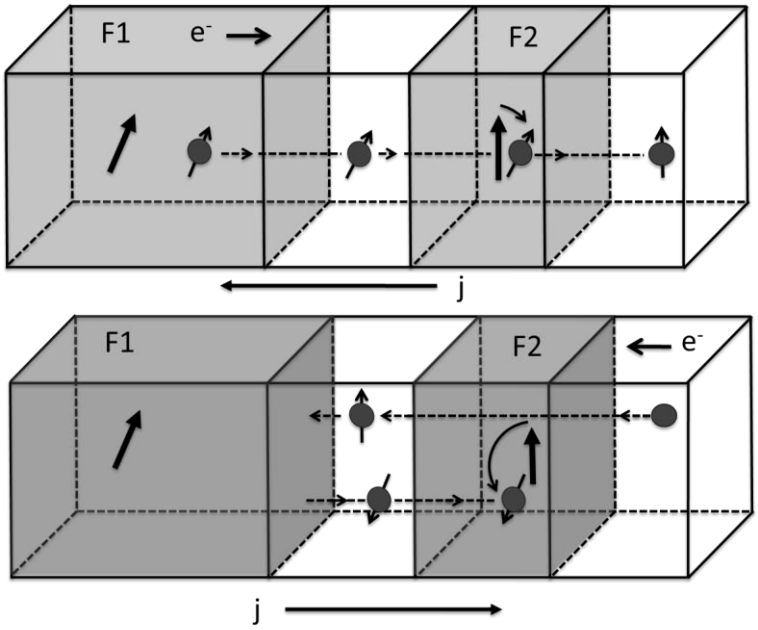

Figure 2.17.5.1 Schematic diagram of a trilayer structure originally proposed by J. Slonczewski for positive positive current (top) and negative current -bottom). The device is made of two magnetic layers F1 (thick layer) and F2 (thin layer) separated by a nonmagnetic layer.

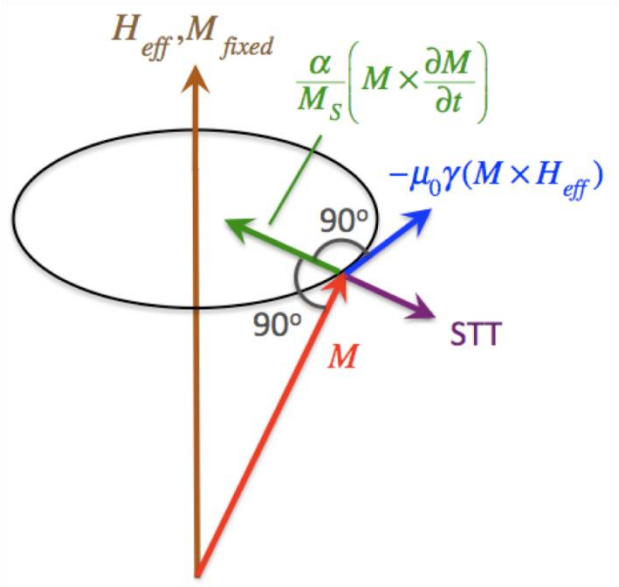

Figure 2.17.5.2 Schematic diagram showing the direction of the damping and spin-torque vectors relative to the effective field and static magnetisation directions.

According to the Slonczewski model the contribution to the time variation of the magnetisation vector $\mathbf{M}_2$ due to STT is given by

$$\frac{d\mathbf{M}_2}{dt} = -P_{transverse}\,\mathbf{M}_2 \times (\mathbf{M}_2 \times \mathbf{M}_1) \qquad (2.17.5.2)$$

where $P_{transverse}$ is proportional to the magnitude of the current and spin polarisation.

The LLG equation for the thin layer (F2) can be written with the inclusion of the STT as

$$\frac{d\boldsymbol{M_2}}{dt} = -\gamma\mu_0(\mathbf{M_2} \times \mathbf{H}_{eff}) + \frac{\alpha}{M_2}(\mathbf{M}_2 \times \frac{d\mathbf{M}_2}{dt}) - a\mathbf{M}_2 \times (\mathbf{M}_2 \times \mathbf{M}_1) + b(\mathbf{M}_2 \times \mathbf{M}_1) \qquad (2.17.5.3)$$

where d_2 is the thickness of the second layer (F2). The effective field $\mathbf{H}_{eff}$ has contributions from the external field ($\mathbf{H}_{ext}$), the uniaxial anisotropy field ($\mathbf{H}_{ani}$), and the demagnetising field of the second layer. The third term is the STT term. The magnetodynamics induced by STT can be understood from the diagram shown in Figure 2.17.5.2. If the spin transfer torque is sufficiently large then the result is a negative damping that leads to a departure from equilibrium.

According to most models the transverse spin current component is completely absorbed within a few lattice spacing from the interface. An additional component of the spin transfer torque lies perpendicular to the plane defined by $\mathbf{M}_1$ and $\mathbf{M}_2$ and is usually smaller than the in plane component [73]. The in-plane component of the STT and out-of-plane component of the STT are denoted by $\boldsymbol{\tau}_{\parallel}$ and $\boldsymbol{\tau}_{\perp}$. The in-plane component of the STT ($\boldsymbol{\tau}_{\parallel}$) can be written as

$$\boldsymbol{\tau}_{\parallel} = -a\mathbf{M}_2 \times (\mathbf{M}_2 \times \mathbf{M}_1). \qquad (2.17.5.4)$$

The out-of plane component of the STT ($\boldsymbol{\tau}_{\perp}$) can be written as

$$\boldsymbol{\tau}_{\perp} = b(\mathbf{M}_2 \times \mathbf{M}_1) \qquad (2.17.5.5)$$

where a and b depend upon the material[74]. The in-plane STT term from equation (2.17.5.4) mainly affects the linewidth of small amplitude oscillating motion and leads to strong dependence of the amplitude with respect to the STT. The Out-of-plane component of the STT from equation (2.17.5.5) behaves as a field-like torque

term and so it can effect the resonance frequency of the system under investigation[75]. The out-of-plane STT component makes a strong contribution to the magnetisation dynamics observed in MTJs, but is usually negligible for metallic spacer layers.

2.18 Summary

The background concepts of fundamental magnetism required for the thesis have been presented in this chapter. The chapter began from the origin of the atomic magnetic moment and has finished with the magnetisation dynamics of spintronic devices, which are the main focus of this thesis.

Chapter 3

Experimental techniques

3 Introduction

This chapter describes the experimental techniques developed for characterizing the magnetisation dynamics of nanoscale devices in both the time and frequency domain. The chapter consists of two parts. The first part describes the development of a time resolved scanning Kerr microscope for characterization of ultrafast magnetisation dynamics in the time domain, while the second part will cover the development of electrical transport measurement techniques for characterization of spintronic devices in the frequency domain.

3.1 Time resolved scanning Kerr microscopy development

3.1.1 General Introduction

Although there has been considerable progress in magnetic imaging in recent years, magneto-optical techniques still have many advantages. The method used for this work is based on the magneto-optic Kerr effect (MOKE) which describes the magnetisation dependent rotation of plane polarized light reflected from an opaque magnetic sample. Kerr microscopy is a versatile and flexible imaging technique. Magnetic fields of arbitrary strength and direction can be applied to the sample, making it possible to observe hysteresis loops. Using time resolved MOKE (TRMOKE), magnetisation dynamics can be studied at arbitrary frequencies covering a whole range of processes ranging from slow dynamics to excitations beyond the gigahertz regime.

3.1.2 Evolution of MOKE as a magnetic microscopy tool

Magneto-optical effects were discovered over a century ago. They played an important role in the development of electromagnetic theory and atomic physics. In 1846, Faraday reported the first magneto-optical effect[76,77]. It causes a rotation of the plane of polarisation of linearly polarized transmitted, which is linearly proportional both to the component of magnetic field in the propagation direction, and the

thickness of the medium of propagation. A number of similar experiments were reported, and the discovery of the Zeeman Effect followed[78].

In 1875, the Rev. John Kerr[79], demonstrated that an electric field influences the polarisation state of optical radiation as it passes through a transparent material. The following year Kerr announced the discovery of the magneto-optic Kerr effect[80](MOKE). MOKE describes the interaction of electromagnetic waves with magnetic materials, which results in a change of the intensity or polarisation of linearly polarized light reflected from a magnetic material. MOKE is used to measure the hysteresis loops of thin magnetic films by plotting the Kerr signal (rotation or ellipticity)[81] as a function of the applied external magnetic field. MOKE can also be used as a scanning microscopy technique, so that magnetic domain imaging with micrometric resolution becomes possible. A recent development of MOKE is the so called quantitative vector-magnetometry (MOKE-VM), which permits quantitative evaluation of different magnetisation components. In this method, the measurement of the MOKE signal depends on three different configurations of the optical polarisation and the applied field. It yields an accurate and complete characterization that enables a three-dimensional tracking of the magnetisation vector, while the external field is swept along certain directions[82, 83]. It provides a qualitative description of the switching process, giving a deeper insight into the mechanism of magnetisation reversal during the hysteresis loop cycle for materials displaying anisotropy (of both crystalline and shape origin)[84]. It reveals the extent to which magnetisation reversal[85] occurs through coherent magnetisation rotation and allows for easy and hard axes to be identified.

3.1.3 Origin of the magneto-optical effect

The optical response of a material at a particular wavelength is defined by the dielectric tensor (ε). Under the application of an electric field (**E**), charge is displaced from its original position and give rise to a polarisation. The overall effect is given by displacement vector (**D**)[86], such that

$$\mathbf{D} = \varepsilon \mathbf{E} \,. \qquad (3.1.3.1)$$

In ferromagnetic materials, the symmetry is broken due to the existence of finite magnetisation. The dielectric tensor is represented by a (3x3) matrix.

The Onsager relations require that $\varepsilon_{mm}(\mathbf{M}) = \varepsilon_{mm}(-\mathbf{M})$ and $\varepsilon_{mn}(\mathbf{M}) = -\varepsilon_{nm}(-\mathbf{M})$, so that diagonal elements are even, whereas off-diagonal elements are odd[87,88,89] with respect to the magnetisation. To first order, the diagonal elements are independent of the magnetisation and the magneto-optic response is represented by off-diagonal elements that are linear in the magnetisation. The dielectric tensor can be written as,

$$\varepsilon = \varepsilon_r \varepsilon_0 \begin{pmatrix} 1 & -iQm_z & iQm_y \\ iQm_z & 1 & -iQm_x \\ -iQm_y & iQm_x & 1 \end{pmatrix} \qquad (3.1.3.2)$$

where m_i are the direction cosines of the magnetisation vector and Q is Voigt's constant. The microscopic origin of MOKE can be explained by either classical or quantum mechanical models. In a classical description, plane polarized light can be decomposed into circularly polarised components (right and left hand). The circularly polarized light drives electrons in circular trajectories. The induced dipole moment of the electron is proportional to the radius of the orbit. When an external magnetic field is applied parallel to the direction of optical propagation, the Lorentz force experienced by an electron driven by light of left and right circular polarisation will have opposite sign, resulting in a trajectory of different radius[90,91,92]. The dielectric constant is therefore different for left and right circularly polarized light, resulting in circular birefringence and dichroism. Ferromagnetic materials can be thought of as containing very large internal magnetic field that gives rise to strong magneto-optical effects.

The very large magneto-optical effects exhibited by ferromagnetic materials can be explained by quantum mechanics. In 1932, Hulme[93] showed that the large magneto-optical effects in ferromagnetic materials are a result of spin-orbit coupling. Spin-Orbit coupling energy $\sim -(\nabla V \times \boldsymbol{p}).\boldsymbol{s}$, results from the interaction of the electron spin moment with the electron motion with momentum *p* due to an electric field $\sim(-\nabla V)$. This energy can be rewritten as $-p.(s \times \nabla V)$ where the second factor may be considered as an effective magnetic vector potential. A strong magneto-optical effect occurs in ferromagnetic materials where there is non-zero net spin polarisation.

3.1.4 Magneto-optical reflection co-efficient

When linearly polarised light is reflected from a ferromagnetic metal the polarisation state of light is modified with respect to that of the incident light, a phenomenon known as the Magneto-Optical Kerr Effect (MOKE). An ellipticity (ε_K) is induced and the plane of polarisation (major axis of the ellipse) is rotated through an angle θ_K(known as Kerr rotation) with respect to the polarisation of the incident beam. Ellipticity and Kerr rotation are proportional to first order in the magnetisation of the ferromagnetic metal upon which the beam is incident. By measuring the change in the plane of polarisation it is then possible to measure the magnetisation in the chosen ferromagnet. Such measurements are performed with either *s*- or *p*-polarised incident beams. Where the electric field vector of s-polarised light is orthogonal to the plane of incidence and for *p*-polarised light it lies in the plane of incidence. The MOKE is illustrated below in Figure 3.1.4.1 for the case of an *s*-polarised incident beam.

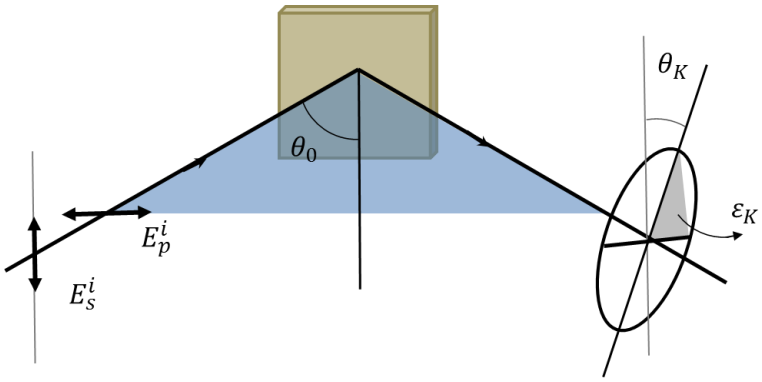

Figure 3.1.4.1 The polarisation of incident *s*- polarised light is changed to elliptically polarised light upon reflection from a ferromagnetic metal become due to the Magneto-Optical Kerr Effect (MOKE). The rotation of the major axis of the ellipse θ_K is the Kerr rotation and ε_K is the Kerr ellipticity.

A detailed understanding of the effect of magneto-optical interaction requires consideration of the optical reflection co-efficients. These are obtained by applying the Maxwell boundary conditions to solutions of the wave equations, which is itself derived from Maxwell's equations[21]. The geometry of a wave propagating towards the interface is given in Figure 3.1.4.2.

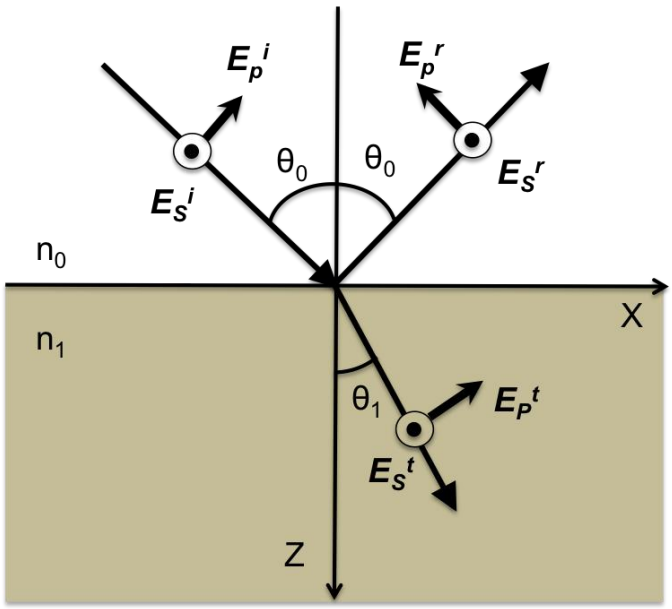

Figure 3.1.4.2 The geometry used for calculation the reflection co-efficient[98].

The relationship between the amplitude components of incident and reflected waves can be expressed by a Jones matrix[94,95,96] .

$$\begin{bmatrix} E_s^t \\ E_p^t \end{bmatrix} = \begin{bmatrix} r_{ss} & r_{sp} \\ r_{ps} & r_{pp} \end{bmatrix} \begin{bmatrix} E_s^i \\ E_p^i \end{bmatrix}. \tag{3.1.4.1}$$

That contains the Fresnel coefficients r_{ij}. The magneto-optical reflection co-efficients for the interface between a magnetic material with refractive index n_1 and a non-magnetic medium with refractive index n_o was given by Metzger et al. by considering terms upto second order in the magneto-optic constant ($\mathcal{Q}$)[97]. Considering only terms of first order in the magneto-optic constant, the reflection co-efficients[98,99] are given by

$$r_{ss} = \frac{n_0 cos\theta_0 - n_1 cos\theta_1}{n_0 cos\theta_0 + n_1 cos\theta_1}, \tag{3.1.4.2}$$

$$r_{pp} = \frac{n_1 cos\theta_0 - n_0 cos\theta_1}{n_1 cos\theta_0 + n_0 cos\theta_1} + \frac{2in_1 n_0 cos\theta_0 sin\theta_1 u_y}{(n_1 cos\theta_0 + n_0 cos\theta_1)^2}, \tag{3.1.4.3}$$

$$r_{ps} = -\frac{iQn_1 n_0 cos\theta_0 (sin\theta_1 u_x - cos\theta_1 u_z)}{cos\theta_1 (n_0 cos\theta_0 + n_1 cos\theta_1)(n_1 cos\theta_0 + n_0 cos\theta_1)}, \tag{3.1.4.4}$$

$$r_{sp} = \frac{iQn_1 n_0 cos\theta_0 (sin\theta_1 u_x + cos\theta_1 u_z)}{cos\theta_1 (n_0 cos\theta_0 + n_1 cos\theta_1)(n_1 cos\theta_0 + n_0 cos\theta_1)}. \tag{3.1.4.5}$$

where $\mathbf{u} = \frac{\mathbf{M}}{|\mathbf{M}|}$ and θ_0 and θ_1 are the angles of incidence and transmission respectively, which are related by Snell's law as $n_0 sin\theta_0 = n_1 sin\theta_1$.The Kerr rotation and ellipticity are given by

$\theta_K = -Re\left\{\frac{r_{sp}}{r_{pp}}\right\}$ and $\varepsilon_K = Im\left\{\frac{r_{sp}}{r_{pp}}\right\}$ for incident p-polarized light,

$\theta_K = Re\left\{\frac{r_{ps}}{r_{ss}}\right\}$ and $\varepsilon_K = Im\left\{\frac{r_{ps}}{r_{ss}}\right\}$ for incident s-polarized light.

θ_K and ε_K are seem to vanish for non-magnetic materials for which $Q = 0$ and hence $r_{sp} = r_{ps} = 0$.

3.1.5 Principal measurement geometries

There are three principal measurement geometries based upon the orientation of the magnetisation with respect to the plane of incidence and the plane of the sample.

3.1.5.1 Polar Geometry

For the polar geometry, the magnetisation vector lies perpendicular to the plane of the sample $(u_x = u_y = 0, u_z = 1)$ and parallel to the incident plane as shown in Figure (3.1.5.1). P_p and P_s represent polarisations parallel and perpendicular to plane of incidence respectively. The magnetisation vector '**M**' is perpendicular to the surface of the sample. For the polar geometry, r_{sp} and r_{ps} are equal. At normal incidence the polar Kerr rotation θ_o is maximum while at grazing incidence it vanishes.

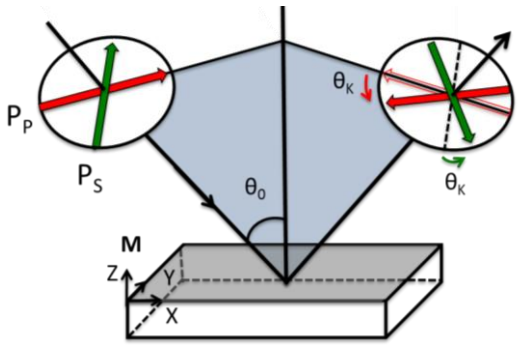

Figure 3.1.5.1 Schematic representation of the polar Kerr effect. Ps and Pp are the two different planes of polarisation perpendicular and parallel to plane of incidence respectively.

3.1.5.2 Transverse Geometry

In this geometry, the plane of incidence and the magnetisation lie in the plane of the sample but are perpendicular to each other ($u_x = u_z = 0, u_y = 1$) as shown in Figure (3.1.5.2). No change in the plane of polarisation of the reflected light is observed with respect to the incident polarisation. In the case of s-polarized light, the plane of polarisation is always parallel to the magnetisation. There is no Lorentz force and therefore no effect upon the reflected light. For p-polarized light, there is a Lorentz force but it acts parallel to the plane of incidence. It does not produce any Kerr rotation, but instead changes the intensity of the reflected light, which can be used to study the magnetic behavior of the sample. No effect is observed at normal incidence.

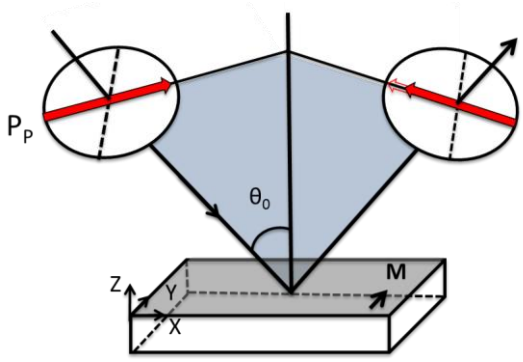

Figure 3.1.5.2 Schematic representation of the transverse Kerr effect. Ps and Pp are the two different planes of polarisation perpendicular and parallel to the plane of incidence respectively.

3.1.5.3 Longitudinal Geometry

In the longitudinal geometry, the magnetisation (**M**) lies both in the plane of the sample and in the plane of incidence ($u_x = 1, u_y = u_z = 0$) as shown in Figure 3.1.5.3. Both p- and s-polarized incident light experiences a Kerr rotation upon reflection from the magnetic surface as shown. However the Kerr effect depends upon the angle of incidence. At normal incidence the electric field vector of p-polarized light lies parallel to the magnetisation. In this case there will not be any Kerr rotation. The electric field vector of s-polarized light lies perpendicular to the magnetisation but the Lorentz force acts within the plane of polarisation of the incident light giving rise to a change in intensity instead of a Kerr rotation. The

angle of incidence must be large (typically between= 5^o to 60^o) for a strong Kerr rotation to occur.

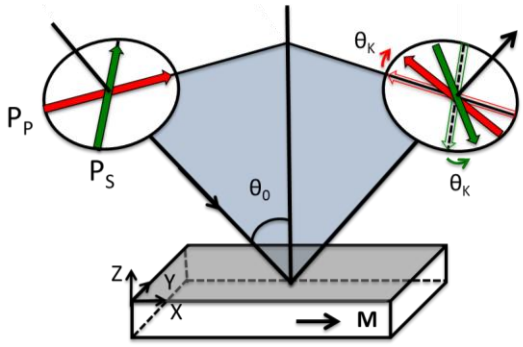

Figure 3.1.5.3 Schematic representation of the longitudinal Kerr effect. Ps and Pp are the two different planes of polarisation perpendicular and parallel to the plane of incidence respectively.

3.1.6 Detection of magneto-optical Kerr effect

The geometry used for detecting the out of plane component of magnetisation has the laser beam at normal incidence to the sample plane. This configuration is not sensitive to in-plane magnetisation. During precession the magnetisation tips out of the sample plane giving rise to Kerr rotation. A microscope objective (MO) has been used to focus the laser beam to a diffraction limited spot size. The back reflected beam is re-collimated by the microscopic objective and sent to the detector. The advantages of using a high numerical aperture (NA) MO is that it can achieve a higher spatial resolution and accept a wider range of angles of incidence.

The range of angles and different planes of incidence also provide sensitivity to different component of the magnetisation. A simple bridge detector consisting of two photodiodes, configured for common mode rejection is used to detect the polar magnetisation component. Using a quadrant bridge detector, both the out of plane component and the longitudinal magnetisation components can be detected simultaneously.

3.1.7 Stroboscopic technique

In time-resolved scanning Kerr microscopy, an ultrafast laser pulse is used to probe the instantaneous non-equilibrium magnetisation after the magnetisation is perturbed by a magnetic pulse. Many pump-probe events are recorded at the same

time delay and then averaged to produce a measurable signal. The time delay is then varied so as to build up the whole temporal profile of the non-equilibrium state.

3.1.8 Time resolved scanning Kerr microscopy

A Ti-Sapphire laser (Spectra-Physics Tsunami)[100] is used to generate the probe pulse. The Ti-Sapphire crystal is pumped by the 5W output of a diode pumped Nd-YVO_4 continuous wave visible (532 nm) laser (Spectra-Physics Millennia V). Regenerative mode locking of the Tsunami with an acoustic-optic modulator within the laser cavity generates a repetition rate of 80 MHz. The laser is tuned to produce a sub 100 fs optical pulse at a wavelength of 800 nm. The average output power is 0.6 W corresponding to 8 nJ per pulse. The beam has a diameter of ~2 mm and a beam divergence of ~1 mrad. The output beam is vertically polarized.

The whole experimental apparatus is shown in Figure (3.18.1). In order to understand the system, the function of each component will now be described in detail. The mirrors M1 and M2 are used to change the height of the beam from 14 cm to 17 cm from the optical table surface. As the beam height changes the polarisation also changes from a vertical to a horizontal polarisation state. A second harmonic generation (SHG) crystal is placed between the Ti-Sapphire laser source and mirror M1 to double the frequency. This improves the spatial resolution, which is limited by the wavelength. After the SHG crystal, the output beam contains both 800 and 400 nm components. Between M2 and the retro-reflector (RR), an electro-optic cell (Con-Optics 305) is inserted for picking the pulse whenever it is necessary to work at a repetition rate less than 80 MHz.

A Potassium deuterium phosphate crystal (KDP) and a polarizing beam splitter are enclosed inside the electro-optic cell to dump the picked beam and allow the unpicked beam to pass. The pulse picker exploits the Pockels effect with the KDP crystal set so that both its fast axis and slow axis lie at 45^0 to the electric field of the p-polarized laser beam. When a voltage is applied to the cell the birefringence of the crystal is modified, changing the relative phase of light polarised along the fast and slow axes. The cell is operated by applying a suitable external voltage to modulate the polarisation state. The polarizer after the crystal dumps one of the linearly polarized beams. The temporal alignment of the modulator driver is achieved by triggering from the fast photodiode from the laser cavity at 80 MHz. The alignment is optimised

using a 16 ns digital time delay. Setting the number '*n*' of pulses to rejected allows only the (*n*+1)th pulse to be transmitted.

The Retro-reflector fitted on top of the delay line is controlled by a 600 mm stepper motor that can delay the optical path by upto 4 ns. The beam after the retro-reflector is passed through the dichroic mirror M3 and mirror M4. The Dichroic mirror is made up of alternating layers of optical coatings with different refractive indexes, built up on a glass substrate. The interfaces between the layers of different refractive index produce phased reflections, selectively reinforcing certain wavelengths of light and interfering with other wavelengths. By proper control and engineering the thickness and number of the layers, the frequency (wavelength) of the pass band of the filter can be tuned. The main function of the dichroic mirror is to select either a blue or red probe beam. For this set up the dichroic mirror is chosen so as to pass a red beam and reflect the blue beam. Mirror M5 directs the beam coming from mirror M4 to a beam expander. The Gaussian beam profile is expanded and collimated by a beam expander (x10) and the uniform (intensity) central cross section (dia.~4 mm) is selected by an Iris to eliminate the possible diffraction from the optical components and to have equal uniform intensity across the probe beam cross section. A neutral density filter (NDF) is used to maintain the beam power below the damage threshold of the sample. The M6 and M7 mirrors raise the beam so that it can be directed vertically downwards to the microscope objective (MO) after passing through a polarizer and beam splitter.

A polarized probe beam is split by a 50/50 beam splitter (BS) and focused onto the sample with a 0.85 numerical aperture objective of x60 magnification. The polarisation of the reflected light is analyzed by a Glan Thomson (GT) polarizing beam splitter used in a simple optical bridge or a dual quadrant detection scheme that simultaneously acquires all three components of the magnetisation at the surface with 0.6 μm spatial resolution is shown in Figure 3.1.8.2. The detection is made phase sensitive by applying a low frequency modulation (gating), provided by a Stanford research signal generator (SRS) at 3.14 kHz to the pulse generator. The polarisation magnetic field generated by a Rohde & Schwarz (SMF 100A-Signal Generator), or a pulsed field generated by Impulse Generator, Picosecond Pulse labs-Model 3600 (PSPL), at the sample lies perpendicular to the static in-plane field **H** maintained by a vector electromagnet. The computer controlled piezo-driven flexure stage raster scans

the sample underneath the laser spot to build a spatial image as shown in Figure (3.1.8.2). To acquire the time resolved Kerr signal, the optical path of the probe beam is delayed with respect to the excitation pulse and the Kerr signal at each time step is detected by a stroboscopic technique. The pulsed magnetic field is generated by a current pulse passed through a conductor. The field profile generated by a micro-stripline is shown in Figure (3.1.8.3).

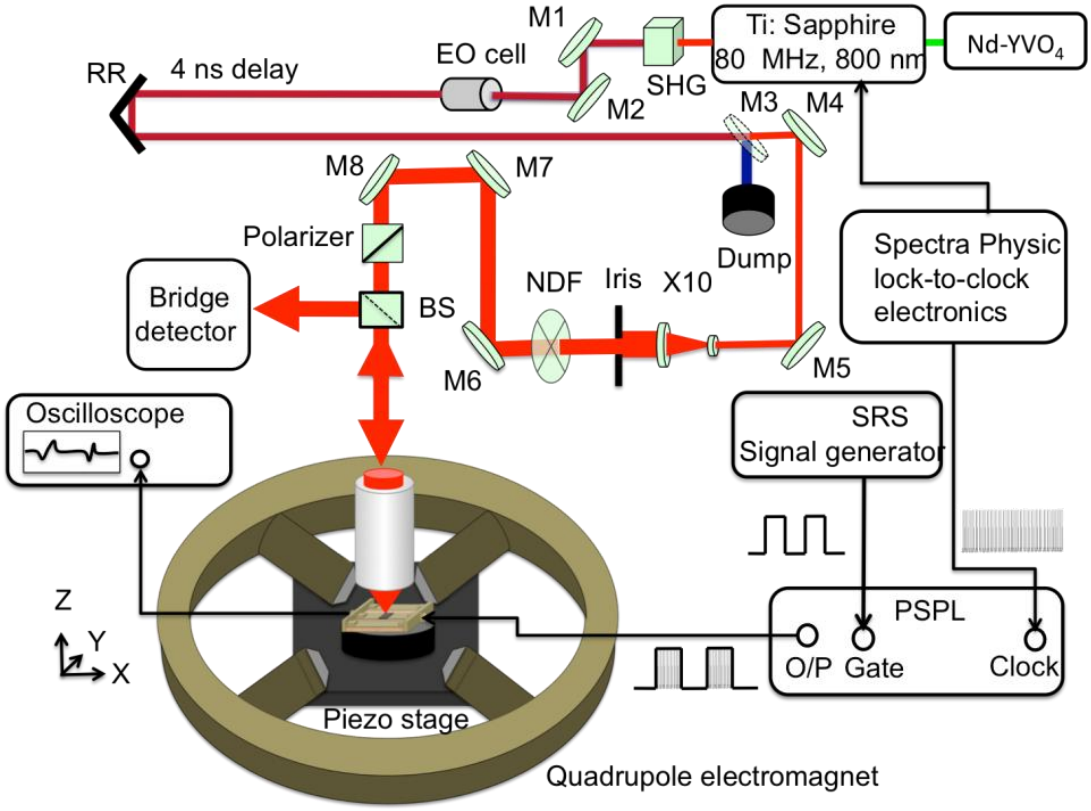

Figure 3.1.8.1 Time resolved scanning Kerr microscope experimental set up.

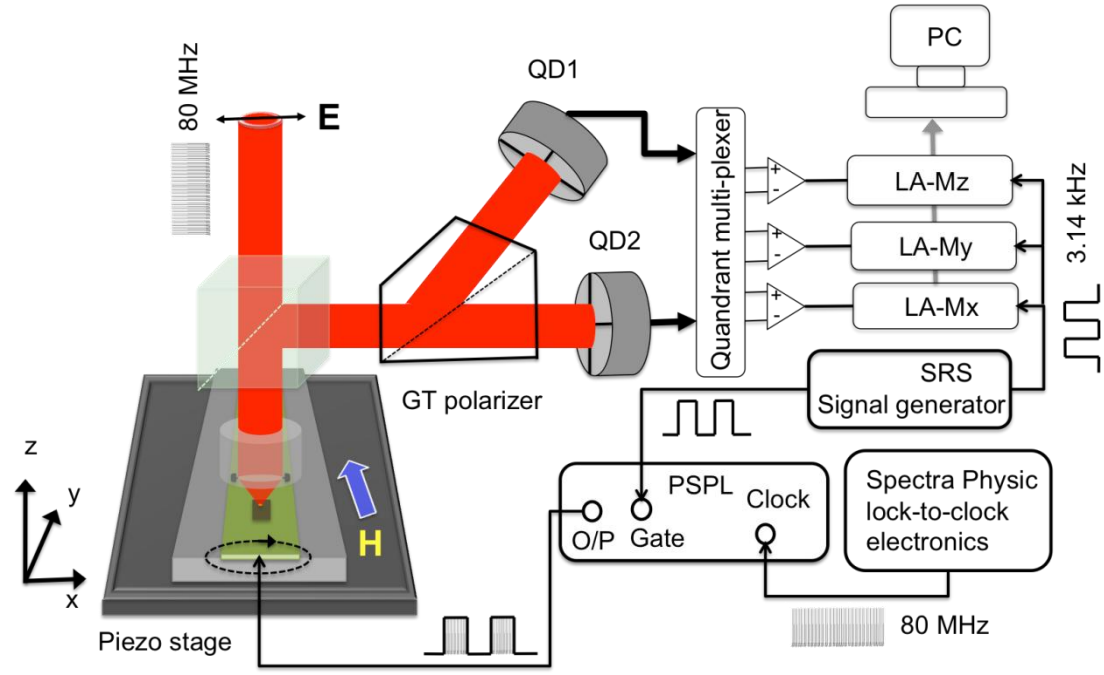

Figure 3.1.8.2 Synchronisation of probe beam with a gated electrical excitation pulse for detecting the Kerr signal using three lock-in amplifiers (LA-Mz, LA-My, LA-Mx).

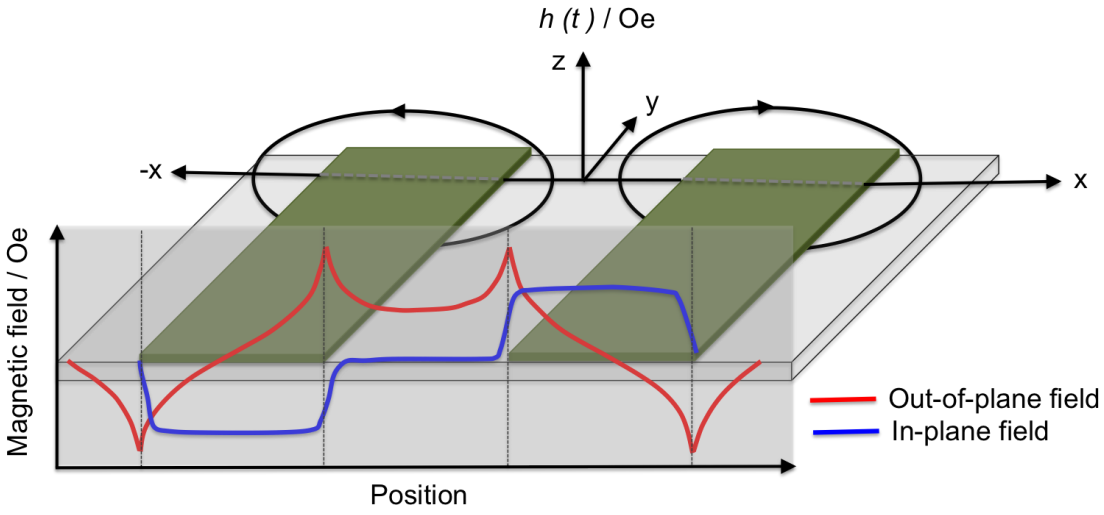

Figure 3.1.8.3 Magnetic field profile generated across a coplanar stripline when a pulsed current is passed through the stripline.

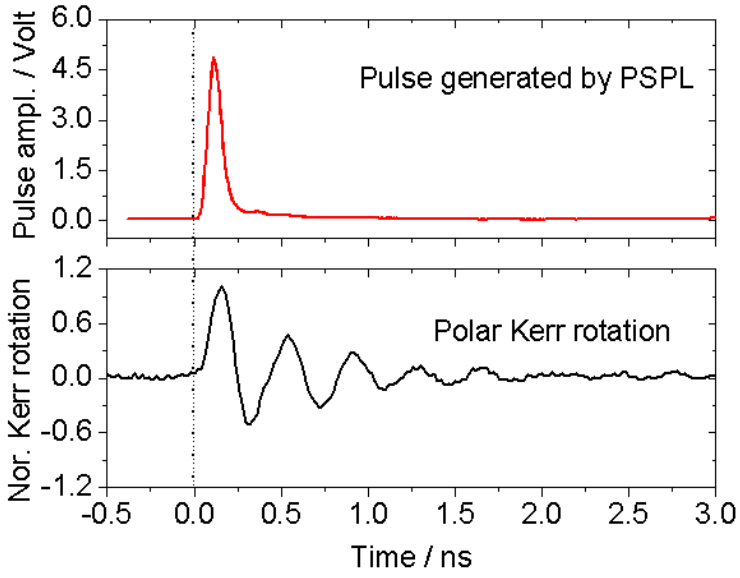

Figure 3.1.8.4 Pulses generated by the PSPL (red curve) excite the sample at zero delay the Polar Kerr rotation signal appears after the electrical pulse has arrived (black curve).

The stroboscopic technique requires synchronization of the whole system to build up either the full temporal profile of the magnetisation or dynamic magnetic images. The signal is detected electronically by low bandwidth circuitry. The picosecond temporal information is retrieved by modulating the excited pulse with a 3.14 KHz square wave from a signal generator (SRS function generator). The sample is excited either by a pulse from the PSPL, or by a harmonic waveform from the R&S. The PSPL excitation pulse has 40 ps rise time, 100 ps fall time, 80 ps pulse width and 7 Volt amplitude. The pulse PSPL waveform is shown in Figure (3.1.8.4) (top curve) which is displayed alongside the Kerr rotation (bottom curve) acquired after excitation of a 200 nm diameter permalloy nanodisc, of 15 nm thickness , by an in-plane field.

3.1.9 Detection concepts

When polarised light is reflected from a magnetic material it's polarisation is generally modified. The principal axis of polarisation of the reflected light is rotated with respect to that of the incident light. The rotation may be detected by means of a balanced optical bridge detector, the key component of which is a Glan-Thomson polarising beam splitter which consists of two right angled calcite prisms cemented together with Canada balsam.

The optical axes of the two prisms are aligned parallel to one another and are orientated perpendicular to the plane of incidence. The optical axis of the Glan-Thompson polarising beam splitter is oriented at 45^{o} to the polarisation of the light that is incident upon it. This splits the light incident on the detector into two components of equal intensity and orthogonal polarisation. These two components arise due to the different refractive indices that occur along different directions in the Glan-Thompson polarising beam splitter due to birefringence. Light with plane of polarisation parallel to the plane of incidence is reflected (ordinary ray) from the interface between the two calcite prisms whereas light with plane of polarisation perpendicular to the plane of incidence (extra-ordinary ray) is transmitted through the interface. After passing through the beam splitter the two beams of orthogonal polarisation are incident upon the active area of separate photodiodes. The difference between the two photodiode signals will be zero when the intensity of the two beams of orthogonal intensity is the same. When the light with rotated polarisation enters the detector there will be a difference in intensity of the two orthogonally polarized beams transmitted by the polarising beam splitter. Clearly in this case the difference in the photodiode signal will be non-zero and the size of this difference signal will depend upon the amount by which the polarisation of the light has rotated with respect to that of the incident beam. Let I_{PD1} and I_{PD2} represent the intensities on photodiodes 1 and 2 respectively. From Malus's law the intensity of light transmitted by a polariser is directly proportional to the square of the cosine of the angle between the transmission axis of the analyser and the plane of polarisation of the incident light, so

$$I_{PD1} \propto \left[cos\left(\frac{\pi}{4} - \theta_K\right)\right]^2, \tag{3.1.9.1}$$

$$I_{PD2} \propto \left[cos\left(\frac{\pi}{4} + \theta_K\right)\right]^2, \tag{3.1.9.2}$$

$$I_{PD1} \propto \left[cos\left(\frac{\pi}{4}\right) cos\,\theta_K + sin\left(\frac{\pi}{4}\right) sin\,\theta_K\right]^2, \tag{3.1.9.3}$$

$$I_{PD1} \propto \left[\frac{1}{\sqrt{2}} + \frac{1}{\sqrt{2}}\theta_K\right]^2. \tag{3.1.9.4}$$

Expanding equation (3.1.9.4) and neglecting higher order terms in θ_K we obtain

$$I_{PD1} \propto \frac{1+2\theta_K}{2} \tag{3.1.9.5}$$

and similarly for photodiode 2

$$I_{PD2} \propto \frac{1-2\theta_K}{2}. \tag{3.1.9.6}$$

Taking the difference signal one obtains

$$I_{PD1} - I_{PD2} \propto \frac{1+2\theta_K}{2} - \frac{1-2\theta_K}{2} = 2\theta_K. \tag{3.1.9.7}$$

By taking the difference of signals from the two photodiodes rather than simply measuring a varying intensity on a single photodiode one can remove the non-magnetic background detected by both photodiodes, a practice known as common mode rejection [101]. The time resolved Kerr signal and dynamic magnetic image acquired from a 2 μm disc are shown in Figure (3.1.9.1).

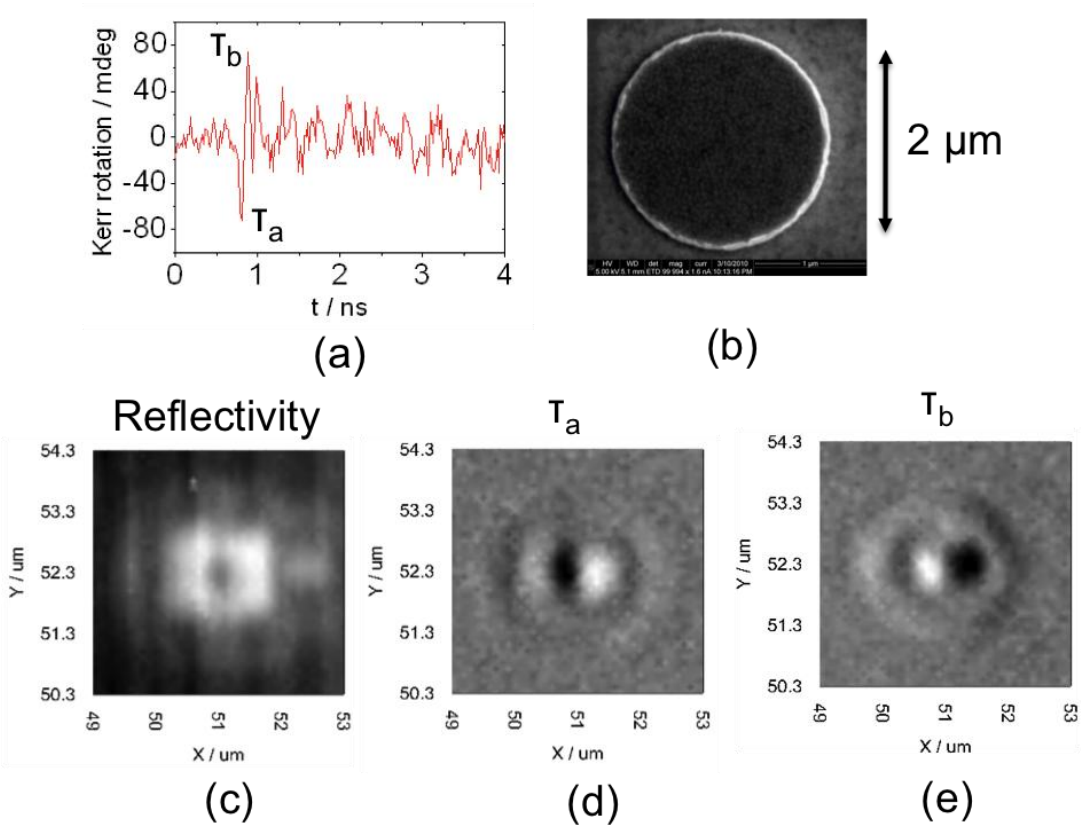

Figure 3.1.9.1 Polar time resolved scanning Kerr signal and dynamic magnetic images acquired from a 2 μm disc of 40 nm thick Permalloy prepared in the remnant state before being subjected to pulsed excitation: (a) Time resolved signal acquired by positioning the probe spot off the centre of the disc, (b) scanning electron micrograph of sample, (c) reflectivity image, (d) and (e) are the dynamic magnetic images from the first negative antinode and first positive antinode respectively. The grey scale is normalized to the maximum Kerr signal: white (black) represents magnetisation pointing into (out of) the plane of the page.

The three Cartesian components of the magnetisation can be detected when a microscope objective of high numerical aperture is used to focus the incident beam onto the sample. Such an approach results in different parts of the incident beam having different angles of incidence and planes of polarisation with different orientations relative to the local magnetisation. As a result different parts of the reflected beam contain different information about the magnetisation vector. Consider a collimated beam of light that is reflected back from the sample as being separated into four quadrants denoted by; L1, L2, R1 and R2. Now consider the beam as two halves; the left L (L1+L2) and the right R (R1+R2).

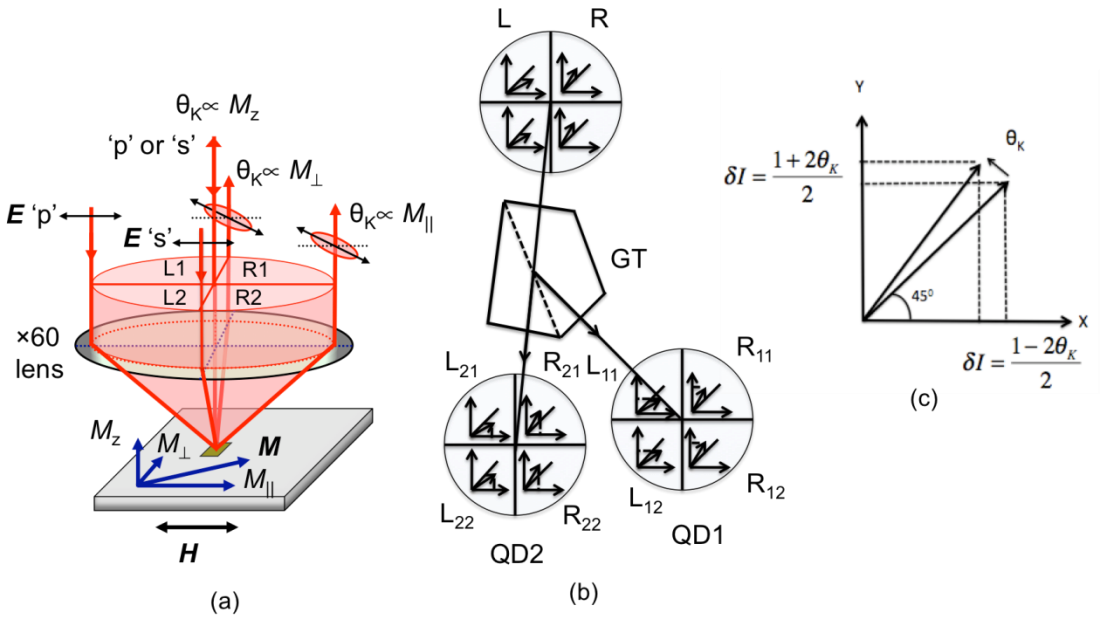

Figure 3.1.9.2 (a) The normally incident laser beam is focused by a large numerical aperture microscope objective resulting in a large range of incident angles[101]. (b) Operation of the Glan-Thomson (GT) polarising beam splitter. The polarized light (rotated with opposite sense in each half) reflected back from the sample is split with the GT polarising beam splitter. The beam incident on quadrant photodiode 2 (QD2) has polarisation projected onto the x-axis. The beam incident on QD1 has it's polarisation projected onto the y-axis[102] (c) A shift of angle δ corresponds to an intensity shift of $(1+\delta)/2^{1/2}$.

The beam incident from the left and exiting from right will sense positive $M_{\parallel}$, whilst the portion of the beam travelling in the opposite direction will sense negative $M_{\parallel}$. The same logic applies for $M_{\perp}$ but not for the out of plane component of the magnetisation (M_z). Adding the left (L1+L2) and right (R1+R2) halves of the beam will give the polar Kerr signal while the $M_{\parallel}$ component will cancel out. Subtraction of the left (L1+L2) and right (R1+R2) halves will remove the polar Kerr signal and leave the $M_{\parallel}$ component. We can measure the $M_{\perp}$ component in a similar way. The Glan-Thompson analyser beam polarizer directs the component of the light with polarisation parallel to the *y*-axis onto quadrant photodiode 1(QD1) and the component with polarisation parallel to the x-axis onto quadrant photodiode 2(QD2). For QD1, (R_{11}+R_{12}) and (L_{11}+L_{12}) will yield signals that increase and decrease respectively and vice-versa for QD2.

The increased and decreased intensities correspond to $\delta I = \frac{1 \pm 2\theta_K}{2}$ as shown in Figure (3.1.9.2) (c). The three Cartesian components of the magnetisation can be expressed as sums and differences of the different outputs of the quadrant photodiodes.

Polar, $M_z \propto (\mathrm{L}_{21} + \mathrm{L}_{22} + \mathrm{R}_{21} + \mathrm{R}_{22}) - (\mathrm{L}_{11} + \mathrm{L}_{12} + \mathrm{R}_{11} + \mathrm{R}_{12})$,

Longitudinal, $M_{\parallel} \propto (\mathrm{L}_{21} + \mathrm{L}_{22} - \mathrm{R}_{21} - \mathrm{R}_{22}) - (\mathrm{L}_{11} + \mathrm{L}_{12} - \mathrm{R}_{11} - \mathrm{R}_{12})$,

Longitudinal, $M_{\perp} \propto (\mathrm{L}_{21} - \mathrm{L}_{22} + \mathrm{R}_{21} - \mathrm{R}_{22}) - (\mathrm{L}_{11} - \mathrm{L}_{12} + \mathrm{R}_{11} - \mathrm{R}_{12})$.

There are a few important points to note when using a quadrant bridge detector. The beam incident on a quadrant diode should have a uniform, symmetric profile and should be centred on the quadrant photodiode to allow nullification. Non-uniformity in the beam cross section leads to off-centre alignment of the beam on the quadrant photodiode to achieve nullification. Off-centre alignment may then introduce cross-talk between the longitudinal components. The cross talk between two longitudinal components is found to be less than 10% when the bridge is well aligned. It is important to maintain a beam diameter~4 mm at the quadrant photodiode to allow the beam to fall equally onto the four quadrants of the photodiode.

It should be noted that the MOKE results in a rotation of the polarisation of the reflected light relative to the incident light, therefore to quantify the size of this effect it is most instructive to recalibrate the measured voltage signal in terms of degrees. This can be done by measuring the change in the difference signal between the intensities incident on the two photodiodes when the relative alignment of the transmission axis of the polarising beam splitter and the polarisation of the light incident upon it is changed by 1 degree. This yields a calibration factor that can be used to relate the change in voltage of the difference signal to a rotation of the polarisation in degrees. . Equation (3.1.9.8) gives the conversion factor for polar Kerr signals, measured with either the simple bridge or the vector bridge.

$$\text{Polar Kerr signal (degree)} = \left(\left(\frac{\text{Kerr signal (Volt)}}{\text{Normalise total intesity}}\right)/100\right) \times (\text{lock} - \text{in sensitivity}) \times \left(\frac{3.14}{\sqrt{2}}\right) \times \frac{1}{(\text{Calibration factor})}. \quad (3.1.9.8)$$

If the vector bridge is used to measure two orthogonal in-plane components simultaneously then half of the beam must be blocked during the calibration procedure so that they may be distinguished from one another. This modifies the calibration factor so that it takes the form

$$\text{Longitudinal Kerr signal (degree)} = \frac{1}{2} \times \left(\left(\frac{\text{Kerr signal (Volt)}}{\text{Normalise total intesity}} \right) / 100 \right) \times$$

$$(\text{lock} - \text{in sensitivity}) \times \left(\frac{3.14}{\sqrt{2}} \right) \times \frac{1}{(\text{Calibration factor})}. \qquad (3.1.9.9)$$

3.2 Development of an electrical transport measurement setup

Nanoscale devices such as recording sensors often have low electrical resistances and so the associated voltage dropped across such a device may be very small. As devices become smaller one needs to be increasingly careful that the current density is not so high as to damage the device. This restricts how the characterization of modern nanoscale devices can be performed.

3.2.1 The concept of a four terminal technique

The resistance of the Device Under Test (DUT) is determined by passing a known current through the DUT and measuring the voltage drop across the DUT. From Ohm's law one can obtain the DUT resistance by dividing the voltage dropped across the DUT by the current passed through it. A two terminal measurement technique is commonly used for devices that have large resistance.

Two terminal techniques are less accurate due to a contribution from the lead resistance to the measured resistance. In very small resistance devices the lead resistance becomes a significant part of the measured resistance. A typical contact resistance lies within the range of 1 mΩ to 10 Ω making it difficult to accurately record the device resistance in a two terminal measurement when the DUT has a resistance in the range of 10 Ω to 100 Ω. Let us assume that R1 and R2 are the contact resistances and the DUT resistance is denoted by R. The voltage drop across the contacts and the DUT is given by I(R1+R2+R). The circuit layout is shown in Figure (3.2.1) (a). All the resistances are connected in series and so one cannot separate the voltage dropped across the contacts from that across the DUT.

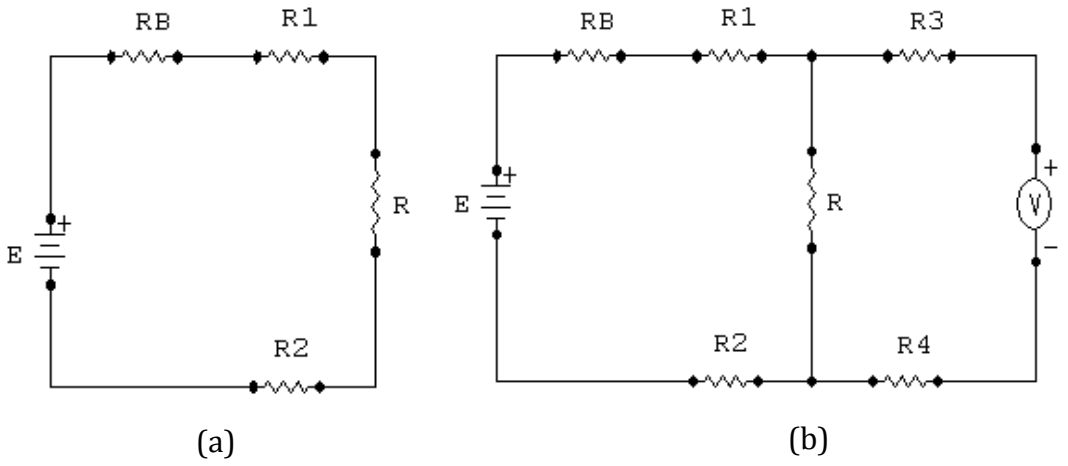

Figure 3.2.1 Electrical circuit diagram for a two terminal measurement (a) and a four terminal resistance measurement (b).

This problem can be solved by using a four terminal approach[103]. A separate pair of contacts are used for the current supplied and the voltage dropped across the DUT. This allows the voltage dropped across the DUT to be separated from that dropped across the contacts and interconnecting wires. An equivalent circuit for such a four terminal measurement is shown in Figure (3.2.1) (b). The current contact and voltage contact resistances are R1, R2, R3 and R4 respectively. R1 and R2 are the current contact resistances. The ideal voltmeter has an infinite input impedance so no current is assumed to pass through R3 and R4. The measured voltage (V=IR) is that generated in R alone and is independent of R1, R2, R3 and R4.

3.2.2 Differential resistance (dV/dI)

For a non-linear device the electrical resistance is no longer a constant so a measurement of the slope of the I-V curve at every point is needed. The derivative of the I-V curve gives the differential conductance which is the reciprocal of the differential resistance. One can either measure just the DC current and voltage (I-V curve method) with a current source and a voltmeter, and calculate the derivative, or use an AC method to measure dV/dI directly. Although the DC method is simple compared to the AC-technique, the calculation of the derivative amplifies the noise and so longer averaging times are required to obtain smooth curves.

3.2.3 I-V Curve method

To obtain a DC I-V curve from the DUT a 6221 AC &DC current source[104] (Keithley) and a 2182A Nanovoltmeter[105] (Keithley) were used. Data was obtained by the delta method so as to eliminate the thermoelectric effect from the contact electrodes.

Delta method

The delta method for the measurement of the DUT resistance is an effective way to eliminate the voltage generated by the thermoelectric effect within the contacts to the DUT. Thermoelectric drift due to heating by the measurement current can be approximated to a linear function, and can be cancelled out by alternating the sign of the current three times so as to make two delta measurements (One is a positive step and the other a negative step). Such an approach is also known as a three point measurement technique[106]. The voltage dropped across the DUT as a function of time with an alternating polarity of applied current is recorded. A voltage is recorded each time the current polarity changes, say V_{M1}, V_{M2}, V_{M3} etc. Each measurement includes a constant thermoelectric voltage offset (V_{emf}) and a linearly changing voltage offset (δV) as shown in Figure (3.2.3.1). The three voltage measurement includes the following voltages:

$$V_{M1}=V_1+V_{emf}, \tag{3.2.3.1}$$

$$V_{M2}=V_2+V_{emf}+\delta\text{V}, \tag{3.2.3.2}$$

$$V_{M3}=V_3+V_{emf}+2\,\delta\text{V} \tag{3.2.3.3}$$

where V_1, V_2 and V_3 are the voltages dropped across the DUT due to the applied current, V_{emf} is the thermoelectric offset voltage at the time V_{M1} is measured and δV is the thermoelectric voltage change.

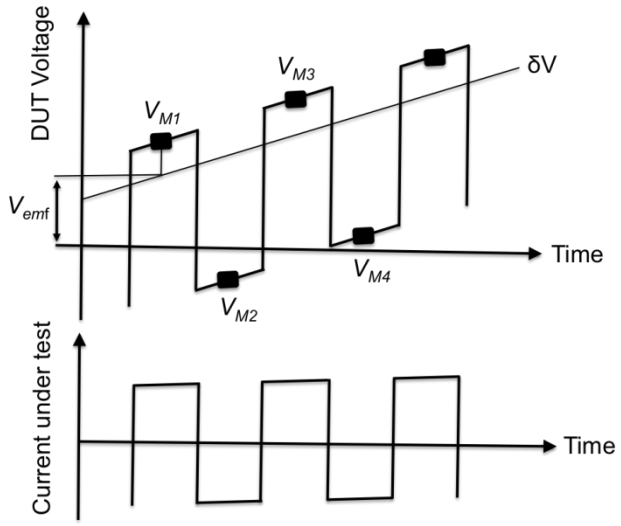

Figure 3.2.3.1 Delta method for cancelling thermoelectrically induced emfs[106].

Cancellation of V_{emf} and δV is then possible by computation of the results obtained from three voltage measurements. Let us define V_A to be half of the difference of the first two measured voltages

$$V_A = \frac{V_{M1}-V_{M2}}{2} = \frac{(V_1+V_{emf})-(V_2+V_{emf}+\delta V)}{2} = \frac{V_1-V_2}{2} - \frac{\delta V}{2}. \qquad (3.2.3.4)$$

Let V_B be the half the difference of the 2nd and 3rd measured voltages.

$$V_B = \frac{V_{M2}-V_{M3}}{2} = \frac{(V_2+V_{emf}+\delta V)-(V_3+V_{emf}+2\delta V)}{2} = \frac{V_2-V_3}{2} - \frac{\delta V}{2}. \qquad (3.2.3.5)$$

Both V_A and V_B are affected by the thermoelectric voltage but the effects are equal and opposite so that the final reading is taken to be the average of V_A and V_B given by

$$V_{final} = \frac{V_A-V_B}{2} = \frac{V_1+V_3-2V_2}{2}. \qquad (3.2.3.6)$$

To allow the linear approximation to be applied the polarity of the current source must alternate quickly and the voltmeter must make accurate measurements within a short period of time.

The three point measurement approach is the best choice for high accuracy resistance measurements and particularly useful for devices where the thermoelectric voltage is a significant fraction of the voltage dropped across the DUT. The use of the linear approximation requires the measurement cycle to be faster than the thermal time constant of the DUT. This requires the synchronisation of the current source and

voltmeter. The current source output must change polarity before the thermally induced voltage changes. The voltmeter measures only when the current source output has settled and the current source output does not switch polarity until the voltage measurement has been completed.

3.2.4 DC-transport measurement technique

The system developed to make three voltage measurements has two possible configurations allowing the user to run the delta measurements either on the front panel or via remote control from a personal computer (PC). The latter will be described in detail. An RS 232 interface between the 6221 AC & DC current source and 2182A nanovoltmeter allows the two devices to communicate with one another. To allow remote control the RS 232 interface for the model 2182A must be on and the selected interface for the 6221 AC &DC must be GPIB (or Ethernet). The GPIB IEEE-488 interface is used for communication with the PC. When correctly configured and connected the current source will automatically send the necessary commands to the voltmeter. Readings from the voltmeter are automatically sent to the current source for processing into delta readings that are then stored in a buffer and displayed on the front panel. Once the measurement is started the trigger synchronization between the current source and the nanovoltmeter is controlled by a dedicated trigger link (8501 Trigger link cable).

Using the above configuration the four probe contact technique is used to measure the resistance of nanoscale devices, as part of the setup shown in Figure (3.2.4.1). The current source outputs a differential current (dI) sweep and the associated differential voltage (dV) is measured. The setup uses the 3 point measurement method to calculate dV. When the start of the current sweep is triggered the current source output changes from the bias level to the start source current level. The output will change in equal steps until the stop level is reached and the output will then return to zero. This is also known as the linear staircase current sweep.

The sweep delay time determines the interval for each step. For all results shown in this thesis the DUT are Magnetic Tunnel Junctions (MTJ). The tunneling magnetoresistance can then be measured using the measurement setup outlined here. MTJs have dimensions in the nanometre regime and so resistance measurements must be performed at low current values to avoid damaging the MTJ. The resistance varies

with the relative orientation of the magnetisations of the reference and free layers. There are two ways of controlling the magnetisation; either by means of an external field or by a DC current. The DC current exerts a Spin Transfer Torque (STT) which can change the orientation of the free layer magnetisation. Parallel (anti-parallel) alignment of the free and reference layers generates minimum (maximum) magnetoresistance. This magnetoresistance (MR) is measured by the nanovoltmeter via the voltage drop across the MTJ. Alternatively a vector electromagnet is used to apply an external field in-, or out-, of-the plane of the MTJ. The voltage drop across the MTJ is measured at each step in the field sweep at a constant bias current, which is controlled from a Labview programme. Two Kepco power (BOP 36-6M) supplies have been used for vector control of the magnetic field generated by the four pole electromagnet. The two power supplies are connected to the output of a data acquisition (DAQ) card which is synchronised with the current source and the nanovoltmeter during the measurement. MR loops are obtained by sweeping the external field at very low current, while I-V characteristics are obtained by sweeping the current at remanence. During a DC current sweep the strength of the STT is dependent on the amplitude and polarity of the current. The STT will act to change the orientation of the magnetisation of the two layers to a more favourable state. If the STT is not large enough to produce a favourable magnetic state then the magnetisation of the free layer may experience auto-oscillations above the threshold regime or thermally excited oscillations in the sub-threshold regime. The oscillation of the magnetisation generates an accompanying oscillatory resistance and hence an oscillatory voltage. The voltage oscillation frequency lies in the microwave regime. The DC voltage signal and the oscillatory voltage are separated by using a bias-T. The DC voltage is sent it to the nanovoltmeter and the AC voltage sent to a spectrum analyzer so that the power spectrum of the oscillation can be obtained. The output oscillation amplitude is expressed in terms of the voltage spectral density (VSD). The spectrum analyser acquires the output power in units of dBm (#dBm=10log (Power/1mW)). Power can be express in terms of voltage (V_{rms}) and impedance (Z) as

$$\text{Power} = V_{rms}^2/Z\,. \qquad (3.2.4.1)$$

The impedance (Z) is the 50 Ohm characteristic impedance of the cables. This is converted into VSD by the Labview programme using the expression

$$VSD=V_{rms}/\text{sqrt (RBW)} \qquad (3.2.4.2)$$

where RBW is the resolution bandwidth of the spectrum analyser set during the data acquisition. In summary the experimental setup described so far can be used to characterize MTJs in the following ways:

1. Magnetoresistance loops can be acquired by sweeping an external field at a constant low bias current value, while I-V characteristics are acquired by sweeping the DC current at zero field. A vector electromagnet is used to apply an external bias field which is used to manipulate the orientation of the magnetisation. MR loops acquired from an MTJ are shown in Figure (3.2.4.2) (a) and (b).
2. The oscillatory voltage generated by the STT can be measured while sweeping the DC bias current at a fixed bias field value with any desired in-plane orientation of the said field. The DC and AC voltages are separated by means of a bias-T with the AC voltage being sent to a spectrum analyser that displays the power spectrum. Field swept spectra acquired with the field applied along the easy and hard axes at fixed bias current are shown in Figures (3.2.4.2) (c) and (d) respectively. Current swept spectra at fixed bias field are shown in Figures (3.2.4.2) (e) and (f), with the bias field applied along the easy axis and hard axis respectively.

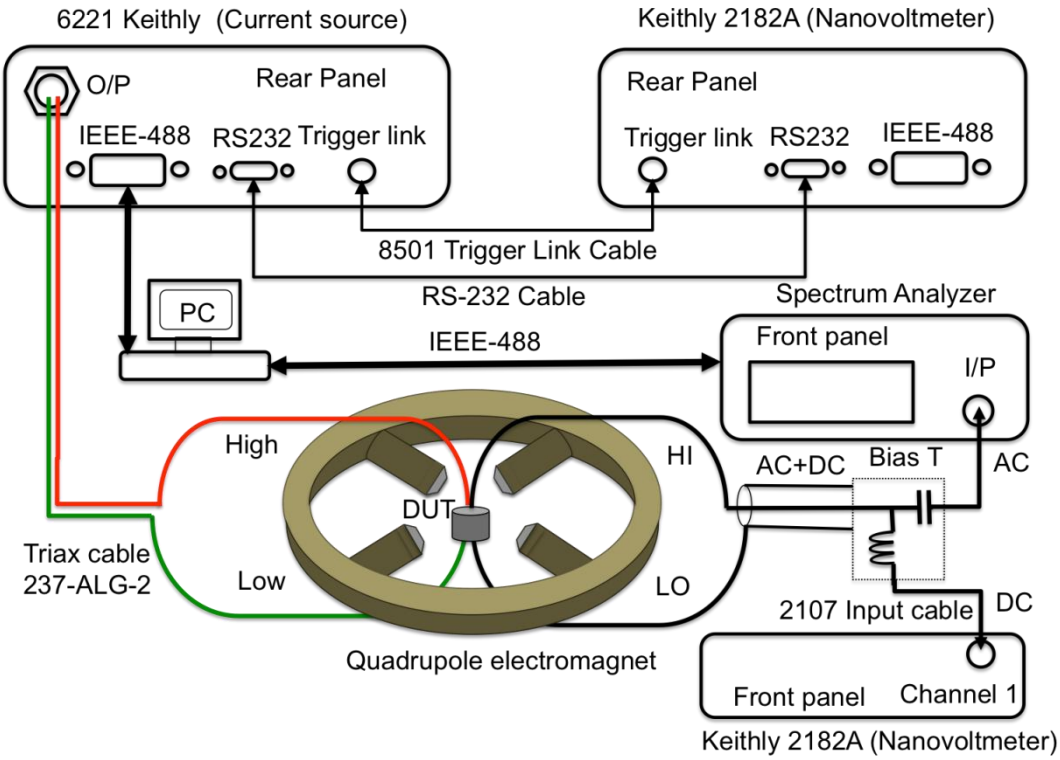

Figure 3.2.4.1 Transport measurement setup for characterization of electrical properties of nanoscale devices.

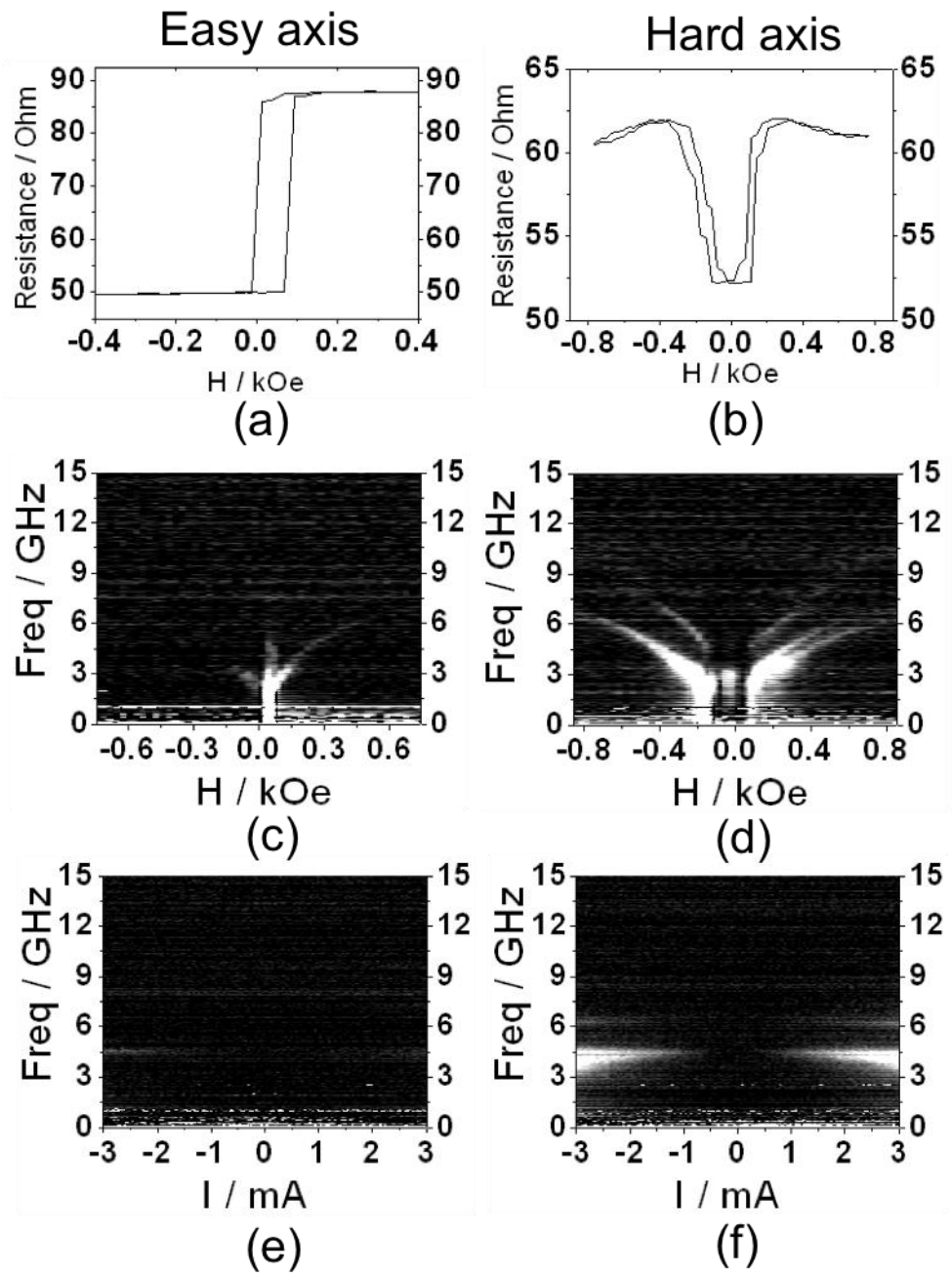

Figure 3.2.4.2 DC transport characterisation for a 150 nm diameter nanopillar MTJ. MR loop for the easy axis (a) and the hard axis (b) obtained at a small DC bias current (0.1 mA) by sweeping the external field. (c) and (d) show the power spectra acquired by the spectrum analyser (Agilent E4448A) at a constant DC bias current of -3 mA by sweeping the external field along the easy and hard axes respectively. (e) and (f) are current sweeps between $\pm$3 mA for a constant bias field of 200 Oe applied along the easy and hard axes respectively.

3.2.5 AC technique

The AC technique is mainly used for measurements of very low resistances. Here we picture a superposition of a small amplitude sine wave and the DC current that is being swept in discrete steps, as shown in schematic form in Figure (3.2.5.1). This AC technique is more complicated than the DC transport measurement setup due to complexity of the circuitry required. It detects the response to a sinusoidal stimulus while sweeping the DC bias through the device.

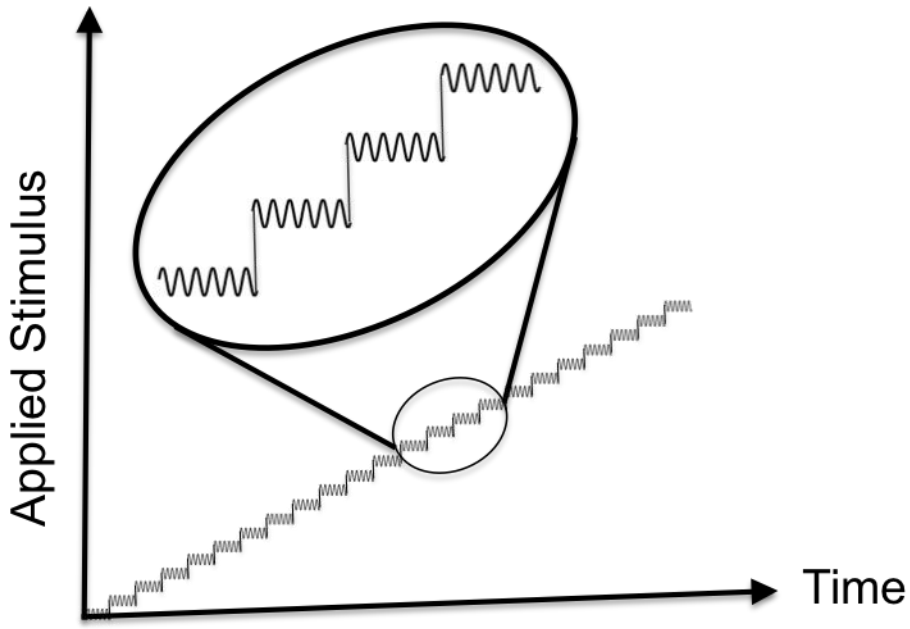

Figure 3.2.5.1 The AC technique measures the response to a sinusoidal stimulus while sweeping the DC bias current through the operating range of the DUT.

Configuration

For setting up the AC measurement technique, two lock-in amplifiers (7265 DSP) have been used. The first lock-in amplifier -outputs an AC stimulus and DC offset and then measures the DC voltage drop across the DUT using a single ended voltage input. The other lock-in amplifier acts as an ammeter and measures the current going to the DUT. The complete setup using the AC technique is shown in Figure (3.2.5.2). For ease of notation the first lock in amplifier will be referred to as lock-in 1 (dV) and the second as lock-in 2 (dI).

The oscillation output of Lock-in 1 acts as the AC source, and the DC offset is applied from the rear panel output (DAC1). The DAC1 (digital to analog converter) output from the rear panel of lock-in 1 has a maximum output of ± 10 V with a resolution of 1mV, while the AC oscillation amplitude and frequency is set, from the front panel, at 0.05 (V_{rms}) and 8 kHz respectively. The DC offset and AC input are combined by a summing amplifier.

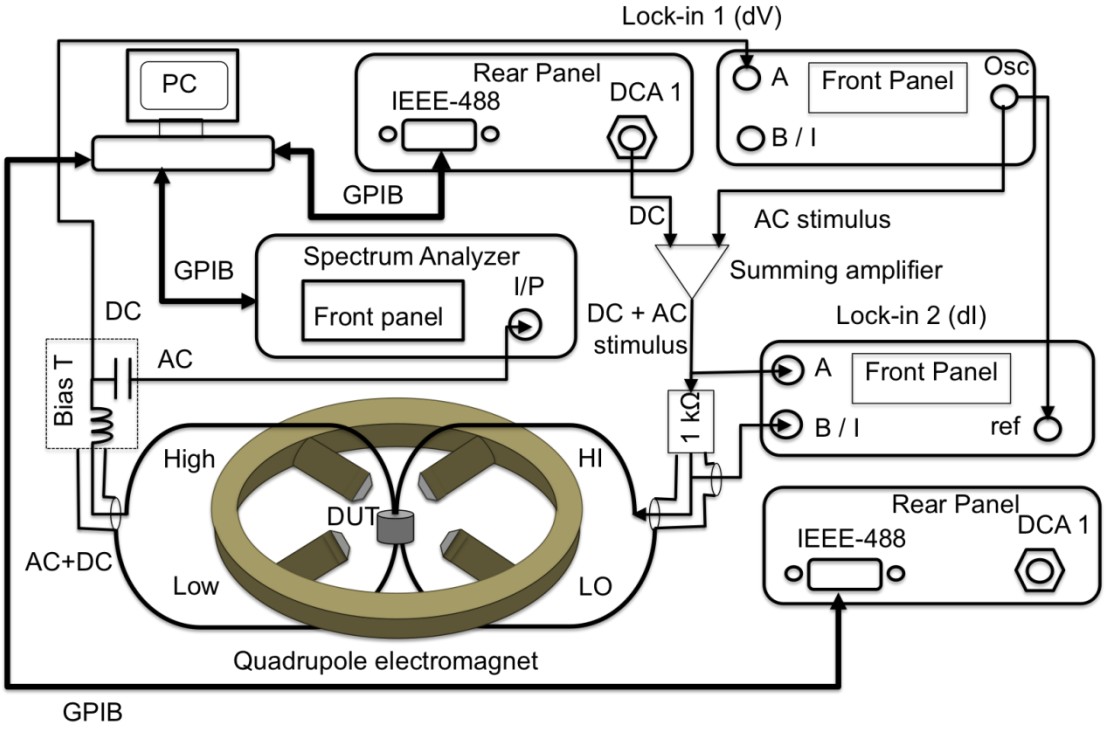

Figure 3.2.5.2 Experimental setup for making low resistance measurements by the AC technique using two lock-in amplifiers.

Usually the reference resistance is chosen to be much larger (1kΩ) than the DUT resistance thus creating an approximately constant current source driving the DUT. The voltage drop across the DUT is measured with the single ended voltage input (A) of lock-in 1. The current through the DUT is measured by lock-in 2 by connecting the differential voltage input across the reference resistance (Rref). For MTJs the output voltage consists of the low frequency voltage drop across the device and the radio frequency (RF) output due to magnetisation oscillations caused by STT. The low frequency voltage and RF voltage are separated by means of a bias T with the low frequency part going to lock-in 1 and the RF part going to a spectrum analyzer.

As for the DC transport measurements described earlier a vector electromagnet is used to manipulate the magnetisation orientation. A GPIB IEEE-488 is used to interface lock-in 1, lock-in 2 and the spectrum analyzer with a PC. However, the electromagnet is controlled from Labview via a DAQ card.

3.2.6 Noise

Various types of noise can be generated as a result of the parasitic resistance present in devices such as MTJs and can be either electrical or magnetic in nature. Several commonly encountered types of noise are described in this section.

Thermal or Johnson noise

Thermal or Johnson noise is normally observed in a resistor (R) due to thermal agitation of charge carriers that is independent of the applied voltage. The power spectral density (S_V) of such a fluctuation is independent of frequency but dependent upon temperature.

$$S_V(f) = 4k_BTR \tag{3.2.6.1}$$

where k_B and T are the Boltzmann constant and the temperature respectively. The mean square voltage ($\bar{V}^2$) fluctuation measure across the resistor with no current is

$$\bar{V}^2 = 4k_BTR\Delta f \tag{3.2.6.2}$$

where the quantity Δf is the bandwidth. If the measurement is performed with a narrow bandwidth the noise will be reduced, leading to an increased signal-to-noise ratio.

Shot noise

Shot noise is the time dependent fluctuation of an electric current due to the discrete flow of charged carriers. The Power spectral distribution (S_I) is independent of frequency

$$S_I(f) = 2eI \tag{3.2.6.3}$$

where I is the current. The current noise (I_{sn}) in a given bandwidth Δf is

$$I_{sn} = \sqrt{2eI\Delta f}. \tag{3.2.6.4}$$

Shot noise can be commonly observed in tunnel junctions at low temperature when there is sufficient current passing through the junction for the shot noise to exceed the Johnson noise. The signal-to-noise ratio is important for sensor head applications. At high frequency the device is affected and the performance is limited by Johnson noise and Shot noise, which vary as $\sqrt{R}$ and $\sqrt{I}$, respectively. Both types of noise are refered to as white noise on account of their flat frequency spectrum.

1/f noise

The power spectral density (S_V) varies as $1/f^{\alpha}$ where $\alpha = 1$. In magnetic sensors 1/f noise is related to the resistance fluctuations that are observed when a constant current is passed through the magnetic sensor. The constant current does not create the observed resistance fluctuations but instead lifts the associated power spectral density above the white noise background. The square of the voltage fluctuation $S_V(t)$ varies as I^2. The *1/f* noise resulting from a resistance fluctuation has been stated by Hooge[107] as follows

$$S_V(f) = \gamma_H {V_a}^2 / N_C f. \qquad (3.2.6.5)$$

The quantity γ_H is the Hooge coefficient, V_a is the applied voltage and N_C is the number of charge carriers in the volume being considered.

Magnetic noise

The origin of the magnetic noise in AMR and spin-valve sensors is the fluctuation of the magnetisation which then causes a fluctuation of the magnetoresistance. This noise is worse when a domain wall is present and less so when a single domain state is realised. The way to reduce the noise in sensor structures is to incorporate a built-in permanent magnet with the sensor so as to create a small bias field and increase the likelihood of a more spatially uniform magnetic state. If the free layer of the sensor head is very thin then the free layer tends to break up into magnetically independent regions. The resulting incoherent collective fluctuations of the magnetisation are a source of noise.

3.3 Summary

This chapter has reviewed the origin and phenomenology of the magneto-optical Kerr effect and the fundamentals of the electrical measurement techniques that are used in this thesis. It also describes the stroboscopic MOKE set up used to acquire the in-plane and out-of-plane components of magnetisation using a vector bridge detector.

The development of a four probe electrical contact measurement technique has been discussed for frequency domain electrical transport characterisation of a magnetic tunnel junction (MTJ) device. The details of the experimental set up and interfacing of different equipment have been presented.

Chapter 4

Large amplitude magnetisation dynamics and the suppression of edge modes in a single nanomagnet

4.1 Introduction

The large amplitude precessional magnetisation dynamics of nanoscale ferromagnetic elements are expected to facilitate increased switching speeds in bi-stable magnetic storage elements and the operation of spin transfer torque oscillators. In the majority of studies the dynamic behaviour of nanomagnets has largely been investigated by studying arrays of nanomagnets in order to obtain a detectable dynamic signal[108,109]. However the inter-element dipolar interaction within arrays can introduce additional collective excitations[110,111,112,113]that, while interesting, must be avoided by increasing the inter-element separation if the dynamic behaviour of an individual nanomagnet is to be clearly resolved. Subtle differences in the structure of the different nanomagnets within the array, *e.g.* shape and edge roughness, can lead to inhomogeneous broadening of the modes detected from the array[109,112], so that modes of slightly different frequency can no longer be resolved. The appearance of collective modes and inhomogeneous broadening can be avoided if measurements can be made upon a single nanomagnet[114]. Recently, cavity enhancement of the magneto-optical Kerr effect was used to study the magnetisation dynamics in single out-of-plane magnetised Ni(150 nm) discs with diameter ranging from 5 μm to 125 nm[115]. In Reference 115 it was shown that the intrinsic properties of a single nanomagnet can no longer be observed when an ensemble of discs is measured.

It is well known that the magnetisation dynamics of an in-plane magnetized square nanomagnet can be complicated by the excitation of center- and edge-type modes when a bias magnetic field is applied along the element edge[108,112,116]. The two modes can also coexist for a range of bias fields while the amplitude of the response shifts from the center to the edge mode as the bias field is decreased[112]. Recently it has been shown that the large amplitude excitation of the center and edge modes of a microscale ellipse can lead to hybridization of the mode character[117].

In this work we use time-resolved (TR) measurements and micromagnetic simulations to demonstrate that large angle magnetisation dynamics in a single nanomagnet can lead to a dynamic response that is dominated by the quasi-uniform center mode, while the non-uniform edge mode is almost completely suppressed.

4.2 Experiment and simulation

Time-Resolved (TR) measurements and micromagnetic simulations of large amplitude magnetisation dynamics have been performed for a single 440×440 nm^2 CoFe(1 nm)/NiFe(5 nm)/CoFe(1 nm) nanomagnet. The sample stack was chosen as it is representative of read head sensors that are currently used in industry. The scanning electron micrograph image (SEM) is shown in Figure 4.2.1 (a). The precessional dynamics of the single nanomagnet were observed experimentally using TR Kerr microscopy with ~ 300 nm spatial resolution at full-width at half maximum (FWHM) and enhanced mechanical stability, as shown in Figure 4.2.1(b) and (c). The spatial resolution was determined by measuring the reflectivity as the laser spot was scanned across the edge of a thin film metallic structure fabricated on a Si substrate.

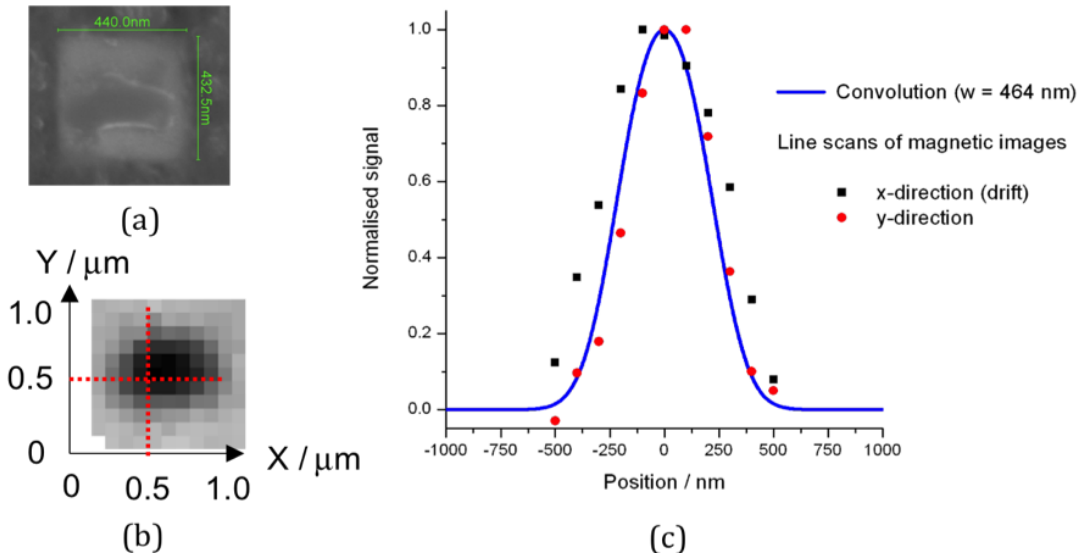

Figure 4.2.1 (a) Scanning electron micrograph image of 440×440 nm^2 nanomagnet, (b) Time-resolved polar Kerr image of an isolated 440 nm square acquired at a precession anti-node, and (c) Lines scans (red) and the convolution of a 440 nm wide "top-hat" function with a Gaussian function of 300 nm FWHM.

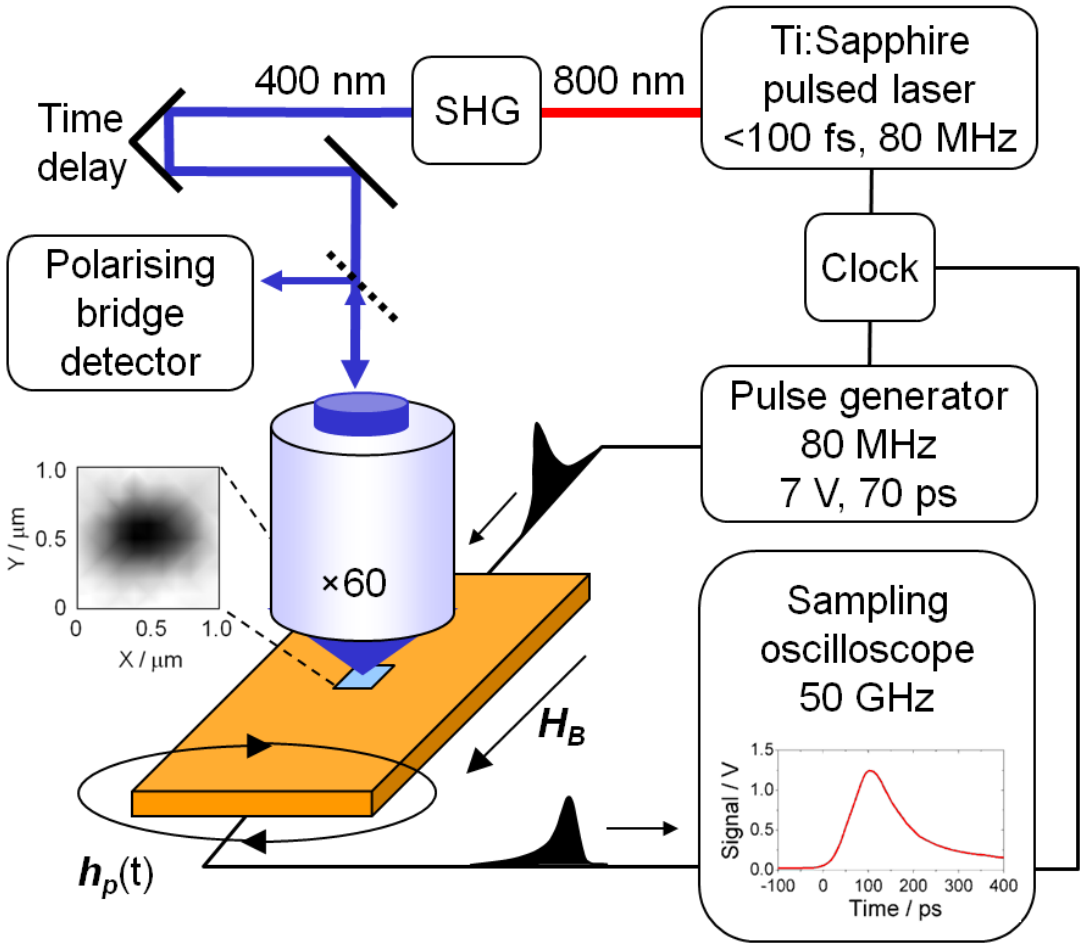

Figure 4.2.2 A schematic of the TR scanning Kerr microscope is shown. A pulse generator and a coplanar waveguide are used to generate a pulsed magnetic field and excite magnetisation dynamics in the 440 nm square fabricated on the center conductor. A phase-locked pulsed optical probe of 400 nm wavelength and 300 nm diameter (FWHM) is used to detect the magnetisation dynamics stroboscopically using the polar Kerr effect.

The derivative of the change in reflectivity is Gaussian and the FWHM provides an estimate of the spatial resolution of the system. The mechanical drift was determined by measuring a scanning reflectivity image of an array of 640 nm squares with 240 nm edge-to-edge separation. The distortion of the image over the period of an hour due to mechanical drift was not more than 200 nm.The experimental set up layout is shown in Figure 4.2.2.

An impedance matched microscale coplanar waveguide (CPW) was used to generate an in-plane pulsed magnetic field $\mathbf{h}_p(t)$ from a current pulse transmitted from a phase-locked impulse generator with 7 V pulse amplitude, < 40 ps rise time, and 70 ps duration. The micro and nanoscale magnetic discs measured in the work outlined in this chapter were fabricated by collaborators at the Hitachi Global Storage

Technologies (HGST) San Jose Research Center, California. The 440 nm square was fabricated on top of the center conductor of the CPW which was tapered to a width of 4 μm in order to enhance the amplitude of the pulsed magnetic field and induce large amplitude magnetisation dynamics. A pulsed field amplitude of ~ 90 Oe was estimated by using the Karlquist equation for the magnetic field generated by a uniform current strip[118] and assuming exponential attenuation of the current pulse amplitude along the CPW. In all measurements the pulsed field orientation was along the edge of the square perpendicular to the CPW.

TR measurements were performed for a range of bias fields $\mathbf{H}_B$ applied in-plane and along the edge of the element for which the observation of center- and edge-type modes was expected. In addition, measurements were performed with the bias field applied along the element diagonal. A scanning polar Kerr image of the single nanomagnet acquired at a precession antinode is shown in Figure 4.2.1 (b) for a bias field of 200 Oe applied along the edge of the element. Black (white) corresponds to a Kerr rotation of ~ 1 mdeg (zero). The enlarged element size corresponds to the convolution of the ~ 300 nm FWHM Gaussian laser spot with the 440 nm square.

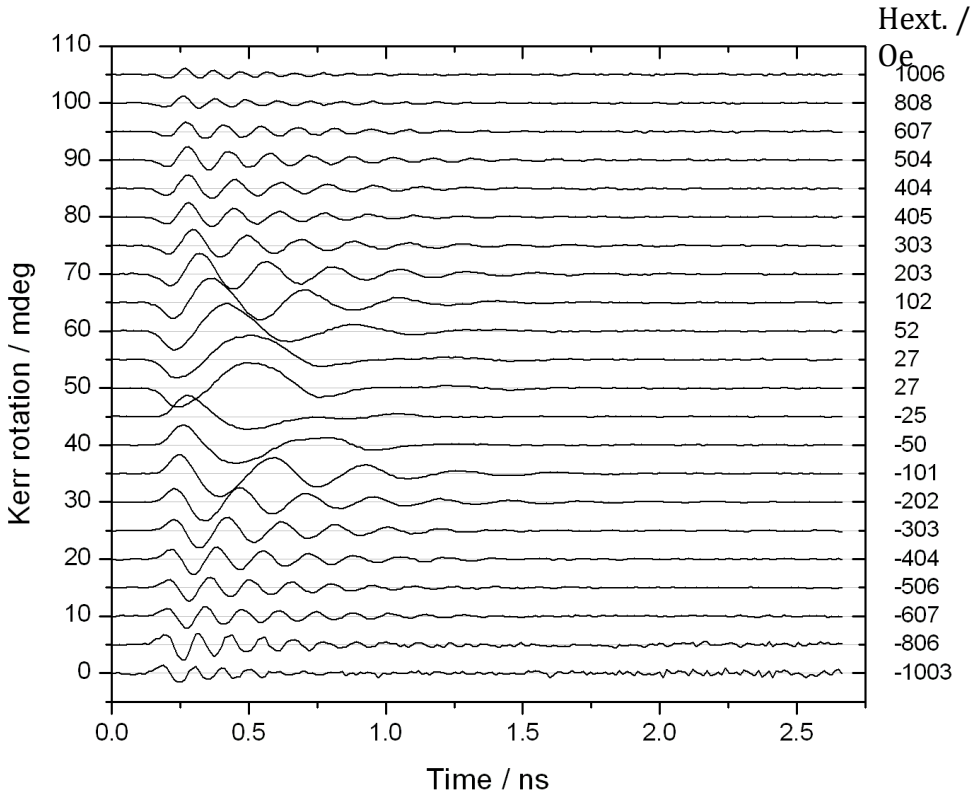

Figure 4.2.3 Time resolved Kerr signals acquired from the 2 μm disc while varying the field from ±1 kOe.

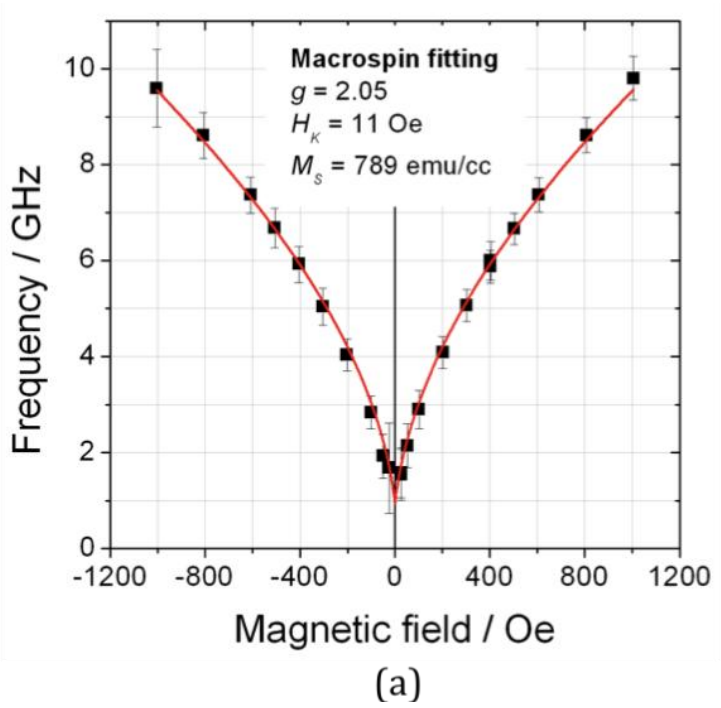

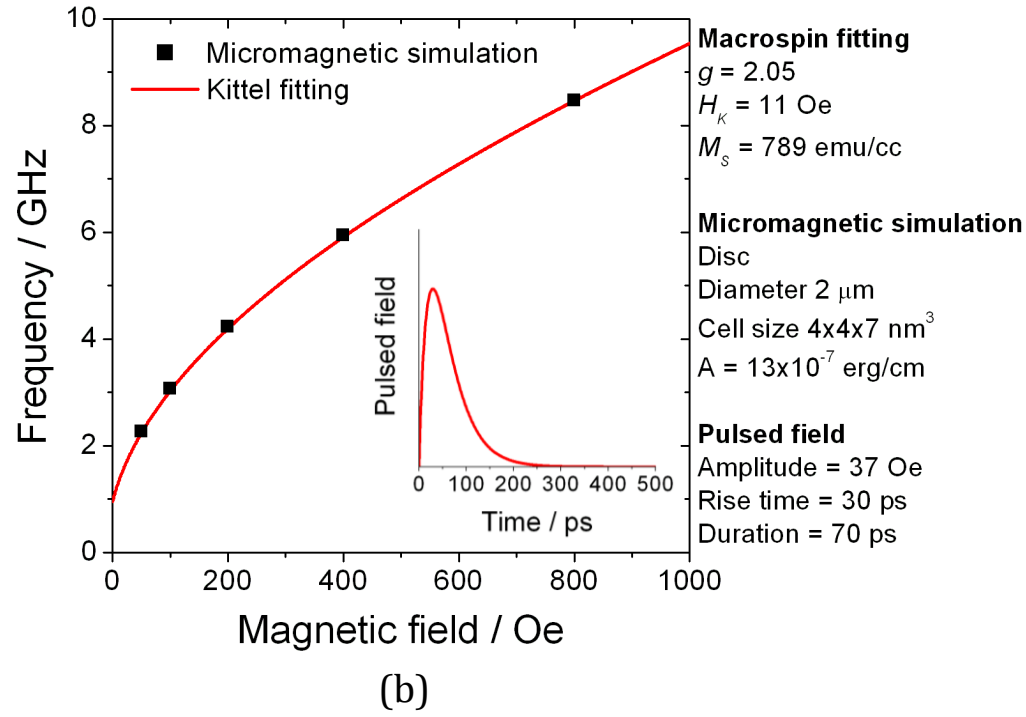

Figure 4.2.4 (a) Material parameters were determined by fitting a macrospin model to the precession frequency as a function of bias field extracted from the TR signals in Figure 4.2.3, and (b) Micromagnetic simulations of a 2 μm disc are consistent with the macrospin fitting of the experimental data.

TR measurements were also performed upon a 2 μm disc fabricated from the same film and on the same CPW. The direction of the uniaxial anisotropy easy axis in the continuous film was set parallel to the length of the CPW by post-deposition field annealing. The easy axis direction of the 440 nm square and 2 μm disc was assumed to be the same as in the continuous film. TR signals were acquired for bias field values in the range ±1 kOe as shown in Figure 4.2.3. The frequency of precession was plotted as a function of the bias field and used to extract the magnetic parameters from a fit of the experimental data to a macrospin model in the quasi-alignment approximation. In this macrospin model, magnetisation reversal takes place at zero temperature by suppression of the barrier due to external magnetic field describe by the Stoner-Wohlfarth model. Values of the saturation magnetisation M_s (789 emu/cm^3), g-factor (2.05), and uniaxial anisotropy constant K_u (4340 ergs/cm^3) were extracted from the fitting and used in the micromagnetic simulations as shown in Figure 4.2.4.

Micromagnetic simulations were performed using the object oriented micromagnetic framework (OOMMF)[119]. A micromagnetic simulator is a computer program designed to compute the local magnetization within a material. The user supplies input parameters such as the material geometry, the initial magnetization and the time evolution of the external magnetic field. It is also necessary to specify several material specific parameters such as the demagnetization field, exchange interaction field and any anisotropy that may be present. The Object Oriented Micro Magnetic Framework (OOMMF) is a commonly used micromagnetic simulation package and was used for in this thesis. OOMMF is a public domain program developed at the National Institute of Standards and Technology (NIST), USA. The code uses finite-difference discretisation and Fast Fourier Transformation (FFT) to perform magnetostatic field calculations. It displays the magnetic moments of a 3-dimensional object in a vector field and displays the calculated changes in the magnetisation distribution as an external magnetic field is applied and subsequently varied in a series of discrete steps. A 440 nm square with rounded corners of radius of 55 nm was modelled as a single layer using a mesh of cell size 4×4×7 nm^3 and an exchange parameter of 13×10^{-7} ergs/cm. Smaller cell sizes of 2×2×7 nm^3 and 1×1×7 nm^3 did not show any significant differences in the simulated dynamics. The magnetisation dynamics were excited by a pulsed field of 70 ps duration, 30 ps rise time, and

amplitude ranging from 5 to 100 Oe. In this study the polar Kerr microscope is only sensitive to the average out-of-plane component of the dynamic magnetisation within the probe spot. Therefore, only the out-of-plane component of the simulated magnetisation dynamics averaged across the 440 nm square was compared to the experimental data.

4.3 Results and discussion

Figure 4.3.1 (a) shows typical TR polar Kerr signals acquired from the square for bias field values ranging from 500 to 100 Oe. When the field was applied along the edge of the element (Figure 4.3.1 (a)) only very weak beating of some of the TR signals was observed, which may indicate that either the center or edge mode dominates the dynamic response of the element. When the field was applied along the diagonal (Figure 4.3.1 (b)) the TR signals were found to have smaller amplitude and exhibit enhanced damping. The reduced amplitude is in part due to the smaller initial torque acting on the static magnetisation when the bias field is no longer orthogonal to the pulsed field.

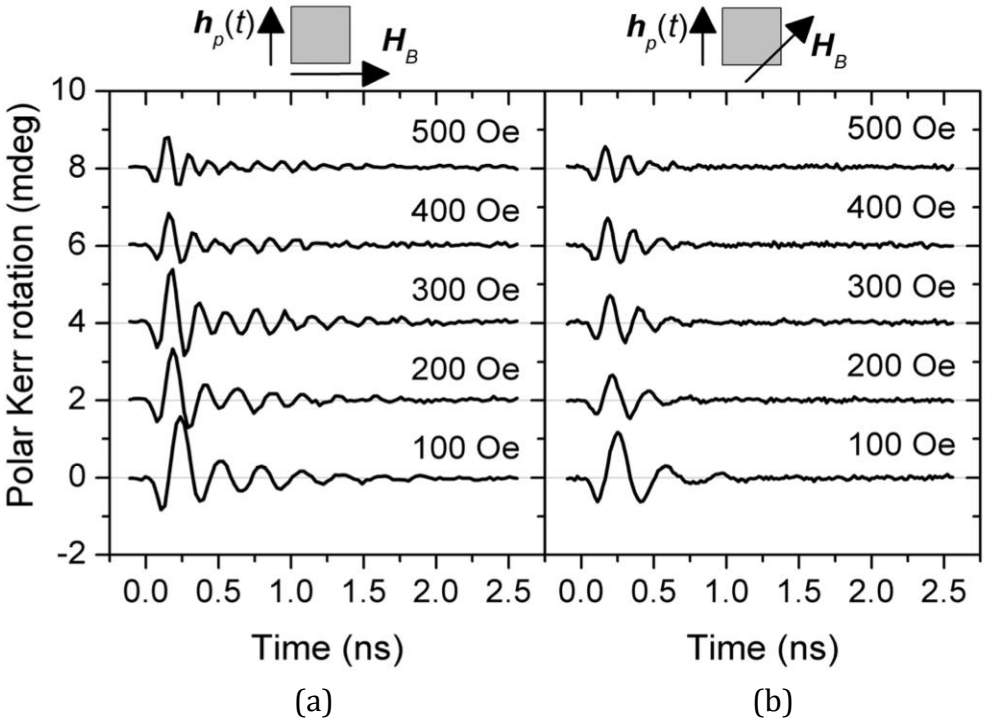

Figure 4.3.1 Typical TR signals acquired from the single 440 nm square at different bias field values when the field is applied along the edge of the element (a) and along the diagonal (b).

Normalized fast Fourier transform (FFT) spectra of the TR signals in Figure 4.3.1 are shown in Figure 4.3.2. The experimental FFT spectra (dark gray shading) are overlaid with FFT spectra calculated from micromagnetic simulations (solid black line). In the micromagnetic simulations the values of α and h_p were initially set to 0.01 and 30 Oe respectively in order to understand the expected small amplitude response of the 440 nm square. The values of M_s and K_u were assumed to be uniform throughout the element. The spectra are shown for bias field values ranging from 700 to 50 Oe and 500 to 100 Oe when the field was applied along the edge and diagonal respectively. These two geometries will be referred to as "parallel geometry" and "diagonal geometry" in the following discussion.

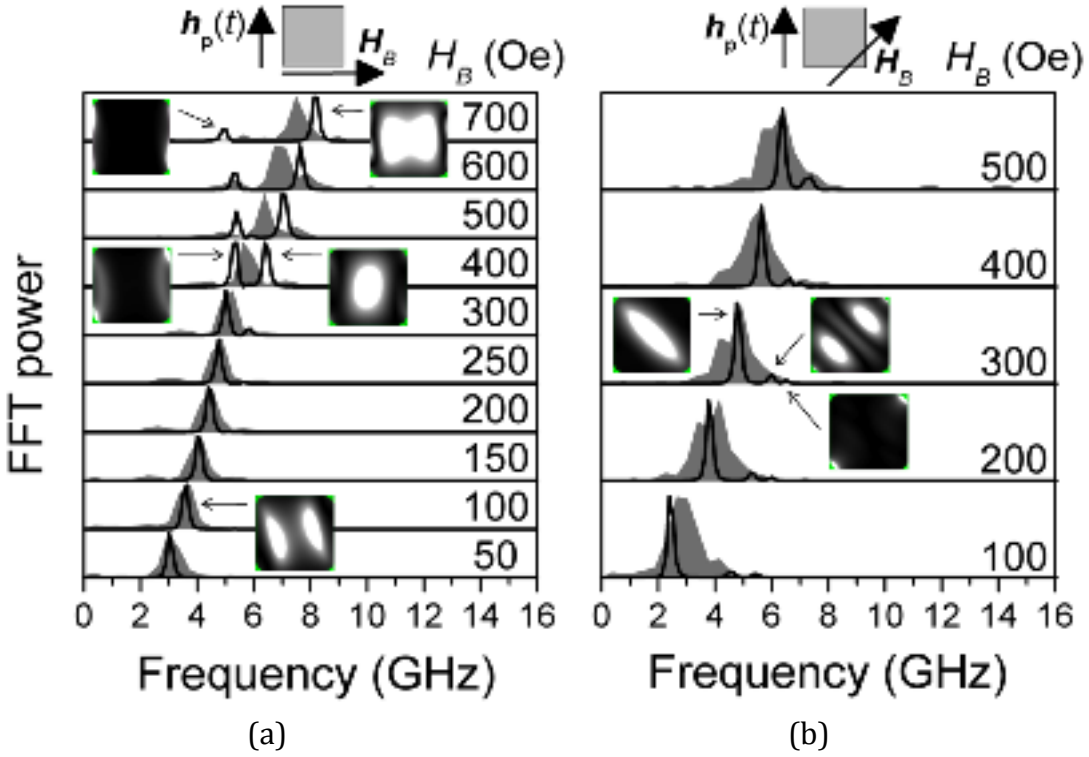

Figure 4.3.2 FFT spectra of the TR signals acquired from the single 440 nm square are shown for the parallel (a) and diagonal (b) geometries. The experimental FFT spectra (dark gray shading) are overlaid with FFT spectra calculated from micromagnetic simulations (solid black line) that assume a uniform value of M_s throughout the element and pulsed field amplitude of 30 Oe. Fourier images of FFT magnitude are shown for bias field values above, below and at the crossover field.

In the parallel geometry (Figure 4.3.2 (a)) the experimental spectra show a single main peak at all field values in addition to low amplitude side peaks that increase in relative amplitude as the bias field increases, particularly above 400 Oe.

For bias field values of 300 Oe and below, the simulated spectra are in very good agreement with the experimental spectra, albeit with a much narrower linewidth. The calculated Fourier images show the spatial character of FFT magnitude where white is large amplitude and black is zero. All modes are normalized to 75% of the maximum magnitude except for highly localized modes at edges or corners of the square that are normalized to 50% for clarity. The green regions surrounding the square are non-magnetic. Fourier images calculated from the simulated vector field maps of the dynamic magnetisation[112] (Figure 4.3.2 (a)) confirm that the lower and higher frequency modes are edge- and center-type modes respectively and the evolution of their spatial character is similar to that described in Reference 112. At 400 Oe a crossover in the dynamic response of the element is observed in the simulated spectra. Above 400 Oe the dynamic response is dominated by the centre mode, while at lower field values edge-type modes dominate the response.

In contrast to the low field values, at field values between 400 and 700 Oe a discrepancy of ~ 1 GHz is seen between the frequency of the center mode and that of the main experimental peak suggesting that the material parameters used in the simulations are not optimized. In addition, the lower amplitude side peaks observed in the experimental spectra are not reproduced by the simulations. The side peaks have constant separation from the main peak at all bias fields and can be suppressed when FFT spectra are calculated from the part of the TR signals that followed the first cycle of precession, as shown by the experimental spectra in Figure 4.3.3. Therefore, the side peaks are understood to be an experimental artefact resulting from the rise and fall of the pulsed field during the first cycle of precession.

In the diagonal geometry (Figure 4.3.2 (b)) for all bias field values, the experimental spectra reveal a single broad peak that is consistent with the enhanced damping seen in the TR signals in Figure 4.3.1. For all bias field values in the diagonal geometry, the frequency of the experimental peak was found to be lower than that observed in the parallel geometry. The shift of the peaks in the experimental spectra to lower frequency in the diagonal geometry is consistent with a change in the static internal field calculated from micromagnetic simulations for the two different field orientations. Other studies of the magnetisation dynamics in square elements of similar aspect ratio have also shown a marked change in the dynamic behaviour when the bias field was applied along the element diagonal [120, 121]. Micromagnetic simulations and Fourier images reveal at least two modes at all field values

corresponding to a lower frequency center-type mode with large amplitude across the element diagonal orthogonal to $\mathbf{H}_B$, and two higher frequency low amplitude modes localized near to the corners parallel to $\mathbf{H}_B$. In the experimental spectra the two modes are unresolved. As for the experimental spectra, the frequency of the largest amplitude mode is lower than that in the parallel geometry.

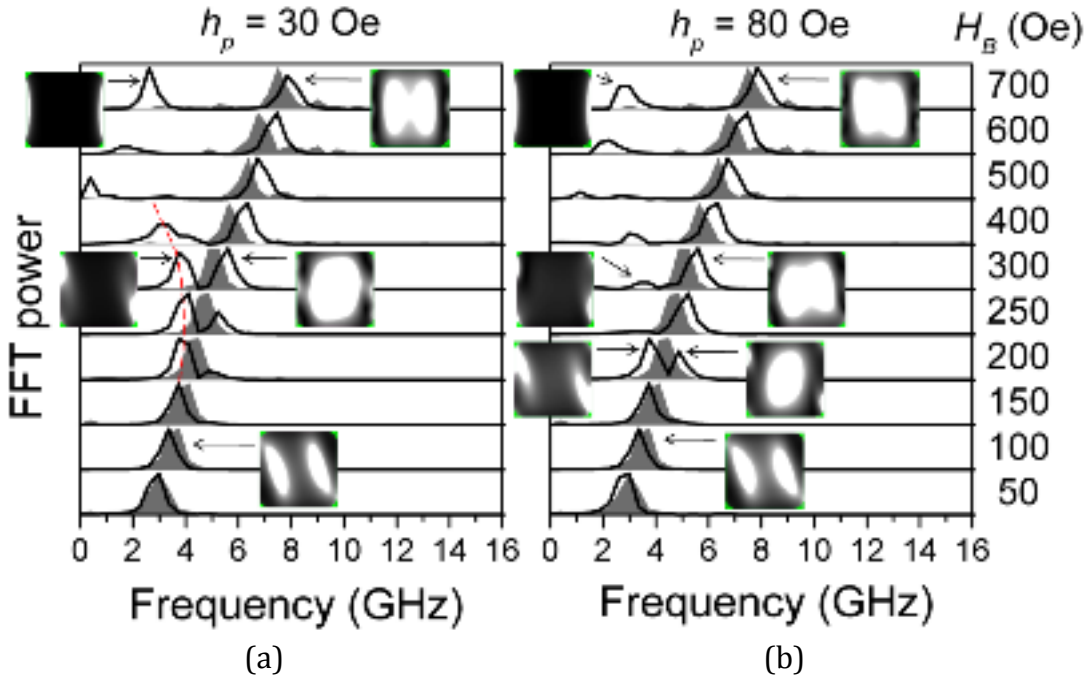

Figure 4.3.3 FFT spectra of the TR signals acquired from the single 440 nm square are shown for the parallel geometry. In (a) and (b) the value of the pulsed magnetic field amplitude was 30 Oe and 80 Oe respectively. The experimental FFT spectra (dark gray shading) are overlaid with FFT spectra calculated from micromagnetic simulations (solid black line) that assume a value of α of 0.03, and a smooth two-dimensional profile of the saturation magnetisation ranging from M_s at the central part of the element to $0.8M_s$ near the edges. Fourier images of FFT magnitude are shown for bias field values above, below and at the crossover field.

In the parallel geometry, the good agreement of the lower frequency edge mode and poor agreement of the higher frequency center mode is surprising. Indeed, the edge mode frequency is expected to be more susceptible to frequency shifts and splitting due to shape defects or edge roughness[109, 112], while the center mode frequency is determined by the magnetic parameters of the material. To check that the micromagnetic model was consistent with the experiment, micromagnetic simulations of the 2 μm disc were performed. As expected, the micromagnetic model accurately

reproduced the dependence of frequency upon the static bias field obtained from the macrospin fit for the field range used in the study of the 440 nm square. Micromagnetic simulations of a variety of models with slightly different size and shape did not affect the frequency of the center mode significantly.

It has recently been reported that nanofabrication processes can lead to a reduction of the saturation magnetisation at the edges of a nanomagnet[122] so that it is necessary to reduce the value of M_s in order to describe the evolution of spin-wave modes of a nanomagnet[123]. Micromagnetic simulations of the 440 nm square assuming a value of $0.8M_s$ and $0.8K_u$ were performed, but resulted in shifting the whole spectra so that the agreement at 300 Oe and below was not as good.

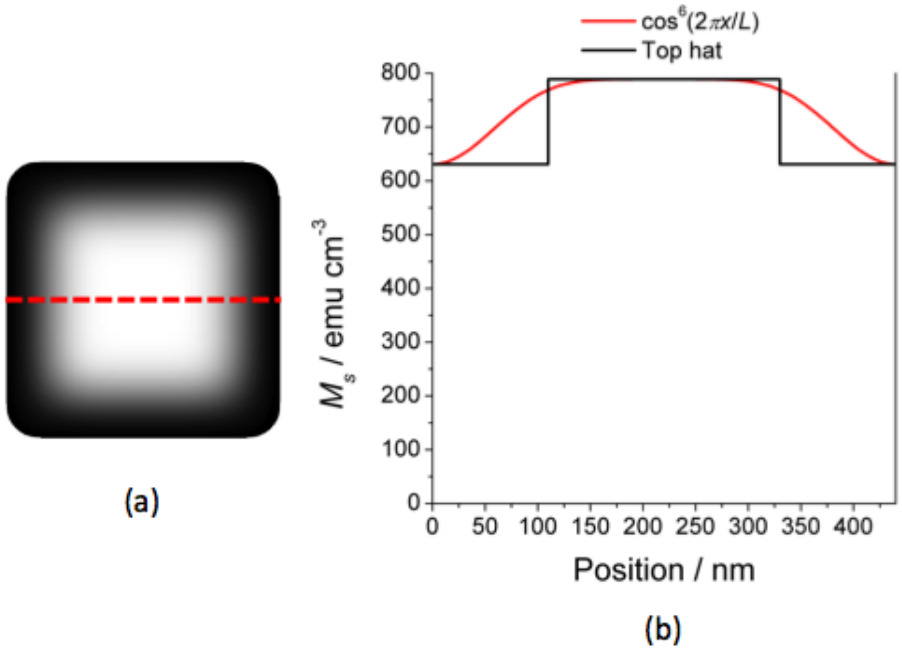

Figure 4.3.4 (a) Grey scale profile of magnetisation on the nanomagnet where grey-white at center represent the saturation magnetisation and black at edge region represent the reduce magnetisation, and (b) The magnetisation profile across the nanomagnet which is extracted form the broken red line from (a).

An improvement in the overall agreement between the experimental and simulated spectra for all bias field values was acquired by assuming a reduced value of M_s near to the edges of the element. The two-dimensional profile of M_s across the element was assumed to have the form $\cos^6(2\pi x/l)\cos^6(2\pi y/l)$ and values of M_s and $0.8M_s$ at the center and the edge of the square respectively, where l = 440 nm and x,y are the spatial coordinates in nanometers as shown in Figure 4.3.4. It should be noted

that although the cosine functions enable the experimental features to be reproduced well in simulations they are trial functions and the possibility of a better functional approximation being found should not be ruled out. In order to reproduce the linewidth of the experimental spectra, the value of α was adjusted so that the temporal relaxation observed experimentally was reproduced in the micromagnetic simulations. For the parallel and diagonal geometries the value of α was 0.03 and 0.05 respectively.

Furthermore, in order to understand the effect of excitation with a large pulsed field the value of the pulsed field amplitude was varied from 5 Oe to 100 Oe in the micromagnetic simulations[124].In Figure 4.3.3 shows the experimental spectra acquired in the parallel geometry overlaid with the simulated spectra for the 440 nm square with reduced edge M_s and $\alpha = 0.03$. In Figure 4.3.3 (a) and Figure 4.3.3 (b) the value of the pulsed field amplitude was 30 Oe and 80 Oe respectively. In Figure 4.3.3 (a) the simulated center mode and the experimental spectra are in better agreement between 700 Oe and 200 Oe (now within ~ 500 MHz), while the edge mode is still in good agreement below 200 Oe. While the quantitative agreement has been improved, further improvement might be achieved by systematically tuning the precise profile of M_s. The reduction of the edge M_s has resulted in a shift in the crossover field from center to edge mode from 400 to 300 Oe, while the larger value of α yields better agreement of the spectral linewidth. At 200 Oe the simulated frequency of the edge mode begins to shift from that of the main peak in the experimental spectra as the bias field value increases (dashed red line). As in Figure 4.3.2 (a) the coexistence of the center and edge mode is not observed in the experimental spectra. The large amplitude mode with frequency of 2.75 GHz in the simulated spectrum at 700 Oe is a highly localized edge mode and is not observed experimentally. Since the ~ 300 nm FWHM laser spot size is smaller than the 440 nm square, the highly localized edge modes at high bias fields are probed by the Gaussian tail of the optical probe. Therefore, the sensitivity to edge modes at high bias fields is expected to be significantly reduced. In addition the micromagnetic simulations revealed a change in the ground state following the onset of the pulsed field in the simulations. At 700 Oe the element was initially in the X-state. Following a pulsed field excitation of 30 Oe the magnetisation switched between X- and S-states. At high bias fields the canted magnetisation that defines the type of ground state is confined to the same narrow region as the localized edge mode. Therefore, at high bias fields both the frequency

and amplitude of the edge mode were found to vary as the value of h_p was increased[124].

In Figure 4.3.3 (b) spectra simulated with a pulsed field amplitude of 80 Oe reveal a remarkable suppression of the edge mode amplitude between 400 and 250 Oe and improved agreement with the experimental spectra. Furthermore, the crossover between centre and edge modes has shifted from 300 to 200 Oe indicating that at larger pulsed field amplitudes the excitation of the center mode is favoured for a greater range of bias field values. While the pulsed field amplitude used in the simulations in Figure 4.3.3 (b) was similar to that estimated in the experiment, partial suppression of the edge mode can be observed in the simulated spectra for a value of the pulsed field amplitude of only 10 Oe[124]. When the value of the pulsed field amplitude is increased from 10 Oe to 30 Oe, the amplitude of the edge mode is found to decrease by 50% at a bias field of 400 Oe. In the experimental spectra only a single mode is observed due to the combined effect of reduced edge mode sensitivity at large bias field values (≥ 500 Oe) and edge mode suppression above the crossover field.

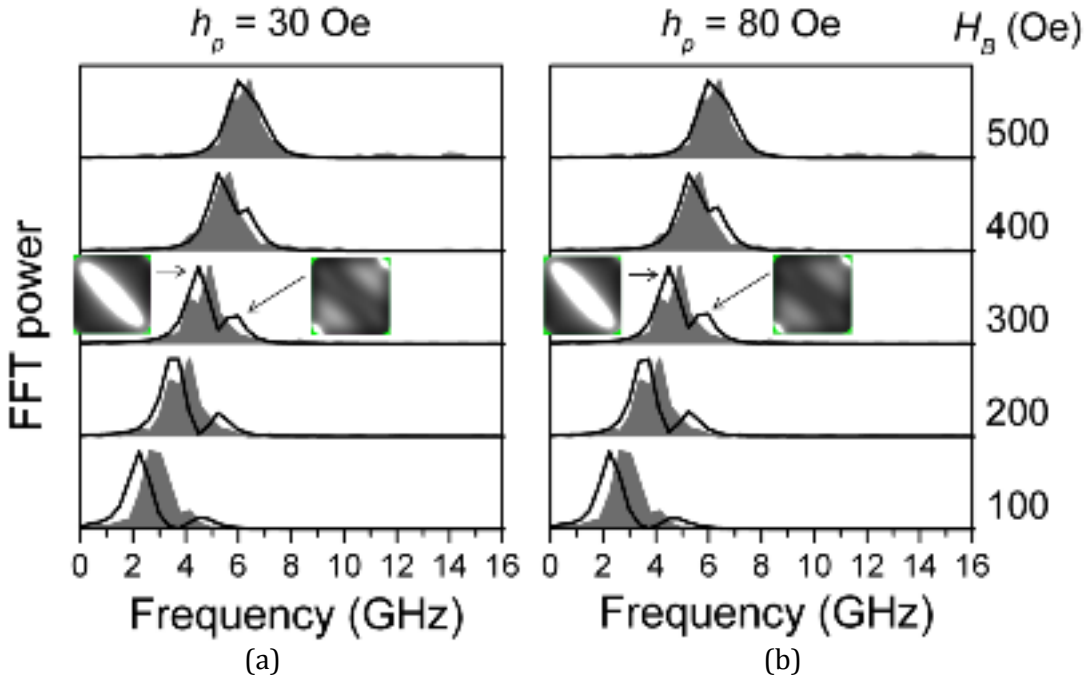

Figure 4.3.5 FFT spectra of the TR signals acquired from the 440 nm square are shown for the diagonal geometry. The experimental FFT spectra (dark gray shading) are overlaid with FFT spectra calculated from micromagnetic simulations (solid black line) that assume a value of α of 0.05 and a reduced saturation magnetisation of $0.8M_s$ near the edges of the square. Fourier images of FFT magnitude are shown for a bias field values 300 Oe.

Figure 4.3.5 shows the experimental spectra acquired in the diagonal geometry overlaid with the simulated spectra for the 440 nm square with reduced edge M_s and α = 0.05. The larger value of α has led to better agreement of the spectral linewidth. It is unsurprising that the observed linewidths and deduced values of α are different for the parallel and diagonal geometries since their ground states are very different. In addition damping mechanisms such as two magnon scattering due to interface or edge roughness[125] are not included in the micromagnetic model and their influence may differ between the parallel and diagonal geometries. In Figure 4.3.5 (a) and Figure 4.3.5 (b) the pulsed field amplitude was 30 Oe and 80 Oe respectively. Remarkably, in the diagonal geometry the simulated spectra in Figure 4.3.5 reveal that the pulsed field amplitude has a negligible effect upon the number of modes excited and their relative amplitude. Fourier images reveal that the single higher frequency mode is a highly localized mode with large amplitude in the corners of the element parallel to the bias field. As discussed for the parallel geometry the sensitivity to highly localized modes is expected to be reduced due to the Gaussian profile of the laser spot.

4.4 Summary

In summary TRSKM measurements of large amplitude magnetisation dynamics within a single nanomagnet have been performed with excellent signal-to-noise ratio without the need for cavity enhancement of the magneto-optical signal. Quantitative agreement between the experimental and simulated spectra was found to depend upon the profile of the saturation magnetisation throughout the element, suggesting that nanofabrication processes do influence the magnetic parameters of the material, particularly near edges, and therefore also the dynamic response as reported in other studies[122]. At the same time differences in the damping in the parallel and diagonal geometries imply that the micromagnetic model does not fully describe the relaxation of the magnetisation dynamics. Such effects would be difficult to isolate in closely packed arrays where inter-element interactions can influence the frequency of the observed dynamics. As device volumes decrease the need for larger amplitude excitation increases so that a detectable signal can be generated.

This work emphasizes the fact that the pulsed field amplitude is an important parameter in micromagnetic modelling of the magnetisation dynamics of a single nanomagnet, where a large amplitude excitation can change the character of the resonant mode spectra in addition to the magnetic ground state. The controlled suppression of the non-uniform edge mode presented in the work has potential applications in the operation of nanoscale spin transfer torque oscillators and bi-stable switching devices for which the amplitude of the magnetisation trajectory is usually large and where a more uniform dynamic response is usually required.

Chapter 5

Isolating the dynamic dipolar interaction between a pair of nanoscale ferromagnetic discs

5.1 Introduction

The rapid development of the fields of spintronics[126] and magnonics[113]has been fuelled by the potential for efficient storage, sensor, computation, and communication technology that exploits the spin rather than the charge of the electron. In spintronic devices the spin angular momentum of conduction electrons can induce magnetisation dynamics[127] and switching[128] by delivering spin transfer torque, while in magnonic devices allowed bands of spin waves, so called magnons, can be manipulated through artificial magnetic periodicity[111]. The ferromagnetic components of devices activated by spin transfer torque are necessarily of nanometer size so that the required density of spin polarised current may be achieved with modest electrical currents, while in magnonic devices artificial periodicity is required at the nanoscale due to the short propagation length of spin waves in metals. Recently spin transfer oscillators have been proposed as highly agile components for microwave signal processing applications, with the bottleneck issues of emitted microwave power and frequency linewidth being overcome by non-linear phase-locking of multiple nanoscale oscillators[129]. On the other hand two-dimensional magnonic crystals have been found to exhibit bands of allowed magnonic states and frequency forbidden magnonic band gaps[130] that may find potential applications in magnonic filters and logic devices. While the technological applications of these multi-component nanoscale systems may differ, their operation relies upon the controlled dynamical coupling between resonances within the individual nanomagnets.

Dynamically coupled systems may possess additional functionality and a richer ferromagnetic resonance spectrum. The magnetic ground state, and hence the resonance spectrum, may occupy a number of metastable configurations that can be selected through the application of a magnetic field[131]. Since an individual nanomagnet with a quasi-uniform ground state exhibits a non-uniform internal magnetic field it may support a number of confined spin wave eigen modes that have very different frequencies and spatial character[108, 116, 112, 132].

Typically a planar nanomagnet with in-plane magnetisation supports a quasi-uniform mode with large amplitude at the centre of the nanomagnet (centre mode) in addition to localised modes with large amplitude at the edges that lie perpendicular to the applied magnetic field (edge mode). While a number of incisive experimental and theoretical studies have led to an improved understanding of the spin wave eigenmodes of individual confined magnetic structures, the most effective means of coupling the magnetisation dynamics of closely spaced nanomagnets is less clear[111, 130, 133,134,135,136]. The most obvious candidate is the magnetic dipolar interaction that is present in any magnetic system. The precessing magnetisation of a nanomagnet generates a magnetic field at a neighbouring nanomagnet that has both constant and time varying components. It is the latter dynamic dipolar field that couples the precession of nanomagnets with a well-defined relative phase so as to yield collective excitations[111, 110, 130] for magnonic applications, and which could enable non-linear phase-locking of spin transfer oscillators for microwave signal processing applications[129,133]. While the minimal spatial separation of edge modes within neighbouring nanomagnets provides potential for strong inter-element coupling, edge modes have also been shown to be very sensitive to variations in shape and magnetic properties associated with the nanofabrication process[112, 137].

The sensitivity of the edge mode frequency to the precise shape of a nanomagnet has been demonstrated in arrays of nanomagnets with varying degrees of shape distortion[138]. However, from studies of arrays it is difficult to identify the effect of dipolar interactions between edge modes due to inhomogeneous broadening of the edge mode resonance associated with structural imperfections throughout the array[112]. The number of collective modes is the product of the number of nanomagnets within the array and the number of eigenmodes associated with each nanomagnet. Therefore the effect of interactions is most easily isolated by measuring the dynamic response of a single pair of nanomagnets. In fact, for an even number of nanomagnets, antisymmetric collective excitations of the centre mode[139] do not couple to a uniform excitation field and so a further simplification of the mode spectrum may be achieved by studying a pair. Since the dipolar field of a magnetic moment decreases as the inverse cube of the distance from the moment, the nanomagnets must be closely spaced to maximize the interaction strength.

It will be shown that the effect of dipolar interactions between two nanomagnets may be isolated when a probe of sufficient spatial resolution, mechanical stability and sensitivity is used to separately measure the phase resolved response of each nanomagnet within the pair. In this work time resolved Kerr signals were acquired by myself and Dr Paul Keatley. The data analysis was carried out by Dr Paul Keatley. The micromagnetic simulations and analysis was performed by Dr Paul Keatley and Dr Mykola Dvornik. Prof Rob Hicken generated the macrospin model and associated code.

5.2 Sample details and experiment

In this work time-resolved scanning Kerr microscopy (TRSKM) with coherent microwave excitation has been used to study the simple but unexplored case of a pair of nanoscale Permalloy ($Ni_{80}Fe_{20}$) discs interacting via dipolar interactions. Pairs of Permalloy discs were fabricated by electron-beam lithography and ion-beam milling from a Cu(6 nm)/$Ni_{80}Fe_{20}$(15 nm)/Cu(3 nm)/Al_2O_3(2 nm) continuous film stack deposited on a 0.5 mm thick Si/SiO_2 substrate. To excite magnetisation dynamics, the discs were fabricated at the centre of a microwave antenna fabricated from an evaporated Ti(10 nm)/Au(100 nm) bilayer using ultraviolet photolithography. The antenna consisted of a coplanar stripline with 10 µm wide transmission lines separated by 30 µm. A 10 µm wide electrical short was used between the ends of the transmission lines to generate an antinode of microwave current and hence an out-of-plane harmonic magnetic field at the centre of the antenna. The discs were 15 nm thick with nominal diameter *d* of 300 nm and edge-to-edge separation *s* ranging from 600 nm to 90 nm corresponding to *s*/*d* values of 2, 1, 0.6, and 0.3.

A schematic rendering of the experiment is shown in Figure 5.2.1(a). The sample was mounted on a cartridge that allowed for optical access within the scanning Kerr microscope and for delivery of a microwave current generated by a microwave synthesiser (Rohde and Schwarz SMF-100A). The cartridge was mounted on a three-axis piezoelectric flexure stage (Physik Instrumente P-509) for precise control of the sample position and focus of the pulsed optical probe. The probe had wavelength of 800 nm and was focused to a diffraction limited spot using a ×60 microscope objective. Images of the pairs of discs were acquired by scanning the sample beneath the focused probe.

The spatial resolution was estimated to be 500 nm, while the long term mechanical drift was estimated to be less than 50 nm. The out-of-plane component of the magnetisation dynamics was detected stroboscopically using sub-100 fs laser pulses from an ultrafast laser (Spectra-Physics Tsunami) to measure the polar Kerr effect using a polarising balanced photodiode detector. The dynamics of each disc were measured independently by positioning each disc of the pair beneath the focused probe in turn. Measurements were repeated to check reproducibility. A 4 ns optical delay line was used to precisely set the phase of the probe pulse with respect to the harmonic excitation. Phase-resolved ferromagnetic resonance spectra of the out-of-plane component of the dynamic magnetisation were acquired by sweeping an applied magnetic field in the plane of the discs while recording the polar Kerr signal. The discs were magnetised in-plane using an external magnetic field **H** that was applied either parallel or perpendicular to the centre-to-centre direction of the pair, hereafter described as the parallel and perpendicular field geometries.

The magnetisation dynamics were driven by a uniform, out-of-plane microwave field $\boldsymbol{h}_{\mathrm{RF}}(t)$ generated by a microwave antenna. A large amplitude excitation estimated to be not more than ~ 20 Oe was used to generate a detectable signal and strong dynamic dipolar interactions between the discs. The harmonic excitation field was synchronised with the arrival of sub-100 fs laser pulses from an ultrafast laser that were used to stroboscopically detect the out-of-plane component of the dynamic magnetisation using the polar magneto-optical Kerr effect. This technique has very high sensitivity to confined spin wave modes that couple to a spatially uniform excitation field. At the same time, the high spatial and temporal resolution of TRSKM allows the response of the modes of each disc to be measured independently.

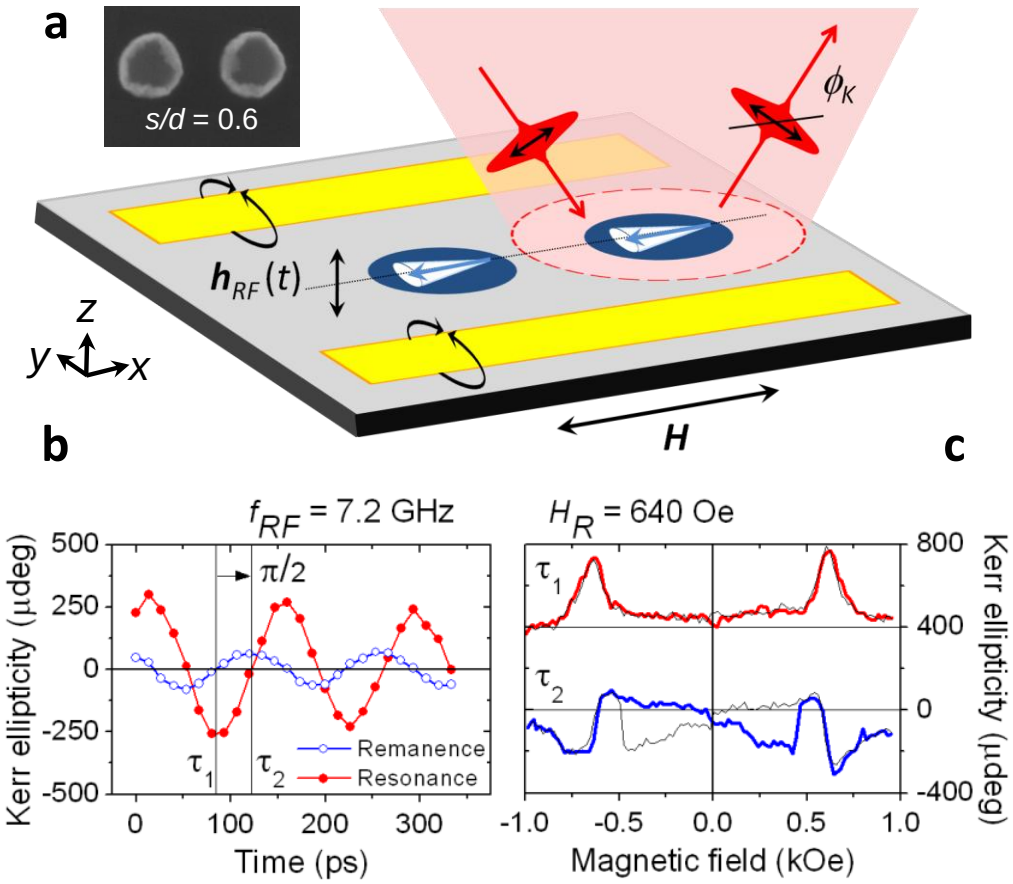

Figure 5.2.1 Experimental geometry and measurements of magnetisation dynamics. A schematic of the geometry for the polar Kerr measurements of the magnetisation dynamics of each disc is shown in (a). A scanning electron microscope image (inset) of a pair of discs with diameter of 300 nm and s/d = 0.6 reveals typical structural distortions of each disc that appear correlated within the pair. In (b) typical time-resolved signals acquired from the left disc in the SEM image are shown for an excitation frequency of 7.2 GHz at remanence (blue curve, open symbols) and at the resonance field (H_R = -640 Oe) of the centre mode (red curve, filled symbols). A $\pi/2$ radian phase shift is observed between these on and off resonance curves. In (c) ferromagnetic resonance curves corresponding to the imaginary and real parts of the out-of-plane susceptibility tensor component χ_{zz} are shown for time-delays corresponding to the node (τ_1) and antinode (τ_2) respectively of the remanence signal shown in (b). In (c) the centre mode resonance can be seen at ±640 Oe.

In Figure 5.2.1(b) typical time-resolved traces of the out-of-plane component of the dynamic magnetisation are shown for the left disc in the scanning electron microscope (SEM) image (inset) in the perpendicular field geometry. At a frequency of f_{RF} = 7.2 GHz and resonance field of H_R = -640 Oe the centre mode is excited.

When the external field is reduced to its remanent value (18 Oe) a $\pi/2$ radian phase shift is observed between the time-resolved signals acquired at resonance and remanence. The phase variation is analogous to that of a driven damped harmonic oscillator when the driving frequency is swept through the resonance frequency. Thus, at resonance the out-of-plane component of the dynamic magnetisation is expected to be $\pi/2$ radians out-of-phase with the out-of-plane harmonic field, while at remanence the dynamic magnetisation is expected to be out-of-phase with the driving field. By setting the time delay to that of a node τ_1 or an antinode τ_2 of the remanence signal (blue curve and open symbols), ferromagnetic resonance (FMR) curves corresponding to the imaginary (τ_1) and real (τ_2) parts of the magnetic susceptibility tensor component χ_{zz} are obtained, as shown in Figure 5.2.1(c), where the z-axis lies normal to the plane of the discs. The FMR curves in Figure 5.2.1(c) were acquired by sweeping the external magnetic field in the plane of the discs from large negative field to large positive field (thick coloured curves), and then to large negative field again (thin black curves) to complete a single hysteresis cycle.

5.3 Spin wave resonances of pairs of discs

To understand the dynamic coupling between a pair of discs it is first necessary to understand the spin wave spectrum of a single disc, such as that shown in Figure 5.3.1(a). The greyscale plot is compiled from FMR curves corresponding to the imaginary part of the susceptibility acquired at different frequencies of the harmonic field excitation ranging from 1 GHz to 12 GHz in steps of 0.4 GHz. The spectrum is shown for the case of a bias field being swept from -1 kOe to +1 kOe (vertical solid white line) and then back to -1 kOe and divided into well-defined regions corresponding to quasi-uniform single domain (SD) or vortex (V) ground states identified from the simulated hysteresis loop in Figure 5.3.1(b).

Figure 5.3.1 (a) shows that the single domain state for static field values ranging from -1 kOe to remanence, centre- and edge-type modes are observed respectively as a higher frequency (black) branch and lower frequency branches (black and white) for which the frequency decreases monotonically as the field is reduced to zero. At remanence (vertical dashed white line) the ground state changes to the vortex state (V) for which the centre and edge modes are no longer supported.

At remanence the vortex gyrotropic mode is not observed since the frequency of vortex core gyration is typically less than 1 GHz.

After passing through remanence, azimuthal modes of the vortex state are observed around 10.5 GHz for small values of the external field (< 200 Oe) for which the cylindrical symmetry of the vortex state is broken[1]. Close to the vortex annihilation field (vertical dotted white line) resonant modes associated with a strongly displaced vortex core[1] can be observed from 7 GHz to 9 GHz. Above the vortex annihilation field the centre and edge modes of the single domain ground state are observed once again as the external field is increased to +1 kOe. These features are also observed for the reverse field sweep from +1 kOe to -1 kOe. In the single domain state for $H > 0$, the opposite contrast of the centre mode branch (black) and edge mode branch (white) indicates that the modes have opposite $\pi/2$-radian phase shifts with respect to the harmonic excitation field resulting from the large variation of the internal magnetic field within the discs. The large demagnetizing field gives rise to an internal field that has opposite sign at the centre of the disc and at the edges of the disc that are perpendicular to the applied field. Therefore the internal field exerts opposite torque on the ground state magnetisation in the centre and edge regions resulting in a π-radian phase difference between the precession of the centre and edge modes.

In the single domain state for $H > 0$ two edge modes are observed experimentally (E_1 and E_2), while only a single edge mode was present in micromagnetic simulations of an ideal disc. In Figure 5.3.1(a) the edge modes seem to be sensitive to the field history. For $H < 0$ the edge mode is less well defined. In addition the edge mode with lower frequency (E_2) has opposite phase with respect to the excitation field when the external field is reversed and appears as a white branch for $H > 0$ and a black branch for $H < 0$. These differences in the edge mode spectra point to small differences in the ground state near to the edge of the disc that result from the non-perfect circular shape.

In summary, in the single domain state at least two modes are observed as a well-defined higher frequency branch (black) and a less well defined lower frequency branches (black and white) that correspond to the centre- and edge-type modes respectively.

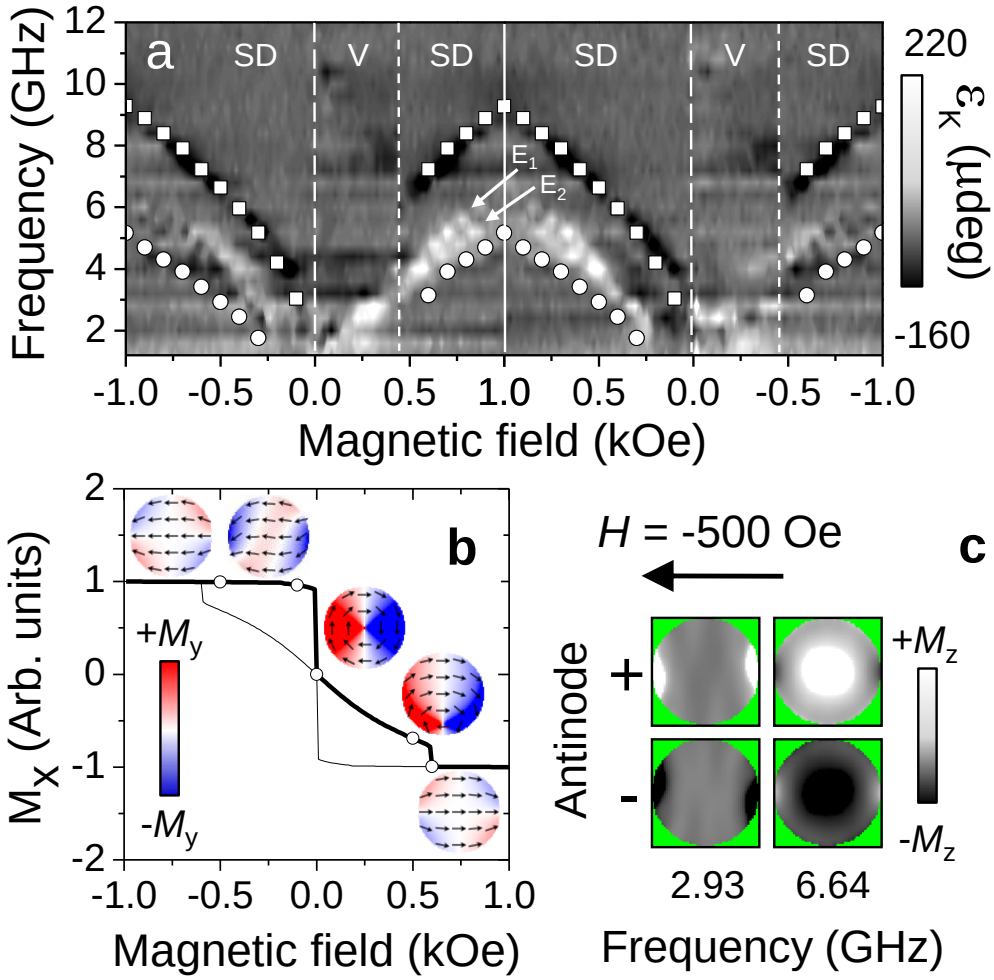

Figure 5.3.1 Single disc spin wave spectrum, ground states and confined spin wave modes. The measured spin wave spectrum of a single 300 nm disc is shown in (a). The greyscale shows the change in polar Kerr ellipticity ε_K due to the change in the out-of-plane component of the dynamic magnetisation as the external field is swept for a fixed excitation frequency. The frequencies of centre and edge modes calculated from micromagnetic simulations are overlaid as squares and circles respectively. The spectrum is divided into regions corresponding to quasi-uniform single domain (SD) or vortex (V) ground states identified from the simulated hysteresis loop in (b). In (b) the ground states correspond to the open symbol data points on the field sweep from -1 kOe to +1 kOe (bold line). The red-white-blue colour scale represents the component of magnetisation M_y orthogonal to the applied field normalized to 75% of the saturation magnetisation for clarity. In (c) the simulated spatial character of the centre and edge modes for an ideal 275 nm disc are shown.

Micromagnetic simulations were performed using the object oriented micromagnetic framework (OOMMF)[119] with a two-dimensional mesh of cell size $5\times5\times15$ nm^3 and exchange parameter 13×10^{-7} ergs/cm. Unless otherwise stated the saturation magnetisation M_s, uniaxial anisotropy constant, g-factor, and Gilbert damping parameter were assumed to have values of 800 emu/cm^3, 5000 ergs/cm^3, 2.05, and 0.01 respectively. The ground state magnetisation was extracted from hysteresis loop simulations that assumed a value of 0.5 for the Gilbert damping in order to allow the magnetisation to relax efficiently. Broadband pulsed magnetic field simulations were performed in order to calculate the frequency of confined spin waves that couple to a uniform out-of-plane field. Frequencies were extracted from fast Fourier transform spectra calculated from the temporal response of the out-of-plane component of the dynamic magnetisation M_z. The spatial character of confined spin waves was extracted at antinodes of opposite polarity (+ and -) in harmonic field simulations with fixed frequency and applied field that was identified from pulsed field simulations. The grayscale represents the out-of-plane component M_z. For clarity the centre and edge mode spatial plots are normalized to 80% and 20% of the maximum M_z value respectively. Simulated ferromagnetic resonance curves were calculated from harmonic simulations performed at static field values from 1 kOe to 0 Oe at 10 Oe intervals. The magnetisation dynamics were driven by an out-of-plane harmonic magnetic field until steady state precession was achieved. The average response of each disc was extracted as a function of field, at time delays corresponding to the node and antinode of the centre mode precession at the resonance field, yielding the real and imaginary parts of the susceptibility tensor component χ_{zz}. Micromagnetic simulations confirm the character of the observed modes; the frequencies of the centre and edge modes calculated from the simulations are overlaid on the experimental spectra, while the simulated spatial character is shown in Figure 5.3.1(c).

In Figure 5.3.1(a) the simulated frequency of the centre mode (square) is in excellent agreement with the experimental spectra, while differences are observed in the number and frequencies of the edge modes. For example, in the single domain state for $H > 0$ two edge modes are observed experimentally (E_1 and E_2), while only a single edge mode is present in the simulations.

The greater number of modes in the experimental spectrum is a result of structural imperfaction[137,138] of the disc that result in an asymmetric internal magnetic field that lifts the resonance field degeneracy of the edge mode at opposite edges of an ideal disc (Figure 5.3.1(c)).

Let us consider an ideal and a real shaped disc and compare the simulated spin wave spectra. In Figure 5.3.2 the simulated spin wave spectrum of a 275 nm ideal disc is shown. The diameter was chosen to be slightly different to the nominal experimental value of 300 nm since some variation in diameter of this order is observed in the SEM images and because the vortex state forms more easily in the simulations for this smaller diameter. The spectrum clearly shows the excitation of a single lower frequency edge mode branch in the single domain regime (SD) either side of the vortex regime (V). The frequencies of the centre and edge modes in the single domain state have already been overlaid on the experimental spectra of Figure 5.3.1(a), while the hysteresis loop and spatial character of the centre and edge modes were shown in Figure 5.3.1(b) and Figure 5.3.1(c) respectively. When the real shape of the disc is taken from the SEM image and used in the simulations (Figure 5.3.2 (b)) two (1, 2) lower frequency modes appear below the centre mode branch as observed in the experimental spectrum in Figure 5.3.1(a). Furthermore the centre mode appears to be split into two modes (3, 4) and shows slightly different field dependence to that of the ideal disc due to the interaction with mode 2 at -500 Oe, and mode 1 at -100 Oe. While these interactions are not clearly observed in the experiment, the experimental spectrum does exhibit complicated behaviour between the centre and edge modes at low values of the applied field.

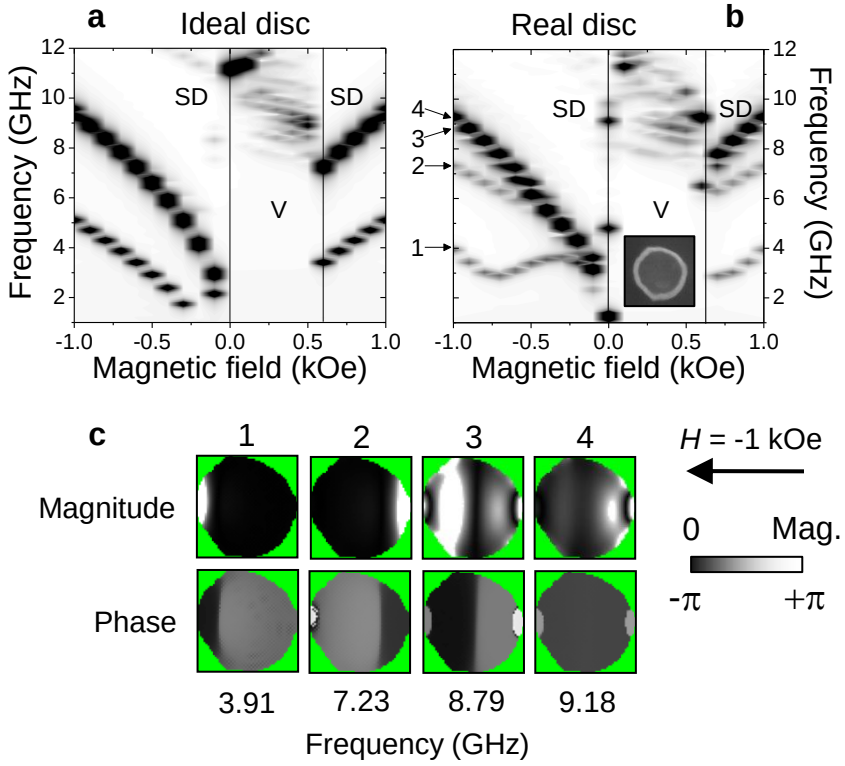

Figure 5.3.2 Simulated spin wave spectra. In (a) and (b) the simulated resonance spectra of an ideal disc and a real shaped disc are shown respectively. The diameter of the ideal disc was 275 nm. In (b) the real shape of the disc was taken from the SEM image of the disc (inset). The spectrum is divided into regions corresponding to quasi-uniform single domain (SD) or vortex (V) ground states. In (c) the simulated spatial character of the centre and edge modes for the real shaped disc is shown in images of the magnitude and phase of the pixel dependent fast Fourier transform (FFT) of the out of plane component of the dynamic magnetisation. For clarity the images of FFT magnitude for modes 1 and 2, and modes 3 and 4 are normalized to 20% and 50% of the maximum value of the FFT magnitude respectively.

In Figure 5.3.2 (c) the Fourier images of magnitude and phase show the spatial character of modes 1 to 4 at -1 kOe. The spatial plots show that modes 1 and 2 are edge modes. The large splitting is due to the very different shape at the edge of the disc, which significantly changes the magnetic ground state and internal field in the region of the edge mode localisation. Due to the 'isolation' of the centre mode from the edge of an ideal disc, it is usually expected that the shape has a reduced influence on the centre mode. However, while the centre mode branch is very similar to that of the ideal disc in Figure 5.3.2(a), the spatial character is very different and complicated further by the spectral overlap of modes 3 and 4.

The spatial plots show that mode 3 is an anti-symmetric mode (3) with a nodal line passing through the disc perpendicular to the applied field. The uniform excitation field is able to couple to the anti-symmetric mode because of the asymmetry of the internal field within the disc due to the real shape. For real shaped nanomagnets, the sensitivity of the centre and edge modes to the precise shape of the disc present significant challenges for the controlled dynamic dipolar coupling of nanomagnets.

While the simulation shows the correct number of edge modes when the real shape of the discs is considered, the nanofabrication process affects the quantitative agreement of the edge mode frequencies through modification of the magnetic parameters at the edge of the nanomagnet[122,123]. Measurements performed upon a pair of discs with $s/d = 0.6$ show that the structural distortions can have a more significant effect on the edge mode splitting than the static dipolar interaction of the discs. In the following discussion we demonstrate the effect of the shape distortion on the spin wave spectra acquired from measurements of a pair of 300 nm discs with $s/d = 0.6$. In Figure 5.3.3 the spin wave spectrum acquired from each disc within the pair is shown for the parallel and perpendicular field geometries. The greyscale plots are compiled from imaginary-type FMR curves (*e.g.* Figure 5.2.1(c)) acquired at different frequencies of the harmonic excitation field and field sweep from -1 kOe to +1 kOe (vertical solid white line) and back to -1 kOe as for the single disc spectra shown in Figure 5.3.1(a).

The response of nominally identical discs excited by a uniform microwave field is expected to be identical. However, for both field geometries the spectra show that the centre mode has larger amplitude in disc 1, shown in Figure 5.3.3 (a) and Figure 5.3.3 (c) by the stronger (black) contrast of the higher frequency branch than in Figure 5.3.3 (b) and Figure 5.3.3 (d).

In the parallel geometry the lower frequency edge mode branch (white) is broad and poorly defined in both discs (Figure 5.3.3 (a) and Figure 5.3.3 (b)). However, in the perpendicular geometry the edge mode branch is clearer. In disc 1 (Figure 5.3.3 (c)) two lower frequency edge modes are observed (E_1 and E_2,) while in disc 2 (Figure 5.3.3 (d)) only a single edge mode is observed. Furthermore, in disc 1 the edge mode with higher frequency (E_1) has opposite phase with respect to the

excitation field when the external field is reversed and appears as a white branch for negative field values and a black branch for positive field values.

The similarity of these effects to those observed in the spectrum of the single disc (Figure 5.3.1(a)) point to the sensitivity of the edge mode to small differences in the magnetic ground state and internal field that result from the non-perfect circular shape of the discs.

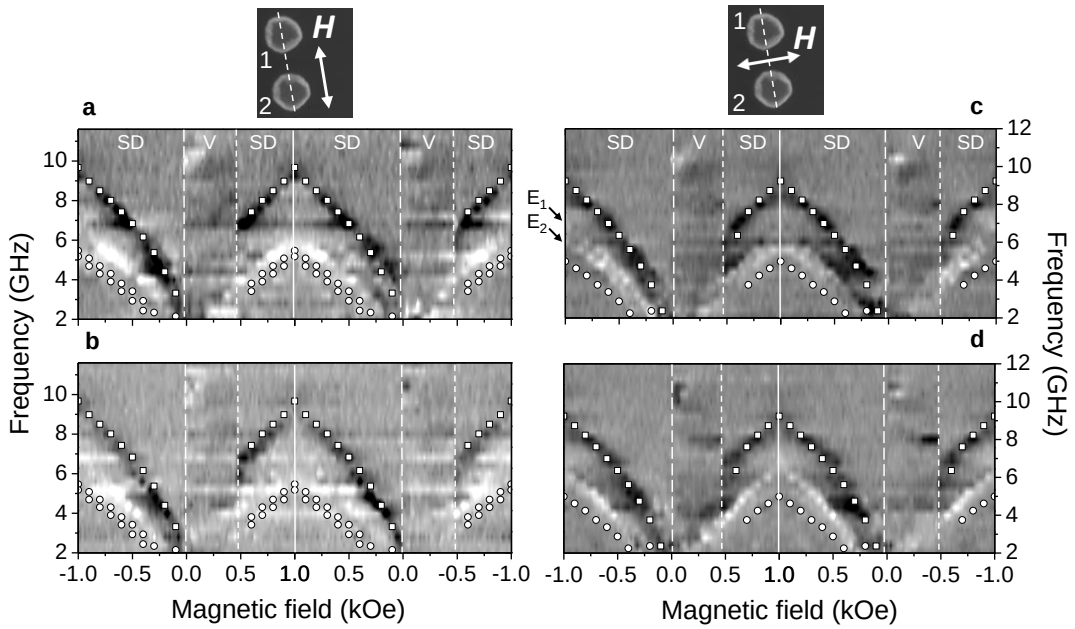

Figure 5.3.3 The experimental spin wave resonance spectra acquired from a pair of 300 nm discs with s/d = 0.6 are shown for the parallel (a) and (b), and perpendicular (c) and (d) field geometries. In both field geometries the spectra were acquired from disc 1 (a) and (c), and disc 2 (b) and (d) shown in the SEM images (inset). The greyscale shows the change in polar Kerr ellipticity due to the change in the out-of-plane component of the dynamic magnetisation as the external field is swept for a fixed excitation frequency. The simulated frequencies of centre and edge modes are overlaid as squares and circles respectively. The spectrum is divided into regions corresponding to either a quasi-uniform single domain (SD) state or a vortex state (V).

The simulated frequencies of the centre (squares) and edge modes (circles) extracted from micromagnetic simulations are overlaid on the experimental spectra. In the parallel geometry the static interaction causes splitting of the edge modes in the simulation. The small splitting is consistent with the broader edge mode branch of the experimental spectra in the parallel geometry that may consist of two modes that are

not resolved experimentally. In the perpendicular geometry only a single edge mode is predicted by the simulations.

The experimental spectrum of disc 2 shows only a single mode, while disc 1 shows strong splitting of the edge mode. The differences in the edge mode branch can be caused by the differences in the shape and size of the discs. The SEM images (inset) reveal that even though the shape of the discs is not ideal, their shape is similar. Therefore additional features of the discs that are difficult to determine experimentally may also contribute to the splitting, for example reduced saturation magnetisation near to the edges resulting from the nanofabrication processes.

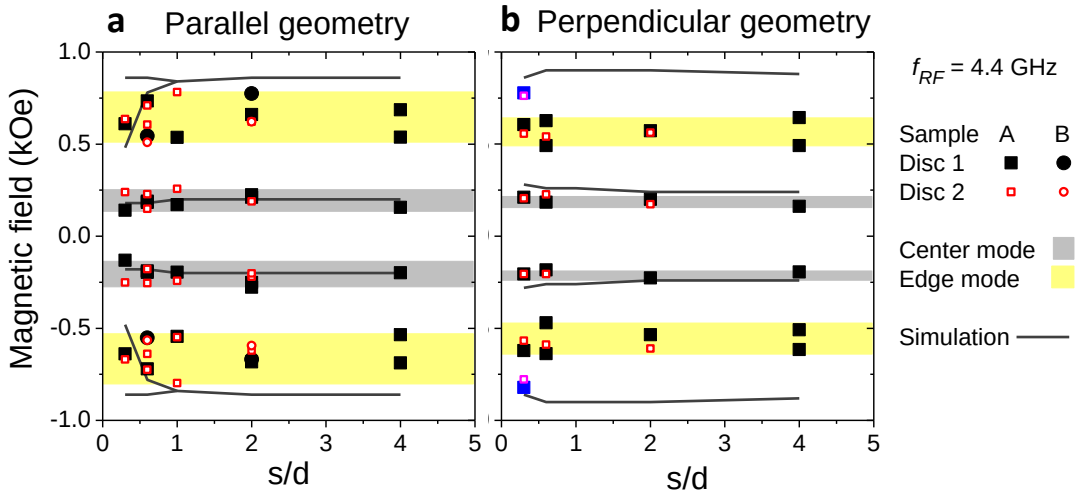

Figure 5.3.4 Dependence of centre and edge mode resonance fields on disc separation. The centre and edge mode resonance fields of pairs of discs with different separation are shown for the parallel (a) and perpendicular (b) field geometries at an excitation field frequency of 4.4 GHz. Data for a single disc are shown at $s/d = 4$, while data for disc 1 and disc 2 of a pair are shown as filled black symbols and open red symbols respectively. Simulated resonance fields are shown as grey curves. In the parallel geometry two samples (A and B) were measured for separation values $s/d = 0.6$ and 2. The range of resonance fields for the centre and edge modes are shown as gray and yellow bands respectively.

In Figure 5.3.4 the dependence of the resonance fields of the centre and edge modes upon the separation (s/d) for the parallel (Figure 5.3.4 (a)) and perpendicular (Figure 5.3.4 (b)) field geometry is shown. The excitation frequency of 4.4 GHz allowed both modes to be observed in the single domain state between 1 kOe and remanence. The resonance fields were extracted from the FMR curves by identifying

the value of the magnetic field at the node (peak) in the real (imaginary) curves respectively, for example at H = -640 Oe in Figure 5.2.1(c).

The amplitude and phase were also calculated from the real and imaginary curves and used to identify the resonance field. The most striking feature of Figure 5.3.4 is the larger range of resonance fields for both centre (grey band) and edge modes (yellow band) in the parallel as opposed to the perpendicular field geometry. In both field geometries the centre mode shows a smaller range of resonance fields than the edge mode, which is understood to be due to the relative 'isolation' of the centre mode from structural distortions at the edges and dipolar interactions. In the parallel geometry, as the disc separation is decreased, the internal magnetic field of the discs becomes asymmetric along the applied field direction due to the non-uniform contribution of the static dipolar field. The degenerate edge modes of an ideal single disc become strongly split due to the difference in the static dipolar field generated by one disc at the opposite edges of the other disc within the pair[140]. The asymmetry of the internal field also modifies the spatial character of the centre and edge modes.

Micromagnetic simulations were performed for a pair of 275 nm discs with *s/d* =0.6 to explore the effect of the interaction. The discs were excited by an out-of-plane harmonic magnetic field with amplitude of 20 Oe, which was estimated to be the upper limit for the field generated in the experiment. In Figure 5.3.5 (a) and (b) the simulated spatial character of the centre and edge modes is shown for the parallel and perpendicular geometry respectively for an applied field of 500 Oe. In Figure 5.3.5 (c) and (d) the dipolar fields are shown respectively for the centre mode at 6.84 GHz and edge mode at 3.32 GHz in the parallel geometry. Due to the strong contribution of the static field of each disc to the internal field of the other, the spatial character of the centre mode is significantly modified from the more cylindrically symmetric profile in an isolated disc (Figure 5.3.1(c)). The strong variation of the static field also splits the edge mode into two modes; an antisymmetric mode at 3.32 GHz with opposite grayscale contrast at opposite edges of the disc along the centre-to-centre direction of the pair, and a symmetric mode at 2.93 GHz. Normally the antisymmetric mode would not couple to a uniform excitation field, however the modification to the internal field of the interacting discs leads to a net out-of-plane component of the precessing magnetisation that couples to the uniform field. The

splitting of the symmetric and antisymmetric modes is small and is therefore difficult to isolate from the effect of structural distortions that are present in the experiment.

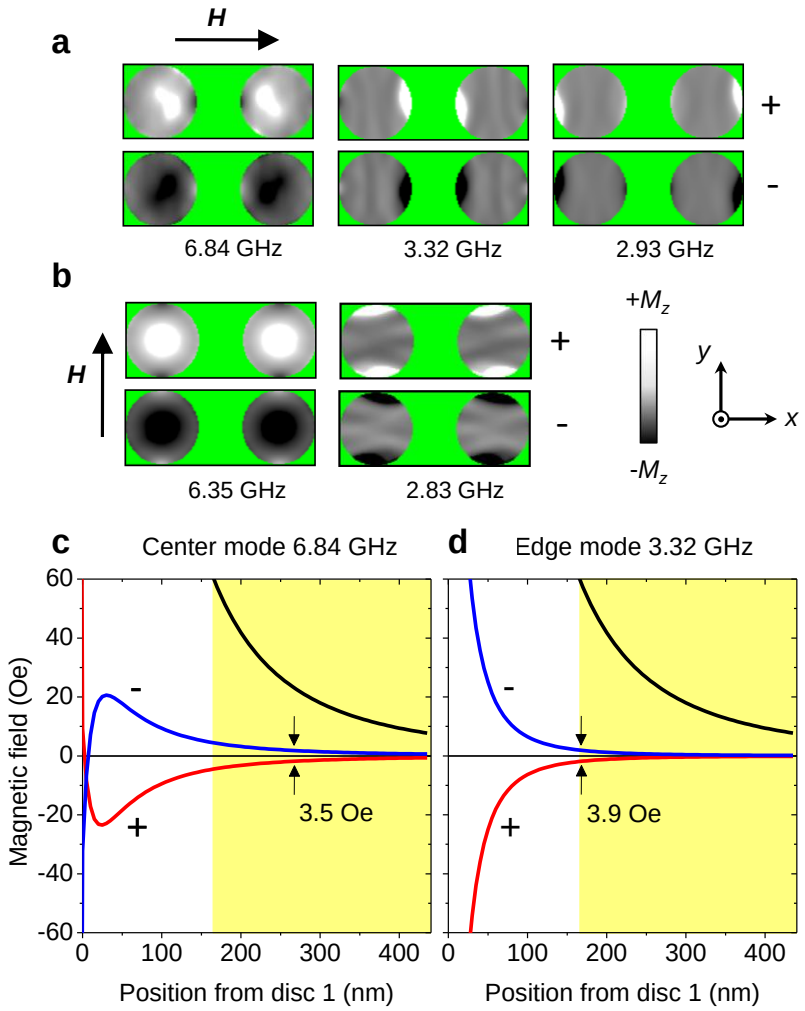

Figure 5.3.5 Simulated spin wave spatial character and dipolar fields of a pair of 275 nm discs with s/d = 0.6. In (a) and (b) the simulated spatial character of the centre and edge modes is shown for the parallel and perpendicular geometries respectively for an applied field of 500 Oe. The greyscale corresponds to the out-of-plane component of the dynamic magnetisation extracted from harmonic simulations at opposite precession antinodes (+ and -). In (c) and (d) the *x*-component of the static field (black curve) and the *y*-component of the dynamic dipolar fields (red and blue curves) are shown for the centre and edge modes respectively as a function of distance from disc 1. The dynamic field is illustrated by the change in total field at opposite precession antinodes (+ and -).

In the perpendicular geometry micromagnetic simulations show that the static dipolar interaction has negligible influence on the internal field. In fact, due to

symmetry, any change in the internal field in the perpendicular geometry will be the same for both regions of edge mode localisation.

As a result the centre mode at 6.35 GHz is symmetric throughout the disc and has lower frequency than the centre mode in the parallel geometry, while the edge modes are degenerate in frequency.

The static field and the dynamic dipolar fields of the centre and edge modes (Figure 5.3.5 (c) and (d)) were calculated from magnetisation maps of the pair of discs. To calculate the dynamic field, maps of the dynamic magnetisation were extracted at opposite precession antinodes, while the static field was calculated from the ground state magnetisation. To extract the dipolar field of disc 1 acting on disc 2, disc 2 was removed from the mesh. The total magnetic field was then calculated from the magnetisation map in disc 1 only without allowing the magnetisation to relax. The extracted fields reveal that the *y*-component of the dynamic field is significantly smaller than the *x*-component of the static field, even for a large harmonic excitation amplitude of 20 Oe. For the centre and edge modes the peak-to-peak amplitude of the dynamic field in the region of large amplitude was ~16% and ~7% of the static field amplitude respectively. The in-plane peak-to-peak cone angles of the largest amplitude regions of magnetisation precession were found to be 38° and 50° for the centre and edge mode respectively. Consequently the dynamic dipolar interaction fields associated with a particular mode depend upon *s/d*.

In the perpendicular geometry for $s/d = 0.3$ one of the edge modes observed in each disc (filled blue square and open magenta square) lies outside the field range observed for larger separations. In the perpendicular geometry, micromagnetic simulations of a pair of ideal discs show that the static dipolar field has negligible influence on the internal field. In fact, any change of the internal field in the perpendicular geometry is identical for both discs and symmetric along the applied field direction. As a result the centre mode has symmetric spatial profile while the edge modes are degenerate in field, as for the single disc in Figure 5.3.1(c). Therefore, the strong splitting of the edge mode for $s/d = 0.3$ in the perpendicular geometry (Figure 5.3.4 (b)) is most likely the result of structural or magnetic imperfections. While SEM images of the discs reveal that the shape of the discs is not ideal (*e.g.*

Figure 5.2.1(a) inset), the structural distortion of the discs in each pair is comparable leading to similar splitting of the modes in disc 1 and disc 2.

In Figure 5.3.4 micromagnetic simulations were performed for discs of 275 nm diameter with s/d = 2, 0.6, and 0.3 to explore the effect of the dynamic dipolar interaction on the frequency of the centre and edge modes. Centre and edge mode frequencies were extracted from fast Fourier transform spectra calculated from the temporal response of the out-of-plane component of the dynamic magnetisation to an out-of-plane pulsed magnetic field with amplitude of 15 Oe. In order to identify small changes in the mode frequencies due to dynamic coupling the resolution of the FFT spectra was enhanced by reducing the damping parameter from 0.01 to 0.0001 and extending the simulation time from 8 ns to 40 ns. Two sets of simulations were performed. In the first set the magnetisation of both discs was free to respond to the excitation. In the second set the ground state magnetisation of disc 1 was fixed, removing the effect of dynamic fields of disc 1 acting on disc 2.

In Figure 5.3.6 the frequency shift of the center and edge modes in Figure 5.3.5 (a) and (b) is shown as a function of disc separation s/d. The frequency shift is the difference in the mode frequency of disc 2 for the cases of free and fixed magnetisation in disc 1 (filled symbols). When disc 2 is fixed instead the frequency shift is very similar (open symbols) due to symmetry. The negligible differences are the result of slight differences in the definition of the discs onto the mesh. In the parallel geometry (Figure 5.3.6 (a)) the centre mode (black line and squares) and the higher frequency edge mode (red line and circles) show a frequency shift due to dynamic dipolar fields.

The spatial character of the modes is shown in Figure 5.3.5 (a). The edge mode shows the largest frequency shift as the separation is reduced, while the lower frequency edge mode (blue line and triangles) shows negligible frequency shift. The magnitude of the frequency shift of the different modes can be understood in terms of the mode separation. The higher frequency edge mode is localised at the near edges of the disc and will therefore experience the largest possible dynamic dipolar field from the corresponding edge mode of the second disc. The separation of the centre mode localisation is larger and so the resulting frequency shift is smaller. For the

lower frequency edge mode the frequency shift is negligible since the modes are localised at the far edges of the discs where the dynamic interaction is weakest.

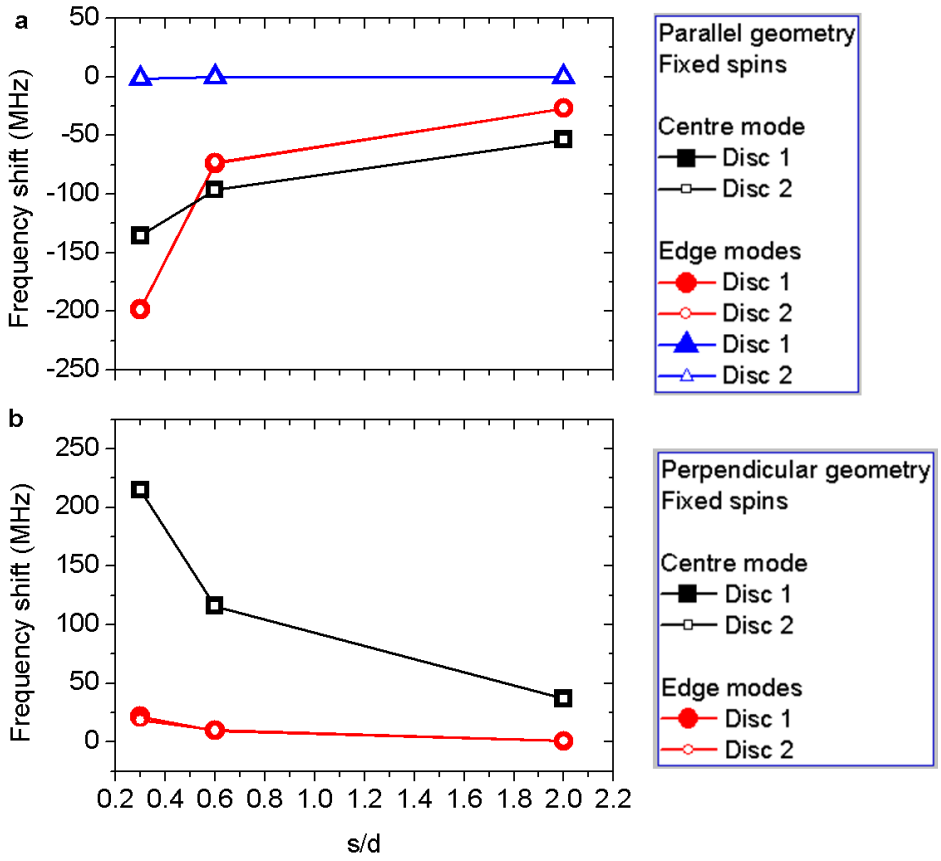

Figure 5.3.6 Frequency shift due to dynamic dipolar interactions. The frequency shift of centre and edge modes due to dynamic dipolar interactions is shown as a function of separation *s/d* for the parallel (a) and perpendicular geometry (b). In (a) the frequency shift is shown for the centre mode (black line and squares), higher frequency edge mode (red line and circles), and lower frequency edge mode (blue line and triangles) shown in Figure 5.3.5 (a). In (b) the frequency shift is shown for the centre mode (black line and squares) and edge mode (red line and circles) shown in Figure 5.3.5 (b).

In the perpendicular geometry (Figure 5.3.6 (b)) only the centre mode (black line and squares) shows a significant frequency shift due to the dynamic dipolar coupling. The frequency shift is approximately a factor of two larger than that of the centre mode in the parallel geometry, which can be understood in terms of the geometry of the dipolar field. The spatial character of the centre and edge mode modes is shown in Figure 5.3.5 (b).While the effect of the dynamic dipolar coupling can be observed in the micromagnetic simulation, the frequency shifts are small in

comparison to the frequencies of the centre and edge modes. Since the shape, size and magnetic parameters of real discs can significantly shift the resonance frequency, or equivalently the resonance field, it is not possible to observe the effect of the dynamic dipolar interactions upon the mode frequencies in the experiment. Furthermore, in order to observe the frequency shift it is necessary to fix the magnetisation dynamics of one of the discs, which is not possible within the experiments. Therefore, a more sensitive probe of the dynamic dipolar interaction is required in which the effects of the actual disc shape upon the spin wave mode resonances is accounted for. While the resonance field was relatively unaffected, the phases of the modes in the free disc were found to change significantly. In the following section we demonstrate that by measuring the phase of the modes in each disc it is possible to isolate the dynamic interaction between modes of similar character.

5.4 Modelling the dynamic dipolar interaction

Simulations of two parallel macrospins coupled by dynamic dipolar interactions illustrate how the phase of the modes can be used to characterise the dynamic dipolar interaction. Harmonic solutions of the linearized Landau-Lifshitz-Gilbert equation for each macrospin were calculated analytically yielding a set of simultaneous equations that were solved numerically to obtain the real and imaginary parts of the susceptibility tensor component χ_{zz}. The effective dipolar field generated by macrospin *i* at macrospin *j* was assumed to have the form

$$\mathbf{H}_{eff} = -\beta_i M_j \mathbf{u}_j , \qquad (5.4.1)$$

for $i \neq j$, where β_i, M_i, and $\mathbf{u}_i$ are the dipolar coupling coefficient, saturation magnetisation and unit vector parallel to the magnetisation of macrospin *i* respectively. The gyromagnetic ratio, saturation magnetisation, and Gilbert damping parameter were assumed to be 2.94 MHz/Oe, 800 emu/cc, and 0.01 respectively. This simplified form has been used for ease of calculation, but it is easily shown that it provides a good approximation to the correct dynamic dipolar fields1 when $\beta_i = -V_j/r^3$ for the parallel geometry and $+2V_j/r^3$ for the perpendicular geometry. Here V_j is the volume of macrospin *j* and *r* is the distance between the centres of the two macrospins. In Figure 5.4.1 the amplitude (a) and phase (b) of the susceptibility tensor component

χ_{zz} for each macrospin, and also the difference of the phases (c) are shown as a function of applied field for different values of the dipolar coupling coefficient β_i in the parallel geometry. The quantity $\beta_i M_i$ has units of magnetic field and was chosen so as to give a dipolar coupling field of similar order of magnitude to the dynamic dipolar field estimated from micromagnetic simulations (as shown in Figure 5.3.5 (c)&(d)). To model the effects of different resonance fields in real shaped discs, the anisotropy field was set to 5 Oe and 15 Oe for macrospin 1 and macrospin 2 respectively. When $\beta_{i,j} = 0$, the amplitude and phase resonance curves are identical for both macrospins, except that for macrospin 2 (red curve) the peak is shifted by 10 Oe to a lower applied field value owing to the larger anisotropy field.

The resulting peak in the phase difference is observed exactly half way between the centres of the two resonances (vertical grey line). When $\beta_{i,j} = +0.01$ two modes are evident in the amplitude and phase in macrospin 2, while only a single mode is apparent in macrospin 1. The larger amplitude mode in macrospin 2 has the same resonance field as the mode in macrospin 1, while the second mode is observed as a shoulder on the low field side of the main peak. The second mode also modifies the phase of macrospin 2 and results in a shift of the phase difference peak to the low-field side of the resonance of macrospin 1. When $\beta_{i,j} = -0.01$, two modes are instead observed in macrospin 1 and the phase difference peak shifts to larger values of the applied field. Measurements of the phase difference peak can be used to identify the dynamic coupling between two macrospins, or for that matter any system of coupled oscillators where the resonant frequencies of the uncoupled oscillators are somewhat different. While the magnetisation dynamics of a nanoscale disc cannot be accurately described by a macrospin model, the same analysis of the phase difference can be applied to micromagnetic simulations. The response of a pair of ideally shaped discs with slightly different diameters of 300 nm and 275 nm, separated by 165 nm (approximately $s/d = 0.6$), were simulated, the different diameters leading to slightly different resonance fields. The excitation frequency was set to 4.4 GHz to observe both centre mode (low field) and edge mode (high field) resonances between 1 kOe and remanence. Two simulations were performed, the first with an excitation amplitude of 2 Oe to avoid non-linear effects, and the second with an excitation amplitude of 20 Oe to observe the effect of large amplitude excitation upon the dynamic coupling.

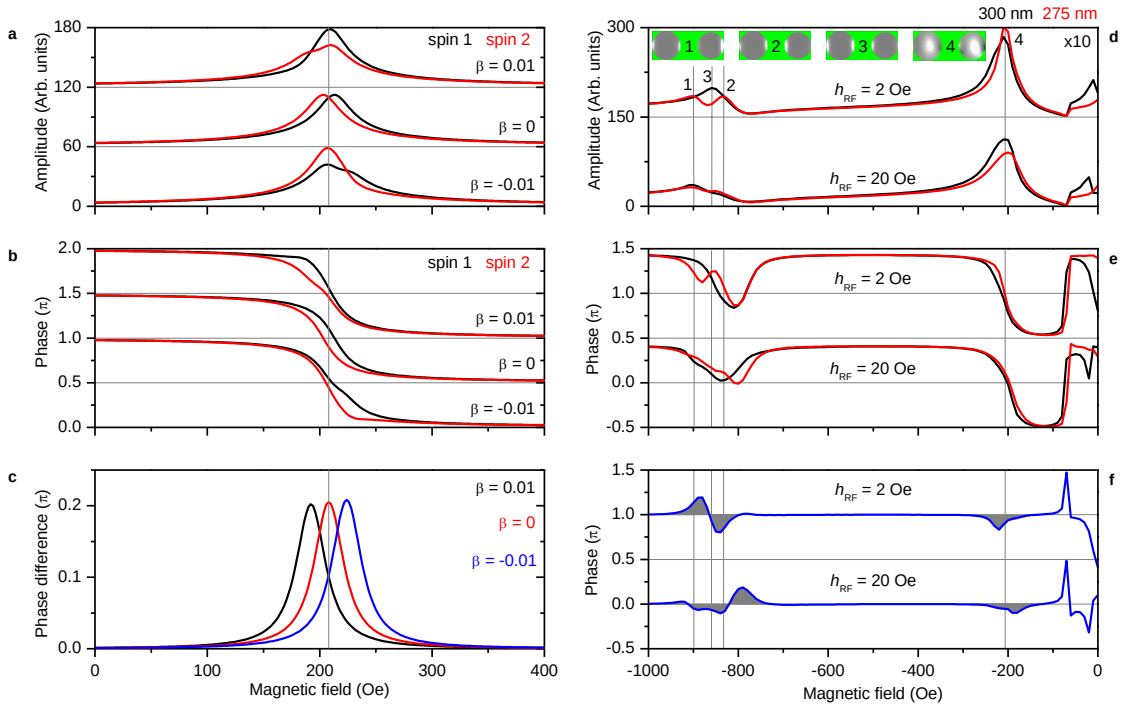

Figure 5.4.1 Identification of dynamic dipolar coupling in macrospin and micromagnetic simulations. The amplitude (a) and phase (b) of the ferromagnetic resonance (FMR) of each macrospin from a pair coupled by dynamic dipolar interactions in the parallel geometry, and the difference in phase (c), are shown for different interaction strengths. In (d) and (e) micromagnetic simulations of FMR amplitude and phase are shown for two interacting discs with diameters of 300 nm (black curves) and 275 nm (red curves) and separation $s/d \approx 0.6$. The curves are shown for the parallel geometry and for two values of the harmonic excitation field amplitude. In (d) the spatial character of the confined spin wave modes for the small amplitude excitation is shown in images of the out-of-plane component of the dynamic magnetisation. The FMR amplitude curves corresponding to the smaller amplitude excitation are scaled (×10) for clarity. In (f) the phase difference calculated from the curves in (e) is shown. The shifts in the peaks in the phase difference in (c) and (f) indicate the presence of the dynamic dipolar interaction. The vertical grey lines are guides to the eye corresponding to the average resonance field for $\beta = 0$ in (a)-(c), and the positions of modes 1-4 in (d)-(e).

In Figure 5.4.1(d) and (e) amplitude and phase curves calculated from the real and imaginary parts of the susceptibility tensor component χ_{zz} are shown for the 300 nm disc (black curves) and the 275 nm disc (red curves). In (d) the simulated mode profiles are shown (inset) for the small amplitude excitation. For each value of the excitation amplitude the centre modes have similar resonance fields and are

relatively insensitive to the slightly different diameters of the discs, showing only small differences in amplitude. In contrast, for an excitation amplitude of 2 Oe the edge mode in the 275 nm disc (right disc) is strongly split into two modes. The higher (*lower*) field edge mode corresponds to a large amplitude region at the far (*near*) edge of the 275 nm disc where the non-uniform static field of the 300 nm disc is small (*large*). The static field of the 300 nm disc acting on the 275 nm disc leads to splitting of the edge modes, while in the 300 nm disc the edge modes remain degenerate in field. For an excitation amplitude of 20 Oe the centre mode resonance is shifted slightly to higher field, while the edge modes exhibit significant broadening and overlap and are less clearly resolved. It was previously reported in chapter 4 that a larger amplitude excitation can lead to the apparent suppression of the edge mode amplitude due to changes in the ground state and internal field.

In Figure 5.4.1(e) differences in the phase related to the value of the excitation amplitude can be seen. At an excitation amplitude of 2 Oe (20 Oe) the phase of the 300 nm (275 nm) disc reveals a shoulder on the high (low) field side of the centre mode resonance resulting in a peak in the phase difference on the high (low) field side of the resonance (Figure 5.4.1(f)). The shift in the position of the phase difference peak indicates that the centre modes are subject to dynamic dipolar interactions. The change in direction of the shift indicates that the dynamic dipolar coupling is strongly dependent on the excitation amplitude, which can be understood in terms of modification of the mode amplitude, spatial character, and, for sufficiently large excitation amplitudes, the ground state. For small amplitude excitation of the edge modes, a bipolar peak in the phase difference is observed. Since the edge mode is strongly split in the 275 nm disc the resonance field and spatial character of the mode is different in each disc. Indeed the different phases of the different modes also lead to peaks in the phase difference. However, the peaks lie precisely between the edge mode resonance fields of the two discs indicating that the dynamic dipolar coupling between the different edge modes is weak (as in Figure 5.4.1(c) for $\beta_{i,j} = 0$). For large amplitude excitation the edge modes of both discs exhibit broadening, suggesting splitting that is masked by the enhanced linewidth of the modes. In the region of the edge mode resonances a complicated variation in the phase difference is observed in addition to a large phase difference peak on the low field side.

5.5 Experimental detection of the dynamic dipolar interaction

The amplitude and phase can be calculated from the measured real and imaginary components of the susceptibility. In addition the amplitude and phase can be extracted directly from measurements in which the time delay is varied while the static field is held constant. In Figure 5.5.2 (a) the amplitude and phase of the centre mode resonance is shown for the pair of discs shown in Figure 5.4.1(a) in the parallel geometry. The excitation frequency was 7.2 GHz and the discs were in a single domain state between -1 kOe and remanence.

The resonance field of the centre mode appears to be different in the two discs for both 7.2 and 4.4 GHz excitation frequencies. Strictly speaking, the response of the pair of discs should be described in terms of their collective modes rather than the modes of the individual non-interacting discs. When two discs with different individual mode frequencies are brought together so that they weakly interact, acoustic and optical modes are formed, for which the precession in the two discs differs by 0 and π radians respectively. The acoustic and optical modes have distinctly different frequencies that lie close to those of the individual modes of the non-interacting discs. However, the amplitude of a particular collective mode within each disc is very different. The amplitude is greatest in the disc that has individual mode frequency close to that of the collective mode in question. As the interaction strength is increased the relative amplitudes within the two discs may become more equal. Therefore in Figure 5.5.2, the acoustic mode is observed in one of the discs while the optical mode is observed in the other disc. In comparison, the micromagnetic simulations of Figure 5.4.1, where one disc is slightly different from the other, showed that the out-of-plane component m_z of the acoustical mode is an order of magnitude larger than that of the optical mode in the smaller disc, while in the larger disc the acoustic and optical modes have similar amplitude. The spatial profile of the acoustic and optical modes found with micromagnetic simulations are shown in Figure 5.5.1. In the simulations the acoustical and optical modes differ in frequency by about 100 MHz, while a difference of 600 MHz is observed experimentally. The larger value observed in the experiment is most likely due to the different shape or magnetic parameters of each disc, which are not included in micromagnetic simulation.

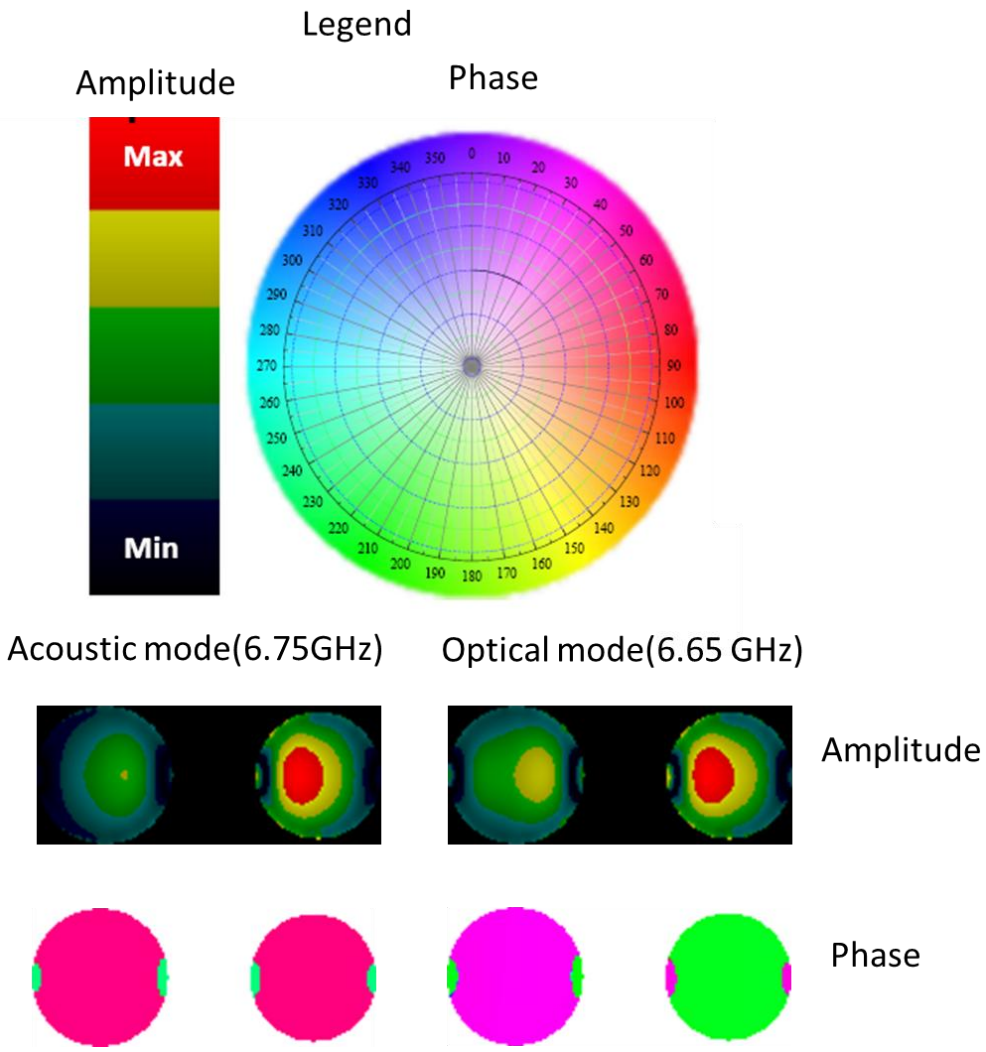

Figure 5.5.1 Micromagnetic simulations show the existence of acoustic and optical modes by looking at the amplitude of the out of plane component of the magnetisation and the relative phase within a pair of discs.

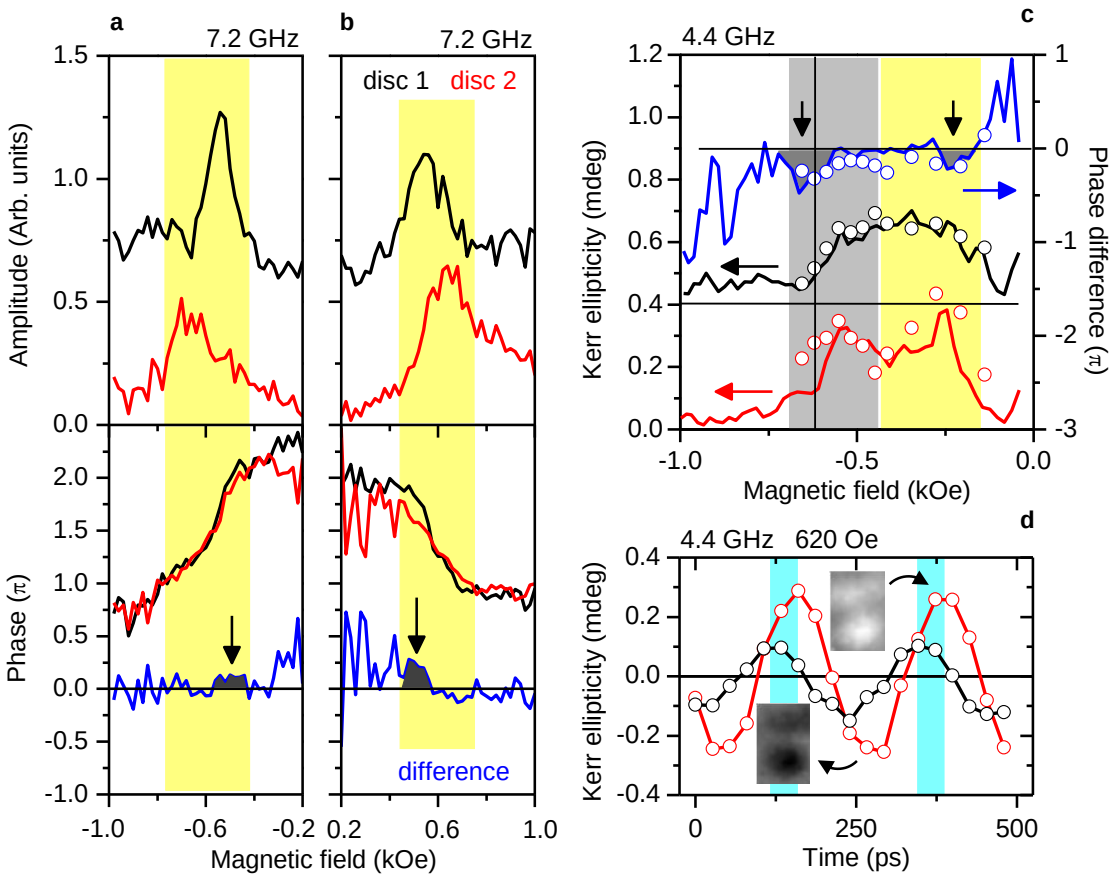

Figure 5.5.2 Experimentally observed dynamic dipolar coupling. Measured FMR amplitude and phase curves are shown for disc 1 (black curves) and disc 2 (red curves) of a pair of discs with $s/d = 0.6$ in the parallel geometry. The shift of the peak in the phase difference (blue curve) with respect to the centre of the resonances indicates dynamic dipolar coupling between the excited modes. The peak is shaded (dark grey) and indicated by arrows for clarity. In (a) and (b) dynamic coupling between the centre modes (yellow band) at an excitation frequency of 7.2 GHz is shown for two single domain quadrants of the hysteresis cycle with opposite field history. In (c) amplitude and phase difference FMR curves are shown for the centre mode (yellow band) and edge mode (grey band) at an excitation frequency of 4.4 GHz. In (d) time-resolved signals corresponding to the edge mode resonance in disc 1 and disc 2 are shown for an excitation frequency of 4.4 GHz and applied field of 620 Oe (vertical black line in (c)). Typical Kerr ellipticity images acquired at 560 Oe are shown inset for opposite antinodes of the precession signal in disc 2. In (c) the open symbols correspond to the amplitude and phase difference is indicated by the blue band.

Since the experimental FMR spectra in Figure 5.5.2 clearly contain noise, the phase noise outside the region of the resonance peak (yellow shading) becomes large since the phase of the noise is random. Therefore it is important to consider only the shaded resonance region. In Figure 5.5.2 (a) the phase difference exhibits a small peak (shaded grey and indicated by an arrow) shifted to the low field side of the average resonance field of the centre modes. A similar peak is also observed in the single domain state between +1 kOe and remanence, as shown in Figure 5.5.2(b). As demonstrated by the micromagnetic simulations (Figure 5.4.1(f)), the shift of the phase difference peak is a signature of the dynamic dipolar interaction of the centre modes.

At lower excitation frequencies both centre and edge modes can be excited in the single domain state between -1 kOe and remanence. Amplitude and phase difference spectra for the centre (yellow shading) and edge mode (grey shading) are shown in Figure 5.5.2(c) for an excitation frequency of 4.4 GHz. At 4.4 GHz the modes are less clearly resolved but still exhibit peaks in the phase difference near to the resonance fields of the centre and edge modes that are shifted to lower and higher field values respectively. We emphasise that the shift of the centre mode phase difference peak to lower field values is consistent with that observed in Figure 5.5.2 (a) and (b) at 7.2 GHz and in the micromagnetic simulation with larger amplitude excitation in Figure 5.4.1(d)-(f). However, while a significant shift in the peak of the edge mode phase difference is observed both experimentally (Figure 5.5.2(c)) and in micromagnetic simulations with larger amplitude (Figure 5.4.1(f)) the sign of the shift with respect to the resonance field does not agree.

The edge modes are particularly sensitive to the effects of shape, size and magnetic parameters at the edge of the discs. Therefore, the nanofabrication process itself may affect the dynamic dipolar coupling of the edge modes. Better agreement between experiment and simulation requires a more detailed knowledge of the spatial variation of structural and magnetic properties within the discs.

Despite the discrepancy with the idealised micromagnetic model in Figure 5.4.1 (d)-(f), the measured phase difference peak is confirmed by the time-resolved signals acquired from each disc at different values of the applied field. The amplitude and phase difference extracted by fitting a sine function to the time-resolved signals

are shown as open symbols in Figure 5.5.2 (c). For example, in Figure 5.5.2 (d) time-resolved signals acquired at -620 Oe reveal a phase shift (blue band) between the edge modes of disc 1 and disc 2 that is clearly resolved and in good agreement with that calculated from the measured real and imaginary parts of the susceptibility tensor component χ_{zz}, dipolar coupling. However, the size and sign of the phase difference peak observed in the experiment and simulation are not always consistent. In fact both the measured linewidth and the shift of the phase difference peak are larger than expected from the micromagnetic simulation. To reproduce the observed linewidth it is necessary to increase the Gilbert damping parameter from a value of 0.01 that is typical for Permalloy to a value of about 0.03, which may be explained by increased two magnon scattering from imperfections at the edges of the disc. Within the macrospin simulation the observed phase peak shift requires the coupling parameter β to be an order of magnitude larger than estimated for a pair of point dipoles located at the position of maximum mode amplitude within each disc. The enhanced coupling may also be a consequence of the nanofabrication process, for example if ion milling leads to a reduction of the exchange parameter at the edges and hence to increased mode amplitude in these regions. Other features of the experimental data lend support to this idea. While the amplitude of the edge mode in the micromagnetic simulations is much smaller than that of the centre mode, the measured spectra show that the two modes in fact have similar amplitude. Modification of the magnetic parameters may also modify the spatial profile of the centre mode with enhanced dipolar coupling being mediated by increased amplitude close to the edges of the element.

5.6 Summary

It has been demonstrated that measurements of the phase of centre and edge modes within each of a pair of nanoscale discs can be used to separate the weak dynamic dipolar interaction from the stronger static interaction and the effects of structural and magnetic imperfections. The method use to isolate the dynamic dipolar interaction could equally well be applied to nanomagnets coupled by other mechanisms, such as the flow of spin current, or for that matter any system of coupled oscillators.

Our results show that the dynamic coupling exhibits a strong dependence on static bias field and that a judicious choice of centre or edge mode excitation may be required if dipolar interactions are to deliver either the formation of collective modes within magnonic crystals or the non-linear phase-locking of spin transfer oscillators for wireless microwave applications. The observation of a dynamic interaction larger than that expected for a pair of ideal homogeneous discs gives impetus to the characterization of local magnetic properties at the deep nanoscale and suggests that enhanced dipolar coupling may be achieved by engineering the spatial variation of magnetic properties, particularly within edge regions.

Chapter 6

Time resolved scanning Kerr microscopy of the vector magnetisation within hard disk writer structures

6.1 Introduction

The storage capacity of magnetic disk drives continues to increase through reduction of bit sizes, presenting challenges in the design of the writer structure. Smaller bits demand either narrower switching field distributions or smaller grain sizes to minimize transition noise. Smaller grain sizes require increased magnetic anisotropy so that the written bits are stable at the operating temperature. The writer used in the latest perpendicular recording technology is essentially a planar electromagnet with one wide and one narrow pole piece. It must produce increased fields, confined within an ever-smaller write bubble at the narrow pole tip, that fall and rise on picosecond timescales. It is essential to characterize the magnetisation dynamics in all parts of the writer if optimum performance is to be obtained.

Measurement techniques such as magnetoresistive sensing[141], magnetic force microscopy (MFM) [142, 143, 144], and time resolved scanning Kerr microscopy (TRSKM)[145,146] have been used to characterize magnetisation processes within the writer. Previous studies have concentrated almost exclusively upon the pole tips and have considered only a single component of the magnetisation or the associated internal field [147, 148, 149, 150]. However the response of the yoke is also of vital importance in maximizing the write field and minimizing the remanence of the pole tips that can lead to problems such as "erase after write". The remanence of the pole tip is influenced by both the geometry of the pole tip and residual flux from the yoke[151]. One strategy for the reduction of remanent magnetisation is to use laminated structures, in which non-magnetic layers break the ferromagnetic coupling within the stack, so that dipolar interactions induce antiparallel alignement in successive ferromagnetic layers[152,153,154]. Residual flux results from the domain configuration within the yoke when the drive current is switched off and depends upon the shape, size and composition of the yoke. Domains with magnetisation parallel to the length of the pole tip are required to enhance the write field, but domains with magnetisation perpendicular to the pole tip deliver the minimum residual flux.

So far no direct measurements of the magnetisation dynamics within the yoke have been reported. It will be demonstrated that TRSKM can yield simultaneous measurements of all three spatial components of the dynamic magnetisation with sub-micron spatial resolution. Time resolved magnetic images provide experimental confirmation of the previously predicted process of "flux-beaming" in which the magnetisation of the yoke material reorients most strongly along the symmetry axis (SA) of the yoke and pole piece.

6.2 Experimental details and device description

Stroboscopic TRSKM measurements are made with an ultrafast laser that generates optical pulses of 80 fs duration and 800 nm wavelength at a repetition rate of 80 MHz, as shown in Figure 6.2.1. Part of the laser output is passed through an optical delay line, with maximum delay of 4 ns, and focused by a high numerical aperture (0.85, x60) microscope objective to a full width half maximum spot size of 600 nm diameter, polarized along the writer SA. The back-reflected beam is directed into a quadrant photodiode polarisation bridge detector[155] that records all three spatial components of magnetisation simultaneously.

A second part of the laser output is collected by a fast photodiode, converted to a transistor-transistor logic (TTL) pulse and used to trigger a digital delay generator (Stanford Research Systems SRS DG645) that triggers the pulse generator (Avtech AVP-AV-HV3-C) used to drive the writer. Due to the limited repetition rate of the delay and pulse generators, and to ensure that the yoke relaxes fully after each pulse, a pulse picker reduces the laser repetition rate to 1 MHz. Due to electronic delay within the pulse generator, the delay generator is used to synchronize the arrival of the electrical pulse triggered by the *n*th optical pulse with the arrival of the *n*+1st optical pulse at the writer. The electrical pulse is delivered by a high frequency probe to a 6 mm long coplanar strip transmission line deposited on the wafer that is connected to the inductive coil of the writer. The transmission line has characteristic impedance greater than 50Ω, leading to partial reflection of the pulse waveform within the cabling. A 50 GHz sampling oscilloscope is used to characterize the pulse waveform before the writer, and to monitor its form continuously after reflection from the writer via a directional coupler.

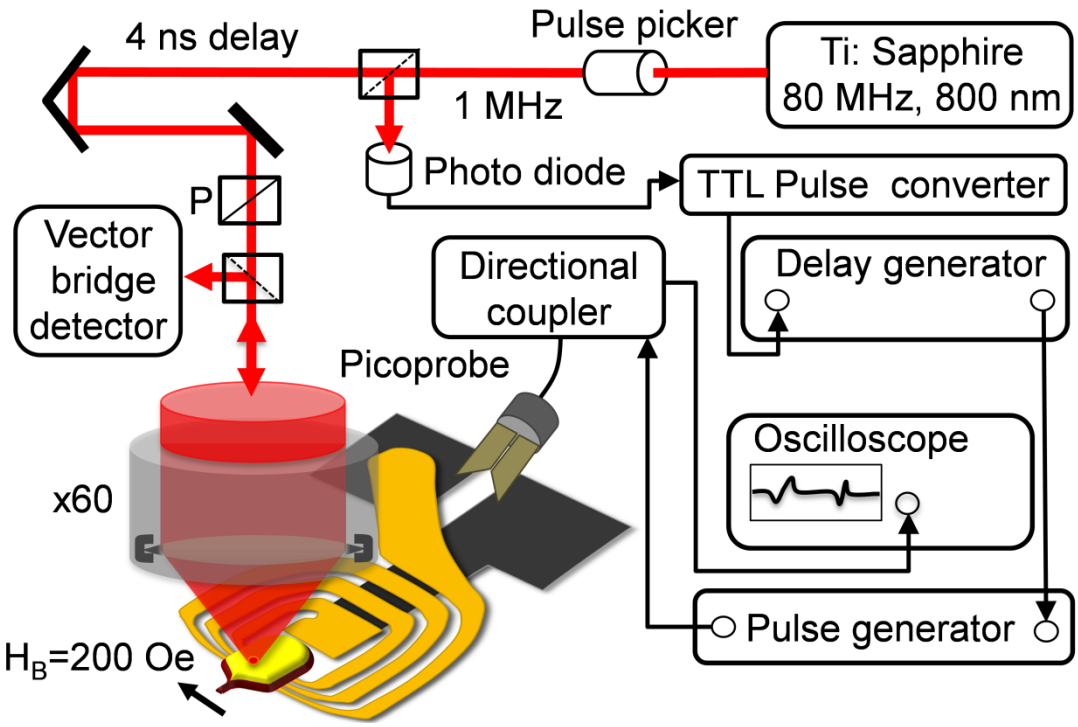

Figure 6.2.1 The time resolved scanning Kerr microscope setup for measurements of magnetisation dynamics within perpendicular inductive write-head structures. P: polarizer.

The amplitude of the pulse train is modulated at audio frequency so that the components of the dynamic magnetisation are recorded using three separate lock-in amplifiers. Measurements were made on a writer with a three turn coil and a single layer CoFe yoke of 200 nm thickness. The yoke had the geometry shown in Figure 6.2.2(a) with paddle width (PW) of 6.3 µm, bridge length (BL) of 2 µm, bridge width (BW) of 0.4 µm, and flare angles FA1 and FA2 of 30^o and 62^o respectively. The writer was magnetized perpendicular to its symmetry axis by an external bias field $\mathbf{H}_B$ of 200 Oe. This configuration is relevant to the performance of multilayered yoke materials that may in principle contain interlayer exchange coupling, exchange bias, or an easy anisotropy axis parallel to the y-axis. The in-plane components of magnetisation (parallel and perpendicular) have been defined with respect to the bias field $\mathbf{H}_B$ direction while the polar component lies parallel to the z-axis, perpendicular to the plane. Measurements were made for pulse amplitudes up to the 34.2V maximum output of the pulse generator. For amplitudes greater than 11.2 V, the time resolved Kerr signal was irreproducible, presumably due to irreversible magnetic processes within the yoke.

The majority of measurements were therefore made with 11.2 V amplitude, 1.6 ns pulse width, and rise time of 553±29 ps (including overshoot) as shown in Figure 6.2.2 (c).

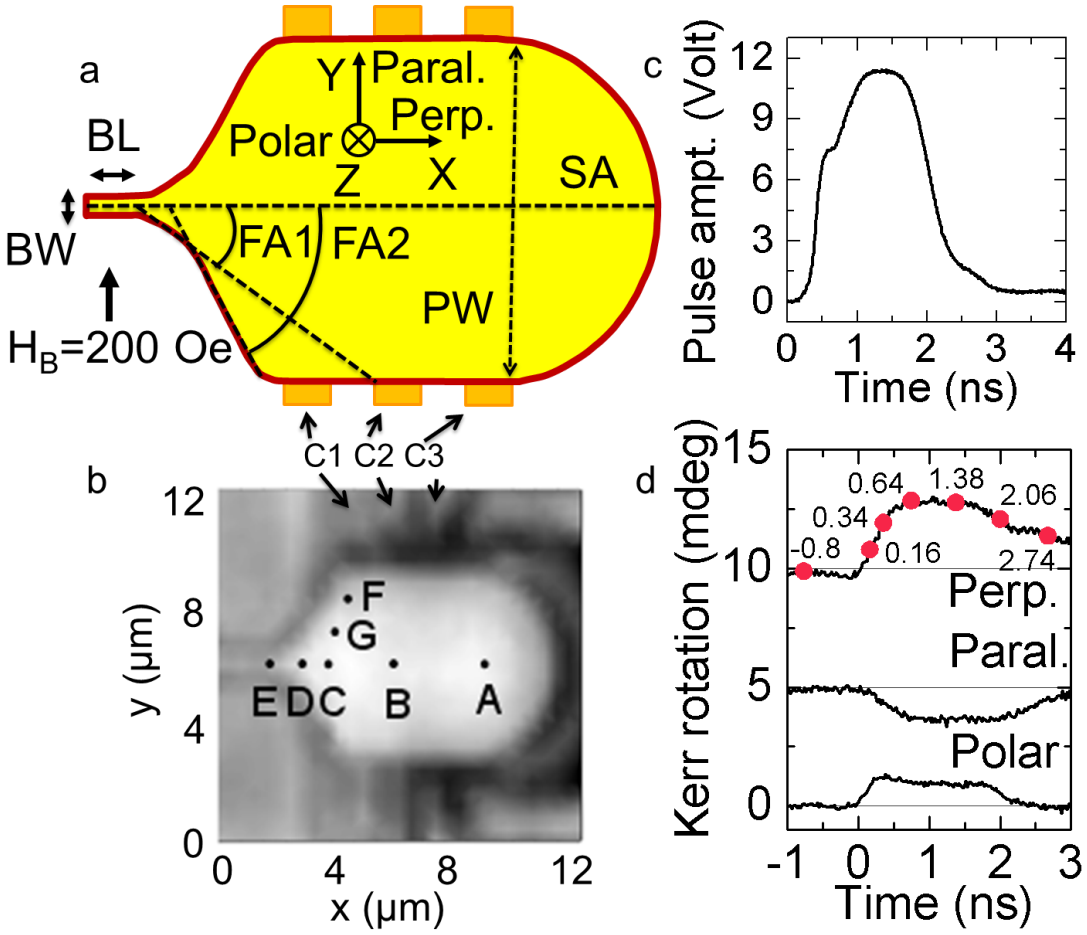

Figure 6.2.2 (a) Schematic layout of the write head structure, (b) reflectivity image acquired by TRSKM defining positions A-F where TR Kerr signals were acquired, (c) pulse waveform acquired immediately before the device, and (d) TR Kerr signal acquired from position B. The points highlighted on the Perp. component curve correspond to time delays at which magnetic images were acquired. PW: paddle width, BW: bridge width, BL: bridge length, SA: symmetry axis, FA1, 2: flare angle1 and 2, and C1,2,3: coil winding1, 2, and 3.

The pulsed field was estimated to have maximum possible value of ~90 Oe immediately above the coil windings, although this value is uncertain due to possible impedance mismatches within the microwave circuitry. The writer position was controlled with a 3-axis piezoelectric scanning stage that allowed signals to be acquired at selected positions for a range of time delays, or for images of the dynamic magnetisation to be acquired at a fixed time delay.

6.3 Result and discussion

The selected measurement positions are shown in Figure 6.2.2 (b). On the axis of symmetry, point A lies above the via to the lower half of the yoke, B is above the center coil winding 'C2', C is immediately to the left of winding 'C1', D lies within the confluence region while E is at the beginning of the bridge. Points G and F lie on the edges of the flared region. Since the coil windings lie orthogonal to the symmetry axis of the yoke as they pass beneath its upper half, the generated magnetic field lies close to in-plane and parallel to the symmetry axis for positions above the coil windings, and perpendicular to the plane at positions to the side of the windings. Prior to the application of the pulse, the magnetisation lies predominantly in the direction of the bias field, parallel to the y-axis. Therefore the initial torque exerted by the pulsed field lies perpendicular to the plane at locations above the coil windings and parallel to either the positive or negative x-axis to the side of the windings. Consequently, at point B in Figure 6.2.3 the polar magnetisation component has a much shorter 10-90 percent rise time of 217±9 ps compared to those of 472±29 ps and 523±26 ps for the perpendicular and parallel components respectively, which are instead comparable to the rise time of the pulsed field. The polar component decreases but remains finite even after the in-plane components have reached constant values, suggesting that there is a small out of plane component of the pulsed field at point B. The signals are presented in units of optical rotation and the in-plane and polar signals appear to be of similar magnitude. However the polar Kerr effect is typically an order of magnitude larger than the longitudinal Kerr effect, so the polar magnetisation component is very likely an order of magnitude smaller than the in-plane components.

Figure 6.2.3 also shows that outside the coil region the rise times of the perpendicular and polar magnetisation components are either comparable to or longer than that of the pulsed field, while the amplitude and rise time of the parallel component is more variable. The polar component follows both the rise and fall of the out of plane driving field. In contrast, the in-plane components experience an additional driving field resulting from the magnetic charge generated as the magnetisation reorients above the coil windings. It seems reasonable that the in-plane magnetisation at points A and C-G should lag that at B. Interestingly the perpendicular component does not fall with the pulsed field and does not fully relax during the 4 ns scan period.

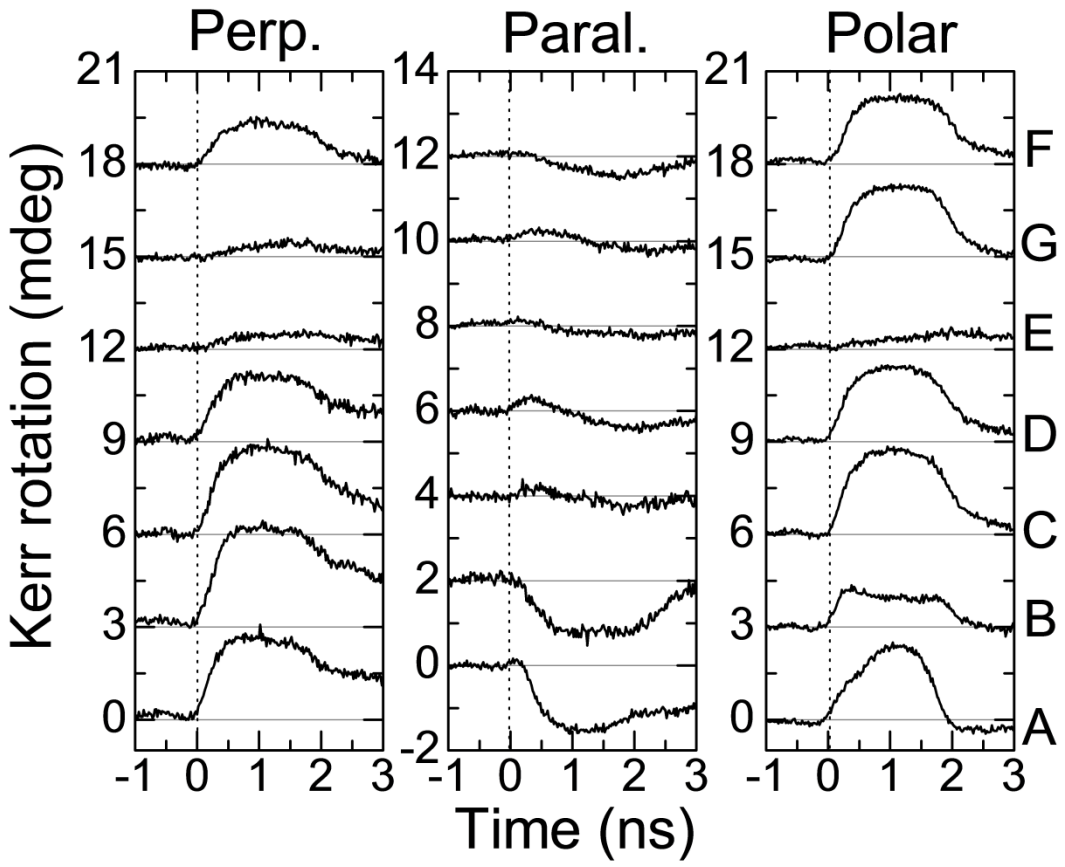

Figure 6.2.3 TR Kerr signals of three components of magnetisation (Perpendicular, Parallel and Polar) at positions A-F shown in Figure 6.2.2 (b).

The small amplitude of the parallel component at positions C, D and G, where the perpendicular component is large, suggests the presence of a finer scale magnetic structure so that the probe spot acquires a spatially averaged signal from regions of anti-parallel magnetisation. The reduced amplitudes of all three components at point E may be related to the fact that the bridge width is smaller than the focused spot size, with an increased susceptibility to mechanical drift, and because of surface topographical variation towards the pole tip so that the focus of the probe spot is less optimal than for the main yoke structure. At points F and G the static magnetisation is expected to be non-uniform due to competition between the bias field and demagnetizing fields associated with the edges. Spatial averaging may again lead to a reduced parallel component while the perpendicular component may tend to be suppressed because the demagnetizing fields prevent the magnetisation aligning normal to the flared edge under the action of the pulsed field.

Figure 6.2.4 shows sets of dynamic magnetic images, together with static reflectivity images, acquired at the time delays indicated in Figure 6.2.2 (d). The contrast for a particular magnetisation component is normalized to the maximum Kerr amplitude observed for that component within the series. The perpendicular and polar images at -0.8 ns show no magnetic contrast as expected. The weak vertical stripes observed for the parallel component might indicate some very slow magnetic process associated with the previous field pulse, but the contrast extends outside the area of the yoke and so is most likely the result of topographic variation above the coil windings combined with mechanical vibration resulting from the modulation of the driving waveform. As the pulse begins to rise at 0.16 ns delay, the perpendicular component rises in the centre of the yoke, close to the symmetry axis and above the coil windings while the polar component rises more uniformly.

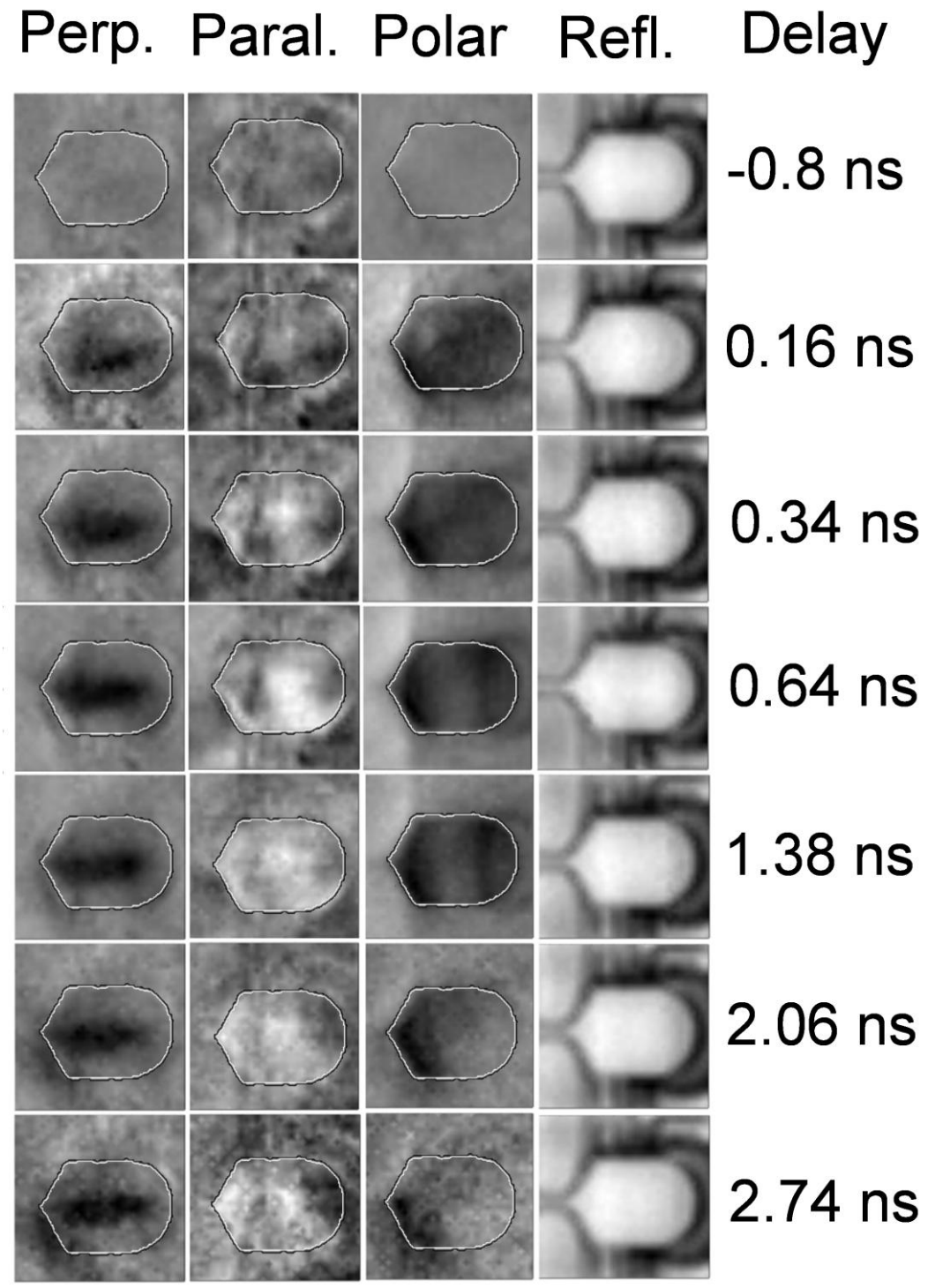

Figure 6.2.4 TR images for three components of the dynamic magnetisation. The contrast for a particular component is normalized to the maximum Kerr amplitude observed for that component within the series. Black/white corresponds to -/+ *z*-direction, -/+ *x*-direction, and +/- *y*-direction for the Polar, Perpendicular, and Parallel components, respectively. Black (white) denote positive (negative) Kerr amplitude.

The most striking feature of the presented images Figure 6.2.4 is the localization of the perpendicular magnetisation component, along the symmetry axis of the yoke and its propagation into the confluence region where it presumably magnetizes the bridge region. These images provide direct experimental confirmation of the "flux beaming" that has been proposed to explain the operation of the yoke[156,157]. The beaming of the magnetic flux along the symmetry axis occurs because the magnetisation at the edges of the yoke is less able to rotate in response to the pulsed field since this would induce magnetic charges at the edges and hence additional demagnetizing fields. A well optimized yoke is designed to spread the magnetic flux into a wider path, when moving from the confluence region past the coil windings towards the back via, so as to retain high permeability, avoid saturation and minimize the time for magnetisation rotation. Although the flux spreading appears greatest within the confluence region for the single layer yoke studied here, the geometry of the spreading may be controlled in laminated yokes with carefully chosen magnetic anisotropy.

The investigation was then extended to measurements made with both a lower step pulse amplitude and a longer pulse duration on the same writer structure. The experimental geometry and the external bias field direction were kept the same as for the 11.2 V pulse amplitude excitation study detailed previously. The pulse had a 2.59 V peak amplitude, a 120 ps rise time and a 8.25 ns pulse width. The input pulse waveform acquired by the oscilloscope is shown in Figure 6.2.5 (a). A time resolved signal acquired from position B is shown in Figure 6.2.5 (b). The rise time, defined as the time taken for each of the perpendicular, parallel and polar components to rise from 10% - 90% of their maximum value, was found to be 420 ps$\pm$17 ps, 410 ps $\pm$48 ps and 407 ps $\pm$17 ps respectively. Interestingly the difference in rise time between the three different components was small compared to that observed when measurements were made with a 11.2 V amplitude pulse (Figure 6.2.2 (d)). A time resolved Kerr signal acquired from a region directly above the centre coil at position B, shows that the perpendicular component yield a larger Kerr rotation signal than either the parallel or polar component. This provides an indication that flux beaming occurs when the write head structure is excited in this manner. A delay in the response of the magnetisation to the excitation is observed for the case of the parallel component, indicating that the deflection of magnetisation first occurs in the polar and

perpendicular directions. Due to the longer pulse duration, the relaxation time of the magnetisation is longer than that observed when using the 11.2 V pulsed excitation. Dynamic magnetic images were acquired for all three components of the magnetisation at different time delays. The relative time delay position is taken from the time resolved Kerr signal at position B.

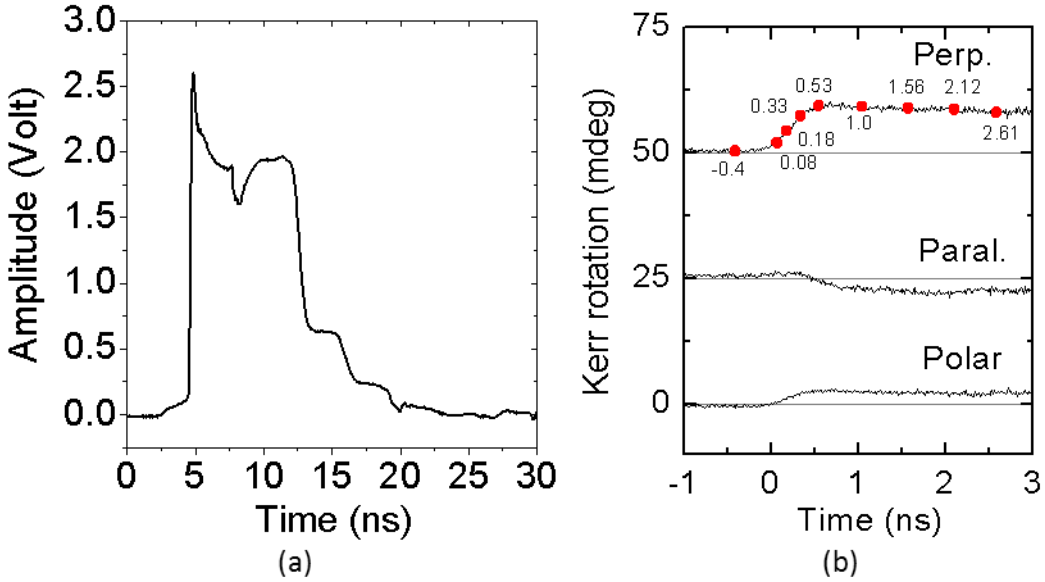

Figure 6.2.5 (a) Pulsed waveform acquired immediately before the device on a fast oscilloscope, and (b) A TR Kerr signal acquired from position B, directly above the writer coils.

The time at which dynamic images were acquired is indicated by the red dots in Figure 6.2.5 (b). The images acquired at negative delay, do not contain any magnetic contrast. These images confirm that the magnetic ground state is fully relaxed before the pulsed excitation arrives at zero delay. The dynamics are observed to start at 0.08 ns in the centre coil region and the via between the top and bottom yoke as shown in Figure 6.2.6. Later the change in the perpendicular component is seen to extend toward the confluence region.

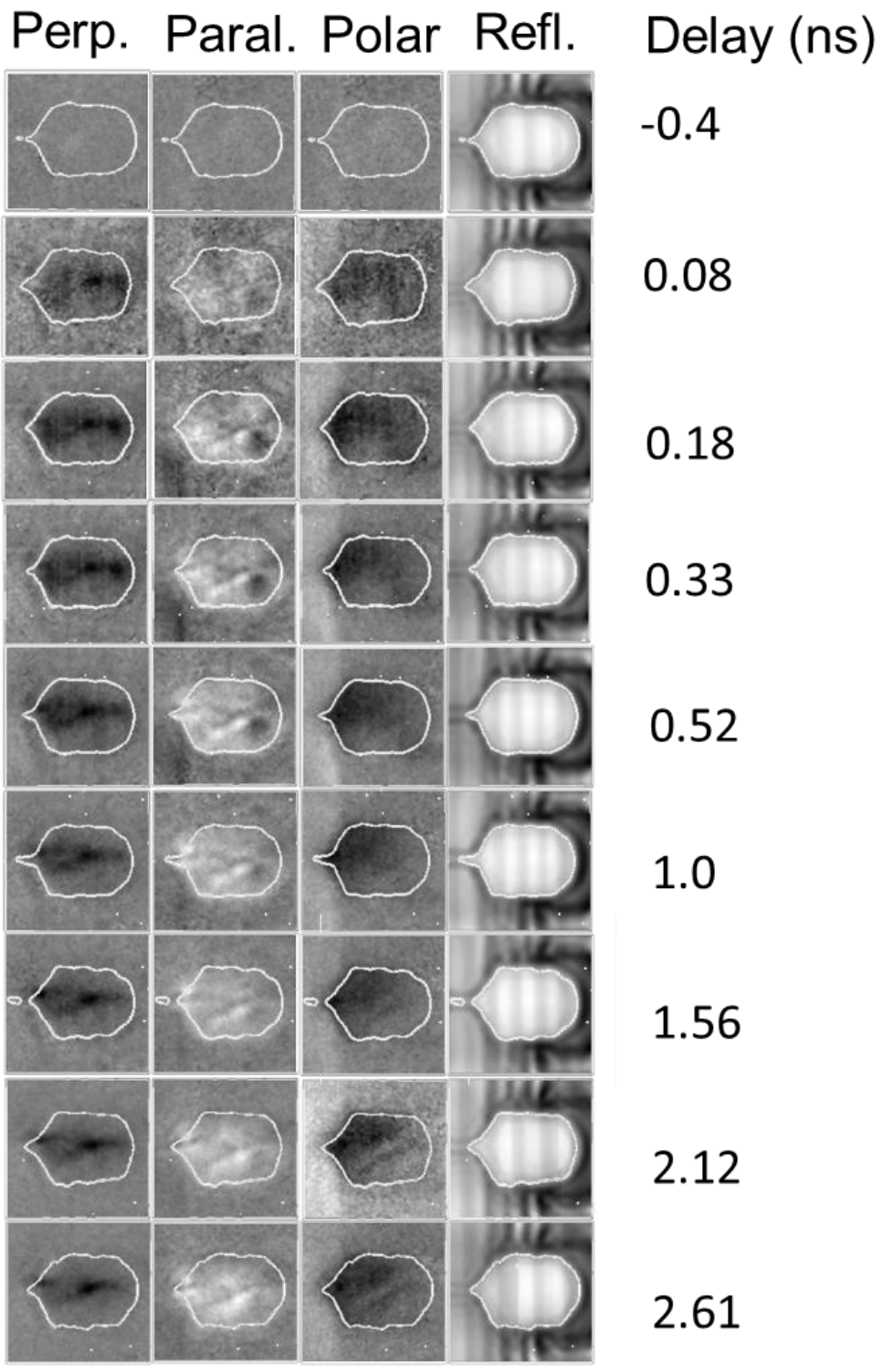

Figure 6.2.6 TR images for three components of the dynamic magnetisation. The contrast for a particular component is normalized to the maximum Kerr amplitude observed for that component within the series. Black/white corresponds to -/+ *z*-direction, -/+ *x*-direction, and +/- *y*-direction for the Polar, Perpendicular, and Parallel components, respectively. Black (white) denote positive (negative) Kerr amplitude.

The maximum spreading of the flux associated with the perpendicular component again occurs in the confluence region between 0.18 ns to 0.52 ns. It can be seen that the perpendicular and parallel components are not symmetric about the symmetry axis of the writer head. The reason for the asymmetry is unknown but presumably is related to the ground state. The polar component has maximum contrast within the confluence region and pole tip. The magnetic contrast for the perpendicular component starts to disappear at the confluence region from 1 ns onwards. Again the contrast is asymmetric above the symmetric axis of the writer both in the centre coil region and the pole tip. The parallel component has a similar spatial distribution but with opposite contrast to the perpendicular component. The polar component does not show a strong variation in contrast during the dynamic image series.

The dynamic image series taken with the 11.2 V pulse excitation shows a greater degree of homogeneity along the symmetry axis within the confluence region than the images taken with a 2.59 V pulsed excitation. We conclude then that there is a threshold value of the driving current amplitude required to overcome inhomogeneities in the magnetic ground state, rotate the magnetisation coherently along the symmetry axis, and provide clear flux beaming.

6.4 Summary

In summary, TRSKM has been used to characterise the magnetisation dynamics of partially built hard disk writer structures. The response times of the three different magnetisation components at different locations have been related to the orientation of the static magnetisation, the torque generated by the coil windings and the propagation of flux through the yoke and pole piece. Flux-beaming within the yoke has been confirmed, demonstrating that TRSKM is a powerful tool for the optimisation of flux propagation within advanced writer head design. The flux beaming was found to have a non-linear dependence upon the amplitude of the pulsed field. The pulsed field must exceed a certain threshold before homogeneous magnetisation rotation occurs within the confluence region.

Chapter 7

Thermal and spin transfer torque excitation of precessional modes in the noise spectra of magnetic tunnel junction recording head sensors

7.1 Introduction

The discovery of Giant Magnetoresistance (GMR)[58] and Tunnel Magnetoresistance (TMR)[67] has resulted in an intensive research effort being focused on the development of devices utilizing such effects for data storage. Spin Transfer Torque (STT) induced magnetisation precession has been intensively studied both theoretically[69,70,158,159] and experimentally[75,160,161,162] in GMR and TMR based devices. There are two possible ways in which STT is used to manipulate the local magnetisation of the free layer by injection of a spin polarized current. The STT can switch the magnetisation state of the free layer between two metastable states which has lead to the development of new forms of data storage such as STT-RAM. Alternatively one can exploit the precession of the magnetisation in the auto-oscillation regime for microwave generation, where prospective devices could be used in new forms of telecommunication.

There are however lots of challenges encountered when attempting to use STT oscillators in real world systems. For example the current level of power output would have to be increased significantly for this fledgling application to take off. In some aspects of device design STT is a hindrance to performance rather than an effect to be utilized. In sensor heads for example, STT is a source of noise during the reading process with a DC current[163] bias. In most studies to date, the orientation of the applied field, **H,** has been set parallel to the easy axis of the free layer magnetisation. However, it was recently shown that the amplitude of the STT induced microwave emission from GMR and TMR nanopillars can be increased by rotating **H** away from the easy axis of the device[161,164]. In this thesis chapter the response of TMR type nanopillars has been studied as a function of the angle between **H** and the easy axis (ϕ_H). As ϕ_H is increased the initial STT and the resistance gradient, dR/dH, also increase. The noise associated with Thermal Magnetic Fluctuations (TMF), also known as mag-noise[165], is more prevalent in devices with higher TMR. The noise amplitude is also proportional to dR/dH[166] so that a number of additional modes

appear in the microwave spectrum as ϕ_H is increased. Although in general all modes are thermally excited ferromagnetic resonance modes, with careful consideration of the dependence of the frequency, full width half maxima (FWHM) and amplitude of the modes upon the field strength H and the current I, modes dominated by STT may be reliably identified. It is also possible to see the effect of shape irregularity by means of the randomization of edge mode frequency with respect to ϕ_H.

7.2 Sample and experimental details

TMR pillars of 100 nm by 300 nm elliptical cross section and 150 nm circular cross section were studied. The thin film stack/IrMn(6.0)/CoFe(2.1)/Ru(0.8)/CoFe(1.2) /Ta(0.15)/CoFeB(1.5)/MgO(0.5)/CoFeB(2.2)/Ta(0.2)/NiFe(6.5)/Ru(1.5)/Ta(10.0)/Ru(5.0)(thick-nesses in nm), in which the fixed and reference layers were antiferromagnetically coupled through a thin Ru spacing layer, was deposited on top of AlTiC substrate. A schematic of the stack is shown in Figure 7.2.1. The magnetic tunnel junctions studied in this chapter were fabricated by collaborators at Seagate Technology, 1 Disc Drive, Springtown Industrial Estate, Derry, Northern Ireland. The stack is similar to that in reference[164] except that the free layer is thicker and of bilayer composition in the present case. The samples were field annealed to set the direction of the exchange bias (easy axis). The long axis of the 100x300 nm^2 element was parallel to the intended exchange bias direction.

In this study negative current corresponds to electrons moving from the reference to the free layer, which favours parallel alignment. The pillar was defined between crossed electrodes with contact pads as shown in Figure 7.2.2 (a) onto which high frequency picoprobes were landed. A DC current source was connected to the input pads. A bias-tee was connected to the output pads and used to take the AC output of the nanopillar to a 50 GHz Agilent E4448A spectrum analyzer. The experimental set up is shown in Figure 7.2.3. The DC-magnetoresistance (MR) was measured simultaneously in a 4-point-probe configuration with a nanovoltmeter connected to the DC port of the bias-tee. A background microwave spectrum was acquired at I = 0, H = 0 and was then subtracted from each individual spectrum that was taken during a current or field swept experiment. The full width half maximum (FWHM) and amplitude of the peaks were determined by fitting to symmetric Lorentzians (see Figure 7.2.2 (b) for a typical spectrum).

Some groups have reported that the bias dependence of the out-of-plane component of the STT is quadratic in the DC current for symmetric MTJs[167,168,169,170,171]. However theory[172] also predicts that breaking the symmetry of the system leads to an additional linear dependence[177,173,174,175] that may become dominant. The devices we studied are asymmetric MTJs, so we expect to see a linear dependence of the out-of-plane STT upon bias current, and are unable to distinguish any quadratic component from the effects of heating. Therefore a quadratic background was subtracted from the frequency shift observed for the 1st mode in both MTJ2 and MTJ3 in order to isolate the linear out-of-plane STT component.

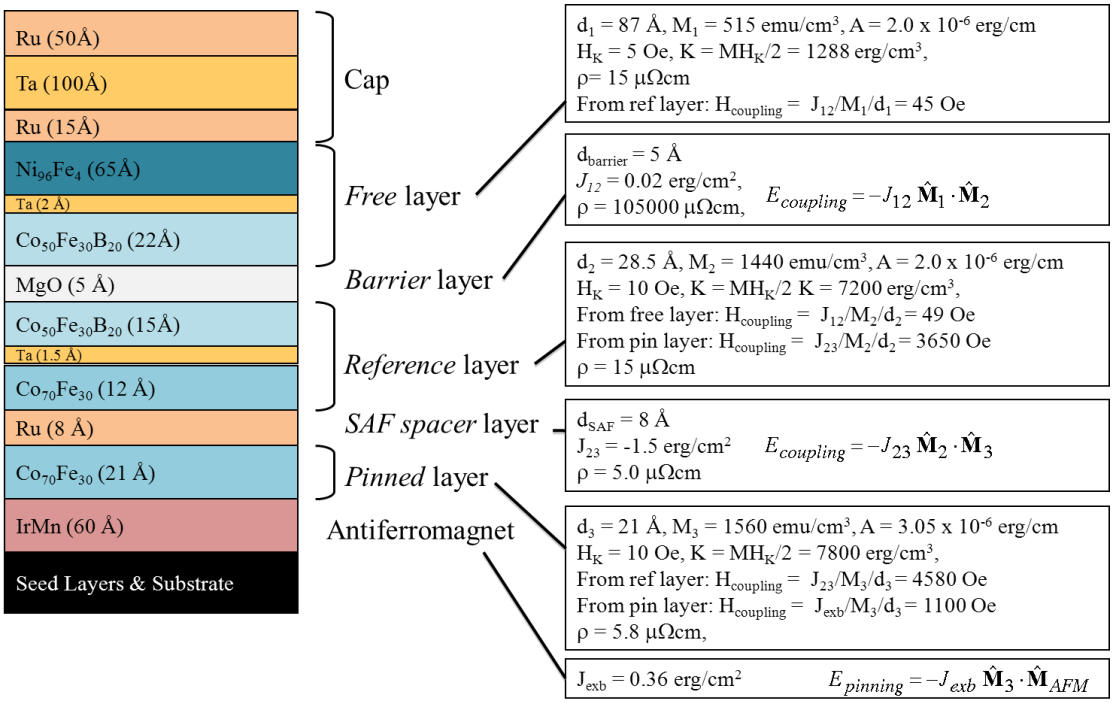

Figure 7.2.1 Schematic of sample stack of MTJs showing the relevant parameters for each layer and the coupling between various interfaces. The parameters are defined as follows. d_1: thickness of composite free layer, d_2: reference layer thickness, $d_{barrier}$: barrier layer thickness, d_{SAF}: SAF spacer layer thickness, d_3: pinned layer thickness, A: exchange constant, H_K: anisotropy field, K: uniaxial anisotropy constant, ρ: resistivity, J_{12}: exchange coupling constant between free layer and reference layer, J_{23}: exchange coupling between reference layer and pinned layer, J_{exb}: exchange bias energy constant from pinned layer, M_1: free layer saturation magnetisation, M_2: reference layer saturation magnetisation, and M_3: pinned layer saturation magnetisation.

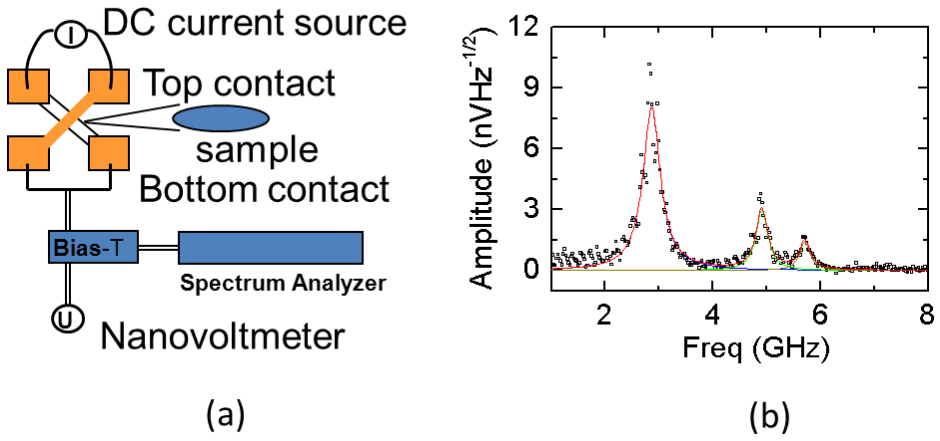

Figure 7.2.2 (a) The experimental configuration used to make a four probe contact, and (b) Typical spectra from a 150 nm circular MTJ for ϕ_H=40°, H=200 Oe and I=-3mA.

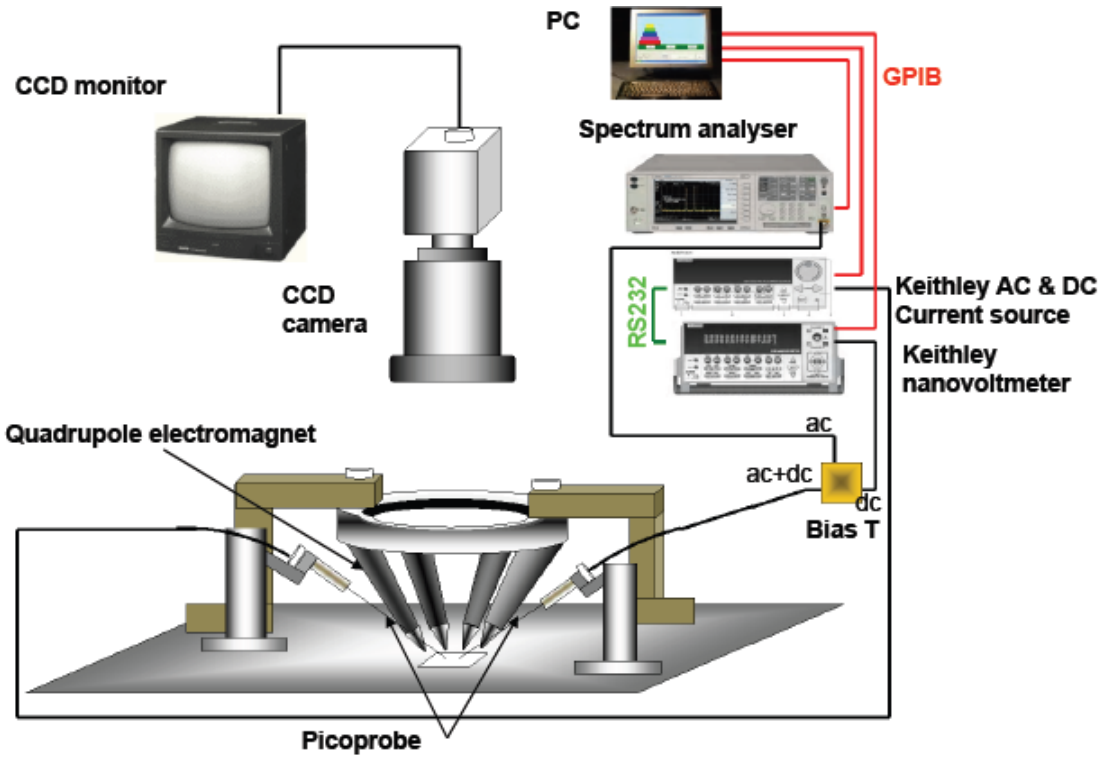

Figure 7.2.3 The experimental setup developed to make four probe contact measurements on MTJs.

7.3 Results and discussions

The measurements described in this chapter were performed on a wide range of devices; 26 elliptically shaped devices of 100x300 nm^2 size, 16 circular devices of 150 nm diameter and 1 elliptical device of 100x70 nm^2 size, the smallest devices being much more susceptible to breakdown than the others. It was found that the

devices could be divided into four different groups characterized by their combination of either a high or low parallel state resistance with either a high or low TMR value. This section will discuss the distribution of devices between these groups and the associated dynamic behavior of each of the four groups. Within the experimental setup already described a positive current is associated with the flow of electrons from the free layer to the reference layer, which favours an anti-parallel alignment of the free and the reference layer magnetisations. MR loops were acquired by sweeping the external magnetic field whilst applying a 0.1 mA DC current bias. Scatter plots of parallel state resistance $R_{\parallel}$ vs TMR is shown in Figure 7.3.1. From the scatter plots four regions can be identified in which the TMR and $R_{\parallel}$ (or equivalently the resistance area product $R_{\parallel}A$) each have High (H) and Low (L) values i.e. HH, HL, LH and LL. More than 85% of the devices tested have high TMR, whilst the LH combination was observed only once and so will not be discussed further.

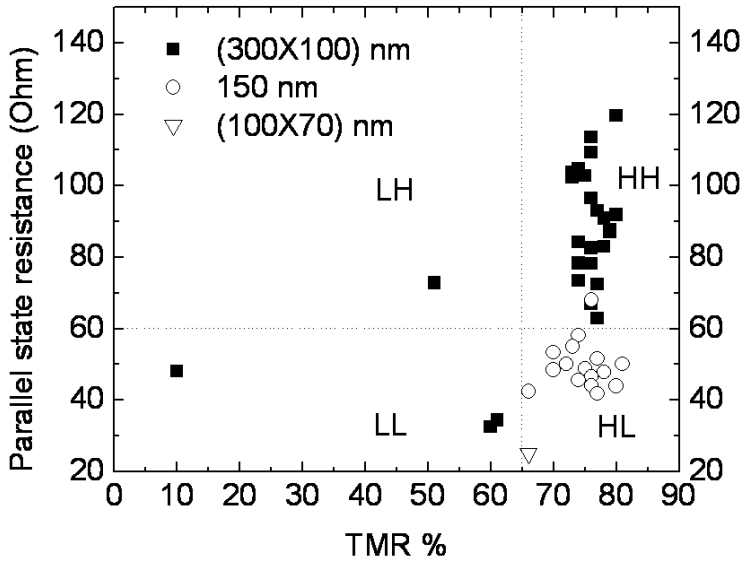

Figure 7.3.1 Scatter plots of parallel state resistance $R_{\parallel}$ vs TMR %. Where; HH: high $R_{\parallel}$ high TMR, HL: high $R_{\parallel}$ low TMR, LH: low $R_{\parallel}$ high TMR and LL: low $R_{\parallel}$ low TMR.

A frequency distribution bar graph for the observed modes at angles of 10^{o}, 40^{o}, 70^{o} and 90^{o} (hard axis) is shown in Figure 7.3.2 for 26 elliptically shaped MTJs of 100x300nm size (top) and 16 circular MTJs of 150nm diameter (bottom). This frequency distribution bar graph is extracted from field swept spectra at a bias field of 200 Oe and a -3mA bias current for both device types. The 150 nm MTJs have 3 modes for a given ϕ_H whereas the 100x300 nm MTJs were observed to have a

maximum of four modes. The frequency distribution of the 1st and 2nd modes is broader than that of the 3rd mode for both the 150 nm and 300x100 nm MTJs. A frequency shift from high to low frequency values is seen as the orientation of the bias field changes from 10° to 90° relative to the easy axis for the 1st (black line) and 2nd (red line) modes observed in the 100x300 nm MTJs. This may be due to the elliptical shape anisotropy.

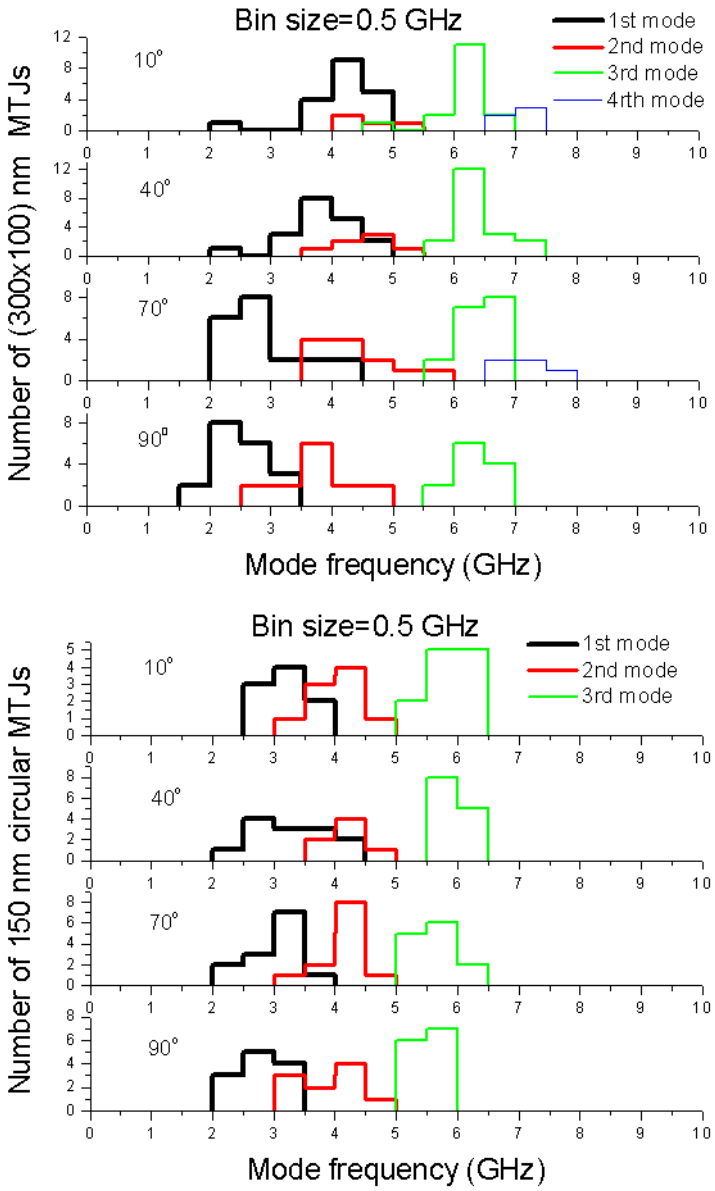

Figure 7.3.2 A frequency distribution bar graph for 26 elliptically shaped MTJs of 100x300 nm size (top) and 16 circular MTJs of 150 nm diameter for ϕ_H values of 10°, 40°, 70° and 90° (hard axis).

The frequency distribution of the 3rd mode (green line) was not observed to undergo a shift in frequency. The frequency shift is much weaker in the 150 nm MTJs than that observed in the 100x300 nm MTJs due to the absence of shape anisotropy. However, a shift to lower frequency for all three modes was seen to occur for the 150 nm MTJs. This may be due to stray field coupling from the reference layer to the free layer. From micromagnetic simulations it was deduced that the two modes of lowest frequency are edge modes and the 3rd mode is a higher order mode.

The microwave output of the devices was recorded with a -3mA DC current bias as an external bias magnetic field was swept from 0 Oe to 600 Oe to -600 Oe to 600 Oe and back to 0 Oe. The bias field was applied in the plane of the device and was rotated in 10° steps away from the easy axis, and therefore towards the hard axis. Further measurements were made by sweeping the current from -3mA to + 3mA in 0.05mA steps in the presence of a constant applied magnetic field. The magnetic field value for the current sweeps was chosen so that the maximum number of modes was visible during the current sweep: 290 Oe for a 100 nm x 300 nm MTJ; and 200 Oe for a 150 nm diameter MTJ. Two devices from the 150 nm circular MTJs which fell into the high TMR% and low $R_{\|}$ (low $R_{\|}A$) bracket and one device from the 300x100 nm MTJs that fell into the high TMR% and high $R_{\|}$ (high $R_{\|}A$) were selected for intensive characterization of the excited modes. In all following discussion the 150 nm circular MTJs having TMR ratio 70% and 76% will be referred to as MTJ1 and MTJ2 respectively. The 300x100 nm elliptical MTJ having a TMR ratio of 76.4% will be referred to as MTJ3. The field needed to switch the free layer magnetisation from parallel (antiparallel) to antiparallel (parallel) alignment with the reference layer magnetisation, and the dipolar coupling field extracted from easy axis (EA) MR loops are tabulated in Table 7.3.1.

Device notation	MTJ dimension (nm)	$R_{\parallel}$ (Ohm)	TMR %	$H_{\uparrow\uparrow\rightarrow\uparrow\downarrow}$ (Oe)	$H_{\uparrow\downarrow\rightarrow\uparrow\uparrow}$ (Oe)	Dipolar coupling (Oe)
MTJ1 (circular)	150 nm	44.26	70	40	40	40
MTJ2 (circular)	150 nm	49.66	76.6	66	13	40
MTJ3 (elliptical)	300x100 nm^2	82.66	76.4	62	12	37

Table 7.3.1 The switching field and dipolar coupling field extracted from easy axis MR loops on several MTJs. $H_{\uparrow\uparrow\rightarrow\uparrow\downarrow}$: field required to switch from parallel to antiparallel and $H_{\uparrow\downarrow\rightarrow\uparrow\uparrow}$: field required to switch from antiparallel to parallel.

MR loops (1st column) and the corresponding field swept frequency spectrum (2nd column) and current swept frequency spectrum (3rd column) for each ϕ_H for MTJ1, MTJ2 and MTJ3 are shown in Figures (7.3.3, 7.3.4, and 7.3.5) respectively. A positive (negative) field direction has a high (low) magnetoresistance value which suggests that a positive field will force the free layer and the reference layer into a state of antiparallel alignment. A reduction in the height of the MR loop as the external bias field direction tends towards the hard axis also suggests that the free layer magnetisation is following the external bias field direction which is then no longer aligned parallel or antiparallel with the reference layer except when the external bias field is applied along the EA.

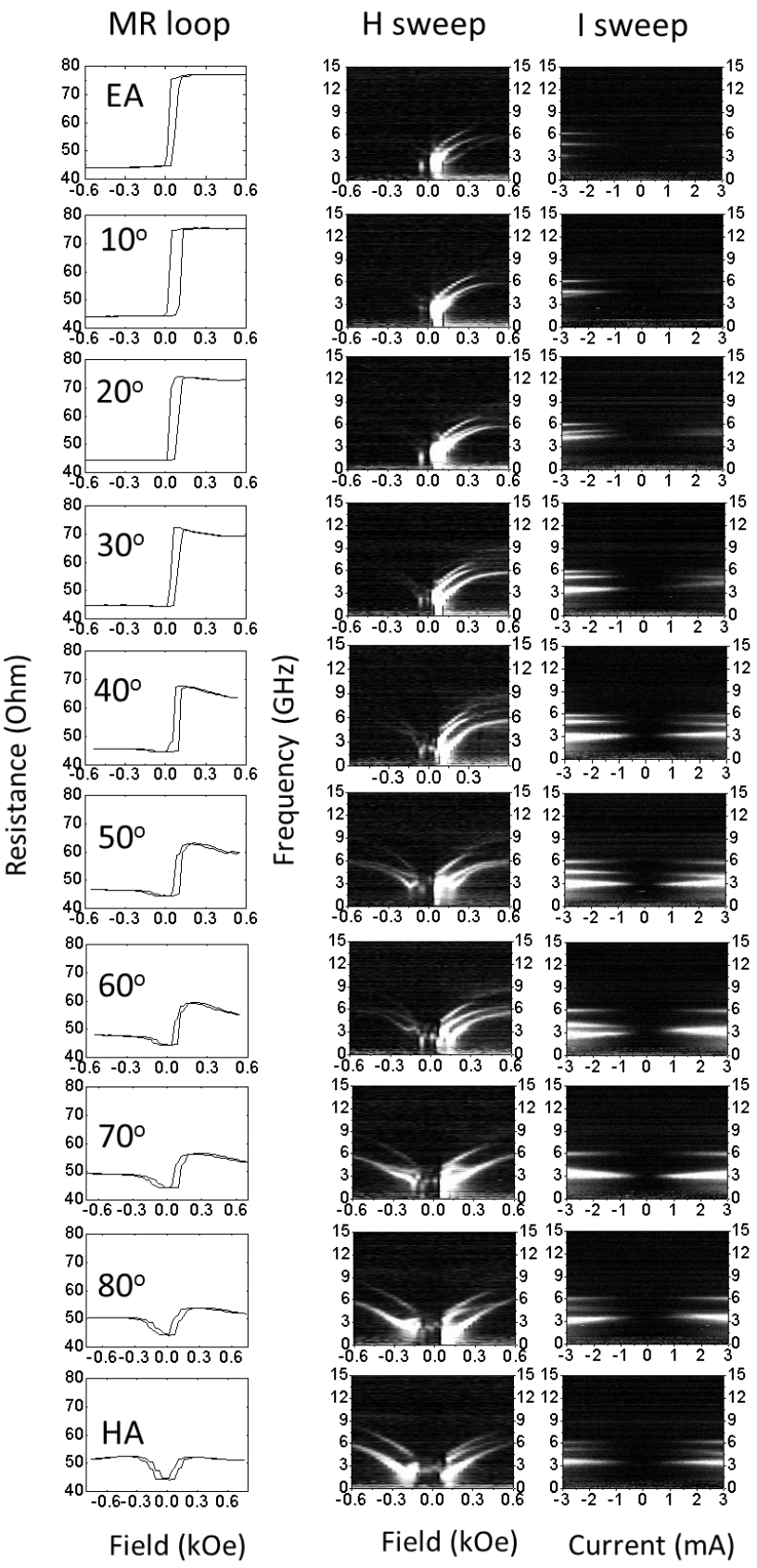

Figure 7.3.3 MR loop (1st column) and microwave output spectrum of field sweep (2nd column) and current sweep (3rd column) acquired from a 150 nm MTJ (MTJ1).

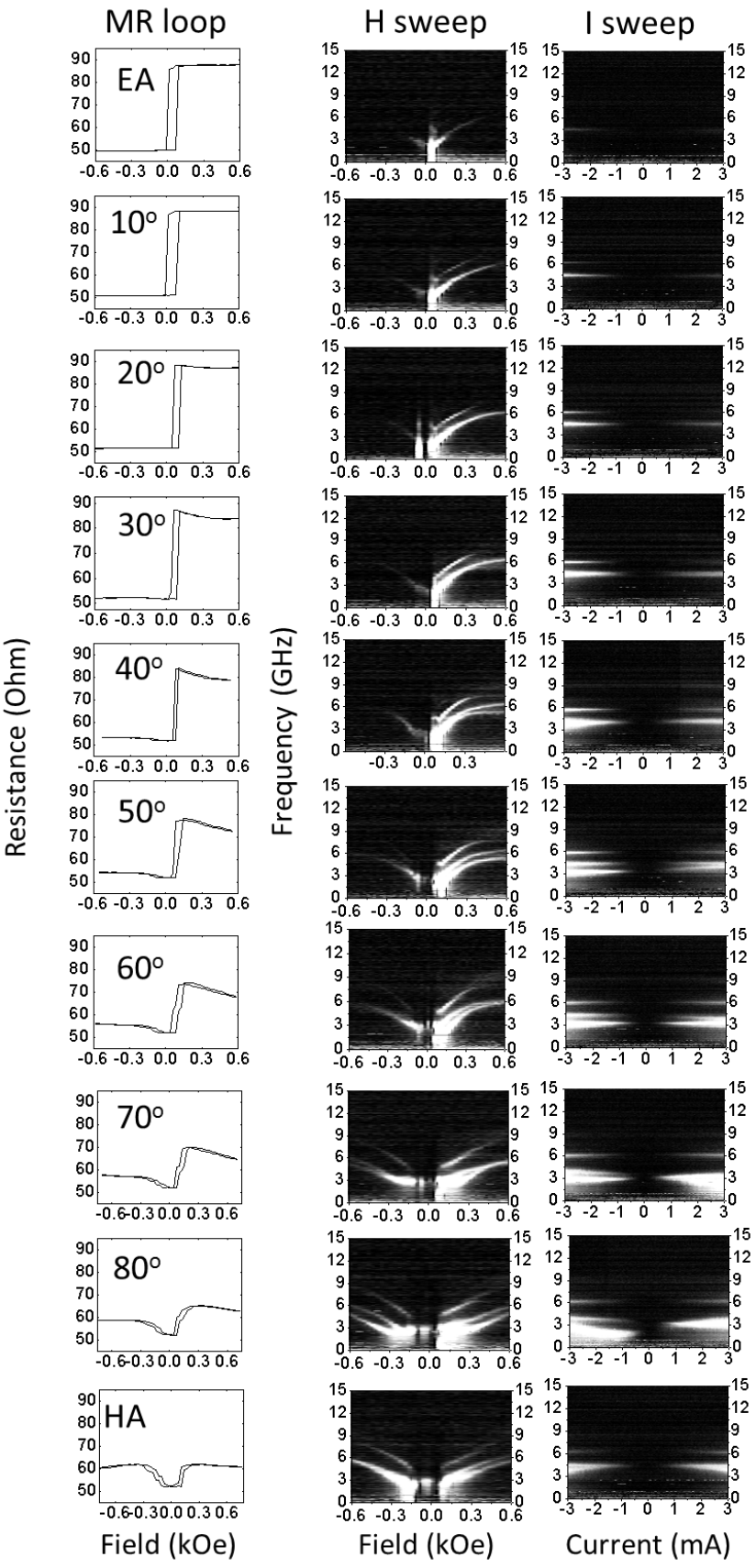

Figure 7.3.4 MR loop (1st column) and microwave output spectrum of field sweep (2nd column) and current sweep (3rd column) acquired from a 150 nm MTJ (MTJ2).

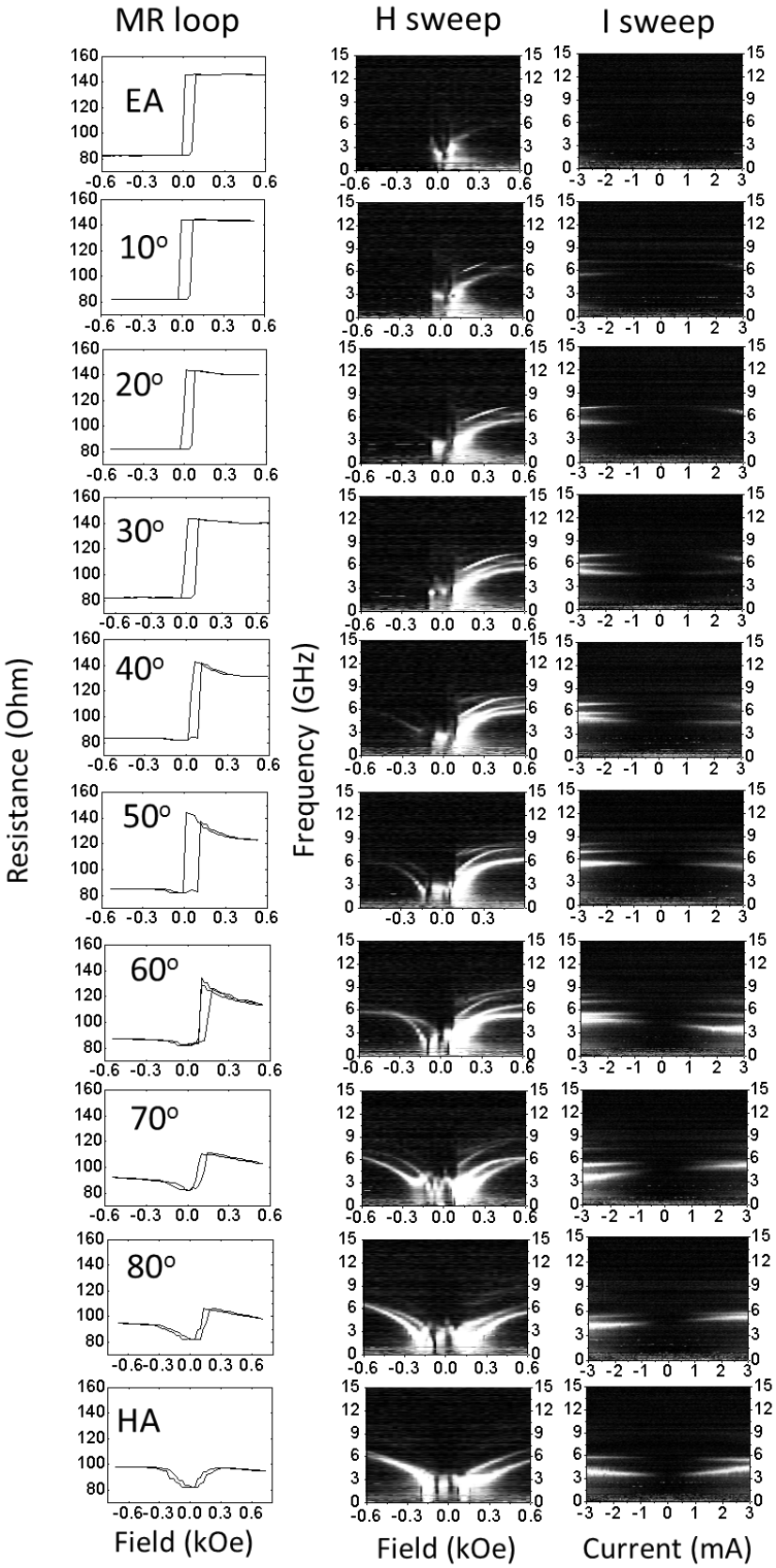

Figure 7.3.5 MR loop (1st column) and microwave output spectrum of field sweep (2nd column) and current sweep (3rd column) acquired from a 300x100 nm MTJ (MTJ3).

MR loops become symmetric when the external field is applied along the HA. In general the background noise level increases with increasing $R_{\parallel}$. For all MTJs with high $R_{\parallel}$ values i.e. all elliptical devices, the number of excited modes reaches a maximum and mode splitting and overlapping is also observed when the external field is applied between 40^{o} and 70^{o} from the EA, as evident in the field swept spectrum for a typical elliptical device (MTJ3) in Figure 7.3.5. When the field is applied along the HA, the two lowest frequency modes continue to be observed but the third and fourth modes are shifted to higher frequency with a reduced intensity so that they are not necessarily observed in the experiment. Three modes have been observed continuously through all angles of the applied field and mode crossover is observed between 60^{o} to 80^{o} for MTJ1 (Figure 7.3.3). The number of excited modes then increases as the applied magnetic field is rotated away from the EA with the maximum number of modes being observed when the external field is applied along the HA for MTJ2 as shown in the acquired field swept spectra (Figure 7.3.4) . Mode splitting and crossover is also observed between 30^{o} to 70^{o}. All modes seen in field swept spectra (200 Oe for MTJ1 and MTJ2 and 290 Oe for MTJ3 at a -3mA bias current) can be reproduced in current swept spectra that are taken for the respective bias field. The current swept measurements suggest that the majority of modes exhibit negative agility (i.e. The frequency decreases with increasing current) indicating an in-plane precession of the magnetisation. After determining the typical response for each field angle between the EA and HA for MTJ1, MTJ2 and MTJ3, it was then possible to select an angle where there is no mode crossover, no overlapping of modes and the highest mode amplitude for all $\phi_H$of the lowest frequency mode. The complete range of bias for all angles for both current and field swept spectra for a range of devices is shown in the appendix 1(A1.1).

Micromagnetic simulations were performed using the LLG Micromagnetics Simulator[176] platform with two dimensional mesh of each cell size (6x6) nm for the stack parameters given in Figure 7.2.1 for a 150 nm circular MTJ. The sample lies in the *xy*-plane. The easy axis is along the *x*-axis. A small in-plane pulse field with amplitude of 10 Oe, 40 ps rise time, 300 ps pulse width, 100 ps fall time applied along the y-axis was used to excite the free layer magnetisation in the presence of a 200 Oe bias field and a -3 mA bias current for all bias field angles. The value of the damping constant (α) assumed for this simulation was 0.01.

The simulations assumed a perfectly circular MTJ cross section. The two lowest frequency modes were identified as edge modes and the higher frequency third mode. The frequencies extracted from field swept experimental data are plotted together with the simulated spectra in Figure 7.3.6. The frequency dispersion as a function of ϕ_H is presented in Figure 7.3.6 (only for MTJ1 and MTJ2). The corresponding map of magnetisation amplitude (M_y component) for the three modes at ϕ_H=40^o are shown in Figure 7.3.7. The simulations produce more modes than are observed in the experiment and so this chapter will only discuss the lowest three frequency modes from the simulations. The experimentally observed 3rd higher order mode frequency is in good agreement with that seen in simulations for both devices. It was found to be very difficult to reproduce the edge mode frequencies observed in experiments and this is attributed to the shape irregularity of the devices and therefore the breakdown of the assumption of perfectly circular MTJ cross sections for MTJ1 and MTJ2. However the higher order 3rd order mode is less affected by shape imperfections. The irregularity of the device shape may arise during the fabrication process and can cause a random distribution of edge mode frequencies across nominally identical devices. Although the higher order 3rd mode extends over both the edge and the centre regions the behaviour in the central region appears to be dominant over that in the edge regions as illustrated by the relatively weak dependence on the frequency of this mode with the bias field angle. The modes from experiment and simulation have been shown in Figure 7.3.6 as a function of ϕ_H for MTJ1 and MTJ2. The corresponding mode frequency extracted from the experimental current swept spectrum at a bias field of 200 Oe for MTJ1 and MTJ2 and 290 Oe for MTJ3 at a -3 mA bias current are shown in Figure 7.3.8 (a), (c) and (e) respectively. The 3rd mode (higher mode) remains at a fixed frequency for all bias ϕ_H but the two lower frequency modes (edge modes) are distributed randomly. This means that it will be impossible for simulations to reproduce the experimentally observed edge mode frequencies which are strongly influenced by shape irregularity.

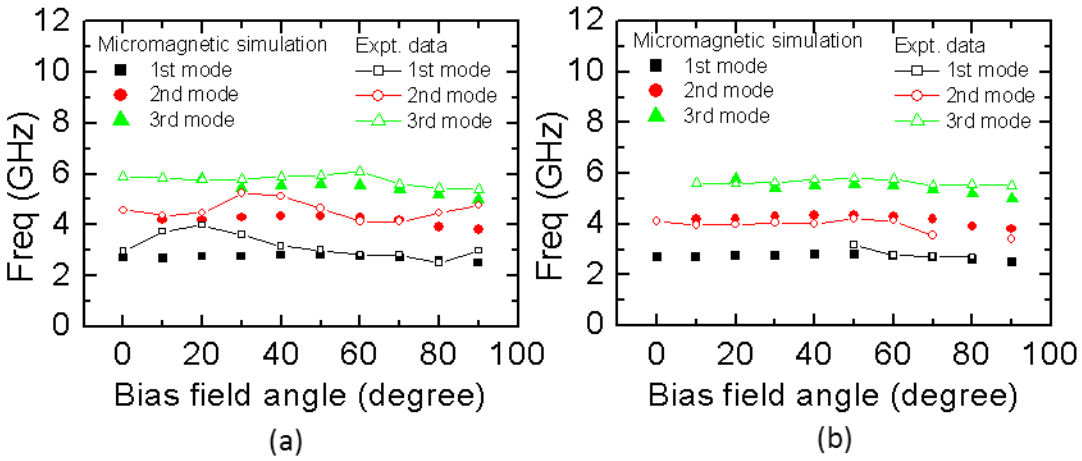

Figure 7.3.6 Mode frequency vs bias field angle (ϕ_H) obtained from LLG micromagnetic simulations and observed in experimental field swept data taken with a 200 Oe bias field and a -3 mA bias current for (a) MTJ1 and (b) MTJ2.

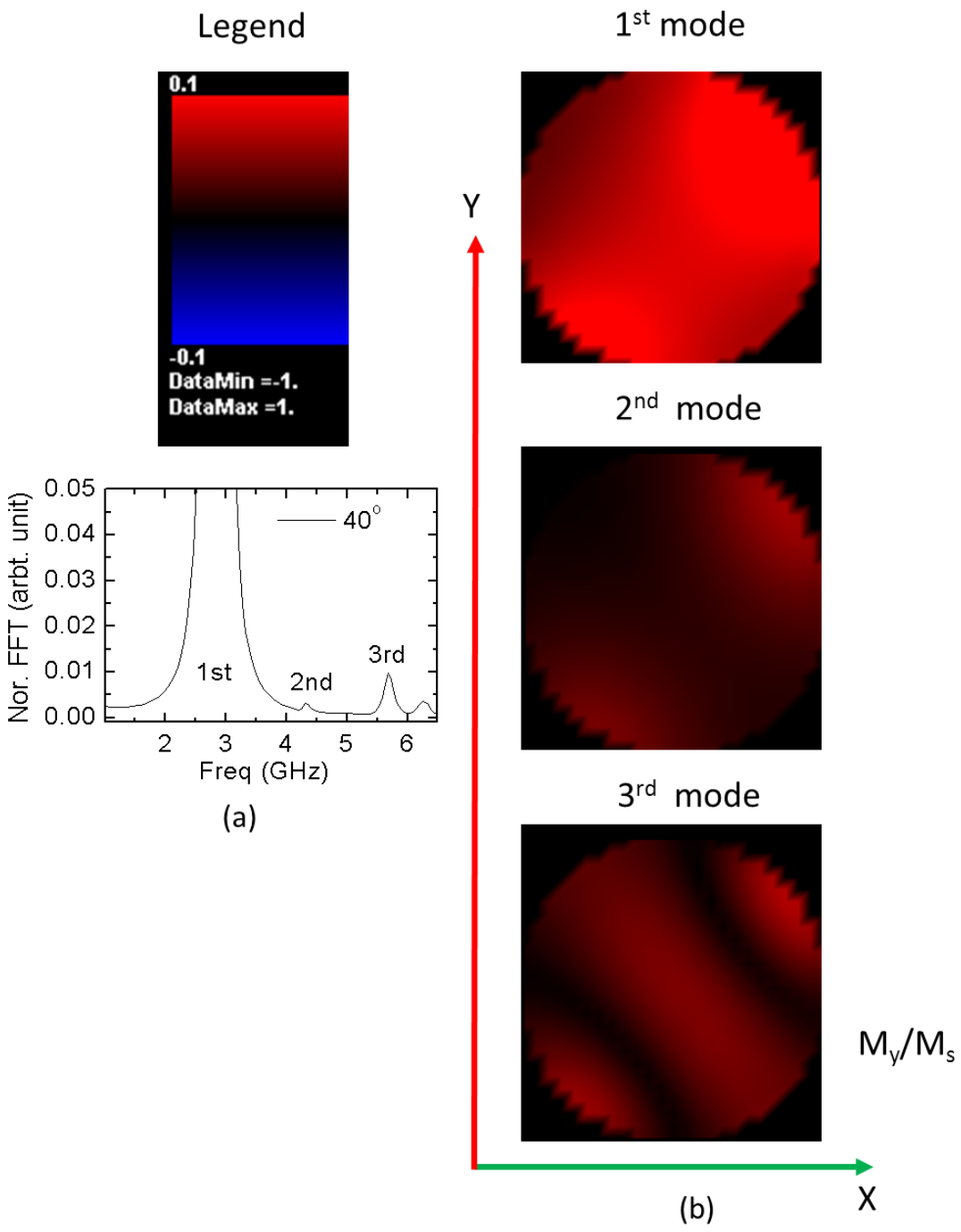

Figure 7.3.7 (a) The Normalized FFT spectra of M_y/M_s component from the simulation at bias field angle ϕ_H =40°, and (b) Corresponding bitmap of the spatial variation of the amplitude of the 1st mode, 2nd mode and 3rd mode respectively. The red contrast shows the positive amplitude of the M_y/M_s component of magnetisation whereas blue shows the magnetisation amplitude pointing in opposite direction.

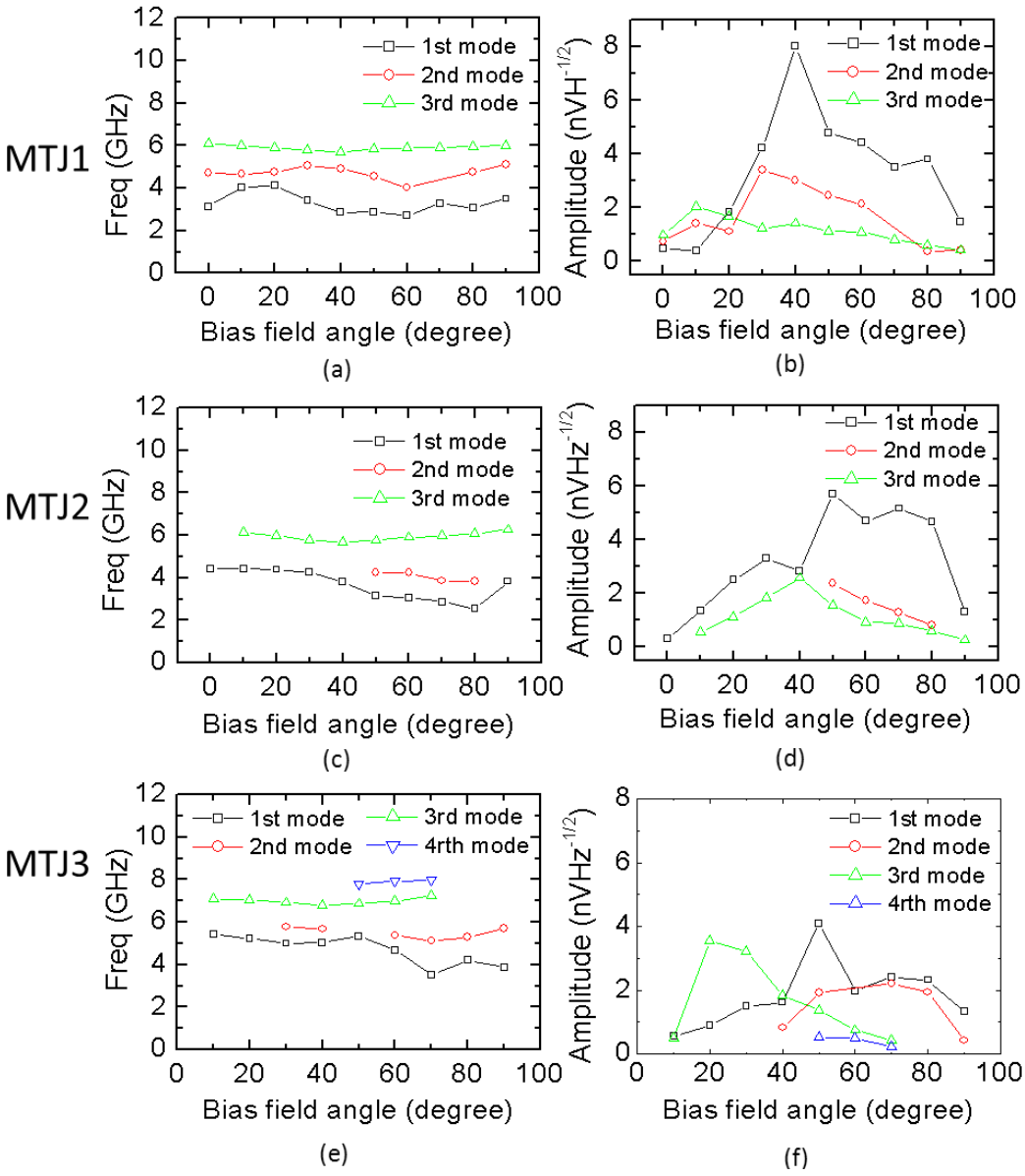

Figure 7.3.8 Mode frequency vs bias field angle (ϕ_H) and mode amplitude angle vs bias field are shown for MTJ1 (a, b), MTJ2 (c, d) and MTJ3 (e, f).

To further quantify the effect of STT on the observed modes, current swept spectra were selected for bias field angles at which the mode amplitudes were a maximum but without crossover or overlapping of modes. Mode crossover and overlapping causes results in interaction between the modes which then modifies their individual character. This can further complicate the task of judging the effect of STT on a given mode and so this regime was not considered in the following analysis. Bias field angles (ϕ_H) of; 40^o, 50^o, and 50^o were selected for MTJ1, MTJ2 and MTJ3 as shown in Figure 7.3.8 (b), (d) and (f) respectively.

The 1st mode (lowest frequency edge mode) is dominant in terms of amplitude and so from hereon only the 1st mode will be discussed in respect to quantification of the STT. Following the sign convention used throughout this thesis, the STT associated with a negative DC current will stabilise a parallel state. The frequency, amplitude and FWHM extracted from current swept spectra for MTJ1, MTJ2 and MTJ3 are shown in Figures 7.3.9, 7.3.10 and 7.3.11 respectively. As expected the STT can enhance the amplitude of thermally excited ferromagnetic resonance modes when the DC current has negative polarity and a positive bias field (antiparallel state) is applied. For a positive bias field, a positive DC current of positive polarity will enhance the damping. The experimental spectra contain three distinct modes for a negative current polarity in contrast to the low amplitude modes observed for a positive current polarity for MTJ1, MTJ2 and MTJ3 (Figure 7.3.9 (b), 7.3.10 (b) and 7.3.11 (b) respectively). This is evidence that STT drives the precession of magnetisation to higher amplitude. As the amplitude increases the frequency should decrease as is seen by the red shift that occurs for a negative current polarity. This observed red shift also indicates the occurrence of in-plane precession of the magnetisation. This allows the STT due to the applied DC current to be further investigated by extracting the critical current by extrapolating the FWHM[75, 177] values to zero as shown in Figures 7.3.9 (d), 7.3.10 (d) and 7.3.11 (d). The critical current values found using this approach for MTJ1, MTJ2 and MTJ3 were -2.40 mA,-1.79 mA and -0.71 mA respectively. The critical current is seen to decrease as $R_{\parallel}$ increases.

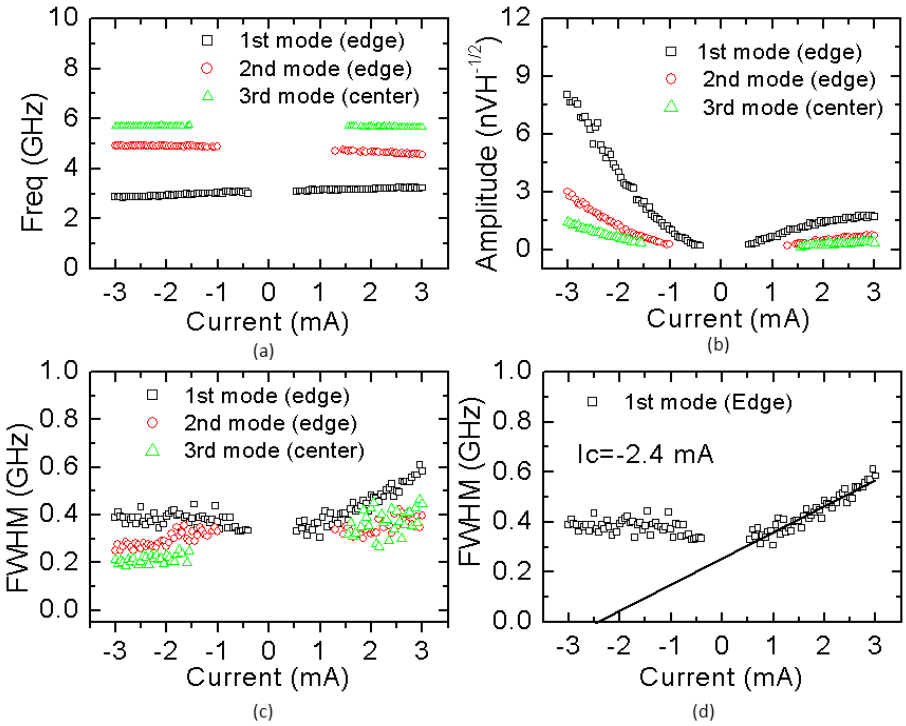

Figure 7.3.9 Parameters extracted from current swept spectra by means of Lorentzian peak fitting for MTJ1: (a) frequency, (b) amplitude, (c) full width half maxima (FWHM) and (d) FWHM extrapolated to zero for 1st mode.

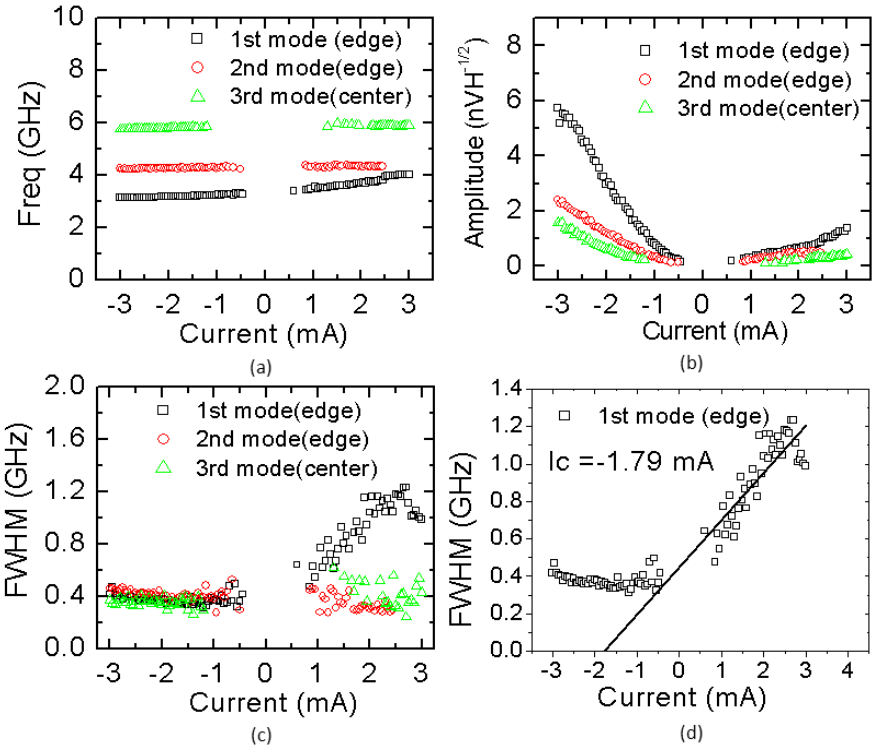

Figure 7.3.10 Parameters extracted from current swept spectra by means of Lorentzian peak fitting for MTJ2: (a) frequency, (b) amplitude, (c) full width half maxima (FWHM) and (d) FWHM extrapolated to zero for 1st mode.

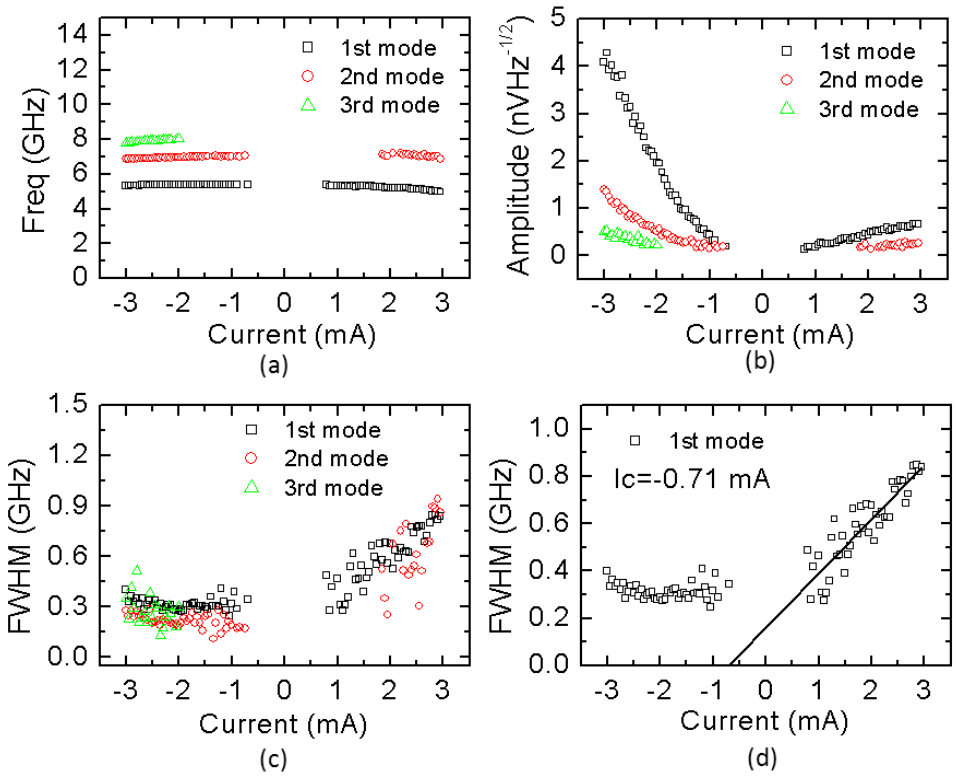

Figure 7.3.11 Parameters extracted from current swept spectra by means of Lorentzian peak fitting for MTJ3: (a) frequency, (b) amplitude, (c) full width half maxima (FWHM) and (d) FWHM extrapolated to zero for 1st mode.

The STT torque term has both an in-plane component and out-of-plane component. The in-plane STT torque term alters the FWHM of the excited mode whereas the out-of-plane STT torque term is a field like torque term that is responsible for the frequency shift of the mode[75,178]. The central frequency, FWHM and amplitude were extracted for all three observed modes by fitting a symmetric Lorentzian peak for each of the three MTJs. The asymmetry between the positive and negative current polarities of the extracted modal amplitude is shown in Figures 7.3.9 (b), 7.3.10 (b) and 7.3.11 (b) for the three MTJs. When a negative current is applied to an MTJ with an antiparallel alignment the STT will cause the initially thermally excited modes to precess with enchanced amplitude. If instead the current polarity is positive the STT will cause enhanced damping of the thermally excited modes[177]. The observed shift to lower frequencies is attributed to the enhanced mode amplitude caused by the STT. The STT acts against the damping term in the case of a negative current polarity and so one would expect that the FWHM should decreases from +3

mA to -3 mA. Surprisingly the observed effect on the FWHM is hard to ascertain due to the smaller than expected variation. The measured devices were driven above the threshold regime and so may go into the nonlinear auto oscillation regime that leads to chaotic magnetisation precession in the free layer. This mechanism may cause the FWHM to remain constant for negative current polarities of increasing magnitude. The FWHM for the 2nd and 3rd modes was seen to be effected by the STT to a lesser extent than the 1st mode by considering the gradient of the FWHM variation with current. For this reason the remainder of this discussion will focus only on the properties of the 1st mode. The FWHM of the 1st mode is slightly larger than that of the other two modes. The FWHM observed in the experiments is larger than those previously observed in the literature[75]. This may be due to the fact that the devices studied in this thesis exhibited multiple rather than single mode excitation and that interactions between modes lead to line broadening. Analytical fitting was performed of the lowest frequency mode using a macrospin model. The LLG equation modified to include the Slonzewski in-plane and out-of-plane torque terms takes the form

$$\frac{d\mathbf{u}}{dt} = -|\gamma|\mathbf{u}\times\mathbf{H}_{eff} + \alpha\mathbf{u}\times\frac{\partial\mathbf{u}}{\partial t} - |\gamma|a_j\mathbf{u}\times(\mathbf{u}\times\mathbf{p}) + |\gamma|b_j(\mathbf{u}\times\mathbf{p}) \qquad (7.3.1)$$

where $\mathbf{u} = \frac{\mathbf{M}}{|\mathbf{M}|}$ for the free layer, α is the damping constant and $\mathbf{p}$ is the polarisation of the fixed layer. a_j and b_j are the in-plane and out-of-plane torque coefficients respectively. The solution in the small amplitude limit yields FWHM $(\Delta\omega)$ and frequency (ω) given by

$$(\Delta\omega)_o = \frac{|\gamma|(\alpha H_a + 2a_j cos\phi_H)}{\sqrt{3}} \qquad (7.3.2)$$

$$\left(\frac{\omega}{|\gamma|}\right)^2 = \left[H + \frac{2K}{M}cos\phi_H - b_j cos\phi_H\right]\left[H + 4\pi M - \frac{2K_\perp}{M} + \frac{2K}{M}cos^2\phi_H - b_j cos\phi_H\right] \qquad (7.3.3)$$

$$H_a = 2H + 4\pi M - \frac{2K_\perp}{M} + \frac{2K}{M}(\cos\phi_H + cos^2\phi_H) - 2b_j cos\phi_H\ . \qquad (7.3.4)$$

H, K, $K_\perp$, M, α and ϕ_H are the external bias field, inplane anisotropy constant, perpendicular anisotropy constant, saturation magnetisation, damping constant and angle between the bias field and EA of the free layer respectively. The detailed derivation of these expressions is given in appendix 1 (A1.2).

The in-plane STT component expected from the macrospin expression $a_j/I = \hbar p/2eM_1d_1A$ is 16 Oe/mA for both MTJ1 and MTJ2 assuming a free layer thickness of d_1 =8.7 nm, saturation magnetisation of free layer M_1 =515 emu/cm^3, and a

polarisation of $|p|$=0.4 where in addition A is the area of the junction, $\hbar$ is the Plank's constant, and e the electron charge. The expected a_j/I for MTJ3 is 12.5 Oe/mA. a_j/I and b_j/I are extracted by fitting with analytical equations (7.3.2 and 7.3.3) and by considering the frequency and FWHM from the experimental data for the 1st mode only. The expected and extracted values of the in-plane and out-of-plane STT components are tabulated in Table 7.3.2 below. The fitted curves for both STT components are shown in Figure 7.3.12 for all three MTJs. The fitting for the in-plane component is considered only for data points where the FWHM decreases from maximum to minimum values and neglects the data points where the FWHM is either unchanged or slightly increased due to the system entering the nonlinear regime[179]. The values of the in-plane STT extracted from the experiments are up to a factor of 5 larger than those expected from a macrospin treatment. The order of magnitude agreement is good and we suggest that detailed differences occur due to the spatial inhomogeneity of the current distribution and the reduced effective fields that occur within the edge regions and which also lead to reduced edge mode frequencies.

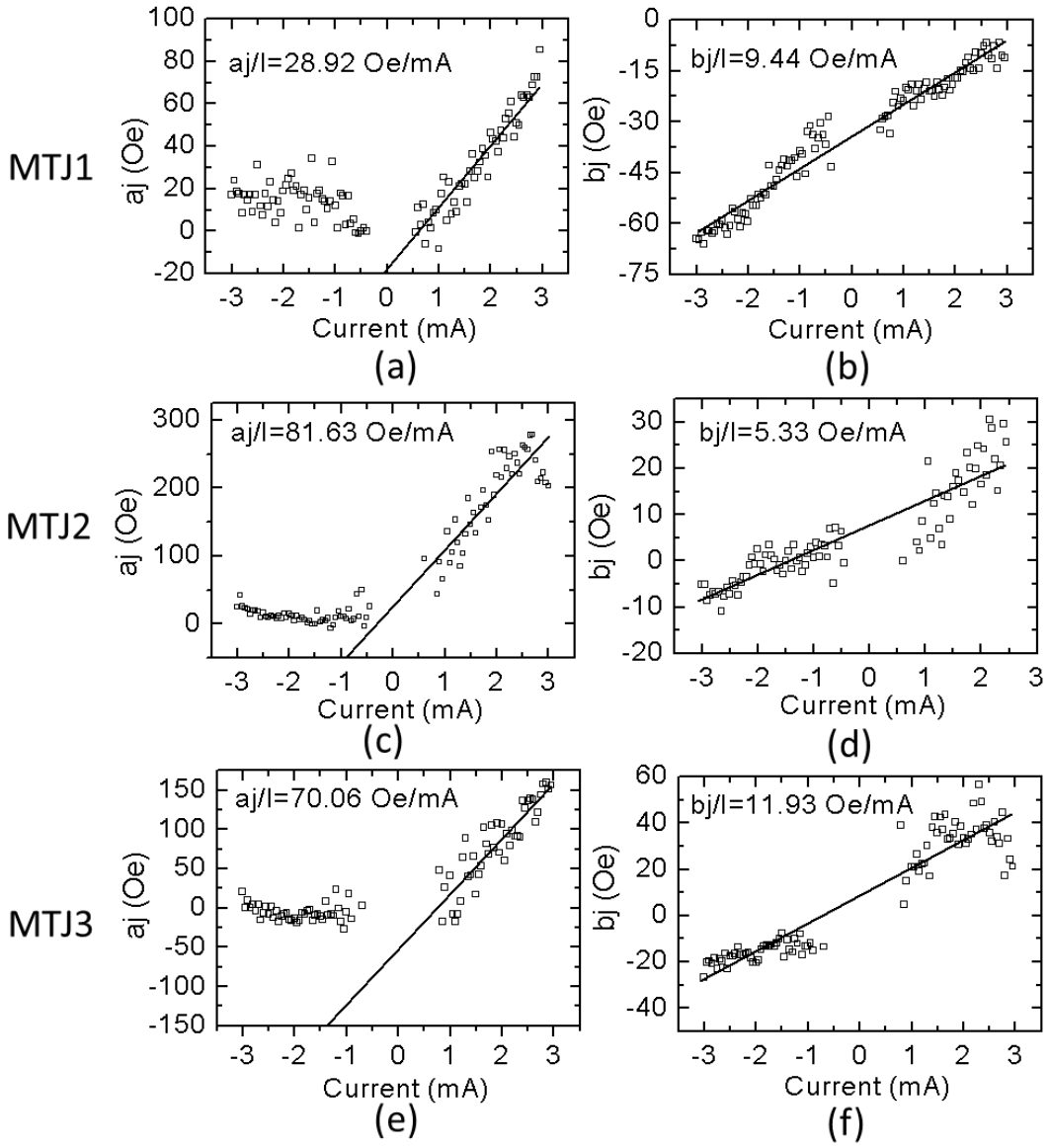

Figure 7.3.12 In-plane (a_j/I) and out-of-plane (b_j/I) STT components obtained from experimental curve fitting and using an analytical model for MTJ1 (a,b), MTJ2 (c,d) and MTJ3 (e,f).

Device	Expected In-plane(a_j/I) (Oe/mA)	Extracted In-plane $\left(\frac{a_j}{I}\right)$ (Oe/mA)	Extractedout-of-plane $\left(\frac{b_j}{I}\right)$ (Oe/mA)
MTJ1	16	28.92	9.44
MTJ2	16	81.63	5.33
MTJ3	12.5	70.06	11.93

Table 7.3.2 Expected and extracted values of in-plane and out-of plane STT components

The analytical model used in the present analysis does not include nonlinear effects and so it is not ideal for the extraction of the STT components when the MTJ enters the nonlinear regime.

7.4 Summary

The microwave emission of Tunnel Magnetoresistance (TMR) nanopillars has been measured as a magnetic field is applied in the plane of the film at different angles ϕ_H with respect to the easy axis. For non-zero values of ϕ_H the free layer magnetisation cants away from the reference and fixed layer magnetisations increasing the initial spin transfer torque (STT) and also the resistance gradient dR/dH. As ϕ_H is increased a more complicated mode spectrum containing several modes is observed. The modes are identified as edge and higher order modes by comparison with LLG micromagnetic simulations and through consideration of the statistical distribution of mode frequencies from many devices. The edge modes show a more random distribution of frequencies with respect to bias field orientation while the 3rd higher order mode remains fixed at a particular frequency. The device shape irregularity is invoked as the cause of the randomness of the edge frequencies and the absence of any such distribution for the 3rd higher order mode frequencies. The in-plane and out-of-plane components of the STT for the 1st mode (edge mode) within three MTJs were extracted by fitting to an analytical model and compared to values predicted by a macrospin model. While the order of magnitude agreement is good the extracted values are larger than expected and suggest that a more detailed treatment is required to understand how STT effects edge modes.

Chapter 8

Summary and future prospects

8.1 Summary

The main aims of the thesis have been to investigate the magnetisation dynamics of a single nanomagnet, the interaction of a pair of nanomagnets, the magnetisation dynamics of partially built write head structures and the thermally excited ferromagnetic resonance modes (mag-noise) in read head sensors. In this thesis the results of time resolved scanning Kerr microscopy (TRSKM) measurements on a single nanomagnet, a pair of nanomagnets and a partially built write head structure have been presented. Electrical transport measurements of recording head sensors have also been presented.

In chapter 2 the background concepts required to understand the rest of the thesis were reviewed. This chapter also explained the motivation for the study of magnetisation dynamics within confined structures.

In chapter 3 the magneto-optical interaction was described and the technique of time resolved scanning Kerr microscopy was presented. Sub-picosecond temporal resolution and sub-micron spatial resolution were demonstrated. The chapter also discussed the capability of TRSKM for simultaneous detection of three Cartesian components of magnetisation. Electrical transport measurements using a four probe contact method were described and the experimental setup was presented.

In Chapter 4 the results of time resolved scanning Kerr microscopy (TRSKM) measurements of large amplitude magnetisation dynamics within a single 440×440 nm^2 CoFe(1 nm)/NiFe(5 nm)/CoFe(1 nm) nanomagnet were presented. Excellent signal-to-noise ratio was achieved without the need for cavity enhancement of the magneto-optical signal. Quantitative agreement between the experimental and simulated spectra was only obtained after modifying the profile of the saturation magnetisation within the element, suggesting that nanofabrication processes influence the magnetic parameters of the material, particularly near edges, and therefore also the dynamic response.

At the same time differences in the damping in the parallel and diagonal external bias field geometries imply that the micromagnetic model does not fully describe the relaxation of the magnetisation dynamics. Such effects would be difficult to isolate in closely packed arrays where inter-element interactions can influence the frequency of the observed dynamics. This work also emphasizes the fact that the pulsed field amplitude is an important parameter in micromagnetic modelling of the magnetisation dynamics of a single nanomagnet, where a large amplitude excitation can change the character of the resonant mode spectra in addition to the magnetic ground state. Time-resolved (TR) measurements and micromagnetic simulations demonstrated that large angle magnetisation dynamics in a single nanomagnet can lead to a dynamic response that is dominated by the quasi-uniform center mode, while the non-uniform edge mode is almost completely suppressed.

In Chapter 5 TRSKM measurements demonstrated that the weak dynamic dipolar interaction can be isolated from the stronger static interaction and the effects of structural and magnetic imperfections by measuring the phase of the center and edge modes of each disk within a pair. The method used to isolate the dynamic dipolar interaction could equally well be applied to nanomagnets coupled by other mechanisms, such as the flow of spin current, or for that matter any system of coupled oscillators. Our results show that the dynamic coupling exhibits a strong dependence on static bias field and that a judicious choice of center or edge mode excitation may be required if dipolar interactions are to deliver either the formation of collective modes within magnonic crystals or the non-linear phase-locking of spin transfer oscillators for wireless microwave applications. The observation of a dynamic interaction larger than that expected for a pair of ideal homogeneous disks gives impetus to the characterization of local magnetic properties at the deep nanoscale and suggests that enhanced dipolar coupling may be achieved by engineering the spatial variation of magnetic properties, particularly within edge regions.

Chapter 6 demonstrated how TRSKM can be been used to make wafer level measurements of magnetisation dynamics within the CoFe yoke and pole piece of partially built inductive perpendicular write head structures. All three Cartesian components of the vector magnetisation were recorded simultaneously using a polarimeter consisting of a beam-splitting polarizer and two quadrant photodiodes.

The rise time, relaxation time, and amplitude of each component were related to the magnetic ground state, the initial torque, and flux propagation through the yoke and pole piece. Dynamic images revealed "flux beaming" in which the magnetisation component parallel to the symmetry axis of the device was largest, and decayed more slowly than the other components along the same symmetry axis, its spatial distribution becoming more irregular as the amplitude of the driving field was reduced. The results show that TRSKM may be used to quantify the effect of yoke composition and geometry upon the magnetisation within the writer pole piece.

Chapter 7 presented the results of high frequency electrical transport measurements on magnetic tunnel junction recording head sensors. The thermal and spin transfer torque (STT) excitation of precessional modes in the noise spectra of Tunnel Magnetoresistance (TMR) nanopillars was measured as a magnetic field was applied in the plane of the film at different angles ϕ_H with respect to the easy axis. For non-zero values of ϕ_H the free layer magnetisation cants away from the reference and fixed layer magnetisations increasing the initial STT and also the resistance gradient dR/dH. As ϕ_H is increased a more complicated mode spectrum containing several modes is observed. The modes are identified as edge and center modes by comparison with LLG micromagnetic simulations and through consideration of the statistical distribution of mode frequencies from many devices. The edge modes show a more random distribution of frequencies with respect to bias field orientation while the center mode remains fixed at a particular frequency. The device shape irregularity is invoked as the cause of the randomness of the edge mode frequencies and the absence of any such distribution for the higher mode frequencies. The in-plane and out-of-plane components of the STT for the 1st mode (edge mode) within three MTJs were extracted by fitting to an analytical model.

8.2 Future prospects

The experimental work detailed in Chapter 4 shows that edge modes can be suppressed and the dynamics of the center mode can be enhanced in the presence of a large amplitude pulsed field excitation. Edge mode suppression enables the magnetisation in a single nanomagnet to precess coherently which is of benefit in the operation of Spin Transfer Torque Oscillators (STO) and bistable switching devices.

Incoherent precession of the magnetisation and a low amplitude magnetisation trajectory in an STO can yield a low output power, while incoherent reduces the reliability of switching in bistable devices. Tailoring a uniform dynamic response of the magnetisation to an excitation whilst also increasing the amplitude of the precessing magnetisation therefore provides potential for increasing STO output power and reducing the noise associated with switching a bistable device.

The low microwave power output of an individual STO could be overcome by the synchronization of arrays of STOs leading to coherent power emission and increased power output. Phase locking STOs is assisted by the intrinsically non-linear nature of the coupled precession. Coupling between two closely spaced STOs mediated by spin wave propagation through a common magnetic layer is effective over the range of the spin decay length (1 μm). Experiments on pairs of STOs in the point contact geometry show that two STOs will phase lock to each other when their spacing is less than 200 nm [180,181]. The observed power output is approximately twice that of the total for two separate resonances at large spacing, showing that phase locking has occurred for small spacing. Long range coupling of STOs could exist via their interaction with the self-emitted microwave current. Injection locking of a single STO to an external microwave signal has been demonstrated and can be used to study some intrinsic properties of STOs [182,183,184,185,186] i.e. the dependence of power, linewidth and agility upon the strength of coupling to the external microwave current. These intrinsic parameters are tuned independently by choosing appropriate values of the injected DC current and applied field. The response has been modelled as a weak forced non-linear single oscillator. The coupling strength is proportional to the injected microwave current, and the coupling to the external signal becomes more efficient as the oscillator becomes more agile. Another possible long range coupling mechanism for STOs is dipolar coupling. The weakness of the dipolar interaction is that the long range coupling falls off as the inverse cube of the distance from the moment. Therefore the dipole-dipole interactions depend strongly on the distance between the STOs. The direction of the magnetisation of each STO e.g. out of plane or in-plane, also plays an important role due to the different dipolar fields generated. The dipolar fields also change during the magnetisation precession, thus changing the dipolar coupling. Future studies will first need to tailor the nature of the dipolar coupling if an array of STOs are to be phase locked so as to achieve microwave output levels large enough to be used for industrial applications.

Static and dynamic dipolar fields give rise to shape anisotropy and influence the group velocity of spin waves that are intrinsic to the operation of magnonic devices. Dipolar coupling via edge modes is favoured over coupling via the center modes of each element. Consideration must be given to the refinement the sample fabrication processes as the shape of the element effects the dipolar field. A periodic array of nanomagnets or holes in a ferromagnetic thin-film, or a three dimensional arrangement of magnetic nanostructures can support a collective spin wave spectrum. The structure determines the wavelength and energy of the dipolar and exchange spin waves. This can lead to the formation of a band gap such that magnon propagation through the magnonic crystal is forbidden for a specific range of spin wave frequencies[187,188,189,113]. The realization of such band gaps in magnonic crystals has created the potential for spin wave filters, spin wave waveguides and storage devices.

Flux beaming within a partially built writer structure has been observed experimentally and detailed in Chapter 6 of this thesis. Future work will investigate the dependence of flux beaming upon the number of energizing coils, different coil positions, as well as looking at the dependence of the size of the flux-beaming effect on both the composition and shape of yoke. This will give a better understanding of yoke performance and allow tailoring of the writing field generated by the yoke.

Noise spectra generated by magnetic tunnel junction recording head sensors were recorded in chapter 7. The spectra were observed to be complicated and the edge mode frequencies were not reproducible. The source of the irreproducibility has been attributed to shape irregularity. Uncontrolled modes within the noise spectra reduce the signal to noise ratio during the reading process within a magnetic data storage system. Further work is required to control the magnetic properties of the edges at the deep nanoscale and hence make the edge mode frequencies more reproducible.

Appendix 1

A1.1 Screen shots of noise spectra acquired from magnetic tunnel junctions

The output oscillation amplitude is expressed in terms of the voltage spectral density (VSD). The spectrum analyser acquires the output power in units of dBm (#dBm=10log (Power/1mW)). Power can be express in terms of voltage (V_{rms}) and impedance (Z) as

$$\text{Power} = V_{rms}^2/Z \qquad \text{(A1.1.1)}$$

The impedance (Z) is the 50 Ohm characteristic impedance of the cables. This is converted into VSD by the Labview programme using the expression

$$\text{VSD}=V_{rms}/\text{sqrt (RBW)} \qquad \text{(A1.1.2)}$$

where RBW is the resolution bandwidth of the spectrum analyser set during the data acquisition. The RBW was set to 150 KHz for all the spectra measured.

The microwave output of the devices was recorded with a -3mA DC current bias as an external bias magnetic field was swept from 0 Oe to 600 Oe to -600 Oe to 600 Oe and back to 0 Oe. The bias field was applied in the plane of the device and was rotated in 10° steps away from the easy axis, and towards the hard axis. The original axis labels show the number of the field point and the number of the frequency point (see Figure A1.1.1) and are the same for all angle. The number field point and frequency are kept fix throughout all angle. Further measurements were made by sweeping the current from -3mA to + 3mA in 0.05mA steps in the presence of a constant applied magnetic field. The magnetic field value for the current sweeps (I sweep) was chosen so that the maximum number of modes was visible during the current sweep: 200 Oe for a 150 nm diameter MTJ. The original axis labels show the number of the current point and the number of the frequency point, as in Figure A1.1.2 for a current sweep with the field applied along the hard axis, and are the same for all angles. The entire screen shot spectrum for the 7 MTJs of 150 nm diameter, MTJ4, MTJ5, MTJ6, MTJ7, MTJ8, MTJ9, MTJ10 for 150 nm MTJs are shown in Figures A1.1.3, A1.1.4, A1.1.5, and A1.1.6.

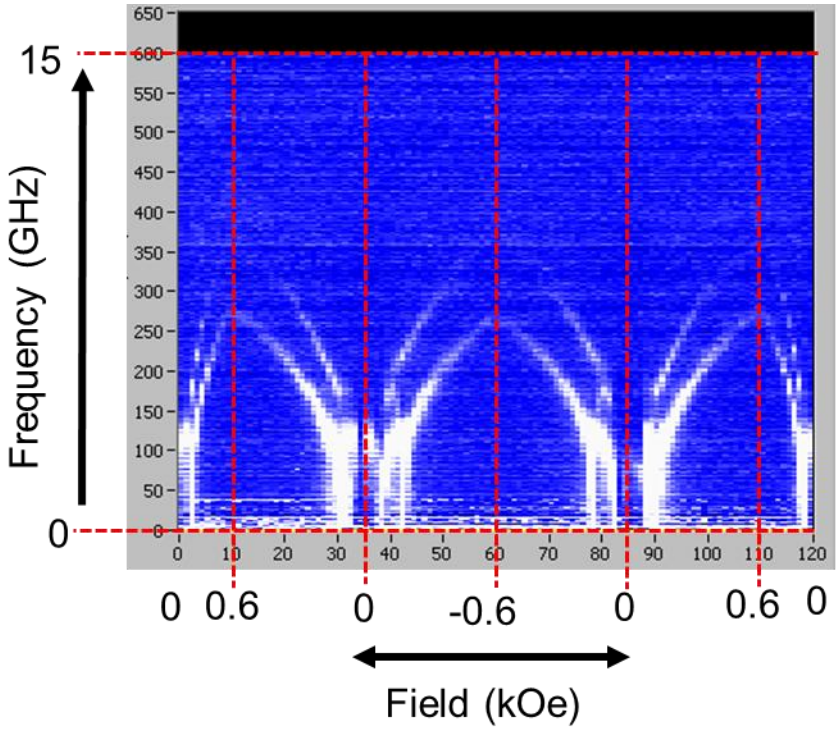

Figure A1.1.1 Screen shot spectra of voltage spectral density taken from field sweeps (H sweep) along the hard axis for MTJ10.

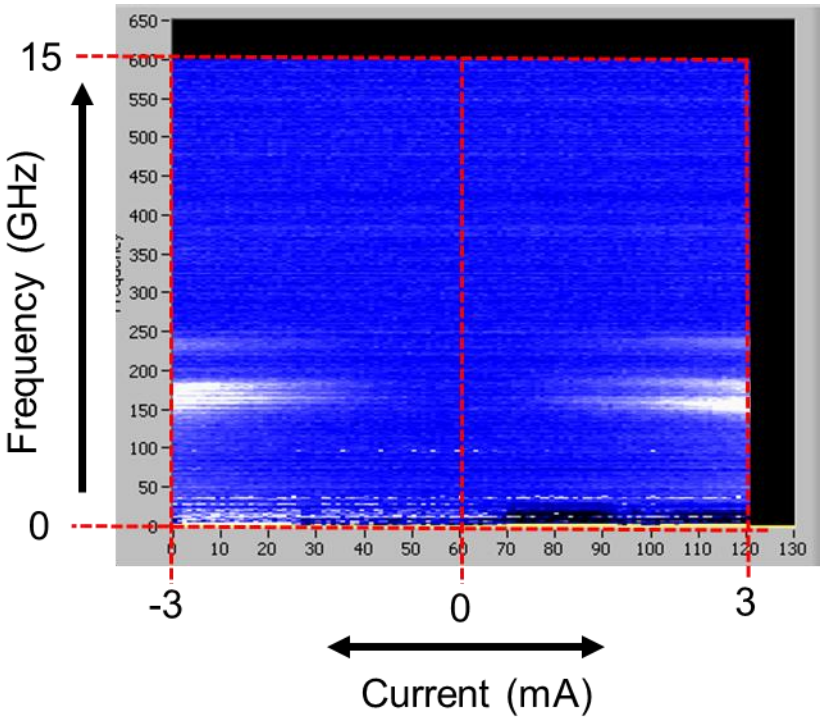

Figure A1.1.2 Screen shot spectra of voltage spectral density taken from current sweeps (I sweep) along the hard axis for MTJ10.

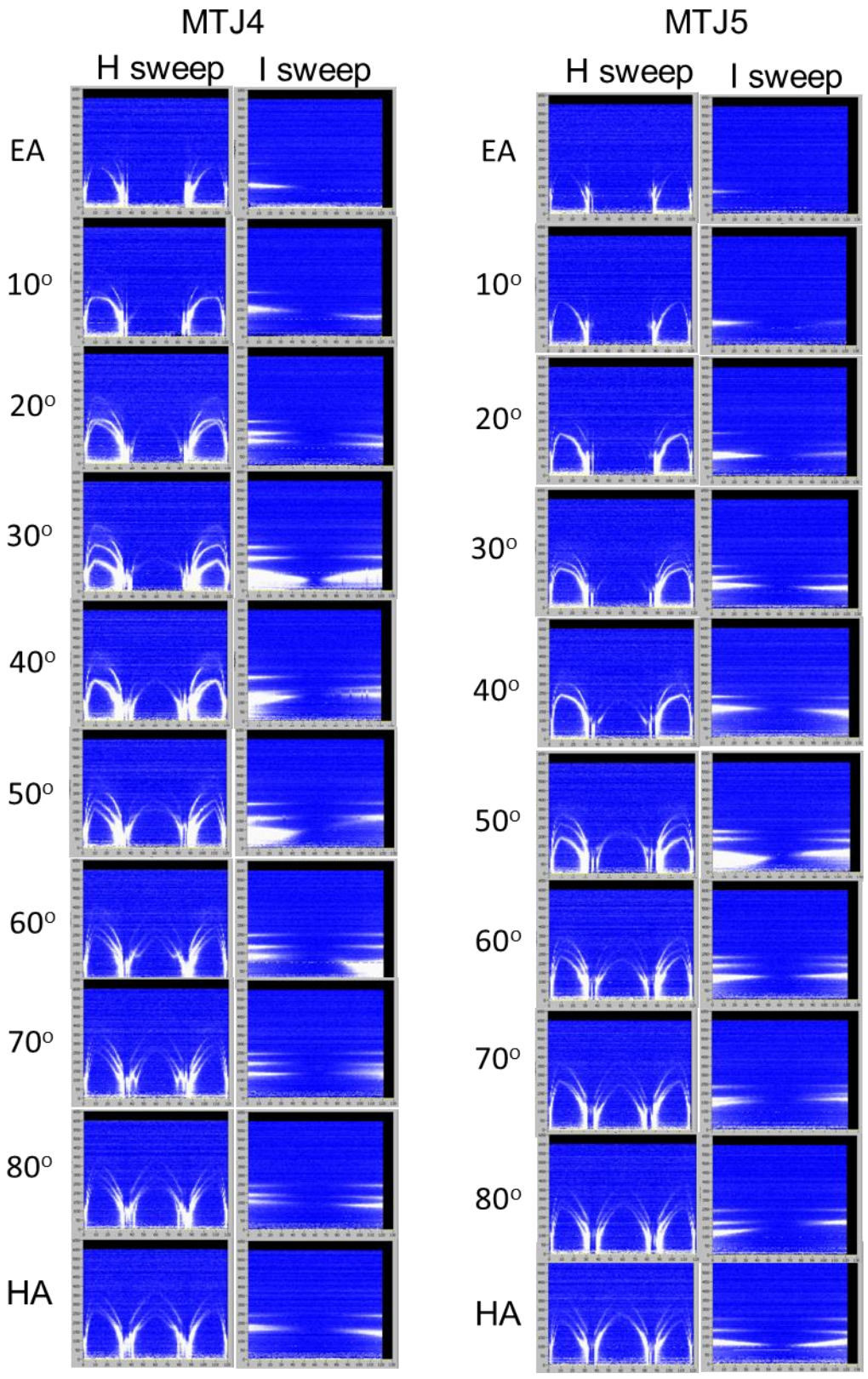

Figure A1.1.3 Screen shot spectra taken from field sweeps (H sweep) and current sweeps (I sweep) from the EA to the HA for MTJ4 (left) and MTJ 5(right).

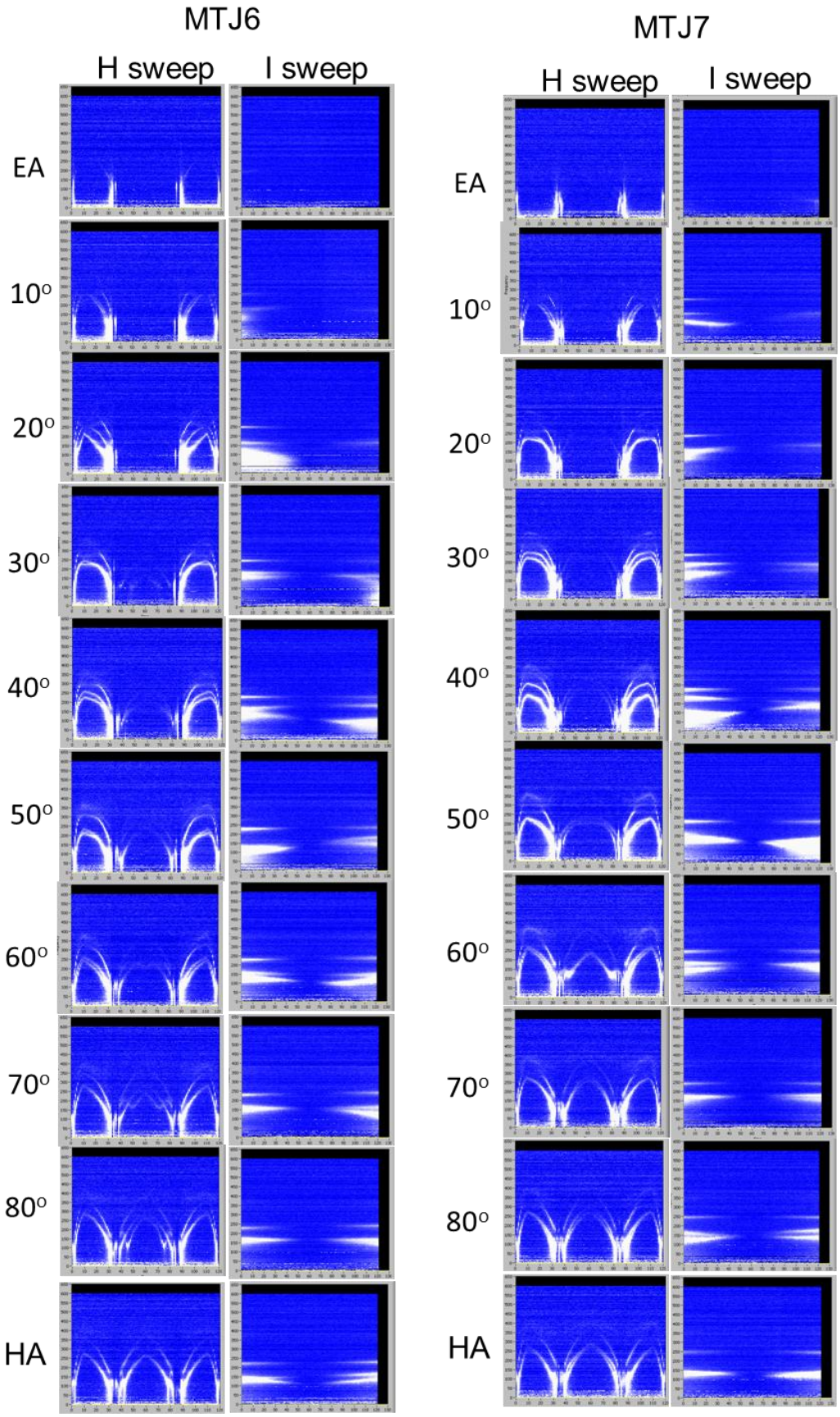

Figure A1.1.4 Screen shot spectra taken from field sweeps (H sweep) and current sweeps (I sweep) from the EA to the HA for MTJ6 (left) and MTJ7 (right).

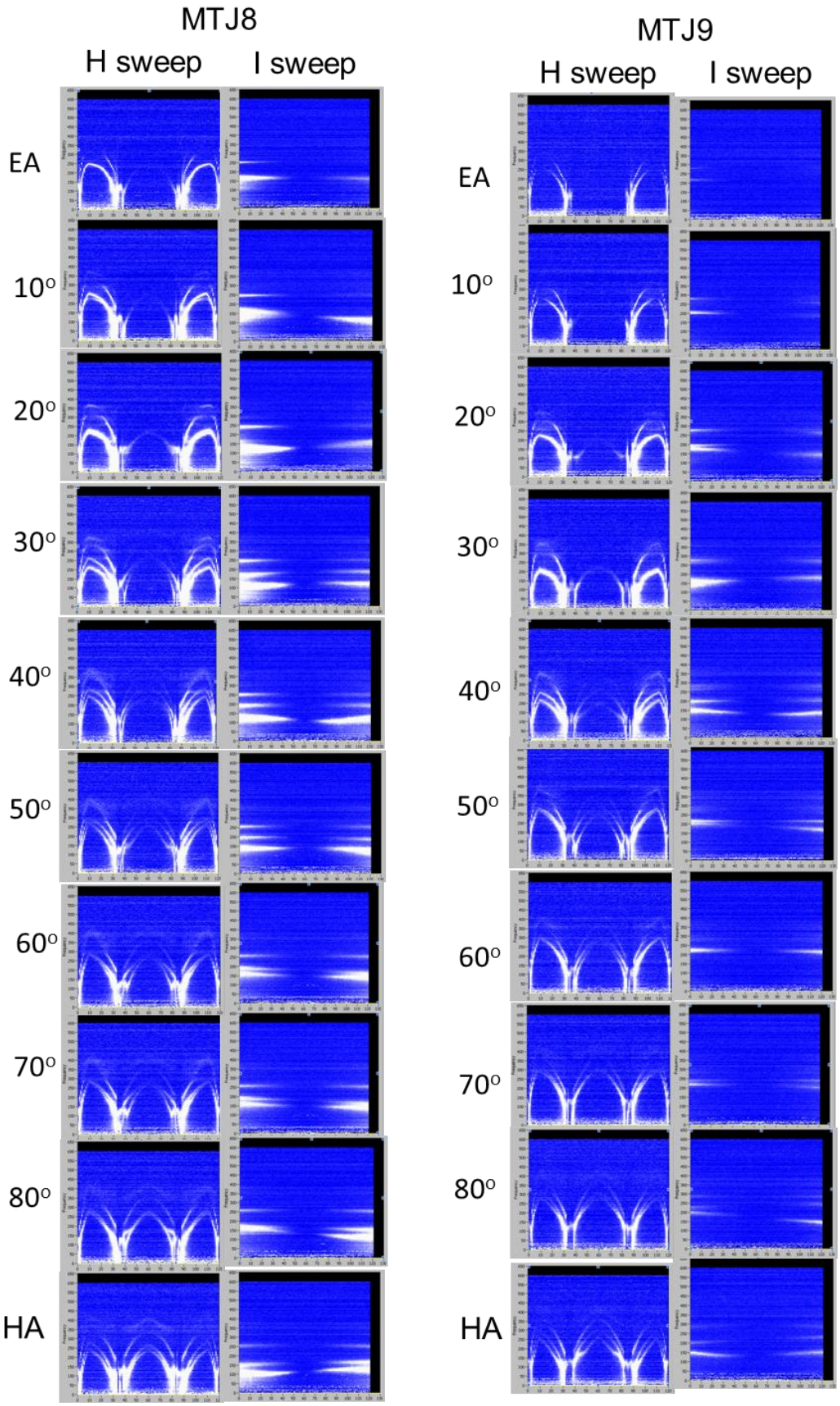

Figure A1.1.5 Screen shot spectra taken from field sweeps (H sweep) and current sweeps (I sweep) from the EA to the HA for MTJ6 (left) and MTJ7 (right).

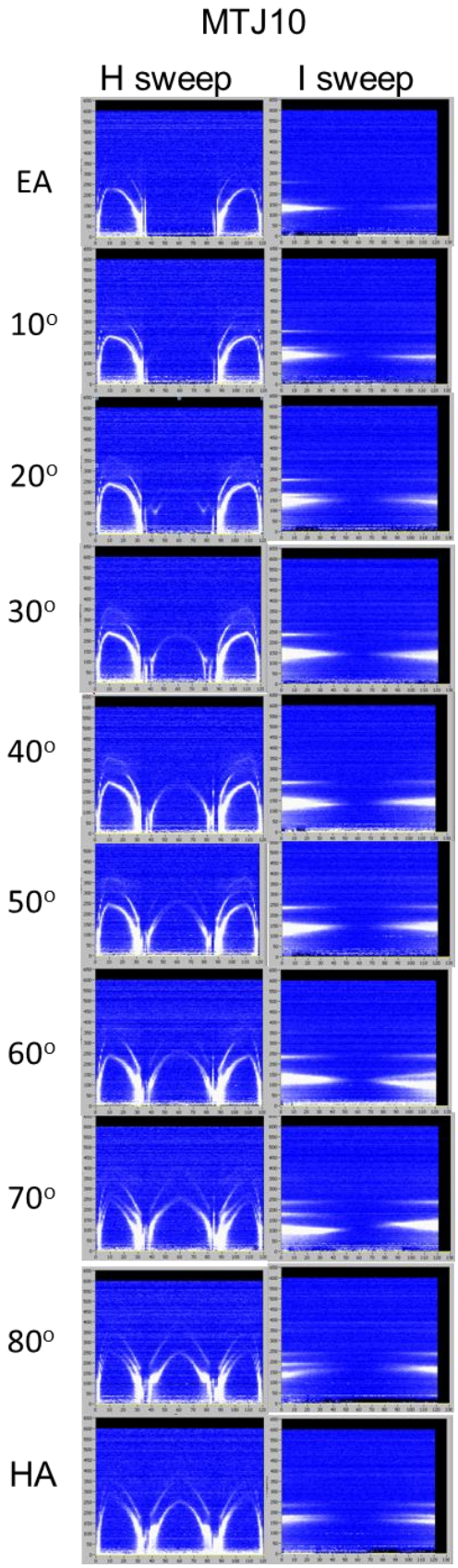

Figure A1.1.6 Screen shot spectra taken from field sweeps (H sweep) and current sweeps (I sweep) from the EA to the HA for MTJ10.

A1.2 Dynamic Susceptibility: spin valve with rigid reference layer and STT

We restrict the calculation to an in-plane bias field **H** parallel to the *z'* axis so that the equilibrium direction of the magnetisation **M** is also in-plane, parallel to the z axis. The *x* axis lies normal to the plane.

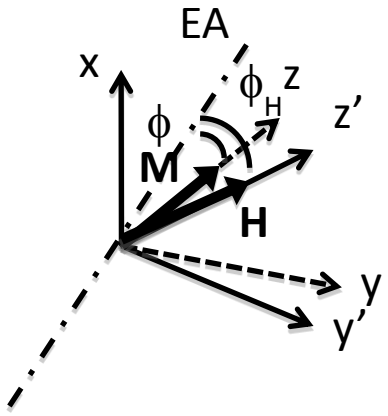

$$\frac{d\mathbf{M}}{dt} = -|\gamma|\mathbf{M}\times\mathbf{H}_{eff} + \frac{\alpha}{M}\mathbf{M}\times\frac{d\mathbf{M}}{dt} - a\mathbf{M}\times(\mathbf{M}\times\mathbf{p}) + \mathrm{b}(\mathbf{M}\times\mathbf{p}) \qquad \text{A1.2.1}$$

$$\frac{d\mathbf{u}}{dt} = -|\gamma|\mathbf{u}\times\mathbf{H}_{eff} + \frac{\alpha}{M}\mathbf{u}\times\frac{d\mathbf{u}}{dt} - aM\mathbf{u}\times(\mathbf{u}\times\mathbf{p}) + \mathrm{b}(\mathbf{u}\times\mathbf{p})$$

$$= -|\gamma|\mathbf{u}\times\left(\mathbf{H}_{eff} - \frac{b}{|\gamma|}\mathbf{p} + a\frac{M}{|\gamma|}\mathbf{u}\times\mathbf{p} - \frac{\alpha}{|\gamma|}\frac{d\mathbf{u}}{dt}\right)$$

A1.2.2

The calculation is intended to be applicable to magnetic tunnel valve noise measurements in which the static field is applied at different angles with respect to the exchange bias direction of the pinned layer. We will assume that the pinned layer is rigid and that the free layer possesses both an in-plane uniaxial anisotropy and a perpendicular anisotropy. A general expression for the demagnetising energy of an oblate ellipsoid will be used so that free elements of elliptical shape can be described. Dipolar coupling between the free and pinned layers may be introduced by adding a current-independent contribution to the coefficient *b* in the field-like spin transfer torque term (STT) term. We begin from the free energy density needed to calculate the effective field $\mathbf{H}_{eff}$.

$$E = -\mathbf{M}\cdot(\mathbf{H}+\mathbf{h}) + \frac{1}{2}\mathbf{M}D\mathbf{M} - K\left(\mathbf{u}.\hat{\mathbf{k}}\right)^2 - K_{\perp}(\mathbf{u}.\hat{\mathbf{x}})^2 \qquad \text{A1.2.3}$$

where $\mathbf{H} = H\mathbf{k}' = Hsin(\phi_H - \phi)\mathbf{j} + Hcos(\phi_H - \phi)\mathbf{k}$

$$\mathbf{h} = h_x\mathbf{i}' + h_y\mathbf{j}' + h_z\mathbf{k}'$$

and in the thin film limit $D_{xx} = 4\pi, D_{yy} = D_{zz} = 0$.

The LLG equation will be solved in the coordinate system defined by the static magnetisation, but we will want to know the susceptibility in the coordinate system defined by the field, so we must transform between the two systems.

$$\begin{pmatrix}\mathbf{i}\\ \mathbf{j}\\ \mathbf{k}\end{pmatrix} = \begin{pmatrix}1 & 0 & 0\\ 0 & cos\phi & sin\phi\\ 0 & -sin\phi & cos\phi\end{pmatrix}\begin{pmatrix}\mathbf{i}'\\ \mathbf{j}'\\ \mathbf{k}'\end{pmatrix}, \begin{pmatrix}\mathbf{i}'\\ \mathbf{j}'\\ \mathbf{k}'\end{pmatrix} = \begin{pmatrix}1 & 0 & 0\\ 0 & cos\phi & -sin\phi\\ 0 & sin\phi & cos\phi\end{pmatrix}\begin{pmatrix}\mathbf{i}\\ \mathbf{j}\\ \mathbf{k}\end{pmatrix} \qquad \text{A1.2.4}$$

$$E = -\mathbf{M}\cdot(\mathbf{H}+\mathbf{h}) + \frac{1}{2}\mathbf{M}D\mathbf{M} - K\left(\mathbf{u}.\hat{\mathbf{k}}\right)^2 - K_\perp(\mathbf{u}.\hat{\mathbf{x}})^2$$

$$\begin{aligned}E = -\left(m_x\mathbf{i} + m_y\mathbf{j} + (M+m_z)\mathbf{k}\right)&\\ \cdot\left(h_x\mathbf{i} + \left(Hsin(\phi_H-\phi)+h_y\right)\mathbf{j} + (Hcos(\phi_H-\phi)+h_z)\mathbf{k}\right)&\\ +\frac{1}{2}\left(\left(D_{xx}-\frac{2K_\perp}{M^2}\right){m_x}^2 + D_{yy}{m_y}^2 + D_{zz}(M+m_z)^2\right)&\\ -\frac{K}{M^2}\left(\left(m_x\mathbf{i}+m_y\mathbf{j}+(M+m_z)\mathbf{k}\right)\cdot(-sin\phi\mathbf{j}+cos\phi\mathbf{k})\right)&\end{aligned}$$

$$\begin{aligned}E = -\left(m_xh_x + m_y\left(Hsin(\phi_H-\phi)+h_y\right) + (M+m_z)(Hcos(\phi_H-\phi)+h_z)\right)&\\ +\frac{1}{2}\left(\left(D_{xx}-\frac{2K_\perp}{M^2}\right){m_x}^2 + D_{yy}{m_y}^2 + D_{zz}(M+m_z)^2\right)&\\ -\frac{K}{M^2}\left(-m_ysin\phi + (M+m_z)cos\phi\right)^2&\end{aligned}$$

$$\begin{aligned}E = -M\left(u_xh_x + u_y\left(Hsin(\phi_H-\phi)+h_y\right) + (1+u_x)(Hcos(\phi_H-\phi)+h_z)\right) +&\\ \frac{M^2}{2}\left(\left(D_{xx}-\frac{2K_\perp}{M^2}\right)u_x^2 + D_{yy}u_y^2 + D_{zz}(1+u_z)^2\right) - K\left(-u_ysin\phi + (1+u_z)cos\phi\right)^2&\end{aligned} \qquad \text{A1.2.5}$$

The equilibrium configuration is obtained when **m**=**h**=0 and in the absence of STT is given by

$$\frac{\partial E}{\partial\phi} = -MHsin(\phi_H-\phi) + 2Ksin\phi cos\phi = 0 \qquad \text{A1.2.6}$$

The effective fields acting on the magnetisation are obtained from $\mathbf{H}_{eff} = -\frac{1}{M}\nabla_{\mathbf{u}}E$

$$E = -M\left(u_x h_x + u_y\left(Hsin(\phi_H - \phi) + h_y\right) + (1+u_x)(Hcos(\phi_H - \phi) + h_z)\right)$$
$$+\frac{M^2}{2}\left(\left(D_{xx} - \frac{2K_\perp}{M^2}\right)u_x^2 + D_{yy}u_y^2 + D_{zz}(1+u_z)^2\right)$$
$$-K\left(-u_y sin\phi + (1+u_z)cos\phi\right)^2$$

We write the unit vector $\mathbf{p}$ as $\mathbf{p} = sin(\phi_p - \phi)\mathbf{j} + cos(\phi_p - \phi)\mathbf{k}$ so that

$$\mathbf{u}\times\mathbf{p} = \begin{vmatrix} \mathbf{i} & \mathbf{j} & \mathbf{k} \\ u_x & u_y & u_z \\ \mathbf{0} & sin(\phi_p - \phi) & cos(\phi_p - \phi) \end{vmatrix}$$

$$= \left(u_y cos(\phi_p - \phi) - (1+u_z)sin(\phi_p - \phi)\right)\mathbf{i} - u_x cos(\phi_p - \phi)\mathbf{j} + u_x sin(\phi_p - \phi)\mathbf{k}$$

A1.2.7

The Landau-Lifshitz-Gilbert equation is written as

$$\frac{d\mathbf{u}}{dt} = -|\gamma|\mathbf{u}\times\left(\mathbf{H}_{eff} - \frac{b}{|\gamma|}\mathbf{p} + a\frac{M}{|\gamma|}\mathbf{u}\times\mathbf{p} - \frac{\alpha}{|\gamma|}\frac{d\mathbf{u}}{dt}\right) \qquad \text{A1.2.8}$$

$$\mathbf{p} = sin(\phi_p - \phi)\mathbf{j} + cos(\phi_p - \phi)\mathbf{k}$$

$\mathbf{u}\times\mathbf{p} = \left(u_y cos(\phi_p - \phi) - (1+u_z)sin(\phi_p - \phi)\right)\mathbf{i} - u_x cos(\phi_p - \phi)\mathbf{j} + u_x sin(\phi_p - \phi)\mathbf{k}$

$$\begin{pmatrix} \dot{u}_x \\ \dot{u}_y \\ \dot{u}_y \end{pmatrix}$$
$$= \begin{pmatrix} -|\gamma|\begin{bmatrix} u_y\left(H_{eff,z} - \frac{b}{|\gamma|}cos(\phi_p - \phi) + \frac{\alpha M}{|\gamma|}u_x sin(\phi_p - \phi) - \frac{\alpha}{|\gamma|}\dot{u}_x\right) \\ -(1+u_z)\left(H_{eff,y} - \frac{b}{|\gamma|}sin(\phi_p - \phi) - \frac{\alpha M}{|\gamma|}u_x cos(\phi_p - \phi) - \frac{\alpha}{|\gamma|}\dot{u}_y\right)\end{bmatrix} \\ -|\gamma|\begin{bmatrix}(1+u_z)\left(H_{eff,x} + \frac{\alpha M}{|\gamma|}\left(u_y cos(\phi_p - \phi) - (1+u_z)sin(\phi_p - \phi)\right) - \frac{\alpha}{|\gamma|}\dot{u}_x\right) \\ -u_x\left(H_{eff,z} - \frac{b}{|\gamma|}cos(\phi_p - \phi) + \frac{\alpha M}{|\gamma|}u_x sin(\phi_p - \phi) - \frac{\alpha}{|\gamma|}\dot{u}_y\right)\end{bmatrix} \\ -|\gamma|\begin{bmatrix} u_x\left(H_{eff,y} - \frac{b}{|\gamma|}sin(\phi_p - \phi) - \frac{\alpha M}{|\gamma|}u_x cos(\phi_p - \phi) - \frac{\alpha}{|\gamma|}\dot{u}_y\right) \\ -u_y\left(H_{eff,x} + \frac{\alpha M}{|\gamma|}\left(u_y cos(\phi_p - \phi) - (1+u_z)sin(\phi_p - \phi)\right) - \frac{\alpha}{|\gamma|}\dot{u}_x\right)\end{bmatrix}\end{pmatrix}$$

A1.2.9

At this point we linearize the equations by assuming

$$u_x, u_y \ll 1, 1 + u_x = \sqrt{1 - u_x^2 - u_y^2} \approx 1 - \frac{1}{2}\left(u_x^2 + u_y^2\right) \approx 1$$

$$h_x, h_y, h_z \ll H, 2K/M$$

and then retaining only 1st order terms from the equations of motion

$$\begin{pmatrix} \dot{u}_x \\ \dot{u}_y \\ 0 \end{pmatrix} = \begin{pmatrix} -|\gamma| \begin{bmatrix} u_y \left(H_{eff,z} - \frac{b}{|\gamma|} cos(\phi_p - \phi) \right) \\ -\left(\left(H_{eff,y} - \frac{b}{|\gamma|} sin(\phi_p - \phi) - \frac{\alpha M}{|\gamma|} u_x cos(\phi_p - \phi) - \frac{\alpha}{|\gamma|} \dot{u}_y \right) \right) \end{bmatrix} \\ -|\gamma| \begin{bmatrix} \left(H_{eff,x} + \frac{\alpha M}{|\gamma|} \left(u_y cos(\phi_p - \phi) - sin(\phi_p - \phi) \right) - \frac{\alpha}{|\gamma|} \dot{u}_x \right) \\ -u_x \left(H_{eff,z} - \frac{b}{|\gamma|} cos(\phi_p - \phi) \right) \end{bmatrix} \\ -|\gamma| \begin{bmatrix} u_x \left(H_{eff,y} - \frac{b}{|\gamma|} sin(\phi_p - \phi) \right) \\ -u_y \left(H_{eff,x} - \frac{\alpha M}{|\gamma|} sin(\phi_p - \phi) \right) \end{bmatrix} \end{pmatrix}$$

A1.2.10

Substituting in the expression for $\mathbf{H}_{eff}$ and again keeping lowest order terms

$$\mathbf{H}_{eff} = \mathbf{i}\left[h_x - \left(D_{xx} - \frac{2K_\perp}{M^2} \right) M u_x \right]$$
$$+\mathbf{j}\left[\left(H\, sin(\phi_H - \phi) + h_y \right) - D_{yy} M u_y - 2K sin\phi \left(-u_y sin\phi + (1 + u_z) cos\phi \right) \right]$$
$$+\mathbf{k}\left[(H\, cos(\phi_H - \phi) + h_z) - D_{zz} M (1 + u_z) + 2K cos\phi \left(-u_y sin\phi + (1 + u_z) cos\phi \right) \right]$$

A1.2.11

$$\begin{pmatrix} \dot{u}_x \\ \dot{u}_y \\ 0 \end{pmatrix} = \begin{pmatrix} -|\gamma| \begin{bmatrix} u_y \left(Hcos(\phi_H - \phi) - D_{zz}M + 2Kcos(\phi_p - \phi)^2 - \frac{b}{|\gamma|} cos(\phi_p - \phi) \right) \\ \begin{pmatrix} Hsin(\phi_H - \phi) + h_y - D_{yy}Mu_y - 2Ksin\phi(-u_y sin\phi + cos\phi) \\ -\frac{b}{|\gamma|} sin(\phi_p - \phi) - \frac{\alpha M}{|\gamma|} u_x cos(\phi_p - \phi) - \frac{\alpha}{|\gamma|} \dot{u}_y \end{pmatrix} \end{bmatrix} \\ -|\gamma| \begin{bmatrix} h_x - \left(D_{xx} - \frac{2K_\perp}{M^2} \right) Mu_x + \left(\frac{\alpha M}{|\gamma|} \left(u_y cos(\phi_p - \phi) - sin(\phi_p - \phi) \right) - \frac{\alpha}{|\gamma|} \dot{u}_x \right) \\ -u_x \left(Hcos(\phi_H - \phi) - D_{zz}M + 2Kcos^2\phi - \frac{b}{|\gamma|} cos(\phi_p - \phi) \right) \end{bmatrix} \\ -|\gamma| \begin{bmatrix} u_x \left(Hsin(\phi_H - \phi) - 2Ksin\phi cos\phi - \frac{b}{|\gamma|} sin(\phi_p - \phi) \right) \\ -u_y \left(-\frac{\alpha M}{|\gamma|} sin(\phi_p - \phi) \right) \end{bmatrix} \end{pmatrix}$$

A1.2.12

We simplify further by grouping zeroth and 1st order terms. The STT terms as assumed to be of 1st order.

$$\begin{pmatrix} \dot{u}_x \\ \dot{u}_y \\ 0 \end{pmatrix} = \begin{pmatrix} -|\gamma| \begin{bmatrix} u_y \left(Hcos(\phi_H - \phi) - D_{zz}M + 2Kcos^2\phi - \frac{b}{|\gamma|} cos(\phi_p - \phi) \right) \\ \begin{pmatrix} Hsin(\phi_H - \phi) + h_y - D_{yy}Mu_y - 2Ksin\phi(-u_y sin\phi + cos\phi) \\ -\frac{b}{|\gamma|} sin(\phi_p - \phi) - \frac{\alpha M}{|\gamma|} u_x cos(\phi_p - \phi) - \frac{\alpha}{|\gamma|} \dot{u}_y \end{pmatrix} \end{bmatrix} \\ -|\gamma| \begin{bmatrix} h_x - \left(D_{xx} - \frac{2K_\perp}{M^2} \right) Mu_x + \left(\frac{\alpha M}{|\gamma|} \left(u_y cos(\phi_p - \phi) - sin(\phi_p - \phi) \right) - \frac{\alpha}{|\gamma|} \dot{u}_x \right) \\ -u_x \left(Hcos(\phi_H - \phi) - D_{zz}M + 2Kcos^2\phi - \frac{b}{|\gamma|} cos(\phi_p - \phi) \right) \end{bmatrix} \\ -|\gamma| \begin{bmatrix} u_x \left(Hsin(\phi_H - \phi) - 2Ksin\phi cos\phi - \frac{b}{|\gamma|} sin(\phi_p - \phi) \right) \\ -u_y \left(-\frac{\alpha M}{|\gamma|} sin(\phi_p - \phi) \right) \end{bmatrix} \end{pmatrix}$$

A1.2.13

The 2nd term in the 3rd row on the RHS may be of 2nd order and from the static condition

$$Hsin(\phi_H - \phi) - 2Ksin\phi cos\phi - \tfrac{b}{|\gamma|} sin(\phi_p - \phi) = 0 \qquad \text{A1.2.14}$$

so that

$$\begin{pmatrix}\dot{u}_x\\ \dot{u}_y\end{pmatrix} = \begin{pmatrix} -|\gamma|\left[u_y\left(H\cos(\phi_H-\phi)+(D_{yy}-D_{zz})M+2K\cos^2\phi-\frac{b}{|\gamma|}\cos(\phi_p-\phi)\right)\right] \\ -|\gamma|\left[\left(-H\cos(\phi_H-\phi)-(D_{xx}-D_{zz})M+\frac{2K_\perp}{M^2}-2K\cos^2\phi+\frac{b}{|\gamma|}\cos(\phi_p-\phi)\right)u_x\right] \end{pmatrix}$$
$$\begin{pmatrix} -h_y+\frac{\alpha M}{|\gamma|}u_x\cos(\phi_p-\phi)+\frac{\alpha}{|\gamma|}\dot{u}_y \\ +\frac{\alpha M}{|\gamma|}u_y\cos(\phi_p-\phi)-\frac{\alpha M}{|\gamma|}\sin(\phi_p-\phi)-\frac{\alpha}{|\gamma|}\dot{u}_x+h_x \end{pmatrix}$$

A1.2.15

The presence of the 3rd to last term on the RHS of the 2nd row suggests that the static solution is incorrect. This can be repaired by allowing the magnetisation to cant slightly out of plane. We already allowed for canting within the plane through inclusion of the variable ϕ. Rather than begining the calculation again we instead let

$$u_x(t)=u_{xs}+u_{xd}(t)\quad,\quad u_y(t)=u_{ys}+u_{yd}(t) \qquad \text{A1.2.16}$$

We revisit the previous page and consider the static case by setting the driving field and all time derivatives equal to zero, then

$$\begin{pmatrix}0\\0\\0\end{pmatrix} = \begin{pmatrix} -|\gamma|\left[u_{ys}\left(H\cos(\phi_H-\phi)+(D_{yy}-D_{zz})M+2K\cos 2\phi-\frac{b}{|\gamma|}\cos(\phi_p-\phi)\right)\right] \\ -|\gamma|\left[+\frac{\alpha M}{|\gamma|}u_{xs}\cos(\phi_p-\phi)-\left(H\sin(\phi_H-\phi)-2K\sin\phi\cos\phi-\frac{b}{|\gamma|}\sin(\phi_p-\phi)\right)\right] \\ -|\gamma|\left[\left(-H\cos(\phi_H-\phi)-(D_{xx}-D_{zz})M+\frac{2K_\perp}{M}-2K\cos^2\phi+\frac{b}{|\gamma|}\cos(\phi_p-\phi)\right)u_{xs}\right] \\ -|\gamma|\left[u_{xs}\left(H\sin(\phi_H-\phi)-2K\sin\phi\cos\phi-\frac{b}{|\gamma|}\sin(\phi_p-\phi)\right)\right] \end{pmatrix}$$
$$\begin{pmatrix} \\ \\ +\frac{\alpha M}{|\gamma|}u_{ys}\cos(\phi_p-\phi)-\frac{\alpha M}{|\gamma|}\sin(\phi_p-\phi) \\ -u_{ys}\left(-\frac{\alpha M}{|\gamma|}\sin(\phi_p-\phi)\right) \end{pmatrix}$$

A1.2.17

We anticipate that ϕ can be chosen so that u_{ys} = 0, so from the 2nd row we choose

$u_{xs} =$

$$-\frac{\alpha M}{|\gamma|}sin(\phi_p-\phi)\left[Hcos(\phi_H-\phi)+(D_{xx}-D_{zz})M-\frac{2K_\perp}{M}+2Kcos^2\phi-\frac{b}{|\gamma|}cos(\phi_p-\phi)\right]^{-1}$$

A1.2.18

This should be small because the STT is small in the sub-threshold regime and because the demagnetizing field term within the square bracket is large. This implies that the term in u_{xs} in the first row is small and can be neglected, in which case the remaining static equations are satisfied when u_{ys} = 0 and

$$Hsin(\phi_H-\phi)-2Ksin\phi cos\phi-\frac{b}{|\gamma|}sin(\phi_p-\phi)=0 \qquad \text{A1.2.19}$$

An alternative strategy is to assume that the angle between **M** and **H** is small so that we can set $\phi=\phi_H$ and solve for u_{xs} and u_{ys} instead. This amounts to assuming that the Zeeman energy dominates

$$\begin{pmatrix} \frac{aM}{|\gamma|}cos(\phi_p-\phi_H)u_{xs}+\left[H+(D_{yy}-D_{zz})M+2Kcos2\phi_H-\frac{b}{|\gamma|}cos(\phi_p-\phi_H)\right]u_{ys} \\ -\left(H+(D_{xx}-D_{zz})M-\frac{2K_\perp}{M}+2Kcos^2\phi_H-\frac{b}{|\gamma|}cos(\phi_p-\phi_H)\right)u_{xs}+\frac{aM}{|\gamma|}cos(\phi_p-\phi_H)u_{ys} \\ \left(-2Ksin\phi_H cos\phi_H-\frac{b}{|\gamma|}cos(\phi_p-\phi_H)\right)u_{xs}+\frac{aM}{|\gamma|}sin(\phi_p-\phi_H)u_{ys} \end{pmatrix} = \begin{pmatrix} -2Ksin\phi_H cos\phi_H-\frac{b}{|\gamma|}sin(\phi_p-\phi_H) \\ \frac{aM}{|\gamma|}sin(\phi_p-\phi_H) \\ 0 \end{pmatrix} \qquad \text{A1.2.20}$$

For a self-consistent solution to exist i.e. are the 3 equations must be linearly dependent. The equations are of the form

$$\begin{pmatrix} Au_{xs}+Bu_{ys} \\ Cu_{xs}+Au_{ys} \\ Du_{xs}+Eu_{ys} \end{pmatrix}=\begin{pmatrix} D \\ E \\ 0 \end{pmatrix},\ \begin{pmatrix} Au_{xs}+\frac{BD}{E}u_{xs} \\ Cu_{xs}+\frac{AD}{E}u_{xs} \\ Du_{xs}+Eu_{ys} \end{pmatrix}=\begin{pmatrix} D \\ E \\ 0 \end{pmatrix} \qquad \text{A1.2.21}$$

This seems possible only if the brackets containing H dominate, but then the calculation becomes as approximate as that outlined previously.

To progress further we assume that the small out of plane canting of the magnetisation exist, in which case we can neglect the lowest order STT term in the second row and we will understand u_x to mean u_{xd}.

$$\begin{pmatrix}\dot{u}_x\\ \dot{u}_y\end{pmatrix}$$

$$= \begin{pmatrix} -|\gamma|\left[u_y\left(Hcos(\phi_H-\phi)+\left(D_{yy}-D_{zz}\right)M+2Kcos2\phi-\frac{b}{|\gamma|}cos\left(\phi_p-\phi\right)\right)\right. \\ \left. -h_y+\frac{aM}{|\gamma|}cos\left(\phi_p-\phi\right)u_x+\frac{\alpha}{|\gamma|}u_y\acute{Y}\right] \\ -|\gamma|\left[\left(-Hcos(\phi_H-\phi)-(D_{xx}-D_{zz})M+\frac{2K_\perp}{M}-\frac{2K}{M}cos^2\phi+\frac{b}{|\gamma|}cos\left(\phi_p-\phi\right)\right)u_x\right. \\ \left. +\frac{aM}{|\gamma|}cos\left(\phi_p-\phi\right)u_y-\frac{\alpha}{|\gamma|}u_x\acute{Y}+h_x\right] \end{pmatrix}$$

A1.2.22

So that the equations of motion may finally be written as

$$\dot{u}_x+\alpha\dot{u}_y+|\gamma|\left[Hcos(\phi_H-\phi)+\left(D_{yy}-D_{zz}\right)M+2Kcos2\phi-\frac{b}{|\gamma|}cos\left(\phi_p-\phi\right)\right]u_y+$$
$$aMu_xcos\left(\phi_p-\phi\right)=|\gamma|h_y \qquad \text{A1.2.22}$$

$$\dot{u}_y-\alpha\dot{u}_x-|\gamma|\left[Hcos(\phi_H-\phi)+(D_{xx}-D_{zz})M-\frac{2K_\perp}{M}+\frac{2K}{M}cos^2\phi-\frac{b}{|\gamma|}cos\left(\phi_p-\right.\right.$$
$$\left.\left.\phi\right)\right]u_x+aMcos\left(\phi_p-\phi\right)u_y=-|\gamma|h_x\ . \qquad \text{A1.2.23}$$

Looking for harmonic solutions of form

$$h_x=h_{x0}exp(-i\omega t),h_y=h_{y0}exp(-i\omega t),u_x=u_{x0}exp(-i\omega t),u_y=u_{y0}exp(-i\omega t)$$

$$-i\omega u_{x0}-i\omega\alpha u_{y0}+|\gamma|\left[Hcos(\phi_H-\phi)+\left(D_{yy}-D_{zz}\right)M+2Kcos2\phi-\frac{b}{|\gamma|}cos\left(\phi_p-\right.\right.$$
$$\left.\left.\phi\right)\right]u_{y0}+aMu_{x0}cos\left(\phi_p-\phi\right)=|\gamma|h_{y0} \qquad \text{A1.2.24}$$

$$-i\omega u_{y0}+i\omega\alpha u_{x0}-|\gamma|\left[Hcos(\phi_H-\phi)+(D_{xx}-D_{zz})M-\frac{2K_\perp}{M}+\frac{2K}{M}cos^2\phi\right.$$
$$\left.-\frac{b}{|\gamma|}cos\left(\phi_p-\phi\right)\right]u_{x0}+$$
$$aMcos\left(\phi_p-\phi\right)u_{y0}=-|\gamma|h_{x0} \qquad \text{A1.2.25}$$

$$\begin{pmatrix}\left[Hcos(\phi_H-\phi)+(D_{xx}-D_{zz})M-\frac{2K_\perp}{M}\right. & -\left[\frac{aM}{|\gamma|}cos\left(\phi_p-\phi\right)-\frac{i\omega}{|\gamma|}\right] \\ \left.+\frac{2K}{M}cos^2\phi-\frac{b}{|\gamma|}cos\left(\phi_p-\phi\right)-\frac{i\omega\alpha}{|\gamma|}\right] & \\ \left[\frac{aM}{|\gamma|}cos\left(\phi_p-\phi\right)-\frac{i\omega}{|\gamma|}\right] & \left[Hcos(\phi_H-\phi)+\left(D_{yy}-D_{zz}\right)M\right. \\ & \left.+\frac{2K}{M}cos2\phi-\frac{b}{|\gamma|}cos\left(\phi_p-\phi\right)-\frac{i\omega\alpha}{|\gamma|}\right]\end{pmatrix}\begin{pmatrix}u_{x0}\\ u_{y0}\end{pmatrix}=\begin{pmatrix}h_{x0}\\ h_{y0}\end{pmatrix}$$

A1.2.26

The inverse of a 2x2 matrix $\begin{pmatrix} A & B \\ C & D \end{pmatrix}$ is $\frac{1}{(AD-BC)}\begin{pmatrix} D & -B \\ -C & A \end{pmatrix}$ and so we can write

$$\begin{pmatrix} u_{x0} \\ u_{y0} \end{pmatrix}$$

$$= \frac{1}{\Delta}\begin{bmatrix} \begin{bmatrix} Hcos(\phi_H - \phi) + (D_{yy} - D_{zz})M \\ +\frac{2K}{M}cos2\phi - \frac{b}{|\gamma|}cos(\phi_p - \phi) - \frac{i\omega\alpha}{|\gamma|} \end{bmatrix} & \left[\frac{aM}{|\gamma|}cos(\phi_p - \phi) - \frac{i\omega}{|\gamma|}\right] \\ -\left[\frac{aM}{|\gamma|}cos(\phi_p - \phi) - \frac{i\omega}{|\gamma|}\right] & \begin{bmatrix} Hcos(\phi_H - \phi) + (D_{xx} - D_{zz})M - \frac{2K_\perp}{M} \\ +\frac{2K}{M}cos^2\phi - \frac{b}{|\gamma|}cos(\phi_p - \phi) - \frac{i\omega\alpha}{|\gamma|} \end{bmatrix} \end{bmatrix}\begin{pmatrix} h_{x0} \\ h_{y0} \end{pmatrix}$$

$$= \frac{1}{M}\chi\begin{pmatrix} h_{x0} \\ h_{y0} \end{pmatrix} \qquad \text{A1.2.27}$$

where

$\Delta =$

$$\begin{bmatrix} Hcos(\phi_H - \phi) + (D_{yy} - D_{zz})M \\ +\frac{2K}{M}cos2\phi - \frac{b}{|\gamma|}cos(\phi_p - \phi) - \frac{i\omega\alpha}{|\gamma|} \end{bmatrix}\begin{bmatrix} Hcos(\phi_H - \phi) + (D_{xx} - D_{zz})M - \frac{2K_\perp}{M} \\ +\frac{2K}{M}cos^2\phi - \frac{b}{|\gamma|}cos(\phi_p - \phi) - \frac{i\omega\alpha}{|\gamma|} \end{bmatrix} +$$

$$\left[\frac{aM}{|\gamma|}cos(\phi_p - \phi) - \frac{i\omega}{|\gamma|}\right]^2$$

$$\Delta = \begin{bmatrix} Hcos(\phi_H - \phi) + (D_{yy} - D_{zz})M \\ +\frac{2K}{M}cos2\phi - \frac{b}{|\gamma|}cos(\phi_p - \phi) \end{bmatrix}\begin{bmatrix} Hcos(\phi_H - \phi) + (D_{xx} - D_{zz})M - \frac{2K_\perp}{M} \\ +\frac{2K}{M}cos^2\phi - \frac{b}{|\gamma|}cos(\phi_p - \phi) \end{bmatrix}$$

$$-\left(\frac{\alpha\omega}{|\gamma|}\right)^2$$

$$-\frac{i\omega\alpha}{|\gamma|}\left[2Hcos(\phi_H - \phi) + (D_{xx} + D_{yy} - 2D_{zz})M - \frac{2K_\perp}{M}\right.$$

$$\left. + \frac{2K}{M}(cos2\phi + cos^2\phi) - \frac{2b}{|\gamma|}cos(\phi_p - \phi)\right] + \left[\frac{aM}{|\gamma|}cos(\phi_p - \phi)\right]^2$$

$$-\left(\frac{\omega}{|\gamma|}\right)^2 - 2\frac{i\omega}{|\gamma|}\frac{aM}{|\gamma|}cos(\phi_p - \phi)$$

$$\Delta = \begin{bmatrix} Hcos(\phi_H - \phi) + (D_{yy} - D_{zz})M \\ +\frac{2K}{M}cos2\phi - \frac{b}{|\gamma|}cos(\phi_p - \phi) \end{bmatrix}\begin{bmatrix} Hcos(\phi_H - \phi) + (D_{xx} - D_{zz})M - \frac{2K_\perp}{M} \\ +\frac{2K}{M}cos^2\phi - \frac{b}{|\gamma|}cos(\phi_p - \phi) \end{bmatrix} +$$

$$\left[\frac{aM}{|\gamma|}cos(\phi_p - \phi)\right]^2 - \left(\frac{\omega}{|\gamma|}\right)^2(1 + \alpha^2) - \frac{i\omega\alpha}{|\gamma|}\left[2Hcos(\phi_H - \phi) + (D_{xx} + D_{yy} - \right.$$

$$\left. 2D_{zz})M - \frac{2K_\perp}{M} + \frac{2K}{M}(cos2\phi + cos^2\phi) - \frac{2b}{|\gamma|}cos(\phi_p - \phi)\right] - 2\frac{i\omega}{|\gamma|}\frac{aM}{|\gamma|}cos(\phi_p - \phi)$$

A1.2.28

We assume that the centre of the resonance coincides with a minimum in the value of Δ and hence $|\Delta|^2$.

$$|\Delta|^2 = \left\{\begin{bmatrix} Hcos(\phi_H-\phi)+(D_{yy}-D_{zz})M \\ +\frac{2K}{M}cos2\phi-\frac{b}{|\gamma|}cos(\phi_p-\phi)\end{bmatrix}\begin{bmatrix} Hcos(\phi_H-\phi)+(D_{xx}-D_{zz})M-\frac{2K_\perp}{M} \\ +\frac{2K}{M}cos^2\phi-\frac{b}{|\gamma|}cos(\phi_p-\phi)\end{bmatrix}+\left[\frac{aM}{|\gamma|}cos(\phi_p-\phi)\right]^2-\left(\frac{\omega}{|\gamma|}\right)^2(1+\alpha^2)\right\}^2+\left\{\frac{\omega\alpha}{|\gamma|}\left[2Hcos(\phi_H-\phi)+(D_{xx}+D_{yy}-2D_{zz})M-\frac{2K_\perp}{M}+\frac{2K}{M}(cos2\phi+cos^2\phi)-\frac{2b}{|\gamma|}cos(\phi_p-\phi)\right]+2\frac{i\omega}{|\gamma|}\frac{aM}{|\gamma|}cos(\phi_p-\phi)\right\}^2$$

A1.2.29

Notice that the second curly bracket contains terms of second order in the damping and STT which can be neglected. Likewise 2nd order terms can be neglected in the first bracket so that

$$|\Delta| \approx \left\{\begin{bmatrix} Hcos(\phi_H-\phi)+(D_{yy}-D_{zz})M \\ +\frac{2K}{M}cos2\phi-\frac{b}{|\gamma|}cos(\phi_p-\phi)\end{bmatrix}\begin{bmatrix} Hcos(\phi_H-\phi)+(D_{xx}-D_{zz})M-\frac{2K_\perp}{M} \\ +\frac{2K}{M}cos^2\phi-\frac{b}{|\gamma|}cos(\phi_p-\phi)\end{bmatrix}-\left(\frac{\omega}{|\gamma|}\right)^2\right\}$$

A1.2.30

And the resonance condition is therefore

$$\left(\frac{\omega}{|\gamma|}\right)^2 = \left[Hcos(\phi_H-\phi)+(D_{yy}-D_{zz})M+\frac{2K}{M}cos2\phi-\frac{b}{|\gamma|}cos(\phi_p-\phi)\right]\times\left[Hcos(\phi_H-\phi)+(D_{xx}-D_{zz})M-\frac{2K_\perp}{M}+\frac{2K}{M}cos^2\phi-\frac{b}{|\gamma|}cos(\phi_p-\phi)\right]$$

A1.2.31

The power absorption per cycle is generally of the form $-\frac{1}{2}\omega\mathbf{h}_0\mathrm{Im}(\chi)\mathbf{h}_0$which is proportional to $1/|\Delta|^2$. It is commonly assumed that this factor dominates the lineshape. So now we write

$$|\Delta|^2 = \left\{\left[\frac{aM}{|\gamma|}cos(\phi_p - \phi)\right]^2 - \left(\frac{\omega^2(1+\alpha^2) - \omega_{res}^2}{|\gamma|^2}\right)\right\}^2$$
$$+ \left\{\frac{\omega\alpha}{|\gamma|}\left[2Hcos(\phi_H - \phi) + (D_{xx} + D_{yy} - 2D_{zz})M - \frac{2K_\perp}{M}\right.\right.$$
$$\left.\left. + \frac{2K}{M}(cos2\phi + cos^2\phi) - \frac{2b}{|\gamma|}cos(\phi_p - \phi)\right]\right.$$
$$\left. + 2\frac{i\omega}{|\gamma|}\frac{aM}{|\gamma|}cos(\phi_p - \phi)\right\}^2$$

$$= \left\{\left[\frac{aM}{|\gamma|}cos(\phi_p - \phi)\right]^2 - \left(\frac{\omega^2(1+\alpha^2) - \omega_{res}^2}{|\gamma|^2}\right)\right\}^2$$
$$+ \left(\frac{\omega}{|\gamma|}\right)^2\left[\alpha H_a + 2\frac{aM}{|\gamma|}cos(\phi_p - \phi)\right]^2$$

A1.2.32

where

$$H_a = 2Hcos(\phi_H - \phi) + (D_{xx} + D_{yy} - 2D_{zz})M - \frac{2K_\perp}{M} + \frac{2K}{M}(cos2\phi + cos^2\phi) - \frac{2b}{|\gamma|}cos(\phi_p - \phi)$$

A1.2.33

$$|\Delta|^2 = \frac{1}{|\gamma|^4}\left\{\left\{[aMcos(\phi_p - \phi)]^2 - (\omega^2(1+\alpha^2) - \omega_{res}^2)\right\}^2 + \omega^2[\alpha|\gamma|H_a + 2aMcos(\phi_p - \phi)]^2\right\}$$

A1.2.34

In the absence of STT, and keeping only lowest terms in the damping constant

$$|\Delta|^2 = \frac{1}{|\gamma|^4}\{(\omega^2(1+\alpha^2) - \omega_{res}^2)^2 + \omega^2[\alpha|\gamma|H_a]^2\}$$

$$= \frac{1}{|\gamma|^4}\{\omega^4(1+\alpha^2)^2 - 2\omega_{res}^2\omega^2(1+\alpha^2) + \omega_{res}^4 + \omega^2[\alpha|\gamma|H_a]^2\}$$

$$= \frac{(1+\alpha^2)^2}{|\gamma|^4}\{\omega^4 - 2\omega_{res}^2\omega^2(1-\alpha^2) + \omega_{res}^4(1-2\alpha^2) + \omega^2(\alpha|\gamma|H_a)^2(1-2\alpha^2)\}$$

$$= \frac{(1+\alpha^2)^2}{|\gamma|^4}\{\omega^4 + \omega^2[(\alpha|\gamma|H_a)^2(1-2\alpha^2) - 2\omega_{res}^2(1-\alpha^2)] + \omega_{res}^4(1-2\alpha^2)\}$$

$$= \frac{(1+\alpha^2)^2}{|\gamma|^4}\{\omega^4 + \omega^2[(\alpha|\gamma|H_a)^2 - 2\omega_{res}^2(1-\alpha^2)] + \omega_{res}^4(1-2\alpha^2)\}$$

$$= \frac{(1+\alpha^2)^2}{|\gamma|^4}\left\{\left(\omega^2 + \frac{1}{2}(\alpha|\gamma|H_a)^2 - \omega_{res}^2(1-\alpha^2)\right)^2 - \left[\frac{1}{2}(\alpha|\gamma|H_a)^2 - \omega_{res}^2(1-\alpha^2)\right]^2 + \omega_{res}^4(1-2\alpha^2)\right\}$$

$$= \frac{(1+\alpha^2)^2}{|\gamma|^4}\left\{\left(\omega^2 + \frac{1}{2}(\alpha|\gamma|H_a)^2 - \omega_{res}^2(1-\alpha^2)\right)^2 + (\alpha|\gamma|H_a)^2\omega_{res}^2 - \omega_{res}^4(1-2\alpha^2) + \omega_{res}^4(1-2\alpha^2)\right\}$$

$$|\Delta|^2 = \frac{(1+\alpha^2)^2}{|\gamma|^4}\left\{\left(\omega^2 + \frac{1}{2}(\alpha|\gamma|H_a)^2 - \omega_{res}^2(1-\alpha^2)\right)^2 + \alpha^2(|\gamma|H_a)^2\omega_{res}^2\right\}$$

A1.2.35

Looking in the curly bracket we see that the denominator has a minimum when $\omega^2 = \omega_{res}^2(1-\alpha^2) - \frac{1}{2}(\alpha|\gamma|H_a)^2$.

So the resonance frequency is as we estimated previously but now with corrections of 2nd order that we can safely neglect, in which case the denominator gives rise to a simple Lorentzian lineshape of form

$$L(\omega) \sim \frac{1}{\Delta^2} \sim \{(\omega^2 - \omega_{res}^2)^2 + c^2\}^{-1} = \{z^2 + c^2\}^{-1} \qquad \text{A1.2.36}$$

Let us calculate the linewidth between the points where this curve has maximum gradient i.e. where

$\frac{d^2L}{dz^2} = 0 = \frac{d}{dz}\left(\frac{-2z}{(z^2+c^2)^2}\right) = \frac{8z^2-2(z^2+c^2)}{(z^2+c^2)^3} = \frac{6z^2-2c^2}{(z^2+c^2)^2}$ which has solution $z = \pm\frac{c}{\sqrt{3}}$ So that

$$\omega^2 = \omega_{res}^2 \pm \frac{c}{\sqrt{3}}\ , \omega = \omega_{res}\sqrt{1 \pm \frac{c}{\omega_{res}^2\sqrt{3}}} \approx \omega_{res} \pm \frac{c}{2\sqrt{3}\omega_{res}}$$

$$\Delta\omega = \frac{c}{\sqrt{3}\omega_{res}} = \frac{c}{\sqrt{3}\omega_{res}}\alpha\omega_{res}|\gamma|H_a = \frac{\alpha|\gamma|H_a}{\sqrt{3}} \qquad \text{A1.2.37}$$

We next repeat the working with STT included

$$|\Delta|^2 = \frac{1}{|\gamma|^4}\left\{\left\{\left[aMcos(\phi_p - \phi)\right]^2 - (\omega^2(1+\alpha^2) - \omega_{res}^2)\right\}^2 + \omega^2\left[\alpha|\gamma|H_a + 2aMcos(\phi_p - \phi)\right]^2\right\} = \frac{1}{|\gamma|^4}\{\{\omega_{STT}^2 - (\omega^2(1+\alpha^2) - \omega_{res}^2)\}^2 + \omega^2[\alpha\omega_a + 2\omega_{STT}]^2\}$$

$$= \frac{1}{|\gamma|^4}\{\omega_{STT}^4 - 2\omega_{STT}^2(\omega^2(1+\alpha^2) - \omega_{res}^2) + \omega^4(1+\alpha^2)^2 - 2\omega^2(1+\alpha^2)\omega_{res}^2 + \omega_{res}^4 + \omega^2[\alpha\omega_a + 2\omega_{STT}]^2\}$$

$$= \frac{1}{|\gamma|^4}\{\omega^4(1+\alpha^2)^2 + \omega^2[(\alpha\omega_a + 2\omega_{STT})^2 - 2\omega_{STT}^2(1+\alpha^2) - 2(1+\alpha^2)\omega_{res}^2 + \omega_{STT}^4 + \omega_{res}^4 + 2\omega_{res}^2\omega_{STT}^2]\}$$

$$= \frac{(1+\alpha^2)^2}{|\gamma|^4}\{\omega^4 + \omega^2[(1-2\alpha^2)(\alpha\omega_a + 2\omega_{STT})^2 - 2(1-\alpha^2)(\omega_{STT}^2 + \omega_{res}^2)] + (1-2\alpha^2)(\omega_{STT}^2 + \omega_{res}^2)^2\}$$

$$|\Delta|^2 = \frac{(1+\alpha^2)^2}{|\gamma|^4}\left\{\left[\omega^2 - (1-\alpha^2)(\omega_{STT}^2 + \omega_{res}^2) + \frac{1}{2}(1-2\alpha^2)(\alpha\omega_a + 2\omega_{STT})^2\right]^2 + (1-2\alpha^2)(\omega_{STT}^2 + \omega_{res}^2)^2 - (1-2\alpha^2)(\omega_{STT}^2 + \omega_{res}^2)^2 - \frac{1}{4}(1-4\alpha^2)(\alpha\omega_a + 2\omega_{STT})^4 + (1-3\alpha^2)(\omega_{STT}^2 + \omega_{res}^2)(\alpha\omega_a + 2\omega_{STT})^2\right\}$$

A1.2.38

And we consider ω_{STT} and $\alpha\omega_a$ to be small quantities that will only be retained to lowest order

$$|\Delta|^2 = \frac{(1+\alpha^2)^2}{|\gamma|^4}\left\{\left[\omega^2 - (1-\alpha^2)(\omega_{STT}^2 + \omega_{res}^2) + \frac{1}{2}(1-2\alpha^2)(\alpha\omega_a + 2\omega_{STT})^2\right]^2 - \frac{1}{4}(1-4\alpha^2)(\alpha\omega_a + 2\omega_{STT})^4 + (1-3\alpha^2)(\omega_{STT}^2 + \omega_{res}^2)(\alpha\omega_a + 2\omega_{STT})^2\right\}$$

$$= \frac{(1+\alpha^2)^2}{|\gamma|^4}\left\{\left[\omega^2 - \omega_{res}^2 + \alpha\omega_{res}^2 - \omega_{STT}^2 + \frac{1}{2}(\alpha\omega_a + 2\omega_{STT})^2\right]^2 + \omega_{res}^2(\alpha\omega_a + 2\omega_{STT})^2\right\}$$

A1.2.39

which reduces to the expression obtained previously when STT is neglected. Again we see that there are some second order corrections to the resonance frequency, while the frequency linewidth may now be written as

$$\Delta\omega = \frac{c}{\sqrt{3}\omega_{res}} = \frac{c}{\sqrt{3}\omega_{res}}\omega_{res}(\alpha\omega_a + 2\omega_{STT}) = \frac{(\alpha\omega_a + 2\omega_{STT})}{\sqrt{3}} = \frac{\left(\alpha|\gamma|H_a + 2aMcos(\phi_p - \phi)\right)}{\sqrt{3}}$$

A1.2.40

$$H_a = 2Hcos(\phi_H - \phi) + \left(D_{xx} + D_{yy} - 2D_{zz}\right)M - \frac{2K_\perp}{M} + \frac{2K}{M}(cos2\phi + cos^2\phi) - \frac{2b}{|\gamma|}cos\left(\phi_p - \phi\right)$$

The main results are the above expression and that obtained for the frequency

$$\left(\frac{\omega}{|\gamma|}\right)^2 = \left[Hcos(\phi_H - \phi) + \left(D_{yy} - D_{zz}\right)M + \frac{2K}{M}cos2\phi - \frac{b}{|\gamma|}cos\left(\phi_p - \phi\right)\right] \times \left[Hcos(\phi_H - \phi) + (D_{xx} - D_{zz})M - \frac{2K_\perp}{M} + \frac{2K}{M}cos^2\phi - \frac{b}{|\gamma|}cos\left(\phi_p - \phi\right)\right]$$

A1.2.41

They are consistent with Petit et al.[177] and Deac et al.[75] in that the Slonczewski damping term modifies the damping and hence the linewidth while the field-like term leads to a frequency shift (although note it also appears in the H_a term). However our expressions suggest that these effects gradually disappear as the free layer magnetisation is oriented close to that of the fixed layer through the application of an external field.

So far we calculated the dynamic susceptibility in the coordinate system defined by **M** the magnetisation. If **M** is canted from **H** then we may prefer the susceptibility in the primed coordinate system.

$$\begin{pmatrix} m_{x0} \\ m_{y0} \\ m_{z0} \end{pmatrix} = \begin{pmatrix} 1 & 0 & 0 \\ 0 & cos\phi & sin\phi \\ 0 & -sin\phi & cos\phi \end{pmatrix}\begin{pmatrix} m_{x'0} \\ m_{y'0} \\ m_{z'0} \end{pmatrix} = \chi\begin{pmatrix} 1 & 0 & 0 \\ 0 & cos\phi & sin\phi \\ 0 & -sin\phi & cos\phi \end{pmatrix}\begin{pmatrix} h_{x'0} \\ h_{y'0} \\ h_{z'0} \end{pmatrix}$$

A1.2.42

$$\mathbf{m}' = \begin{pmatrix} m_{x'0} \\ m_{y'0} \\ m_{z'0} \end{pmatrix} = \begin{pmatrix} 1 & 0 & 0 \\ 0 & cos\phi & -sin\phi \\ 0 & sin\phi & cos\phi \end{pmatrix}\begin{pmatrix} \chi_{xx} & \chi_{xy} & 0 \\ \chi_{yx} & \chi_{yy} & 0 \\ 0 & 0 & 0 \end{pmatrix}\begin{pmatrix} 1 & 0 & 0 \\ 0 & cos\phi & sin\phi \\ 0 & -sin\phi & cos\phi \end{pmatrix}\begin{pmatrix} h_{x'0} \\ h_{y'0} \\ h_{z'0} \end{pmatrix} = \chi'\mathbf{h}'$$

A1.2.43

$$\chi' = \begin{pmatrix} \chi_{xx} & \chi_{xy} & 0 \\ cos\phi\chi_{yx} & cos\phi\chi_{yy} & 0 \\ sin\phi\chi_{yx} & sin\phi\chi_{yy} & 0 \end{pmatrix}\begin{pmatrix} 1 & 0 & 0 \\ 0 & cos\phi & sin\phi \\ 0 & -sin\phi & cos\phi \end{pmatrix}$$

$$= \begin{pmatrix} \chi_{xx} & cos\phi\chi_{xy} & sin\phi\chi_{xy} \\ cos\phi\chi_{yx} & cos^2\phi\chi_{yy} & cos\phi sin\phi\chi_{yy} \\ sin\phi\chi_{yx} & cos\phi sin\phi\chi_{yy} & sin^2\phi\chi_{yy} \end{pmatrix} \qquad \text{A1.2.44}$$

This final expression may be useful for numerical calculations

Summary of principal results

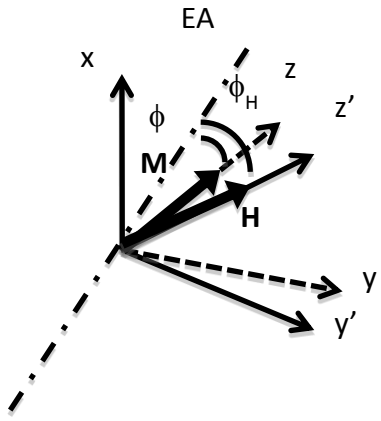

$$\frac{d\mathbf{u}}{dt} = -|\gamma|\mathbf{u}\times\mathbf{H}_{eff} + \frac{\alpha}{M}\mathbf{u}\times\frac{d\mathbf{u}}{dt} - aM\mathbf{u}\times(\mathbf{u}\times\mathbf{p}) + \mathrm{b}(\mathbf{u}\times\mathbf{p})$$

$$= -|\gamma|\mathbf{u}\times\left(\mathbf{H}_{eff} - \frac{b}{|\gamma|}\mathbf{p} + a\frac{M}{|\gamma|}\mathbf{u}\times\mathbf{p} - \frac{\alpha}{|\gamma|}\frac{d\mathbf{u}}{dt}\right)$$

$$E = -\mathbf{M}\cdot(\mathbf{H}+\mathbf{h}) + \frac{1}{2}\mathbf{M}D\mathbf{M} - K\left(\mathbf{u}.\hat{\mathbf{k}}\right)^2 - K_\perp(\mathbf{u}.\hat{\mathbf{x}})^2,\ D_{xx} = 4\pi, D_{yy} = D_{zz} = 0,$$

Static conditions are $-Hsin(\phi_H - \phi) + 2Ksin\phi cos\phi - \frac{b}{|\gamma|}sin(\phi_p - \phi) = 0$

$$u_{xs} = \frac{\alpha M}{|\gamma|}sin(\phi_p - \phi)\left[Hcos(\phi_H - \phi) + (D_{xx} - D_{zz})M - \frac{2K_\perp}{M} - 2Kcos^2\phi - \frac{b}{|\gamma|}cos(\phi_p - \phi)\right]^{-1}$$

which we need to verify is a small quantity

$$\chi = \frac{M}{\Delta}\begin{pmatrix} \left[Hcos(\phi_H - \phi) + (D_{yy} - D_{zz})M + \frac{2K}{M}cos2\phi - \frac{b}{|\gamma|}cos(\phi_p - \phi) - \frac{i\omega\alpha}{|\gamma|}\right] & \left[\frac{aM}{|\gamma|}cos(\phi_p - \phi) - \frac{i\omega}{|\gamma|}\right] \\ -\left[\frac{aM}{|\gamma|}cos(\phi_p - \phi) - \frac{i\omega}{|\gamma|}\right] & \left[Hcos(\phi_H - \phi) + (D_{xx} - D_{zz})M - \frac{2K_\perp}{M} + \frac{2K}{M}cos^2\phi - \frac{b}{|\gamma|}cos(\phi_p - \phi) - \frac{i\omega\alpha}{|\gamma|}\right] \end{pmatrix}$$

A1.2.45

$$\Delta = \begin{bmatrix} Hcos(\phi_H - \phi) + (D_{yy} - D_{zz})M + \\ \frac{2K}{M}cos2\phi - \frac{b}{|\gamma|}cos(\phi_p - \phi) \end{bmatrix} \begin{bmatrix} Hcos(\phi_H - \phi) + (D_{xx} - D_{zz})M - \frac{2K_\perp}{M} + \\ \frac{2K}{M}cos^2\phi - \frac{b}{|\gamma|}cos(\phi_p - \phi) \end{bmatrix} +$$

$$\left[\frac{aM}{|\gamma|}cos(\phi_p - \phi)\right]^2 - \left(\frac{\omega}{|\gamma|}\right)^2(1+\alpha^2) - 2\frac{i\omega}{|\gamma|}\frac{aM}{|\gamma|}cos(\phi_p - \phi) - \frac{i\omega\alpha}{|\gamma|}\left[2Hcos(\phi_H - \phi) + (D_{xx} + D_{yy} - 2D_{zz})M - \frac{2K_\perp}{M} + \frac{2K}{M}(cos2\phi + cos^2\phi) - \frac{2b}{|\gamma|}cos(\phi_p - \phi)\right]$$

A1.2.46

from which the resonance frequency and linewidth are given by

$$\left(\frac{\omega}{|\gamma|}\right)^2 = \left[Hcos(\phi_H - \phi) + (D_{yy} - D_{zz})M + \frac{2K}{M}cos2\phi - \frac{b}{|\gamma|}cos(\phi_p - \phi)\right] \times \left[Hcos(\phi_H - \phi) + (D_{xx} - D_{zz})M - \frac{2K_\perp}{M} + \frac{2K}{M}cos^2\phi - \frac{b}{|\gamma|}cos(\phi_p - \phi)\right]$$

A1.2.47

$$\Delta\omega = \frac{c}{\sqrt{3}\omega_{res}} = \frac{c}{\sqrt{3}\omega_{res}}\omega_{res}(\alpha\omega_a + 2\omega_{STT}) = \frac{(\alpha\omega_a + 2\omega_{STT})}{\sqrt{3}} = \frac{\left(\alpha|\gamma|H_a + 2aMcos(\phi_p - \phi)\right)}{\sqrt{3}}$$

A1.2.48

$$H_a = 2Hcos(\phi_H - \phi) + (D_{xx} + D_{yy} - 2D_{zz})M - \frac{2K_\perp}{M} + \frac{2K}{M}(cos2\phi + cos^2\phi) - \frac{2b}{|\gamma|}cos(\phi_p - \phi)$$

Let's consider the case that **H** is sufficiently large that **M** and **H** are quasi-aligned and $\phi = \phi_H$. Furthermore let us assume that H is still sufficiently small that the pinned layer magnetisation remains parallel to the EA of the free layer i.e. $\phi_p = 0$, and let us ignore in-plane demagnetizing fields, then

$$\chi = \frac{M}{\Delta}\begin{pmatrix} \left[H + \frac{2K}{M}cos2\phi_H - \frac{b}{|\gamma|}cos\phi_H - \frac{i\omega\alpha}{|\gamma|}\right] & \left[\frac{aM}{|\gamma|}cos\phi_H - \frac{i\omega}{|\gamma|}\right] \\ -\left[\frac{aM}{|\gamma|}cos\phi_H - \frac{i\omega}{|\gamma|}\right] & \left[H + 4\pi M - \frac{2K_\perp}{M} + \frac{2K}{M}cos^2\phi_H - \frac{b}{|\gamma|}cos\phi_H - \frac{i\omega\alpha}{|\gamma|}\right] \end{pmatrix}$$

A1.2.49

$$\Delta = \left[H + \frac{2K}{M}cos2\phi_H - \frac{b}{|\gamma|}cos\phi_H\right]\left[H + 4\pi M - \frac{2K_\perp}{M} + \frac{2K}{M}cos^2\phi_H - \frac{b}{|\gamma|}cos\phi_H\right] + \left[\frac{aM}{|\gamma|}cos\phi_H\right]^2 - \left(\frac{\omega}{|\gamma|}\right)^2(1+\alpha^2) - 2\frac{i\omega}{|\gamma|}\frac{aM}{|\gamma|}cos\phi_H - \frac{i\omega\alpha}{|\gamma|}\left[2H + 4\pi M - \frac{2K_\perp}{M} + \frac{2K}{M}(cos2\phi_H + cos^2\phi_H) - \frac{2b}{|\gamma|}cos\phi_H\right]$$

A1.2.50

$$\left(\frac{\omega}{|\gamma|}\right)^2 = \left[H + \frac{2K}{M}cos2\phi_H - \frac{b}{|\gamma|}cos\phi_H\right]\left[H + 4\pi M - \frac{2K_\perp}{M} + \frac{2K}{M}cos^2\phi_H - \frac{b}{|\gamma|}cos\phi_H\right]$$

A1.2.51

$$\Delta\omega = \frac{(\alpha|\gamma|H_a + 2aMcos\phi_H)}{\sqrt{3}}$$

A1.2.52

$$H_a = 2H + 4\pi M - \frac{2K_\perp}{M} + \frac{2K}{M}(cos2\phi_H + cos^2\phi_H) - \frac{2b}{|\gamma|}cos\phi_H$$

A1.2.53

We can then compare with Petit et al.[177] for the case that $\phi_H = 0$.

$$\frac{d\mathbf{u}}{dt} = -|\gamma|\mathbf{u}\times\mathbf{H}_{eff} + \frac{\alpha}{M}\mathbf{u}\times\frac{d\mathbf{u}}{dt} - a_j\mathbf{u}\times(\mathbf{u}\times\mathbf{p}) + b_j(\mathbf{u}\times\mathbf{p})$$ i.e. $a_j = \frac{aM}{|\gamma|}$, $b_j = \frac{b}{|\gamma|}$

They neglect the uniaxial in-plane and out of plane anisotropy terms and choose the x-axis to lie normal to the plane. They state only one component of the susceptibility

$$\chi_{yy} = \chi'_{yy} + \chi''_{yy}$$

A1.2.54

$$\chi'_{yy} = |\gamma|M\frac{|\gamma|H'[\omega_0^2 - (1+\alpha^2)\omega^2] + \alpha\Delta\omega^2}{[\omega_0^2 - (1+\alpha^2)\omega^2]^2 + \Delta^2\omega^2},\ \chi''_{yy} = |\gamma|M\omega\frac{\Delta|\gamma|H' - \alpha[\omega_0^2 - (1+\alpha^2)\omega^2]}{[\omega_0^2 - (1+\alpha^2)\omega^2]^2 + \Delta^2\omega^2}$$

A1.2.55

$$H'_b = H_b + b_j,\ H' = H'_b + 4\pi M,\ \omega_0^2 = |\gamma|^2\left[H'H'_b + a_j^2\right],\ \frac{\Delta}{|\gamma|} = \alpha\left[4\pi M + 2H_b + 2b_j\right] + 2a_j$$

$$\omega_r^2 \approx |\gamma|^2\left[H'H'_b - \frac{\alpha^2}{2}H'(H' + 3H'_b) - \alpha\left(2H' + H'_b a_j\right)\right]$$

A1.2.56

Now we reduce our expressions further by making similar assumptions. Hence

$$\chi_{yy} = \frac{M}{\Delta_0}\left[H + 4\pi M - \frac{b}{|\gamma|} - \frac{i\omega\alpha}{|\gamma|}\right]$$

A1.2.57

The subscript 0 has been introduced to distinguish our quantity Δ from that introduced by Petit

$$\Delta_0 = \left[H - \frac{b}{|\gamma|}\right]\left[H + 4\pi M - \frac{b}{|\gamma|}\right] + \left[\frac{aM}{|\gamma|}\right]^2 - \left(\frac{\omega}{|\gamma|}\right)^2 (1+\alpha^2) - 2\frac{i\omega}{|\gamma|}\frac{aM}{|\gamma|} - \frac{i\omega\alpha}{|\gamma|}\left[2H + 4\pi M - \frac{2b}{|\gamma|}\right]$$

$$\Delta_0 = H'H_b' + a_j^2 - \left(\frac{\omega}{|\gamma|}\right)^2 (1+\alpha^2) - \frac{i\omega}{|\gamma|}\{\alpha[4\pi M + 2H_b + 2b_j] + 2a_j\} = \left(\frac{\omega_0}{|\gamma|}\right)^2 - \left(\frac{\omega}{|\gamma|}\right)^2 (1+\alpha^2) - \frac{i\omega\Delta}{|\gamma|^2}$$

A1.2.58

Therefore

$$\chi_{yy} = \frac{M}{\Delta_0}\left[H' - \frac{i\omega\alpha}{|\gamma|}\right] = \frac{|\gamma|^2 M}{[\omega_0^2 - (1+\alpha^2)\omega^2 - i\omega\Delta]}\left[H' - \frac{i\omega\alpha}{|\gamma|}\right] = \frac{|\gamma|^2 M[\omega_0^2 - (1+\alpha^2)\omega^2 + i\omega\Delta]}{\{[\omega_0^2 - (1+\alpha^2)\omega^2]^2 + \omega^2\Delta^2\}}\left[H' - \frac{i\omega\alpha}{|\gamma|}\right]$$

$$= \frac{|\gamma|M\{[\omega_0^2 - (1+\alpha^2)]|\gamma|H' + \alpha\omega^2\Delta + i\omega[\Delta|\gamma|H' - (\omega_0^2 - (1+\alpha^2)\omega^2)\alpha]\}}{\left\{[\omega_0^2 - (1+\alpha^2)\omega^2]^2 + \omega^2\Delta^2\right\}} \qquad \text{A1.2.59}$$

which is exactly the result of Petit et al.. Next we also reduce our more general results for the resonant frequency and linewidth

$$\left(\frac{\omega}{|\gamma|}\right)^2 = \left[H + \frac{2K}{M}cos2\phi_H - \frac{b}{|\gamma|}cos\phi_H\right]\left[H + 4\pi M - \frac{2K_\perp}{M} + \frac{2K}{M}cos^2\phi_H - \frac{b}{|\gamma|}cos\phi_H\right] = H_b'H'$$

A1.2.60

Which agrees with Petit to first order in the small quantities. Next

$$H_a = 2H + 4\pi M - \frac{2K_\perp}{M} + \frac{2K}{M}(cos2\phi_H + cos^2\phi_H) - \frac{2b}{|\gamma|}cos\phi_H = 2H + 4\pi M - \frac{2b}{|\gamma|} = 2H_b + 4\pi M + 2b_j$$

A1.2.61

so that $(\Delta\omega)_0 = \frac{(\alpha|\gamma|H_a + 2aMcos\phi_H)}{\sqrt{3}} = \frac{(\alpha|\gamma|(2H_b + 4\pi M + 2b_j) + 2|\gamma|a_j)}{\sqrt{3}} = \frac{\Delta}{\sqrt{3}|\gamma|}$ A1.2.62

Our full linewidth is the same as the "resonance peak linewdth" of Petit et al but for a factor of 1/√3 which relates to the different definitions of the linewidth. If we instead take the linewidth to be the FWHM then

$$L(\omega)\sim\{(\omega^2-\omega_{res}^2)+c^2\}^{-1},\ L_{max}=\frac{1}{c^2}\ \text{then for}\ L=\frac{1}{2}L_{max} \qquad \text{A1.2.63}$$

$$\frac{1}{[(\omega^2-\omega_{res}^2)+c^2]}=\frac{1}{2c^2},\ (\omega^2-\omega_{res}^2)^2=c^2$$

$$\omega=\sqrt{c+\omega_{res}^2}=\omega_{res}\sqrt{1+\frac{c}{\omega_{res}^2}}\approx\omega_{res}\pm c/(2\omega_{res}) \qquad \text{A1.2.64}$$

Therefore the FWHM linewidth $\frac{c}{\omega_{res}}$ should be compared to the form $\frac{c}{\sqrt{3}\omega_{res}}$ that we derived previously, and the different numerical pre-factors are fully explained.

Glossary

Acronyms

SHG	Second Harmonic Generation
KDP	Potassium deuterium phosphate
NDF	Neutral Density Filter
GT	Glan Thomson
BS	Beam Splitter
DUT	Device Under Test
DAQ	Data Acquisition
VSD	Voltage Spectrum Density
RBW	Resolution Bandwidth
MR	Magnetoresistance
STT	Spin Transfer Torque
STO	Spin Transfer Torque Oscillator
MTJ	Magnetic Tunnel Junction
GMR	Giant Magnetoresistance
TRSKM	Time Resolved Scanning Kerr Microscopy
MO	Microscope Objective
NA	Numerical Aperture
RR	Retro-reflector
MOKE	Magneto-optic Kerr effect
FWHM	Full Width Half Maxima
CPW	Coplanar Waveguide

OOMMF	Object Oriented Micromagnetic Framework
FFT	Fast Fourier Transform
SEM	Scanning Electron Microscope
FMR	Ferromagnetic Resonance
MFM	Magnetic Force Microscopy
SA	Symmetry Axis
TTL	Transistor-Transistor Logic
PW	Paddle Width
BL	Bridge Length
BW	Bridge Width
FA	Flare Angles
TMF	Thermal Magnetic Fluctuations
TMR	Tunnel Magnetoresistance

Bibliography

[1] A.H. Morrish, *The Physical Principles of Magnetism*, John Wiley & Sons (1965).

[2] Charles Kittel, Phys. Rev. **71**, 270 (1947).

[3] P. Zeeman, Philos. Mag., **5**, 226 (1897).

[4] L.D. Landau and E.M. Lifshitz (1977). *Quantum Mechanics: Non-Relativistic Theory*. **Vol. 3** (3rd ed.). Pergamon Press. ISBN 978-0-080-20940-1.

[5] H.N. Russel and F.A. saunders, Astrophysics J. **61**, 38 (1925).

[6] P. E. S. Wormer, Chemical Physics Letters, vol. **5**, 355 (1970).

[7] N.W.Ashcroft and N.D.Mermin, *Solid State Physics* (Philadelphia: Saunders College, 1976).

[8] J.H. Van Vleck, Science, New Series, **201**, 4351 (1978), pp. 113-120.

[9] Cullity; C. D. Graham (2008). *Introduction to Magnetic Materials, 2nd ed.* New York: Wiley-IEEE. pp. 116. ISBN 0471477419.

[10] J.H. van Vleck, Rev. Mod. Phys. **17**,27 (1945).

[11] C. Herring, Rev. Mod. Phys. **34**, 631 (1962).

[12] L. Pauling, Phys. Rev. 54 (1938), p. 899.

[13] J.H. Van Vleck, Rev. Mod. Phys. **25**, 220 (1964).

[14] Soshin Chikazumi, *Physics of Ferromagnetism*, Oxford University Press, New York, 1997, page 125, ISBN 0-19-851776-9.

[15] R. Stuart, W. Marshall, Phys. Rev. **120**, 353 (1960).

[16] M.A.Ruderman, C.Kittel, Phys. Rev. **96**, 99 (1954).

[17] T Kasuya, Progr. Theor. Phys. **16**, 45 (1956).

[18] K.Yoshida, Phys. Rev. **106**, 893 (1957).

[19] R. C. O'Handley, *Modern Magnetic Materials; Principles and Applications*, NewYork:Wiley (1999).

[20] P.W. Anderson. Phys. Rev. **115** , 2 (1959).

[21] David J. Griffiths, *Introduction to Electrodynamics*, third edition, Pearson Education Asia (2003).

[22] J. H. Van Vleck, Phys. Rev. **52**, 1178 (1938).

[23] J. Slater, Rev. Mod. Phys. **25**, 199 (1953).

[24] E. Wigner, Phys. Rev. **46**, 1002 (1934).

[25] L. Pauling, PROC N.A.S. **39**, 551(1953).

[26] J. C. Slater, Phys. Rev. **49**, 537 (1936).

[27] Peter Mohn, *Magnetism in the solid state*, Spinger-Verlag Berlin Heidelberg (2003).

[28] J. M. D. Coey, *Magnetism and Magnetic Materials*, Cambridge University Press (2010), p 134.

[29] Hubert and R. Schafer, *Magnetic Domains*, Berlin: Springer (1998).

[30] C. Kittel, Rev. Mod. Phys. **21**, 541 (1949).

[31] John C. Slonczewski, IEEE Trans. Magn., **21**, NO. 4, (1991).

[32] Schryer and Walker, JAP **45** (12), 5406 (1974).

[33] Guimarães, Alberto P., *Principles of Nanomagnetism*, Ser: NanoScience and Technology © Springer-Verlag Berlin Heidelberg 2009.

[34] J.Fidler, T Shrefl, W. Scholz, D. Suess, V.D. Tsiantos, R. Dittrich, M Kirschner, Physica B **343**, 200-205 (2004).

[35] J. Nogu´es, J. Sort, V. Langlais. Phys. Rep. **422**, 65 (2005).

[36] J. Nogu´es, I.K. Schuller, J. Magn. Magn. Mater. , **192**, 203(1999).

[37] Beaurepaire, E.; Bulou, H.; Scheurer, F.; Jean-Paul, K. (Eds.). *Magnetism and Synchrotron Radiation*, New Trends, Springer Proceedings in Physics, Vol. 133 (2009).

[38] L. R. Walker, Phys. Rev. **105**, 390 (1957).

[39] M. J. Hurben, C. E. Patton, J. Magn. Magn. Mater. **139**, 263 (1995).

[40] B. A. Kalinikos, IEEE Proc., **127** pt. H,4-10 (1980).

[41] S.O. Demokritov, B. Hillebrands, and A.N. Slavin, Phys. Rep. **348**, 442 (2001)

[42] D. D. Stancil. *Theory of Magnetostatic Waves.* Springer Verlag, New York (1993).

[43] R. W. Damon, J. R. Eshback, J. Phys. Chem. Solids, 308-320 (1961).

[44] B. A. Kalinikos, A. N. Slavin. J. Phys. C19, 7013 (1986).

[45] E. C. Stoner and E. P. Wohlfarth, Proc. Phys. Soc. (London), Ser. A, Mathematical and Physical Sciences. **240**, 599 (1948).

[46] Thomas L. Gilbert, IEEE Trans. Magn. **40**, 3443 (2004).

[47] J. A. Osborn, Phys. Rev. **67**, 351 (1945).

[48] Charles Kittel, Phys. Rev. **73,** 155 (1948).

[49] W. A. Yager, R. M. Bozorth, Phys. Rev. **72**, 80 (1947).

[50] C. Kittel, Introduction to Solid State Physics, 5th ed., John Wiley & Sons (1976).

[51] N.F. Mott, Proc. Phys. Soc. (London), Ser. A **153**, 699 (1936).

[52] N.F. Mott, Proc. Phys. Soc. (London), Ser. A **163**, 368 (1936).

[53] N.F. Mott, H. Jones, *The theory of the Properties of Metals and Alloy* (Dover, New York, 1958).

[54] N.F. Mott, Rev. Mod. Phys. **40**, 677 (1968).

[55] T.R. McGuire, R.I. Potter, IEEE Trans. Magn., **11**, 1018 (1975).

[56] A. Fert, I.A. Campbell, Phys. Rev. Lett. **21**, 1190 (1968).

[57] H. Brooks, Phys. Rev. **58**, 909 (1940).

[58] M. N. Baibich, J.M. Broto, A. Fert, F. Nguyen Van Dau, F. Petroff, P. Etienne, G. Creuzet, A. Friederich, and J. Chazelas, Phys. Rev. Lett. **61**, 2472 (1988).

[59] S. S. P. Parkin, N. More, and K. P. Roche, Phys. Rev. Lett. **64**, 2304 (1990).

[60] E.Y.Tsymbal, D.G.Pettifor, *Solid State Physics*, ed. by H. Ehrenreich and F. Spaepen, Vol. **56** (Academic Press, 2001) pp.113-237.

[61] A. Barthélémy, A. Fert, J-P. Contour, M. Bowen, V. Cros, J.M. De Teresa, A. Hamzic, J.C. Faini, J.M. George, J. Grollier, F. Montaigne, F. Pailloux, F. Petroff, C. Vouille , J. Magn. Magn. Mater. 246-245 (2002)68-76.

[62] T. Valet and A. Fert, Phys. Rev. B **48**, 7099 (1993).

[63] Stuart Parkin, Hyunsoo yang, See-Yun Yang, Masamitsu Hayashi, *Handbook of Magnetism and Advanced Magnetic Materials*, Edited by Helmut Kronmuller and Stuart Parkin. Volume 5: Spintronics and Magnetoelectronics. © 2007 John Wiley & Sons, Ltd. ISBN: 978-0-470-02217-7.

[64] John G. Simmons, J. Appl. Phys. **35**, 2655 (1964).

[65] John G. Simmons, J. Appl. Phys. **34**, 1793 (1963).

[66] Thomas E. Hartman, J. Appl. Phys. **35**, 3283 (1964).

[67] M. Julliere, Phys. Lett. **54A**, 225 (1975).

[68] Jagadeesh S. Moodera, George Mathon, J. Magn. Magn. Mater. **200**, 248 (1999).

[69] L. Berger, Phys. Rev. B **54**, 9353 (1996),.

[70] Slonczewski, J. Magn. Magn. Mater. **159**, L1 **(**1996**)**.

[71] A. Schuhl, D. Lacour C. R. , Physique **6**, 945 (2005).

[72] F. Bloch, Phys. Rev. **70**, 460 (1946).

[73] J.Z. Sun and D.C. Ralph , J. Magn. Magn. Mater. **320**, 1227 (2008).

[74] S. Zhang, P.M. Levy and A. Fert, Phys. Rev. Lett. **88**, 236601 (2002).

[75] A. M. Deac et al., Nat. Phys. **4**, 803 (2008).

[76] H.S. Bennett and E.A. Stern, Phys. Rev. **137**, A448(1965).

[77] Osamu Yamashita, Optik - International Journal for Light and Electron Optics, (2011).

[78] Jenkins F.A. and White H.E., "*Magneto-Optics and Electronics",* Chapter 32, Fundamentals of Optics, 4th ed. 1957. pp. 679-686.

[79] Z. Q. Qiu and S. D. Bader, in *Nonlinear Optics in Metals*, edited by K. H. Bennemann **(**Clarendon, Oxford, 1998**)**, pp. 1–41.

[80] Weinberger, P. Philosophical Magazine Letters **88** (12): 897–907(2008).

[81] C. C. Robinson, J. Opt. Soc. Am. **53**, 681 (1963).

[82] E. Carpene, E. Mancini, C. Dallera, E. Puppin and S. De Silvestri, J.Appl.Phys.**108**, 063919 (2010).

[83] J.M. Florczak, E. Dan Dahlberg. J. Appl. Phys. **67** (12), (1990).

[84] C. Daboo, R. Hicken, E. Gu, M. Gester, S. Gray, D. Eley, E. Ahmad, J. Bland, R. Ploessl and J. Chapman.. Phys. Rev. B, **51,** 15964 (1995).

[85] J. M. Florczak and E. D. Dahlberg , Phys. Rev. B **44**, 9338 (1991).

[86] Etienne du TREMOLET de LACHEISSERIE, Damien GIGNOUX and Michel SCHLENKER, *Magnetism Fundamentals*, Springer (2006).

[87] Lars Onsager, Phys. Rev., **37**(4), 405(1931).

[88] Lars Onsager, Phys. Rev., **38**(12), 2265 (1931).

[89] Herbert B. Callen, Phys. Rev., **73**(11), 1349 (1948).

[90] H. A. Lorentz, *The Theory of Electrons* (B. G. Tuebner, Leipzig, 19(9)).

[91] G. Wannier, Phys. Rev., **72**, 304 (1947).

[92] A.V. Sokolov, *Optical Properties of Metals,* Blackie and Son Limited, Bishopbriggs, Glasglow (1961).

[93] H. R. Hulme, Proc. R. Soc. London, Ser. A **135**, 237 (1932).

[94] J. Zak, E.R. Moog, C. Liu and S.D. Badger, J. Magn. Magn. Mater. 89, 107 (1990).

[95] P.Q.J. Nederpel and J.W.D. Matens, Rev. Sci. Instrum. **56**(5), May 1985.

[96] Eugene Hecht, *Optics*, Fourth edition, Pearson Education (2006).

[97] Z. Q. Qiu and S. D. Bader, J. Magn. Magn. Mater. **200**, 664 **(**1999**)**.

[98] J. Wu, J.R. Moore and R.J. Hicken, J. Magn. Magn. Mater. **222**, 189 (2000). (2002).

[99] M.J. Freiser, IEEE Trans. Magn. MAG **4**, 152 (1968).

[100] Spectra-Physics Tsunami Mode-Locked Ti:sapphire Laser, User Manual, Part Number 0000-232A (1995).

[101] Paul Steven Keatley, PhD Thesis, *Time-Resolved Magneto-Optical Investigations of Picosecond Magnetisation Dynamics in Arrays of Non-Ellipsoidal Ferromagnetic Nano-Elements,* University of Exeter (2008).

[102] W.K. Hiebert, PhD Thesis, *Experimental Micromagnetic Dynamics: Ultrafast Magnetisation Reversal Using Time Resolved Scanning Kerr Effect Microscopy*, University of Alberta (2001).

[103] John H. Scofield, *Four-Probe Resistance primer,* Advance Laboratory, Physics 414 (2000).

[104] Model 6221AC &DC Current source, Referenece Manual, 622X-901-01, Rev. A (2004), Keithley Instruments, Inc. Cleveland, Ohio, USA.

[105] Model 2182&2182A Nanovoltmeter, User's Manual, 2182A-900-01, Rev. A (2004), Keithley Instruments, Inc. Cleveland, Ohio, USA.

[106] "*Low Level Measurements handbook*", 6th edit., Keithley Instruments, Inc. Cleveland, Ohio, USA.

[107] F. Hofman, R.J.J. Zijlstra, Solid State Communcations, **72**, 12, 1163-1166 (1989).

[108] V.V. Kruglyak, A. Barman, R.J. Hicken, J.R. Childress, and J.A. Katine, Phys. Rev. B **71**, 220409(R) (2005).

[109] J.M. Shaw, T.J. Silva, M.L. Schneider, and R.D. McMichael, Phys. Rev. B **79**, 184404 (2009).

[110] V.V. Kruglyak, P.S. Keatley, A. Neudert, R.J. Hicken, J.R. Childress, and J.A. Katine, Phys. Rev. Lett. **104**, 027201 (2010).

[111] S. Tacchi, M. Madami, G. Gubbiotti, G. Carlotti, H. Tanigawa, T. Ono, and M.P. Kostylev, Phys. Rev. B **82**, 024401 (2010).

[112] P.S. Keatley, V.V. Kruglyak, A. Neudert, E.A. Galaktionov, R.J. Hicken, J.R. Childress, and J.A. Katine, Phys. Rev. B **78**, 214412 (2008).

[113] V.V. Kruglyak, S.O. Demokritov, and D. Grundler, J. Phys. D-Appl. Phys. **43**, 264001 (2010).

[114] Z. Liu, R.D. Sydora, and M.R. Freeman, Phys. Rev. B **77**, 174410 (2008).

[115] A. Barman, S. Wang, J.D. Maas, A.R. Hawkins, S. Kwon, A. Liddle, J. Bokor, and H. Schmidt, Nano Letters **6**, 2939 (2006).

[116] G. Gubbiotti, M. Madami, S. Tacchi, G. Carlotti, A.O. Adeyeye, S. Goolaup, N. Singh, and A.N. Slavin, J. Magn. Magn. Mater. **316**, 338 (2007).

[117] V.E. Demidov, M. Buchmeier, K. Rott, P. Krzysteczko, uuml, J. nchenberger, G. Reiss, and S.O. Demokritov, Phys. Rev. Lett.**104**, 217203 (2010).

[118] J.P. Nibarger, R. Lopusnik, Z. Celinski, and T.J. Silva, Appl. Phys. Lett. **83**, 93 (2003).

[119] M. Donahue and D.G. Porter, OOMMF User's Guide, Version 1.0, NISTIR 6376 (National Institute of Standards and Technology, Gaithersburg, MD, 1999): see http://math.nist.gov/oommf.

[120]A. Barman, V.V. Kruglyak, R.J. Hicken, A. Kundrotaite, and M. Rahman, Appl. Phys. Lett. **82**, 3065 (2003).

[121] V.V. Kruglyak, P.S. Keatley, R.J. Hicken, J.R. Childress, and J.A. Katine, Phys. Rev. B **75**, 024407 (2007).

[122] S. Cornelissen, L. Bianchini, A. Helmer, T. Devolder, J.-V. Kim, M.O. de Beeck, W. Van Roy, L. Lagae, and C. Chappert, J. Appl. Phys.**105**, 07B903 (2009).

[123] Z. Zeng, K.H. Cheung, H.W. Jiang, I.N. Krivorotov, J.A. Katine, V. Tiberkevich, and A. Slavin, Phys. Rev. B **82**, 100410 (2010).

[124] See supplementary material of Keatley PS, Gangmei P, Dvornik M, Hicken RJ, Childress JR, Katine JA. Applied Physics Letters 98, 082506 (2011).

[125] B.B. Maranville, J. Mallett, T.P. Moffat, R.D. McMichael, A.P. Chen, and J.W.F. Egelhoff, J. Appl. Phys. **97**, 10A721 (2005).

[126] Hickey, B. J. & Marrows, C. H., Phil. Trans. R. Soc. A **369**, 3025 (2011).

[127] M. Tsoi, A. G. M. Jansen, J. Bass, W.-C. Chiang, M. Seck, V. Tsoi, and P. Wyder, Phys. Rev. Lett. **80**, 4281(1998).

[128] Katine, J. A., Albert, F. J., Buhrman, R. A., Myers, E. B. & Ralph, D. C. Phys. Rev. Lett. **84**, 3149 (2000).

[129] Dussaux, A. *et al.* Large microwave generation from current-driven magnetic vortex oscillators in magnetic tunnel junctions. Nat Commun **1**, 8 (2010).

[130] R. Zivieri, F. Montoncello, L. Giovannini, F. Nizzoli, S. Tacchi, M. Madami, G. Gubbiotti, G. Carlotti, and A. O. Adeyeye, Phys. Rev. B **83**, 054431 (2011).

[131] Topp, J., Heitmann, D., Kostylev, M. P. & Grundler, D. Phys. Rev. Lett. **104**, 207205 (2010).

[132]Farkhad G. Aliev, Juan F. Sierra, Ahmad A. Awad, Gleb N. Kakazei, Dong-Soo Han, Sang-Koog Kim, Vitali Metlushko, Bojan Ilic, and Konstantin Y. Guslienko. Phys. Rev. B **79**, 174433 (2009).

[133] Ruotolo A, Cros V, Georges B, Dussaux A, Grollier J, Deranlot C, Guillemet R, Bouzehouane K, Fusil S and Fert A. Nature Nanotechnology **4**, 528 (2009).

[134] A. Dussaux, A. V. Khvalkovskiy, J. Grollier, V. Cros, A. Fukushima, M. Konoto, H. Kubota, K. Yakushiji, S. Yuasa, K. Ando, A. Fert. Appl. Phys. Lett. **98**, 132506 (2011).

[135] Demidov, V. E., Urazhdin, S. & Demokritov, S. O. Nat Mater **9**, 984 (2010).

[136] M. Madami, S. Bonetti, G. Consolo, S. Tacchi, G. Carlotti, G. Gubbiotti, F. B. Mancoff, M. A. Yar and J. Åkerman. Nature Nanotechnology **6**, 635 (2011).

[137] Shaw, J. M., Silva, T. J., Schneider, M. L. & McMichael, R. D. Phys. Rev. B **79**, 184404 (2009).

[138] H. T. Nembach, Justin M. Shaw, T. J. Silva, W. L. Johnson, S. A. Kim, R. D. McMichael, and P. Kabos. Phys. Rev. B **83**, 094427 (2011).

[139] Henning Ulrichs, Vladislav E. Demidov, Sergej O. Demokritov, Alexey V. Ognev, Maxim E. Stebliy, Ludmila A. Chebotkevich, Alexander S. Samardak . Phys. Rev. B **83**, 184403 (2011).

[140] Dvornik, M., Bondarenko, P. V., Ivanov, B. A. & Kruglyak, V. V. J. Appl. Phys. **109**, 07B912 (2011).

[141] P. Czoschke, S. Kaka, N. J. Gokemeijer, and S. Franzen, Appl. Phys. Lett. **97**, 242504 (2010).

[142] R. Proksch, P. Neilson, S. Austvold, and J. J. Schmidt, Appl. Phys. Lett. **74**, 1308 (1999).

[143] W. Lu, Z. Li, K. Hatakeyama, G. Egawa, S. Yoshimura, and H. Saito, Appl. Phys. Lett. **96**, 143104 (2010).

[144] M. Abe and Y. Tanaka, IEEE Trans. Magn. **40**, 1708 (2004).

[145] A. Neudert, P. S. Keatley, V. V. Kruglyak, J. McCord, and R. J. Hicken, IEEE Trans. Magn. **44**, 3083 (2008).

[146] P. S. Keatley, V. V. Kruglyak, A. Neudert, M. Delchini, R. J. Hicken, J. R. Childress, and J. A. Katine, J. Appl. Phys, **105**, 07D308 (2009).

[147] M. R. Freeman and J. F. Smyth, J. Appl. Phys. **79**, 5898 (1996)

[148] S. Wakana, T. Nagai, and Y. Sakata, J. Magn. Magn. Mater. 235, 231 (2001).

[149] T. Nagai, H. Sekiguchi, and A. Ito, IEEE Trans. Magn. **39**, 3441 (2003).

[150] M. R. Freeman, A. Y. Elezzabi, and J. A. H. Stotz, J. Appl. Phys. **81**, 4516 (1997).

[151] D. Z. Bai, J.-G. Zhu, P. Luo, K. Stoev, and F. Liu, IEEE Trans. Man. **42**, 473 (2006).

[152] D. Z. Bai and J.-G. Zhu, J. Appl. Phys. **93**, 6540 (2003).

[153] M. Mochizuki, C. Ishikawa, Y. Okada, and K. Nakamoto, J. Magn. Magn. Mater. 287, 372 (2005).

[154] O. Heinonen, A. Nazarov and Martin L. Plumer, J. Appl. Phys. **99**, 08S302 (2006).

[155] P. S. Keatley, V. V. Kruglyak, R. J. Hicken, J. R. Childress, and J. A. Katine, J. Magn. Magn. Mater. **306**, 298 (2006).

[156] M. Mallary, Chapter 11 "*Recording Head Design*" within "*The Physics of Ultrahigh-Density Magnetic Recording"*, ed. M.L. Plumer, J. van Ek, and D. Weller, Springer Series in Supolarisationace Sciences (2001).

[157] M. Mallary, US Pat#5,085,935, Flux Spreading Thin Film Magn. Dev. 2/4/92.

[158] D. V. Berkov and N. L. Gorn, J. Phys. D **41**, 164013 (2008).

[159] M. D. Stiles and J. Miltat, Spin Transfer Torque and Dynamics (Springer, Berlin Heidelberg, 2006), pp. 225–308.

[160] S. I. Kiselev, J. C. Sankey, I. N. Krivotorov, N. C. Emley, R. J. Schoelkopf, R. A. Buhrmann, and D. C. Ralph, Nature **425**, 380 (2003).

[161] K. V. Thadani, G. Finocchio, Z.-P. Li, J. C. Sankey, I. N. Krivotorov, Y.-T. Cui, R. A. Buhrmann, and D. C. Ralph, Phys. Rev. B **78**, 024409 (2008).

[162] K. Mizushima, T. Nagasawa, K. Kudo, Y. Saito, and R. Sato, Appl. Phys. Lett. **94**, 152501(2009).

[163] J.A. Katine, Eric E. Fullerton, J. Magn. Magn. Mat.**320**,1217-1226 (2008).

[164] Z. M. Zeng, P. Upadhyaya, P. K. Amiri, K. H. Cheung, J. A. Katine, J. Langer, K. L. Wang, and H. W. Jiang, Appl. Phys. Lett. **99**, 032503 (2011).

[165] N. Smith and P. Arnett, Appl. Phys. Lett. **78**, 1448 (2001).

[166] A. V. Nazarov, K. Nikolaev, Z. Gao, H. Cho, and D. Song, J. Appl. Phys. **103**, 07A503 (2008).

[167] Sankey, J. C. et al. Nature Phys. **4**, 67 (2008).

[168] Kubota, H. et al. Nature Phys. **4**,37 (2008).

[169] Theodonis, I., Kioussis, N., Kalitsov, A., Chshiev, M. & Butler, W. H. Phys. Rev. Lett. **97**, 237205 (2006).

[170] Heiliger, C. & Stiles, M. D., Phys. Rev. Lett. **100**, 186805 (2008).

[171] M. H. Jung, S. Park, C.-Y. You, and S. Yuasa, Phys. Rev. B **81**, 134419 (2010).

[172] J. Xiao, G. E. W. Bauer, and A. Brataas, Phys. Rev. B **77**, 224419 (2008).

[173] P. K. Muduli, O. G. Heinonen, and J. Akerman, Phys. Rev. B **83**, 184410 (2011).

[174] S. Oh, S. Park, A. Manchon, M. Chshiev, J. Han, H. Lee, J. Lee, K. Nam, Y. Jo, Y. Kong, B. Dieny, and K. Lee, Nat. Phys. **5**, 898 (2009).

[175] O. G. Heinonen, S. W. Stokes, and J. Y. Yi, Phys. Rev. Lett. **105**, 066602 (2010).

[176] Michael R Scheinfein and Elizabeth A Price, *LLG User Manual v2.50* (E. Aspen DriveTempe, AZ 85282, 2008), *http://llgmicro.home.mindspring.com/*.

[177] Petit *et al.*, Phys. Rev. Lett. **98**, 077203 (2007).

[178]S. Petit, N. de Mestier, C. Baraduc, C. Thirion, Y. Liu, M. Li, P. Wang, and B. Dieny, Phys. Rev. B **78**, 184420 (2008).

[179] Yisong Zhang, Hui Zhao, Andrew Lyle, Paul A. Crowell, and Jian-Ping Wang, Appl. Phys. Lett. **100**, 032405 (2012).

[180] S. Kaka, M. R. Pufall, W. H. Rippard, T. J. Silva, S. E. Russek, and J. A. Katine, Nature(London) **437**, 389 (2005).

[181] F. B. Mancoff, N. D. Rizzo, B. N. Engel, and S. Tehrani, Nature (London) **437**, 393 (2005).

[182] B. Georges, J. Grollier, M. Darques, V. Cros, C. Deranlot, B. Marcilhac, G. Faini, and A. Fert, Phys. Rev. Lett. **101**, 017201 (2008).

[183] B. Georges, J. Grollier, V. Cros, A. Fert, arXiv:0804.4855 (2008).

[184] J. Persson, Yan Zhou, and Johan Akerman, J. Appl. Phys. **101**, 09A503 (2007).

[185] J. Grollier, V. Cros, and A. Fert, cond-mat/0509326(2005).

[186] S. M. Rezende, F. M. de Aguiar, R. L. Rodriguez-Suarez, and A. Azevedo, Phys. Rev. Lett. **98**,087202 (2007).

[187] S. Neusser, G. Duerr, S. Tacchi, M. Madami, M.L. Sokolovskyy, G. Gubbiotti, M. Krawczyk, and D. Grundler, Phys. Rev. B. **84**, 094454 (2011).

[188] S. Neusser, B. Botters, M. Becherer, D. Schmitt-Landsiedel, and D. Grundler, Appl. Phys. Lett. **93**, 122501 (2008).

[189] S. Neusser, B. Botters, and D. Grundler, Phys. Rev. B 78, 054406 (2008).